CRANFIELD UNIVERSITY

JIALUO DING

Thermo-mechanical Analysis of Wire and Arc Additive Manufacturing Process

School of Applied Science
Manufacturing and Material Department

PhD thesis
Academic Year: 2008- 2012

Supervisor: Professor Stewart Williams
January 2012

CRANFIELD UNIVERSITY

School of Applied Science
Manufacturing and Material Department

PhD Thesis

Academic Year 2008 - 2012

JIALUO DING

Thermo-mechanical Analysis of Wire and Arc Additive Manufacturing Process

Supervisor: Professor Stewart Williams

January 2012

This thesis is submitted in partial fulfilment of the requirements for the degree of Doctor

ABSTRACT

Conventional manufacturing processes often require a large amount of machining and cannot satisfy the continuously increasing requirements of a sustainable, low cost, and environmentally friendly modern industry. Thus, Additive Manufacturing (AM) has become an important industrial process for the manufacture of custom-made metal workpieces. Among the different AM processes, Wire and Arc Additive Manufacture (WAAM) has the ability to manufacture large, low volume metal work-pieces due to its high deposition rate. In this process, 3D metallic components are built by depositing beads of weld metal in a layer by layer fashion.

However, the non-uniform expansion and contraction of the material during the thermal cycle results in residual stresses and distortion. To obtain a better understanding of the thermo-mechanical performance of the WAAM process, a study based on FE simulation was untaken in this thesis. The mechanism of the stress generation during the deposition process was analysed via a 3D transient thermo-mechanical FE model which is verified with experimental results. To be capable of analysing the thermo-mechanical behaviour of large-scale WAAM components, an efficient FE approach was developed which can significantly reduce the computational time. The accuracy of this model was validated against the transient model as well as experimental measurements.

With the help of the FE models studies on different deposition parameters, deposition sequences and deposition strategies were carried out. It has been proved that the residual stresses and the distortions are possible to be reduced by using optimised deposition parameters and sequences. In addition, a robot path generation prototype has been developed to help efficiently integrate these optimised process settings in the real-wold WAAM process.

ACKNOWLEDGEMENTS

I would like to thank my husband Dr Jörn Mehnen for his advices, encouragement and unshakable faith in me throughout the duration of this research. And also I would like to thank my parents for their consistently encouragement and the support on my life. And thanks to my daughter Kim Anne Mehnen for the joys and smiles she gives to me.

I wish to express my sincere appreciation to my supervisor Prof. Stewart Williams for his support and help in the completion of this research. I would like to thank Dr Paul Colegrove for his advice on this research and Prof. David Allen for providing helpful suggestions on the committee meetings. I would like to thank Dr Supriyo Ganguly and Dr Anna Paradowska for their support on the stress analysis. I would also express my thanks to all the RUAM members for their technique support and assistance during this research.

I also would like to thank Cranfield Innovative Manufacturing Research Centre (IMRC) and the Chinese Scholarship Council (CSC) for their sponsorship for my research. And I would like to say thanks to all the staffs in Manufacturing Department and also Welding Engineering and Research Centre for their support.

TABLE OF CONTENTS

LIST OF FIGURES

LIST OF TABLES

LIST OF EQUATIONS

NOMENCLATURE

a_f	The length of the frontal ellipsoid of the heat source model
a_r	The length of the rear ellipsoid of the heat source model
AIP	Average Instantaneous Power
ALH	Average Layer Height
AM	Additive Manufacturing
b	the width of the heat source
c	the depth of the heat source
CAD	Computer Aided Design
CAM	Computer Aided Manufacture
CMT	Cold Metal Transfer
CTWD	Contact Tip to Work Distance
DoE	Design of Experiment
EWW	Effective Wall Width
FE	Finite Element
f_f	The factor for distributing the power to the front of the heat source
f_r	The factor for distributing the power to the rear of the heat source
FZ	Fusion Zone
GWAM	Gas Metal Arc Welding
HAZ	Heat Affected Zone

HI	Heat Input
ISM	Iterative Substructure Method
LoHS	Length of the Heat Source
MTS	Mismatched Thermal Strain
MIG	Metal Inert Gas
P	Penetration
Q	The energy input rate
RM	Rapid Manufacturing
RP	Rapid Prototyping
RT	Rapid Tooling
RUAM	Ready-to-use Additive Manufacture
SA	Submerges Arc
SLS	Selective Laser Sintering
SLC	Selective Laser Cladding
SMD	Shape Metal Deposition
TCS	Thermal Contraction Strain
TIG	Tungsten Inert Gas
TS	Travel Speed
WAAM	Wire and Arc Additive Manufacture
Wav	Surface Waviness
WFS	Wire Feed Speed

LIST OF PUBLICATIONS

Journal papers

Ding, J., Colegrove, P., Mehnen, J., Ganguly, S., Sequeira Almeida, P.M., Wang, F., and Williams, S. (2011) “Thermo-mechanical analysis of Wire and Arc Additive Layer Manufacturing process on large multi-layer parts”, Computational Materials Science, vol. 50, pp. 3315-3322.

Mehnen, J., Ding, J., Lockett, H., and Kazanas, P. (2012) “Design for wire and arc additive manufacture”, International Journal of Product Design (accepted).

Ding, J., Colegrove, P., Mehnen, J., Williams, S., Wang, F., Sequeira Almeida, P.M., and Coules, H. (2012) “A computationally efficient finite element model of wire and arc additive manufacture”, Finite Element in Analysis and Design (submitted).

Conference papers

Mehnen, J., Ding, J., Lockett, H., and Kazanas, P. Design for wire and arc additive layer manufacture. Proceedings of the 20th CIRP Design Conference, Nantes, France, 19-21 April, 2010. Ed. A. Bernard

Ding J, Wessing S, Trautmann H, Mehnen J & Naujoks B. (2010) Sequential Parameter Optimisation for Multi-Objective Evolutionary Optimisation of Additive Layer Manufacturing, Naples.

Conference presentation

Ding, J., Mehnen, J., and Almeida, P., (2009) Modelling and Multi-objective Optimisation of Weld Bead Formations in Additive Manufacturing. In: *IFCS Conference of the International Federation of Classification Societies*, Dresden, Germany, 13 - 18 March 2009.

1 INTRODUCTION

1.1 Research Background

Conventional manufacturing processes which often result in a high rate of machining cannot satisfy the continuously increasing requirements of a sustainable, low cost, and environmentally friendly modern industry. Thus, Additive Manufacturing (AM) has become an important industrial process for the manufacture of custom-made metal workpieces. The AM process takes CAD data and converts it into layers and then CNC language and process parameters. In this way, freeform components can be fabricated.

As shown in Figure 1-1 the basic metal AM system comprises four parts: CNC controller, motion system, heat source for melting the metal and a material supply system. Current commercial metal AM systems are based around power beam heating sources (usually lasers) and material supply in the form of powder, most commonly in the form of a powder bed. In this approach a roller is used to add a layer of metallic powder and the laser is scanned over the surface of the powder fusing or melting a patterned layer. The same process is repeated for the subsequent layers until the component reaches the designed height (Kruth et al., 2007). This kind of systems are capable of producing extremely complex structures and enable either weight saving or added functionality to existing or future components. These systems feature build rates of a few tens of grams per hour and build volumes typically 0.3 x 0.3 x 0.3 m^3. Due to the sensitivity of powders to contamination and for safety reasons, all power beam systems need an environmental chamber (known as in-chamber) filled with an inert gas. Consequently AM components made by these methods have a very high build cost because of the system complexity and the slow build rates. As a result the market for these systems is limited to niche areas such as medical implants, small complex high value parts (e.g. engine components) and jewellery.

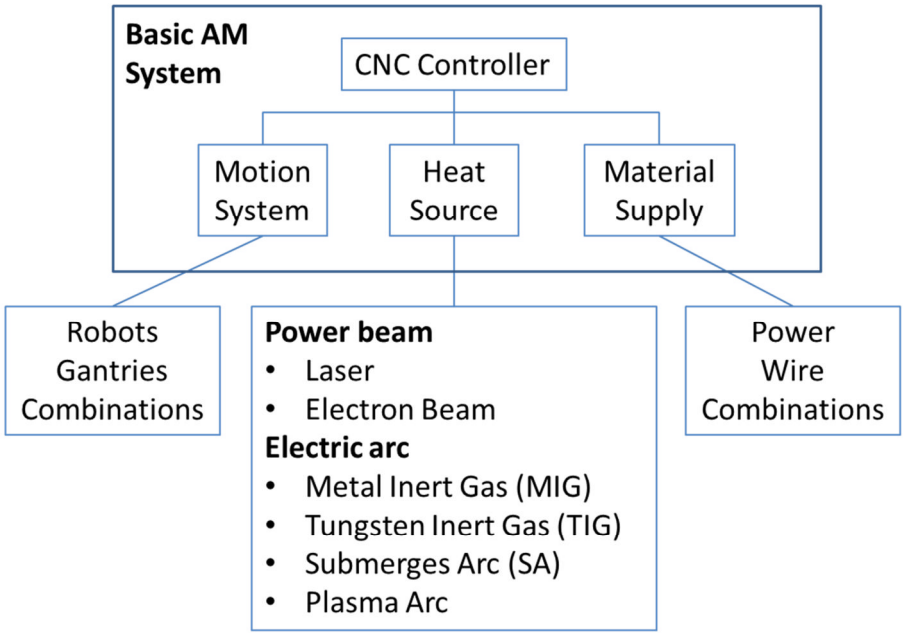

Figure 1-1: Basic Additive Manufacture system.

A promising breakthrough for metal AM technology is the Wire and Arc Additive Manufacture (WAAM) process which combines electric arc heating sources with a metallic wire feeding system. In the WAAM process, 3D metallic components are built by depositing beads of weld metal in a layer by layer fashion. The WAAM system can be built by combining the standard wire based welding equipment and the common motion system such as industrial robots (Figure 1-2 (a)) and gantries (Figure 1-2 (b)). The WAAM system can also be easily retrofitted onto existing machine tools which is capable of both deposition and machining (Figure 1-2 (b)). The hardware cost for the WAAM system is typically an order of magnitude less than the laser powder systems and it can achieve deposition rates two orders of magnitude higher than laser powder systems (typically 2-4 kg/hour). In the current research of the WAAM process, a local shielding technique is utilised for fabricating the highly reactive metallic components (Almeida and Williams, 2010). As an environmental chamber is not necessarily required (out-of-chamber), the build volume is unlimited. Various materials that are weldable can be used in the WAAM process, such as steel, Ni alloys, Al alloys and Ti alloys.

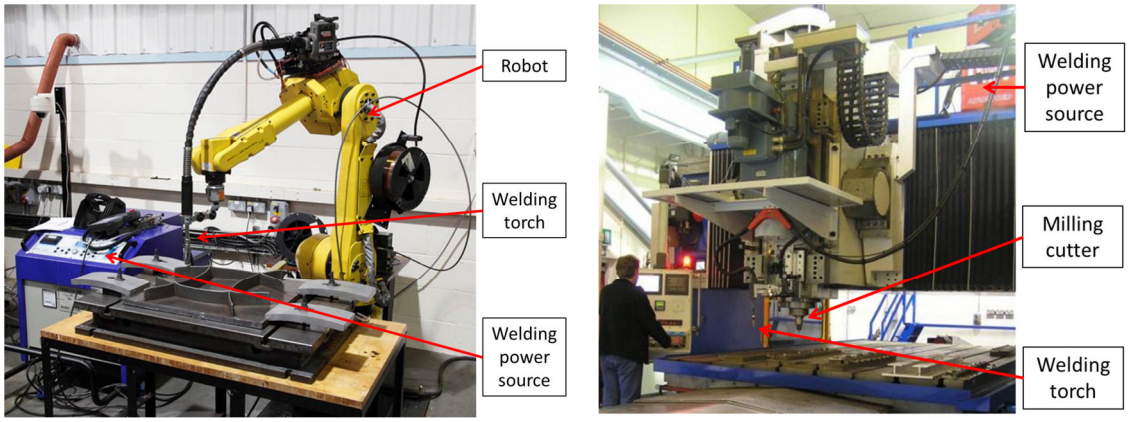

(a) (b)

Figure 1-2: WAAM system: (a) robot with MIG welding equipment; (b) WAAM incorporating milling process.

The WAAM system allows the production of large custom-made and low volume metal workpieces with high deposition rates. Specific components have been produced as required by industrial partners using the WAAM process. Figure 1-3 (a) shows the building of four mild steel projectile casings each with a mass of 32 kg. The deposition rate for building these parts is 3.31 kg/h. Figure 1-3 (b) shows a part illustrating that components with numerous cross overs and intersections can be built using WAAM process. Figure 1-3 (c) shows a typical titanium aerospace part that has been built using the WAAM process (out-of-chamber). This component highlights the benefits of the WAAM process over the current process of machining from billets for these kinds of parts. The final component weight is 6.2 kg and to machine from a solid would require a starting billet weight of 27kg which gives a buy-to-fly ratio of over 4. This is extremely wasteful in terms of material. In contrast using the WAAM process the base plate has a weight of 5 kg and 1.5 kg of material is added with 0.3 kg machined away to get the final profile. This gives a material saving of 19.3 kg and a buy-to-fly ratio of near to 1. The deposition time for this part is only 1 hour.

Figure 1-3: Components built by the WAAM process: (a) shell castings; (b) part with crossovers and intersections; (c) Ti aerospace component.

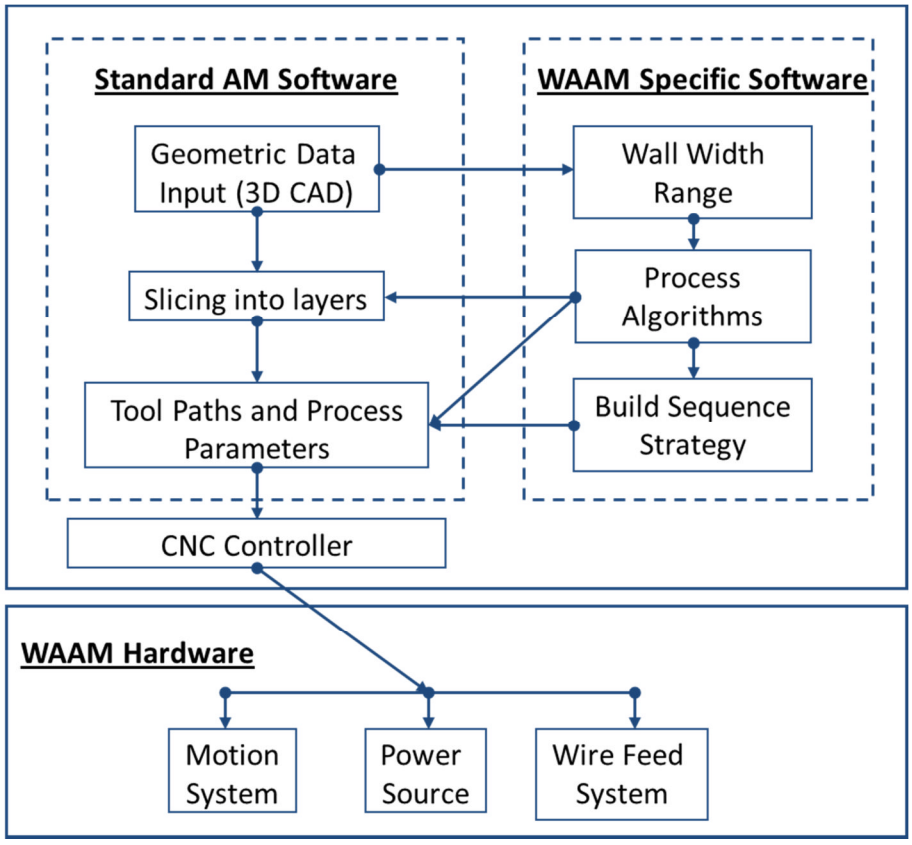

Figure 1-4: Wire and Arc Additive Manufacture system

To fully automate the WAAM process, a CNC controller needs to be developed which can provide the WAAM hardware with build path and deposition parameters. As illustrated in Figure 1-4, the WAAM controller needs to contain the basic functions of standard AM software structure which can transfers the 3D CAD data into sliced layers and then generates tool paths and process parameters in the form of CNC codes. Moreover, this controller needs to

integrate the knowledge gained from the systematic researches of the WAAM process, including design study of WAAM, process modelling, and process simulation. Optimal process parameters and build strategies will be decided automatically for different WAAM applications and be complied by the WAAM hardware.

One important factor that need to be considered when one decides the deposition parameters and build path are the residual stresses and distortions generated during the WAAM process. Although these thermally induced issues are unavoidable for the WAAM process, using a proper deposition parameter and build path can control the residual stresses and minimise the distortion level without any extra process. Therefore, a numerical model needs to be developed which can provide predictions of the residual stresses and the distortions of the WAAM components. This thesis aims on the thermo-mechanical analysis of the WAAM process using the FE approaches, with a special research focus on the efficient FE modelling approaches for large WAAM components.

1.2 Parent EPSRC Project

This thesis is part of the wider research project called Ready-to-Use Additive Manufacture (RUAM) project. The RUAM project is funded by Cranfield IMRC (Innovative Manufacturing Research Centre) and EPSRC and involves 21 industrial partners as well as two University partners. It was launched October 2007 with a proposed duration of four years. It aims to improve industry's ability to manufacture high precision ready-to-use functional parts for a wide range of applications especially for large aerospace structures.

Six subprojects, including part design, FE analysis of WAAM process, AM via welding (two subprojects), grinding, and material properties (University of Manchester), are carried out in parallel to achieve the RUAM goals. The author was responsible for the thermo-mechanical analysis of the WAAM process using the FE approaches.

1.3 Problem Statement

The wire based welding techniques used in the RUAM project, such as gas tungsten arc welding (TIG) and gas metal arc welding (MIG), can provide high deposition rates. However, the non-uniform expansion and contraction of the materials during the thermal cycles result in residual stresses. It is accompanied with distortions which are one of the most problematic issues arising from the WAAM process. Therefore, it is highly important to understand the thermo-mechanical performance during the WAAM process, and moreover, to improve the WAAM process to reduce the residual stress and distortion level.

Finite Element (FE) analysis is a common method to study the thermo-mechanical performance of the AM process. The most widely used FE analyses of AM processes utilise transient models with a moving heat source. Element birth technique is used for simulating addition of material, providing accurate predictions (Song et al., 2005; Nickel et al., 2001; Mughal et al., 2006). However, the transient aspect and the highly non-linear material behaviour result in long computational time, and hence the models are usually limited to a small scale. To investigate large-scale WAAM components, which can scale to several meters, this conventional transient FE approach is not suitable. Efficient FE approach needs to be developed to provide fast estimations of the temperature distribution, residual stresses and distortions. The efficient FE model will be helpful for deciding the best deposition parameters and build strategies.

1.4 Outline of Thesis

This thesis is comprised of the following chapters:

Chapter1

This chapter gives an introduction of the research conducted for this thesis.

Chapter 2

Chapter 2 summarises the state-of-art of the related area of this research including such themes as:

- Additive manufacturing
- Thermo-mechanical issues during the AM process
- Thermo-mechanical modelling of welding process
- Thermo-mechanical modelling of AM process
- Control of residual stresses and distortions

Chapter 3

This chapter outlines the research aim and objectives of this thesis. The research scope, methodology as well as research deliverables are also introduced in this chapter.

Chapter 4

A transient FE model for the WAAM process is introduced in this chapter with experimental validations. The thermo-mechanical performance of the WAAM process is investigated with this FE model.

Chapter 5

Computationally efficient thermo-mechanical FE approaches for the WAAM process are introduced in this chapter. They can greatly reduce the computational time.

Chapter 6

This chapter introduces the process study of WAAM which has been performed in variety aspects through case studies using FE models. Recommendations and building strategies are drawn from this study to improve the WAAM process.

Chapter 7

Chapter 7 introduces a robot program generation tool which can generate robot programme directly from the CAD files and can efficiently integrate the building strategies.

Chapter 8

The findings of this research are discussed in this chapter and the conclusions are also summarised.

1.5 Summary

The research background of this research has been introduced in the beginning of this chapter. The parent project (RUAM project) has been introduced and the role of this sub project has been outlined. The motivation of this research has been presented as the problem statement. A summary of the chapters that included in this thesis has also been provided. Chapter 2 gives the literature review undertaken as a key part of this research.

2 LITERATURE REVIEW

2.1 Introduction

This chapter introduces the main fields of research surrounding the topic of this thesis. As the WAAM process uses arc welding techniques, the knowledge of arc welding processes are also investigated as the main literature source. Among all these areas, a particular attention is focused on the thermo-mechanical modelling techniques of welding processes. The state-of-art techniques are discussed and their advantage and weakness are also summarised. The knowledge gained from this literature survey inspires new approaches proposed in this thesis.

2.2 Additive Manufacturing

Additive Manufacturing (ALM) is a novel technique which fabricates 3D components in a layer by layer fashion. It was originally developed for Rapid prototyping and Rapid Tooling (RP and RT) which are the processes of producing functional prototypes and null-series for tests with metal or higher grade plastics. In the recent years, AM techniques have been moved to Rapid Manufacturing (RM) to meet the requirement of producing end-use parts with near-net shape and full functionality (Levy et al., 2003). Great research interests were induced on this novel process because of its significant benefits of time saving, material saving, flexibility, and more friendly to environment (Morrow et al., 2006; Sreenivasan et al., 2010).

The AM process discussed in this thesis is focused on metallic materials only. Different techniques and concepts have been developed in the metal AM area during the last two decades to provide industry with light weighted and fully functional metallic parts. Hybrid systems, which integrate the machining process with AM process, were also developed recently to provide net shape functional components with high surface quality (Song et al., 2005a; Song and Park, 2006; Sreenathbabu et al., 2004; Qian et al., 2010; Karunakaran et al., 2010).

Classified by the type of the heat sources AM techniques contains several groups, such as Laser Melting (LM), Ultrasonic Additive Manufacturing (UAM), Electron Beam Melting (EBM), Plasma Deposition (PD), and Gas Metal Arc Welding (GWAM) etc. Metallic wire and metallic powder are the two main material feeding methods. By combining the different heat sources with different material feeding methods various AM techniques have been developed.

The combination of laser and powder is probably the most widely applied option. A lot of different processes have been developed by the researchers which are introduced in Santos' review paper (Santos et al., 2006). These processes can be classified into two groups: Selective Laser Sintering (SLS) and Selective Laser Cladding (SLC). In SLS the metal powder is placed as an extensive powder bed before the laser scans (Das, S.; Kruth et al., 2003b; Sreenivasan et al., 2010), while in SLC the metal powder is fed directly in the molten pool created by the laser beam (Mazumder et al., 2001; Hu et al., 2002; Cao and Miyamoto, 2006; Qi et al., 2009).

With the highly focused laser power and accurately controlled powder feeding, the parts can be fabricated with detailed features and with high accuracy. However, the low deposition rate and the complexity of the system constrain the dimension of the AM parts to a rather small scale (Mok et al., 2008a). These powder based techniques usually require additional support items for building non-vertical structures (Martina, 2010). Moreover, a lot of quality issues can be raised in the powder system, such as non-fully dense parts (Kruth et al., 1996; Rombouts et al., 2006), the mechanical properties are not consistent in all directions (Kruth et al., 2003a), and pore formation (Choi and Chang, 2005). In addition, only part of the powder can be actually used which cause an issue of waste material (Heralic et al., 2010).

Wire based AM process is gaining more favour because of its higher deposition rates and higher efficiency (Syed et al., 2005b). The deposition of metallic wire with high power diode laser was studied by Syed and Li (2005a) on mild steel and by Mok et al. (2008a; 2008b) on Ti-6Al-4V. High power fibre laser has been considered as the heat source for the deposition of Ti-6Al-4V wire (Miranda et

al., 2008) because of its high efficiency, low maintenance cost, and the flexibility in beam position and manipulation. Fully dense components can be fabricated using this process (Syed et al., 2005b; Medrano et al., 2008; Mok et al., 2008b).

The electron beam freeform fabrication (EBF3) layer additive manufacturing process was developed by NASA to fabricate complex geometry components directly in a vacuum chamber (Taminger and Hafley, 2006). Metallic wire is utilised as the filler material medium. This technique has been utilised for fabricating light metallic aerospace components with Ti and Al alloys (Brice et al., 2009; Domack et al., 2006).

Wire and arc manufacturing (WAAM) process combines the arc welding techniques with wire feeding. Standard wire based welding processes such as Metal Inert Gas (MIG) and Tungsten Inert Gas (TIG) are low cost solutions employed as heat sources, providing high deposition (Sequeira Almeida and Williams, 2010). As the system can be easily mounted on industrial robots and CNC machines, it is possible to fabricate large scale components. The concept of WAAM has actually been around for almost a century – the first patent was filed in 1920 by Baker (Baker, 1920). However, it was until the last two decades that this idea was extensively developed with modern welding and automation technologies.

Shape Welding (Schmidt et al., 1990) process is one of the successful applications of WAAM process, which showed its capability of building large reactor coolant components for up to 10.5 m in length and 5.8 m in diameter. Multi-head welding was utilised to give high deposition rate. These components retained approximately 80% of the unmachined weight which gained a huge benefit comparing the 28% effective weight by the traditional forging process.

The Welding Engineering Research Centre of Cranfield University is another leading research group of WAAM process since 90's. Ribeiro and Norrish developed an automated additive manufacturing system for Rolls-Royce and subsequently called it Shape Metal Deposition (SMD). This system enabled direct creation of metal objects from a CAD model (Ribeiro et al., 1994; Ribeiro

and Norrish, 1996; Ribeiro and Norrish, 1997; Ribeiro, 1998). A welding robot and a conventional MIG power source were used. This system successfully linked the CAD drawing, slicing routine, simulation, robot, and rotating table. Welding parameters for desired geometries can also be automatically generated by the program. In this project grinding process was performed separately for the surface finish. Ribeiro suggested an important improvement could be the integration of a machining centre linked to his system (Ribeiro, 1998).

The SMD system was further studied by Spencer on the surface roughness issues due to the heat built-up during the deposition (Spencer et al., 1998). Their deposition system utilised MIG process, and used a robot to manipulate the welding torch. Some simple free-standing parts were successfully fabricated from this process. Improved surface finishing has been achieved using temperature control at the expense of reduced process efficiency. Suggestions were made on optimisation the welding parameters and taking thermal issues into account.

The SMD process was further developed by a European project called Rapid Production of Large Aerospace Components (RAPOLAC) which was initiated in 2005 by the Advanced Manufacturing Research Centre (AMRC) at the University of Sheffield in collaboration with seven partners from across Europe. The aim of this project was to build large parts with a variety of aerospace materials. The SMD process is proposed to be improved by process automation, material properties control, and process parameters optimisation. Robotic TIG welding is utilised in the RAPOLAC cell, and a fully automatically controlled SMD system has been implemented using video feedback algorithms (Muscato et al., 2008). The microstructure and mechanical properties of the Ti-6Al-4V components made by SMD process has been examined by Baufeld et al. (2010; 2011).

The current RUAM project developed on the success of Ribeiro's work and improves the previous process by using the modern welding technologies, such as Cold Metal Transfer (CMT) process and plasma welding. Moreover,

achievements have been made on the process modelling of WAAM with different materials and welding process, the manufacturing of Ti alloy components in an out-of-chamber environment (Sequeira Almeida and Williams, 2010), WAAM process design (Kazanas et al., 2010), process optimisation (Mehnen and Trautmann, 2008), thermo-mechanical modelling of WAAM process, and microstructure of the WAAM components (Wang et al., 2011).

Table 2-1 lists the comparison between the WAAM process and the laser based AM processes. Compared to the AM processes using laser plus powder or wire solutions, the system for the WAAM process is much cheaper and easier to be built. The power efficiency and productivity of the WAAM process are much higher than the laser based system. These process advantages make the WAAM process especially suitable to be used for fabricating large scale components. However, due to the process constrains of arc welding, the complexity of the WAAM components is comparatively low. The finishing quality is also not as good as the laser based AM processes.

Table 2-1: Process comparison between WAAM and laser based AM processes

Process	**WAAM**	**Laser based AM processes**
Power source	Standard welding facilities	Expensive high power laser system with complex optical systems
Material feeding system	Standard wire feed systems	Sophisticated powder handling and delivery apparatus required
Shielding system	Local shielding system	Chamber required
Power	Power source and thermal transfer efficiencies typically	Laser power source efficiency typical 20%, transfer (coupling

efficiency	both >80%	efficiency) up to 40% for conduction processes
Productivity	Deposition rate typically 2-4 kg/hour	Build rates of a few tens of grams per hour for powder systems
Material utilisation	100%	Only part of the powder can be used for different applications
Component size	Large. Up to several meters	Small due to the constrain of the system dimension
Component complexity	Low to medium	High
Finishing quality	Observable surface waviness, need post finishing process to achieve required accuracy	Low surface roughness, may not require extra finishing process

2.3 Thermo-mechanical issues during the deposition process

By applying arc welding techniques, the WAAM process faces similar problems of residual stresses and distortions as in the arc welding processes. As illustrated in Figure 2-1, during the deposition process the area where the heat source locates is heated up sharply and fused locally. A large area of compressive stress is generated in front of the fusion zone due to the thermal expansion of the heated material which is being constrained by the surrounding cold material. The stress in the fusion zone is very low because of the significantly reduced yield stress level by the high temperatures. After the heat

source passes, the heated material cools down in a short time. It results in tensile stresses in the region behind the heat source due to the contraction of the cooling material, and this material contraction is restrained by the surrounding cold material which consequently results in tensile stresses. If the tensile and compressive stresses exceed the yield limit then plastic stress generates (Radaj, 1992).

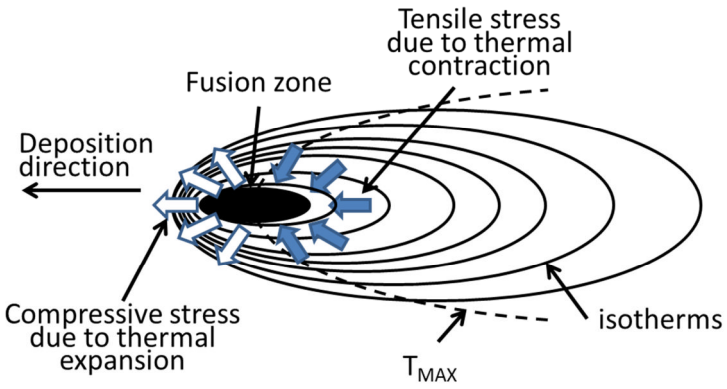

Figure 2-1: Temperature and stress field around a welding heat source (Radaj, 1992).

To explain how residual stresses generate, the longitudinal stress and temperature histories for two points are schematically illustrated in Figure 2-2. Point X locates at the edge of the weld pool while Point Y is slightly further away from the weld pool but is still in the region where the residual stress generates. As the heat source approaches, the temperature of both points rises. As a consequence of the metal expansion a compressive stress generates, first appears elastically as shown by line AB in both figures of Figure 2-2, and then turns into plastic flow when it exceeds the yield limit as shown by line BC. After the heat source passes, the temperature of the material drops and a tensile stress develops due to the contracting material being restrained by the surrounding material. In the case of Point Y all the tensile stress is accommodated elastically with no plastic flow occurring as shown by the line CD in Figure 2-2 (b). In the case of Point X some of the tensile stress exceeds the yield limit and develops plastic flow as shown by the line DE in Figure 2-2 (a). When the material has cooled back down to room temperature a tensile

residual stress is present as shown by the large grey arrows in both figures of Figure 2-2.

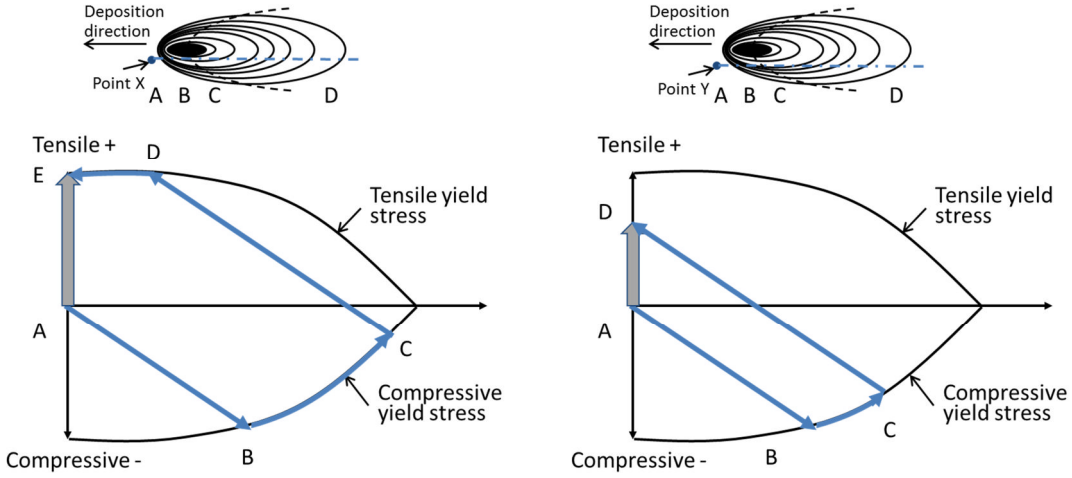

(a) (b)

Figure 2-2: Temperature stress histories for different material points: (a) point X is at the edge of the weld pool; (b) point Y is slightly further from the weld pool.

It can be understood from the preceding analysis that the tensile residual stress is produced due to an unequal balance of elastic and plastic flow during the heating and cooling cycles. A typical longitudinal residual profile for the mild steel across the weld centreline is shown in Figure 2-3. The high tensile stresses (reaching the yield limit) distribute in the region adjacent to the weld centreline (as explained by Figure 2-2 (a)). In this region a big amount of compressive plastic flow develops during the heating cycle due to the high peak temperature. As the material is soft in this region tensile plastic flow occurs as the tensile stress exceeds the yield stress. This compensates for some of the compressive plastic flow that happens during the heating cycle and finally develops tensile residual stress with the magnitude of the yield stress when the material cools down to the room temperature. For the points further away from the weld centreline the magnitude of the tensile stress reduces. For these points all the tensile stress that has been generated during material cooling cycle remains elastically (as explained by Figure 2-2 (b)). And the further the point locates away from the edge of the weld zone the lower peak temperatures it will

reach. It consequently results in the development of less compressive plastic flow on this point during the heating cycle which leads to lower tensile residual stress after the temperature drops back down to the room temperature. As the sum of the stresses in any one direction is equal to zero, the tensile residual stress in the weld zone is balanced by compressive residual stress further out in the component.

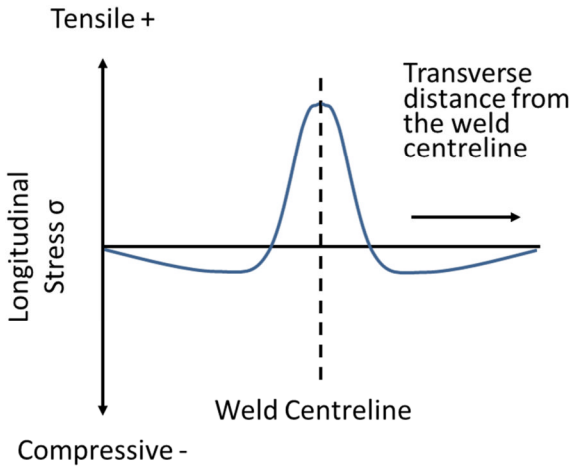

Figure 2-3: Typical longitudinal residual profile across the weld centreline.

Classified by different directions, residual stresses contain three components. These are the longitudinal stress in the direction of welding, transverse stress which is perpendicular to the direction of welding and normal stress through the thickness of the material. The longitudinal stress is usually the dominant component among the residual stresses due to the significant longitudinal contraction of the weld as it cools down. The normal stress is usually comparatively small due to the small variation in temperature and small material restrains in the thickness direction.

There are various techniques for measuring residual stresses, and they can be divided into two categories: destructive ones and non-destructive ones. The destructive techniques remove some of the material from the samples to allow the stresses to relax. The residual stress can be calculated based on the displacement incurred by the stress relieving (Withers and Bhadeshia, 2001). Methods such as hole drilling (Withers and Bhadeshia, 2001), sectioning

(Tebedge et al., 1973), contour method (Prime, 2000), and deep hole drilling (Leggatt et al., 1996) are included in this category.

Non-destructive techniques usually obtain residual stress by measuring the elastic strain of specific atomic lattice planes (Withers et al., 2008). The most well-known non-destructive techniques are X-ray diffraction (Prevey, 1977), Neutron diffraction (Dann et al., 2004) and Synchrotron X-ray (Webster et al., 2001). The conventional X-ray diffraction have limited penetration (Withers et al., 2008), and the neutron have the advantage over X-rays for the possibility of obtaining diffracted intensity from only a small volume (Withers and Bhadeshia, 2001). The typical penetration depth of neutron diffraction method is some centimetres for steel (Withers et al., 2008).

The diffraction techniques were developed based on the Bragg's law which is given by the equation:

$$n\boldsymbol{\lambda} = 2\mathrm{d}\sin\theta \tag{2-1}$$

Where n is an integer, $\boldsymbol{\lambda}$ is the wavelength, θ is the Bragg angle for crystallographic planes, d is the lattice spacing. The lattice spacing d in individual crystallite grains expands (or contracts) under a tensile (or compressive) stresses. This change can be detected as a shift of Bragg peak which can be recorded as a shift in angle, wavelength or time of flight (Withers and Bhadeshia, 2001).

The strain (ε) can be calculated by

$$\varepsilon = \frac{d_i - d_0}{d_0} \tag{2-2}$$

where d_0 is the strain-free lattice spacing, and d_i is the lattice spacing under stress. The strain-free lattice spacing d_0 can be measured using a stress free reference cube which is cut from an outfield area of the sample (Price et al., 2006). The residual stresses of the sample can be calculated from the strain data.

Arising from the residual stresses welding deformations is another problem from the welding processes. As shown in Figure 2-4, six primary forms of distortions can be classified by their appearance, namely, longitudinal shrinkage, transverse shrinkage, rotational distortion, angular change, longitudinal bending and buckling (Masubuchi, 1980). The first three cases of deformation occur due to the movement of the material towards the weld zone. The angular change and longitudinal bending are due to the non-uniform transverse and longitudinal shrinkage over the thickness of the plate, respectively. Buckling distortion is generated when the applied weld load, which is produced by the compressive residual stresses form the outer regions of the plates, exceeds the critical buckling load of the plates.

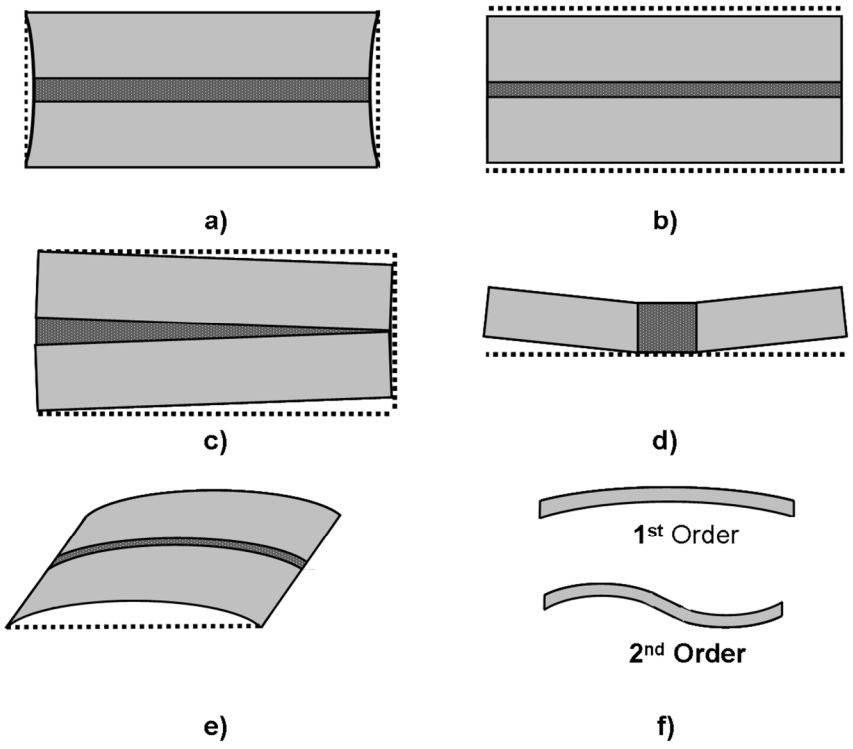

Figure 2-4: Welding deformation patterns (Masubuchi, 1980). (a) longitudinal shrinkage, (b) transverse shrinkage, (c) rotational distortion, (d) angular change, (e) longitudinal bending, (f) buckling

2.4 Thermo-mechanical Modelling of Welding Process

Residual stresses and distortions are the two major problems which are induced by the thermal cycles of the welding process. They can cause critical mechanical effects of the weld parts and also generate errors to the geometrical accuracy. A great attention has been focused on developing predictive models of the thermo-mechanical performance of welding process since the middle of the last century. Empirical methods where knowledge about welding distortions was obtained through systematically performed experiments were common approaches used in the early years (Guyot, 1947; Spraragen and Claussen, 1950). The first analytical solution was generated by Rosenthal (1946) to compute the heat transfer of welding process, and was then followed by other researchers to study the deformations of the welding processes (Moshaiov and Song, 1991). The application of these analytical solutions is limited by their inability of handling complex geometry and temperature-dependent material behaviour.

With the fast developed computer capability Finite Element Analysis (FEA) become the most powerful tool for solving the thermo-mechanical phenomena. It was first utilised in the applications where safety aspects are very important, such as aerospace and nuclear power plants, then extended to other heavy industries such as ship building, automotives, and aeronautics. The continuously improved FE technique allows researchers to study the welding process on a detailed level. The close coupling between the heat transfer, microstructure evolution and mechanical performance can be accurately described in the model. Three dimensional transient thermo-mechanical models are widely used in welding studies to give simulations as close as the real life welding process. However, the enormous requirement for computing time and processing memory becomes the major obstacle for these kinds of models to be used for the real engineering purpose. Many computationally efficient approaches, on the other hand, try to give the thermo-mechanical predictions in practical time. These approaches can be classified into two main categories, which are reducing the model size via using simplified meshes and solving the

problem with static analyses. The books of Goldak and Akhlaghi (2005) and Lindgren (2007) provide a rich source of the techniques in the area of computational welding mechanics.

2.4.1 Physics of Welding Process

The thermo-mechanical analysis of welding process can be very challenging because of the complex interactions between thermal, mechanical, metallurgical, and fluid flow of weld pool (Goldak and Akhlaghi, 2005). The fluid flow of weld pool is usually neglected because of its subtle influence on the other elements. Figure 2-5 shows the coupling relations between the different fields when generate the welding model. The bold arrow lines demonstrate the dominant couplings in welding, while the dash arrow lines show the secondary couplings which are insignificant in most of the cases. Focused on the dominant couplings only, the welding analysis can be treated as weakly coupled problems. Based on this simplicity, most of the FE models for the welding process are developed in a sequentially coupled way which calculate the temperature distribution first and then use the results for the mechanical analysis.

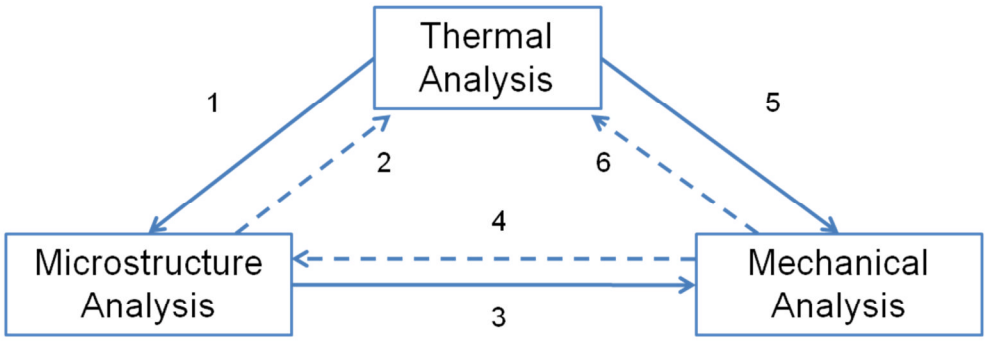

1 Transformation Rates (microstructure evolution depends on temperature).
2 Latent Heats (each phase transformation can have an associated latent heat).
3 Phase Transformations (volume changes due to phase changes, plastic and elastic material behaviour depend on the microstructure of material).
4 Transformation Rates (microstructure evolution can particularly martensitic and bainitic transformations, depend on mechanical deformation).
5 Thermal Extension (mechanical deformations depend on temperature).
6 Plastic Work (mechanical deformation generates hear in the material and changes the thermal boundary conditions).

Figure 2-5: Coupling between different fields in welding analysis (Goldak and Akhlaghi, 2005)

2.4.2 Modelling Strategies of Different Accuracy Categories

Before starting to develop the FE models, one thing needs to be clear in one's mind is what level of accuracy needs to be achieved. A successful FE model is to assign the computational effort to the essential features problem while ignoring the less significant elements to reduce the computational cost of the analysis. Different modelling strategies were summarised by Lindgren in his paper (2002) for different accuracy categories of welding simulation. The accuracy categories can be classified by the modelling target as shown in the following table:

Table 2-2: Modelling accuracy categories (Lindgren, 2002)

Accuracy category	**Modelling target**
Reduced accuracy	To get fast estimations at design stage with simple models.

Basic simulation	To get overall residual stresses and final deformations.
Standard simulation	“Basic” target + transient residual stresses and final deformations.
Accurate simulation	“Standard” target + microstructure of the weld and the heat affected zone.
Very accurate simulation	To get the microstructure of the weld and heat affected zone as well as the performance of the high temperature.

Most research focus on the models from the basic level up to the accurate level. Models of the very accurate simulation category should be chosen if details around the weld pool are of interest. Finer meshes, smaller time steps and more detailed material models and heat input models are required for the models with higher accuracy. Additional microstructure information needs to be included in the material model in order to achieve the accurate and very accurate simulation.

It is reported by Lindgren (2007) that the correct net heat input is more important for the basic and standard model rather than the detailed parameters for the heat source shape as the overall deformation and stresses are not particularly sensitive to the details of the heat distribution. A simpler heat input model with constant flux in the weld pool region can be utilised for the lowest accuracy category. This could make the implementation of the FE model easier. The heat source model with Gaussian distribution, which is described in section 2.4.3, can be used for all the accuracy categories.

It is recommended to use temperature dependent thermal and mechanical material properties for all accuracy categories. The material model is discussed in detail in section 2.4.3. Three aspects of the material model, including cut-off temperature, the effect of phase and microstructure changes, and the rate-dependent plastic behaviour at higher temperatures, need to be considered differently for achieving different accuracy levels.

The use of cut-off temperature is firstly due to the scarce experimental data for the high temperatures and secondly because of the convergence difficulty of the FE model caused by the soft material performance in the high temperature. The cut-off temperature is set as the upper limit of the temperature in the mechanical analysis, and no changes in the mechanical material properties are accounted above the cut-off temperature (Lindgren, 2001). Different relations between the cut-off temperature T_{cut} and the melting temperature T_m have been suggested by Lindgren (2007) for different accuracy categories (Table 2-3) based on the reviews of previous researches on welding modelling. The study performed by Tekriwal and Mazumder (1991) found that the differences on the residual stresses of mild steel welds are lower than 15% when the cut-off temperature varied from 600°C up to the melting temperature. Lower cut-off temperatures overestimated the residual stresses.

Table 2-3: Material model for different accuracy categories (Lindgren, 2007)

Accuracy category	**Material model**
Basic simulation	$T_{cut} \geq 0.5T_m$
Standard simulation	$T_{cut} \geq 0.7T_m$
Accurate simulation	$T_{cut} \geq 0.7T_m$
Very accurate simulation	$T_{cut} \geq T_m$

Volume changes due to phase changes can be ignored in the basic simulation, while the effects of phase changes on material properties are recommended to be included in the models for higher accuracy levels. Rate dependent material model as well as fluid flow effect are suggested to be included in the very accurate simulations only to have accurate high-temperature behaviour (Alberg and Berglund, 2003).

As the main target of this thesis is focused on the prediction of the overall residual stresses and distortions during the WAAM process, the researches in the basic simulation and standard simulation category have been considered for

the literature review. The findings from these researches are summarised in section 2.4.3. The simplified modelling approach of the welding process which fits the reduced accuracy category is another major interest topic for this thesis. The key researches are summarised in section 2.4.4.

2.4.3 Transient Thermo-mechanical FE Model

As welding processes can be treated as weakly coupled problems (Goldak and Akhlaghi, 2005), the thermo-mechanical performance is usually solved sequentially in two stages. In the first stage the transient thermal analysis is performed, and the nodal temperature histories from this analysis are imported to the subsequent mechanical analysis. In this way the transient residual stresses and distortions can be simulated. This kind of models utilise a time increment scheme to model the moving welding torch, which can give predictions close to the real welding process. Researches can be found dealing with different welding processes (Dong, 2005), such as the butt-weld process (Casalino et al., 2008; Grey et al., 2005), multi-welding process (Murugan et al., 2001; Deng and Murakawa, 2006; Deng et al., 2008), and bead-on-plate study (Smith et al., 2008a; Smith et al. 2008b, Bouchard, 2009; Shan et al., 2007; Ficquet et al., 2009). The following key modelling aspects are usually included in this kind of transient model:

- FE meshes
- Heat source model
- Material model
- Boundary conditions
- Filler material model

FE Meshes

Usually elements with the same geometries are used in the thermal and mechanical analyses. With the increasing performance of the modern computer

models with 3D continuum elements are commonly used because they can provide detailed information in all the directions (Deng et al., 2005; Jiang et al., 2005). Most commercial FE codes provide linear elements andquadratic elements. The linear element uses two nodes per edge which assumes a linear variation in properties across the element. The quadratic element uses three nodes per edge which allows the properties to vary in a quadratic manner across the element. The greater flexibility makes the quadratic elements more accurate than the linear elements. However, compared to the linear elements the quadratic elements are significantly slower due to their greater complexity (Preston, 2000).

Considering the shape of the element, tetrahedrons and hexahedrons (bricks) are usually utilised in the FE simulations. The tetrahedrons are geometrically versatile and it is very convenient to mesh a complex 3D shape with tetrahedrons using automatic meshing algorithms provided by most of the commercial FE software. However, hexahedrons are preferred in the thermo-mechanical studies of welding because they perform better than the latter in terms of accuracy and computational efficiency (Benzley et al., 1995; Abaqus User's Manual, 2010). Moreover, hexahedrons have a better convergence rate than tetrahedrons (Abaqus User's Manual, 2010).

Fully integrated linear elements with two integration points in each direction can perform over constrained (known as "shear locking") for the problems that are subjected to bending. This issue can be explained using a pure bending deformation problem represented in Figure 2-6 (a). Figure 2-6 (b) shows the deformation of a fully integrated linear element. The integration points are represented as the intersection points of the dashed lines. As the edges of the linear element are unable to curve, the angle between the vertical dash lines and horizontal dash lines which are initially 90° need to be changed. This indicates that the shear stresses are generated at these integration points, which is incorrect because the shear stress in the material under pure bending is zero (Abaqus User's Manual, 2010).

To avoid the “shear locking” problem, linear reduced integration elements are suggested to be used in the thermo-mechanical simulations of welding process (Elcoate et al., 2003). Reduced integration elements use one fewer integration point in each direction than the fully integrated elements. As shown in Figure 2-6 (c), neither of the dash lines which pass through the integration point has changed in length. The angle between them is also unchanged. This avoids generating the incorrect shear stress, however reduced integration elements can result in under-stiff response which produces meaningless results (known as “hourglass mode”, shown in Figure 2-7). In Abaqus a small amount of artificial “hourglass stiffness” is introduced in linear reduced integration elements to limit the propagation of hourglass modes. In order to get accurate simulations, a fine mesh of linear reduced elements need to be used where high level distortions are expected (Abaqus User’s Manual, 2010).

Nearly all the researchers use biased meshes in the welding simulation. To apply the heat flux more accurately, dense meshes are adopted in the weld zone and its vicinity. The element size increases progressively with distance from the weld centreline on the direction perpendicular to the direction of welding and through thickness. The mesh density can be decided through a mesh sensitivity study to get an optimal compensation between the accuracy and calculation speed (Gilles et al., 2009).

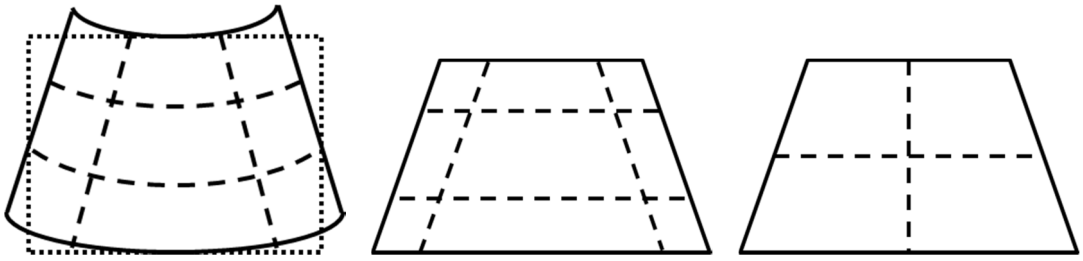

(a) (b) (c)

Figure 2-6: The effect of integration scheme on element behaviour. (a) Pure bending deformation; (b) linear response full integration; (c) linear response reduced integration.

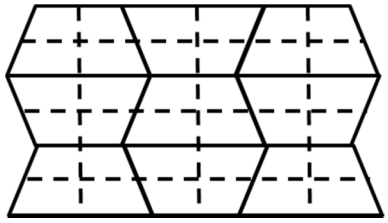

Figure 2-7: “Hour glass” linear element deformation mode.

Heat source model

The moving heat source was first introduced by Rosenthal in the late 1930s (Rosenthal, 1946) as an analytical method. Point heat source model and line heat source model were the most popular heat source models used in the analytical methods for calculating the thermal history of welds. Rosenthal’s solution could give quite accurate results in the regions of the workpiece where the temperature is less than about 20% of the melting point, but serious error was reported in and near the fusion zone and heat-affected zone (Goldak and Akhlaghi, 2005). The error is due to the assumption that the temperature is infinite at the heat source and the use of temperature independent thermal material properties.

The utilisation of FEM dramatically improved the heat flow analysis in welds. The FE models treat the welding arc as a finite heat source and the heat sources are modelled as applied heat flux or distributed power density in the weld pool. Pavelic et al. in the first time suggested that the heat source should be distributed and developed a Gaussian distribution of flux deposited on the surface of the workpiece (Pavelic et al., 1969). The Pavelic’s model described the heat source in a circular with the following equation:

$$\boldsymbol{q(r) = q(0)e^{-Cr^2}} \tag{2-3}$$

where $q(r)$ is the heat flux at radius r; $q(0)$ is the maximum heat flux at the centre of the arc; C is the concentration coefficient related to the arc width, and r is the radial distance from the centre of the arc to the point of calculation. The FE analysis utilised Pavelic’s model achieved significantly better thermal

predictions in the fusion zone and heat affected zone compared to Rosenthal's approach.

A more accurate heat source model proposed by Goldak et al. (Goldak et al., 1984) described the heat source in a non-axisymmetric way which the power density was dispensed with a Gaussian distribution in a combined double ellipsoid as shown in Figure 2-8. Because the temperature gradient in front of the heat source is steeper than that trailing edge of the molten pool, the power density of the region in front of the arc centre and the region behind the arc centre is defined separately.

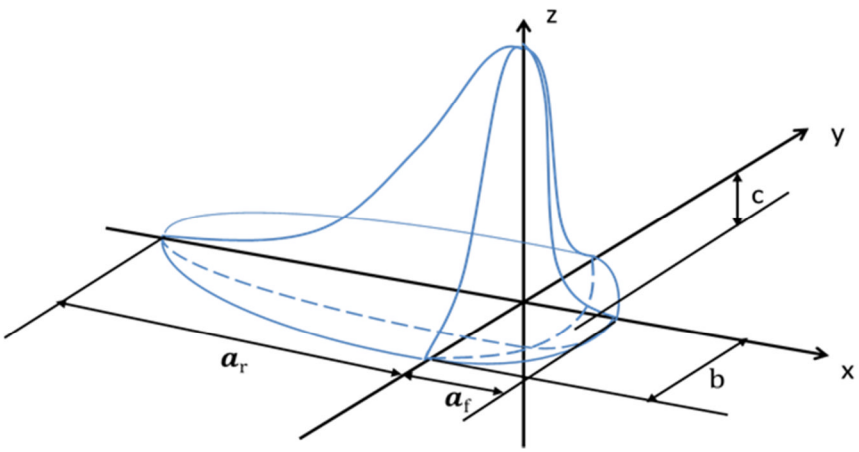

Figure 2-8: Goldak's double ellipsoid heat source model (Goldak et al., 1984)

The power density distribution in the front quadrant can be described as:

$$q_f = \frac{6\sqrt{3}Qf_f}{\pi\sqrt{\pi}a_f bc} e^{\left[-3\left(\frac{x^2}{a_f^2}+\frac{y^2}{b^2}+\frac{z^2}{c^2}\right)\right]} \tag{2-4}$$

And the power density distribution for the rear quadrant is:

$$q_r = \frac{6\sqrt{3}Qf_r}{\pi\sqrt{\pi}a_r bc} e^{\left[-3\left(\frac{x^2}{a_r^2}+\frac{y^2}{b^2}+\frac{z^2}{c^2}\right)\right]} \tag{2-5}$$

Where a_f and a_r are the length of the frontal ellipsoid and the rear ellipsoid, respectively; b is the width of the heat source; c is the depth of the heat source;

Q is the energy input considering the factor of efficiency; f_f and f_r are the factors for distributing the power to the front and rear of the hear source, and they have the relation that $f_f + f_r = 2$.

Goldak's double ellipsoid heat source model is flexible to fit different welding processes by adjusting the parameters in the model. The parameters a, b, and c, which describe the weld pool size and shape, are usually estimated from cross-section metallographic data and from weld pool surface ripple markings. Different values of a, b, c can be used for the front and rear quadrants in case where the fusion zone is more complicated.

From all the parameters, heat input plays the most important role on the temperature distribution of the model (Gilles et al., 2009). The geometry parameters of the heat source influence the FZ and HAZ boundaries (Grey et al., 2005).

Material model

Material modelling is crucial to modelling the welding process. With the development of the modelling techniques and the increasing capability of the model computers, significant improvement has been made to the material models for welding process. Lindgren (2001b) summarised different aspects of the material models in his review paper.

Most studies utilise temperature-dependent thermal conductivity and specific heat for the thermal analysis of the welding process. Phase transformations are always ignored in the thermal models, except for the latent heat. It needs to be specified for modelling the heat of fusion, either by assigning the latent heat value in the FEM code (Shan et al., 2009) or by artificially increasing the liquid specific heat (Hu and Kovacevic, 2003). In order to take the effect of fluid flow in the weld pool into consideration, an artificially increased thermal conductivity is assumed for temperatures above the melting point. It is suggested to set the conductivity 2 to 5 times at the liquidus to the value at the solidus (Mahin et al., 1991; Michaleris and DeBiccari, 1997).

It is common to ignore the microstructure change and assume that the mechanical material properties depend only on temperature. Microstructure simulation is important to the materials that the material properties are changed a lot due to the phase transformations (Lindgren, 2001b). If the mechanical performance near the weld zone is not particularly of interest, the mechanical material properties at high temperatures are usually treated simply with the aforementioned 'cut-off temperature'. According to the accuracy level that needs to be achieved, different value is required to the cut-off temperature (see Table 2-3).

It is suggested to use kinematic or combined kinematic and isotropic hardening material properties in order to get accurate stresses in the weld metal (Lindgren, 2001b; Smith et al, 2008b; Gilles et al., 2009). However, due to the lack of material data isotropic hardening model is used in most studies (Shan et al., 2009; Lee et al., 2008). It is sometimes neglected for the materials which the effect of hardening is not significant (Deng and Murakawa, 2007). The annealing effect where a material loses its hardening history at a certain temperature needs to be considered in the mechanical model. It is usually modelled by setting the equivalent plastic strain to zero when the temperature is higher than the annealing temperature (Elcoate et al., 2003; Shan et al., 2009; Lee et al., 2008).

Although temperature-dependent material properties are required for the thermo-mechanical simulation of a welding process, complete temperature-depended material data are sometimes difficult to obtain in practice. Assumptions and simplifications are often needed. Zhu et al. systematically investigated the effects associated with each of the material properties in a welding simulation (Zhu et al., 2002). They found that among the thermal material properties, the thermal conductivity has the most effect on the distribution of transient temperature field during welding. For the mechanical performance, yield stress has the most significant effect on the residual stress and distortion. Except for the yield stress, it is recommended to use material

properties at room temperature when detailed temperature-depended data are not available.

Boundary conditions

Heat loss due to radiation and convection are the main thermal boundary conditions that need to be included in the thermal model of a welding process. Compared to the heat input, the effect of convection and radiation is secondary. Many studies use temperature-dependent film coefficient for the convection (Deng and Murakawa, 2008; Deo et al., 2003), while a lot of others utilise constant values in their models (Shan et al., 2009; Lee et al., 2008; Cheng, 2005; Grey et al., 2005). For the arc welding process, the heat loss through radiation is just around 0.2% of the conductive heat flow (Preston, 2000). Therefore, this is usually not modelled explicitly. In most cases a constant emissivity is used in the thermal model (Shan et al., 2009; Lee et al., 2008; Cheng, 2005). Additional heat loss needs to be considered in the model if cooling system or backing bars are included. This can be modelled with an equivalent convection coefficient which needs to be decided by matching the predicted temperature profiles especially the cooling rate to the experimental results (Li et al., 2004; Colegrove et al., 2009; Zain-ul-Abdein et al., 2009).

Constraint conditions developed by clamps and backing plate are considered to be an important factor to welding deformation. The clamps are usually modelled using contact spring elements, while the backing plate is denoted as a rigid surface owing to its small deformation during the welding process (Gu et al., 1997; Liu and Zhang, 2009). The fixed displacement boundary conditions on the spring elements are released to simulate the release of the clamps. Except for constraints from clamps, additional constraint needs to be added to prevent rigid body motion.

Filler material model

A lot of studies modelled the filler material in a simple way that all the elements of the weld bead are present in the model throughout the analysis with its

associated thermal properties. However, this may cause underestimates of the temperature due to the heat conducted via the elements behind the heat source and also bring false plastic deformations due to the incorrect rigidity. These potential errors have been discussed by Shan et al. (2007) for the temperature prediction and by Cheng (2005) for the distortion analysis, respectively.

Considering the nature of the weld metal deposition, ‘element birth technique’ and ‘quiet element approach’ are developed to simulate the filler material more accurately. ‘Element birth technique’ is a process which deactivates all weld bead elements at the first step of the analysis and then activates the elements as the analysis goes on (Shan et al., 2007; Jiang et al., 2005). A subroutine is usually required to implement this gradually rebirth procedure which increases the complexity of the model development. However, no waste computational effort is made to the elements which are not activated.

‘Quiet element approach’ includes all the elements of the weld bead from the initial step of the calculation. However, these elements are made passive by setting material properties which do not affect the rest of the model. The magnitude of thermal conductivity and stiffness of the material are set to a very low value before the filler material is deposited. Actual material properties are assigned to the elements when the moving weld pool encompasses them (Lindgren et al., 2001b; Mughal et al., 2006a). This method is comparatively easier to be accomplished through coding the material properties. However, inefficient computational cost is made due to the calculation of the full system with all the elements. In addition, fictitious temperature gradients and strains can be accumulated in the quiet elements which may cause inaccurate heat flux and stress (Chiumenti et al., 2010).

The continuous development of computer hardware and software has greatly increased the computational efficiency. However, it is still not satisfactory for the increasing size of the welding model. Therefore, many different numerical techniques and modelling choices have been evaluated for efficient simulations.

2.4.4 Computationally Efficient FE Approaches

To save the computational time and processing memory, many computationally efficient FE approaches have been developed for predicting the thermo-mechanical performance of the welding processes. These methods can be classified into two main categories. The methods classified in the first category use modelling techniques to reduce the complexity of the model. Hybrid solid-shell element, adaptive meshing, local-global approach and sub-structure are typical techniques included in this group. The methods in the second category solve the transient thermo-mechanical performance with static approaches. Eulerian finite element approach, inherent strain method, applied weld load method, and efficient FE model using 'Thermal Contraction Strain' (TCS) algorithm and 'Mismatched Thermal Strain' (MTS) algorithm, and simplified approach based on welding plastic deformation are the main approaches.

2.4.4.1 Reduced model complexity using modelling techniques

The computational time is strongly influenced by the size of the model and the complexity of the material properties. Using less nodes and elements in FE models can reduce the model size. However, new modelling approaches need to be developed to keep high simulation accuracy. The utilisation of highly non-linear material properties in welding simulation is another reason of the long computational time. This can be solved by utilising non-linear material properties only locally to the critical area. The following modelling techniques are summarised:

Solid-shell element

The most straightforward way for reducing the computational time is reducing the model dimension to 2D or 1D. However, this dramatically increased speed is obtained at the expense of accuracy. The low dimensional models were found not satisfactory in some cases for providing accurate distortions and stress distributions (Deng et al., 2005; Mughal et al., 2006; Shan et al., 2007; Jiang et al., 2005). 3D shell model is another consideration to replace 3D solid

model for thin-walled structures (Lindgren, 2007). It was found that the 3D shell model can give a closer approximation of the 3D solid model than the 2D model for the thin-walled structures. Introduced in Goldak's book, another way of improving the computational efficiency is using a combination of shell and solid elements as shown in Figure 2-9 (Goldak and Akhlaghi, 2005). This composite model was reported more accurate than the shell model and computationally cheaper than the 3D solid model.

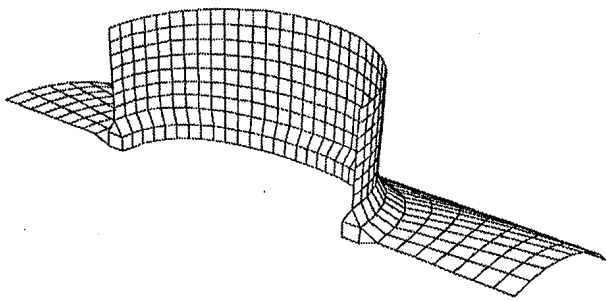

Figure 2-9: model built with combination of shell and solid elements (Goldak and Akhlaghi, 2005)

Graded meshing

Using biased meshes is also a common way in most of the welding FEM simulations. Small meshes were utilised for modelling the weld bead, and the meshes were coarse at large distances from the weld bead. A more efficient way of graded 3D meshing is McDill's grading scheme shown in Figure 2-10 (McDill et al., 1989). Comparing with uniform meshing, McDill's method can save the computational time and memory a lot, and its advantage become greater dealing with large models.

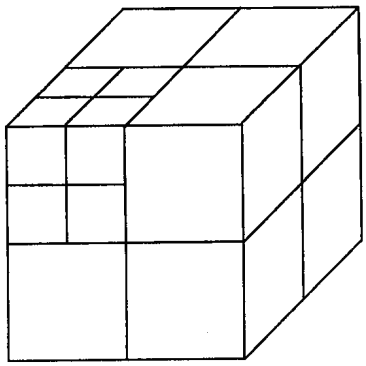

Figure 2-10: McDill's grading scheme (McDill et al., 1989).

Adaptive remeshing

Based on McDill's grading scheme, a dynamic and adaptive meshing method was developed by Lindgren and his colleagues (1997). The model was built with a dense element mesh that follows the heat source. Thus, the nonlinear thermo-mechanical effects close to the moving heat source can be accurately expressed. This automatic remeshing procedure was found to be effective. About 60% of the CPU time was reduced without any loss in accuracy.

Runnemalm et al. improved Lindgren's approach by integrating an error indicator to predicting areas of refinement (Runnemalm et al, 2000). In this way, the mesh refinement and coarsening is more accurately guided (Figure 2-11). Both of the heat flux-driving remeshing and the stress-driving remeshing approaches performed by Runnemalm can give good results. The author suggested using a combined procedure in welding applications which would be necessary when modelling complex three-dimensional welding problems. Hyun combined the element smoothing technique to the error estimator and get faster convergence to optimal meshes (Hyun, 2001). Hamide et al. (2008) used an adaptive remeshing procedure for simulating coupled thermal-metallurgical welding which reduced the calculation time by almost one-third.

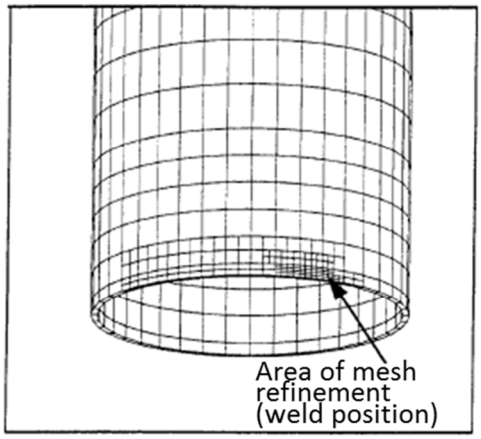

Figure 2-11: remeshing of a tube using heat flux (Runnemalm et al, 2000)

Local-global approach

Souloumiac et al. (2001) proposed a local-global approach to calculate the residual distortions of a ship assembly geometry and optimised the welding sequence. The plastic strains induced by welding process were assumed to be located close to the welding path and only depend on local thermal and mechanical conditions. Thus, a small scale local 3D transient model was built to calculate these plastic strains which were introduced as the initial strains in a global elastic shell model in order to get the global distortions of the whole part. The computational time of the global model was only around 6 minutes for this ship assembly application which had two welds about 5 meters in total. This approach has been proved very efficient and helpful in the design stage of the ship assembly to minimise the distortion with optimised welding sequences (Souloumiac et al., 2001). The larger the model, the more significant saving on the computational time will be obtained.

Using a similar method, Ploshikhin et al. (2010) performed an analysis on welding distortions after laser beam welding of large samples of aircraft panels up to 10 meters. In their study, a local non-linear thermo-mechanical FE model was performed and the plastic strain distribution after the welding process was calculated. The plastic strain was mapped to a global linear FE model to

calculate the welding distortion of the whole structure. Very good agreement was observed comparing with experimental measurements.

Substructuring

Substructuring is another efficient tool for reducing the size of the model, especially for large models. The basic idea of this technique is to utilise the complicated non-linear model for the heat influence region, while using a linear model for the rest of the region. A model which combined substructuring with dynamic remeshing technique was described in Lindgren's review paper (2006). This local-global model is efficient and a total of 8 m welding was simulated in a ship welding assembly study. The iterative substructure method (ISM) improved the substructuring approach to a dynamic process (Nishikawa et al., 2007; Zhang et al., 2007). ISM transforms welding problems into a combination of a large linear region and a small but moving strong non-linear region. In this way the computational speed can be greatly improved while keeping a high accuracy. The computational time of an engine component simulation was 2.7 hours, while it would be more than 1 day if the simulation was carried out by a transient model. Like the local-global approach, time saving of using substructuring is more significant in the simulations of larger models.

2.4.4.2 Efficient Models of Static Nature

The most commonly used transient models usually involve a huge amount of calculation increments, which is the main reason for the long computational time that these models require. If not considering the difference of the thermo-mechanical performance on the start and end area, a quasi-steady state temperature field exists in certain long welds. The materials along the weld line experience a similar thermal cycle. This phenomenon inspired the following welding simulation methods which treat the welding process as a steady state process and solve this time dependent transient problem fully or partially with static analyses:

Eulerian finite element method

The Eulerian finite element method is one of the main approaches with static nature. It developed based on the steady-state formulations for stress and distortion of welds (Gu and Goldak, 1994). New developments have been made to make this approach more accurate, such as taking temperature-dependent material properties into account (Shanghvi and Michaleris, 2001), and including rate dependent elasto-visco-plastic material behaviour to the area near the fusion zone (Qin and Michaleris, 2009).

Huge savings on the computational time and memory storage are the main advantages summarised by all the researchers using Eulerian finite element approach (Gu and Goldak, 1994; Shanghvi and Michaleris, 2001; Qin and Michaleris, 2009; Zhang and Michaleris, 2004; Wang et al., 2009). This advantage benefits from the modelling strategy which is totally different to the conventional transient approach. The transient models are built in a stationary Lagrangian reference frame, and the welding torch needs to move in this reference frame with the total time as same as the real world welding process. In the Eulerian finite element method the reference frame is attached to the welding torch and the material “flows” through the meshes (As shown in Figure 2-12).

As the Eulerian finite element solves the welding process in a steady state way, it does not need so many time increments as the conventional transient model. Moreover, the steady state method does not require a uniform mesh with high density along the heat line. The mesh can be graded to lower density away from the heat source, which is another reason for the reduction of calculation time. It has been reported by Zhang and Michaleris (2004) that the Eulerian FE method can be two orders of magnitude faster than the conventional transient model for long weld. However, the Eulerian finite element approach is not suitable for the study of short parts. The minimum length of an Eulerian model needs to be identified for different problems (Zhang and Michaleris, 2004).

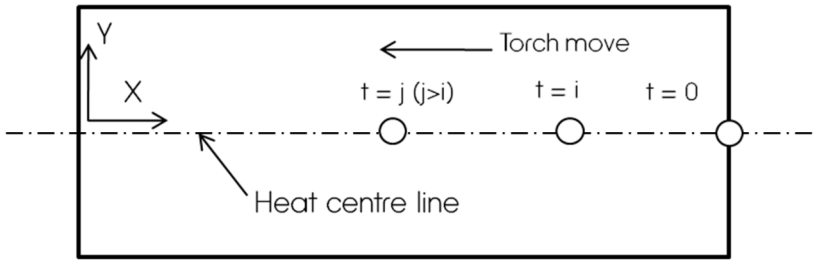

(a)

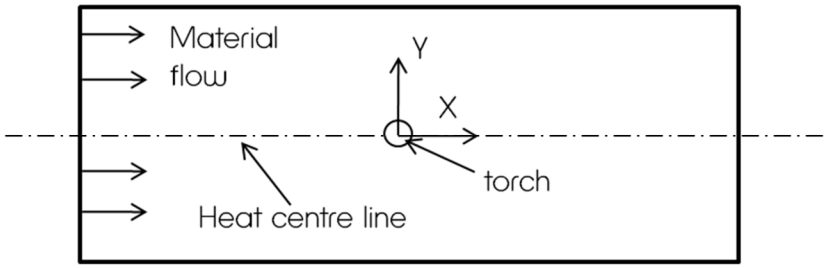

(b)

Figure 2-12: Model with different reference frames. (a): Lagrangian reference frame (b) Eulerian reference frame

Inherent strain method

Another approach for reducing the computational effort employs the concept of inherent strain. Inherent strain is defined as a composite which contains plastic, thermal, creep strains and the strains caused by the phase transformation. Deformation of the welding process can be estimated by introducing the inherent strain into a linear elastic FE model as the initial strains (Ueda et al., 1993). The inherent strain components can be transferred from the corresponding inherent deformations which are usually obtained either from elastic-plastic FE simulations or from experiment measurements of small scaled samples (Liang et al., 2006). Four inherent deformations, namely longitudinal shrinkage, transverse shrinkage, longitudinal bending, and transverse bending are the fundamental components that need be included in the model (Deng and Murakawa, 2008).

Deng and his colleagues (2007) utilised the inherent strain approach to analyse the welding distortions of a large welded frame structure three meters long. They classified the whole parts into two types of T-joints and one cross-shaped joint, and then calculated the inherent deformations of these three joints with thermal elastic-plastic finite element models. Inherent strains, which were transferred from the corresponding inherent deformations, were introduced to the elastic FE model for the final deformation of the whole part. Good agreement has been observed with the experiment results.

Wang et al. (2009) applied the inherent strain to an elastic-shell FE model to predict thin plate welding deformations. The authors also built a data base of inherent deformations for different weld materials, which can provide data for fast predictions of welding deformations for engineering application.

Elastic material nature of the inherent strain method results in very short simulation time. It is reported that the computational time for a 60 mm butt-weld joint was less than 1 minute while it took a transient thermo-mechanical model 12 hours for the same case (Deng and Murakawa, 2008). In addition, only the elastic modulus and the Poisson's ratio at room temperature are needed in the elastic FEM. This method can deal with the situation when the detailed temperature-dependent material data are not available. In this case, inherent strains need to be obtained from experiments.

Applied weld load method

The applied weld load method, proposed by Michaleris and Debiccari (1997), is a two-step process for the mechanical analysis. In the first step a 2D elastic-plastic simulation was performed to calculate the thermal strains, and then the thermal strains were transferred to a 3D structural analysis in the form of equivalent thermal load in the second step. The thermal load is decided by using a unit thermal load to the weld region of the structural model, and then scaling up by a factor γ which can be calculated as

$$\gamma = \frac{\sigma_{res}}{\sigma_1} \tag{2-4}$$

where, σ_{res} is the computed residual stress in the 2D model, and σ_1 is the stress resulting from the unit thermal load in the 3D structure model.

A comparison was made predicting the buckling deformations of a fillet weld using the applied weld load model, 2D model, 3D small deformation model, and 3D large deformation model (Michaleris et al, 2006). Compared to the 3D large deformation model which is the slowest, the applied weld load model can save more than 99% of the computational time. And the applied weld load model can provide accurate predictions of the magnitude of the buckling distortion. However, the angular distortion calculated by this model is not accurate.

Efficient FE model based on MTS and TCS algorithms

Camilleri et al. (2004) proposed an efficient model focused on out-of-plane distortion of butt welds. It was assumed that the transient aspect of the thermal pattern has an insignificant effect on the evolution of welding residual stresses. The thermal weld strains for the longitudinal deformation and the angular deformation were solved separately based on analytical approaches 'Mismatched Thermal Strain' (MTS) algorithm and 'Thermal Contraction Strain' (TCS) algorithm, respectively. These results were then applied to a 3D non-linear elastic FE model with orthotropic coefficients of expansion to provide prediction of the final angular and overall deformations of the weld part. The maximum temperatures experienced at each node during the thermal cycle were utilised as the main input for the mechanical analysis. These thermal data were obtained from a 2D thermal transient model with moving heat source model. Compared to the 3D transient model, the Efficient FE model based on MTS and TCS algorithms can save more than 99% computational time (Mollicone et al., 2006).

It was found that the driving power of the longitudinal deformation is the cooling phase of the process in the region behind the travelling heat source. The materials near the weld line start to cool before the materials from adjacent regions further away from the weld centre. This results in the development of 'mismatched thermal strain' which leads to the longitudinal contraction force. In

Camilleri and his colleague's approach (2004), the maximum temperatures that each node experienced during thermal cycles are essential to determine the distribution and the magnitude of the thermal strains. Depending on the maximum value of the nodal temperature, the whole mechanical model can be separated into different zones on the transverse cross section as shown in Figure 2-13. The centre zone A, where the thermal strain level exceeds twice the yield stain, is a fully plastic zone. A temperature load that equals to (T_a – ε_Y/α) is applied to this zone. The outer zone C, which is defined by the thermal strain level less than the yield strain, remains elastic throughout the heating and cooling cycle. No loads are applied in this area. Zone B which locates between zone A and zone C is a partial yield zone. Temperature loads corresponding to ($2T_a + \varepsilon_Y/\alpha - T_m(x)$) are applied.

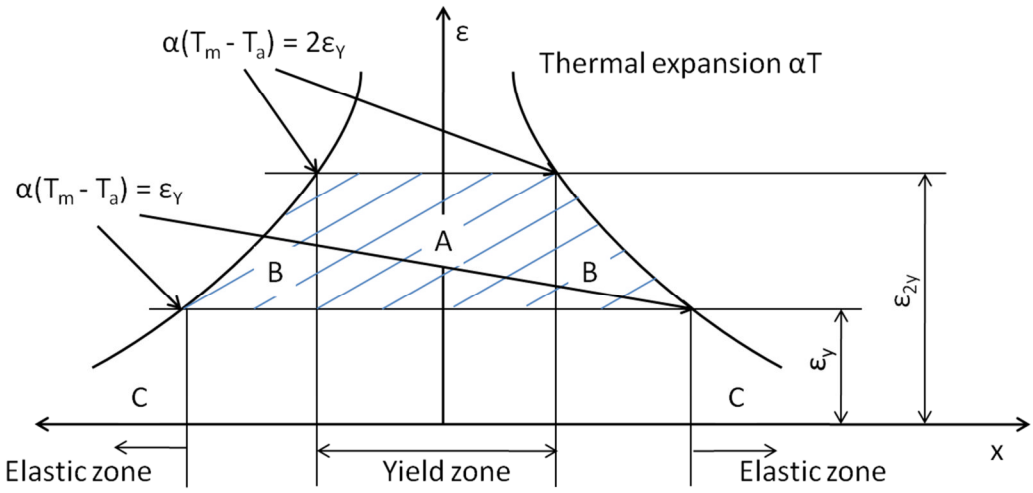

Figure 2-13: Formulation of contraction force via MTS (Camilleri et al., 2004). Where, α is thermal expansion ratio, T_m is the nodal maximum temperature, T_a is the ambient temperature, ε_Y is yield stress.

For the angular distortion, assumptions have been made that the major driving forces are the cooling contraction forces developed by the fusion zone elements (Camilleri et al., 2004). The parent material outside the fusion zone deforms elastically and does not contribute thermal strain to the total deformation. In this method, a starting temperature T_s (assumed to be 1000 °C in the study of mild steel) was used at which the cooling material begins to develop some strength.

Typically T_s is higher than the temperature defining the width of zone A. Therefore, an orthotropic coefficient of expansion was used to generate required thermal strains in the fusion zone. The actual coefficient of expansion α was used in the longitudinal axis for the whole model, and the coefficient of expansion was set to zero in the normal direction. In the transverse direction, a coefficient of expansion was set to the whole model apart from in the fusion zone, where it was set to a value α_T given by

$$\alpha_T = \frac{(T_a - (1-k)T_s)\,\alpha}{T_a - \varepsilon_Y/\alpha} \tag{2-5}$$

where k is a coefficient which was introduced to describe the restraint of the contraction offered by the parent material connected to the fusion zone. The value of k is decided by a number of factors, such as the fusion zone shape, thickness of the base plate, penetration depth, width of the fusion zone, material expansion coefficient, yield stress, and the starting temperature (Camilleri et al., 2005).

Mollicone et al. (2006) proved the effectiveness of the MTS algorithm on the prediction of longitudinal stress patterns and distortions. However, the predictions of the angular deformation based on the TCS algorithm cannot provide accurate angular deformation in the cases when external restraints are applied. To solve this problem, two derivative FE approaches were developed by Camilleri and Grey (2005), namely ‘non-linear maximum thermal strain approach’ and ‘sequential hybrid approach’. In the non-linear maximum thermal strain approach a 3D model with no-linear elastic-plastic material performance was utilised. The whole model was subdivided into a number of sections along the longitudinal direction, and the maximum nodal temperatures were applied as the thermal loads in a stepwise way on the subsections. In this way, the restrains from the external clamps can be simulated. Compared to the 3D transient model, around 90% computational time was saved. However, this approach overestimated the angular distortion even with a high number of subsections (Camilleri and Grey, 2005).

In the sequential hybrid approach, the evolution of angular distortion and longitudinal bending were treated independently. The transverse deformation was firstly calculated in a stepwise manner as in the non-linear maximum thermal strain approach, and the longitudinal contraction was established subsequently using the MTS algorithm with one single-step elastic analysis (Camilleri and Grey, 2005). Using a model with 10 subsections an accurate angular deformation was achieved (Mollicone et al., 2008). Compared to the 3D transient model, 92% computational time was saved. However, this model underestimated the longitudinal stress by 30% (Camilleri and Grey, 2005).

With the efficient FE model based on the MTS and TCS algorithms and its derivatives, residual stresses and deformations of large multiply-stiffened structure was studied (Camilleri et al., 2007). It is recommended to use the computationally efficient elastic model for the simulations at a global or large-structure level to analyse the major influences of configuration and fabrication sequence, while use the hybrid stepped method to deal with the external restraint on angular contraction or more accurate predictions of residual stress.

Simplified approach based on welding plastic deformation

Most of the efficient FE models introduced above need complex subroutines or home generated code. They can yield fast calculations, however the methods themselves are not easy to implement with commercial FE software. Cheng (2005) developed an approach based on welding plastic deformation, which is able to provide FE estimations with little effort on the implementation. This approach is similar to the MTS algorithm in terms of treating the whole model differently according to the maximum nodal temperatures. From the study of the relation between the plastic strain distribution and the maximum temperature that each node experienced during the thermal cycle, the author found there are two critical temperatures which can divide the whole model into three different zones. The first critical temperature defined the lower bound of the material's plastic temperature which is the lowest temperature that the plastic strains generate (473 K for mild steel in this study). Another critical temperature is the upper bound of the material's plastic temperature (1173 K for mild steel in this

study). Plastic flow generates easily as the elastic Modulus and yield stress become extremely small when the temperature of the material is above this threshold.

Different equivalent temperature loads were laid simultaneously along the entire part to the three zones. In the zone where the nodal peak temperatures were below the lower bound of the material's plastic temperature, room temperature was utilised as the equivalent thermal load throughout the mechanical analysis. For the zone where the nodal peak temperatures were above the upper bound of the material's plastic temperature and the zone where the nodal peak temperatures are between the lower bound and the upper bound of the material's plastic temperature, the average value of the nodal peak temperatures in each zone was applied as the equivalent thermal load. Two calculation steps were set up for loading and unloading the equivalent thermal loads. The thermal loads were loaded and unloaded simultaneously for the whole model (Cheng, 2005).

Compared to the transient thermal-mechanical model, this approach saved more than 90% computational time. Using this simplified approach, welding distortions of large scale automotive body structures were studied. Although the plastic strain field was not perfectly predicted, the distortion pattern and maximum magnitude was closely approximated (Cheng, 2005).

2.4.4.3 Summary of the computationally efficient FE models

Table 2-4 lists the comparison between these efficient FE approaches. In general, the efficient FE approaches which try to reduce model complexity via using modelling techniques can provide more accurate stress and distortion predictions than the approaches which solve the welding process fully or partially with static analyses. However, the implementation of these approaches is difficult. In the contract, the approaches of static analyses except for the Eulerian FE method are easier to be implemented with the commercial FE codes. Although the accuracy of these approaches may not be perfect, they can provide fast estimations on stresses and distortions which are very useful for

process optimisation. However, these approaches may not be flexible to solve the thermo-mechanical problem of the components with complex multi-dimensional features. And indeed there are no reported applications of these methods for multi-layer deposition.

Table 2-4: Comparison between different efficient FE approaches

FE approaches	Time saving compared to transient model*	Limitations
Solid- shell element	unknown	Not supported by the commercial FE codes.
Graded meshing	$(7\log_2 n + 1)/n^3$, n is the number of elements along an edge in a uniform mesh.	Not supported by the commercial FE codes.
Adaptive remeshing	About 60%	Difficult to implement in commercial FE codes. Home developed code is required.
Local-global approach	More than 95%	Difficult to implement in commercial FE codes. Cannot give accurate predictions when external restraints are applied.
Substructuring	About 90%	Difficult to implement in commercial FE codes. Complex subroutine or home developed code is required.
Eulerian FE method	More than 99%	Based on complicated mathematical transformation

		and would be difficult to apply to components with complex multi-dimensional features.
Inherent strain method	More than 99%	Not flexible. Highly related to the weld configuration.
Applied weld load method	More than 99%	It is difficult to accurately define the region in the 3D elastic model where the artificial thermal loads are applied. The prediction of angular distortion was not accurate.
Efficient FE model based on MTS & TCS algorithms and its derivatives	90% - 99%	Difficult to get the accurate mechanical predictions on longitudinal and transverse directions at the same time.
Simplified approach based on welding plastic deformation	Around 90%	Can only provide accurate predictions on distortion pattern and maximum magnitude. Did not accurately predict the plastic strain field.

* Note that the time saving also depends on the size of the model. The data listed in the table are from the literature reviews that discussed in this section.

2.5 Thermo-mechanical modelling of metal additive manufacturing process

Compared to the welding simulations, the literature source in the FE modelling of metal AM process is quite limited. Nearly all the literatures found in this area utilise transient approach. The FE models for the metal AM process share

similar modelling strategies and techniques for the welding simulations which have been mentioned in section 2.4.3. Temperature-dependent material properties, Gaussian heat input model and effective filler material model are commonly used in these models.

Investigating thermal behaviours of single-bead wall shaped structures during the additive manufacturing process is one of the main research focuses. Important thermal information, such as dynamic thermal cycles, peak temperatures, and cooling rate can be obtained from thermal FE models (Ye et al., 2006; Yang and Wang, 2008). Studies of the relation between the laser parameters and the melt pool shape were performed using thermal models to help selecting appropriate process parameters of an SLC process (Vasinonta et al. 2001, Hu and Kovacevic, 2003; Neela and De, 2009). The dynamically changed underlying substrate geometry has a significant influence on the molten pool geometry and heat transfer condition, thus influent the quality of the welding-based deposition process. This phenomenon has been studied by Jandric and Kovacevic (2004) with the help of FE thermal simulations.

A two-step thermal simulation was performed by Peyre et al. (2008) to predict the shapes of manufactured structures and thermal loadings induced by an SLC process. An analytical model together with a FE model were utilised to predict the geometry of the walls, followed by an FE calculation to describe the thermal behaviour of the deposition process. The 3D FE model developed by Alimardani et al. (2007) can also give an accurate prediction of the final geometry of the fabricated wall, as well as thermal and stress fields.

Material evolution during the metal AM process was also studied based on the thermal FE models. Costa et al (2005) investigated the influence of substrate size and idle time between the deposition of successive layers on the microstructure and hardness of a 10 layer tool steel wall built by laser powder deposition. The temperature history during fabricating a Ti-6Al-4V wall with the SLC process was simulated by Qin et al. (2005) using a 2D FE model. The thermal results were correlated with observed microstructures to study the material evolution during the thermal cycles of an SLC process. Charles (2008)

developed a microstructure model for Ti-6Al-4V which can be coupled to a thermo-mechanical model of the metal deposition process.

Thermally induced stresses and distortions during the metal AM process were analysed using sequentially coupled thermo-mechanical models. Chin et al., (1996) generated a 1D and a 2D FE model for a thermo-mechanical study of metal AM process on a droplet level. The temperature and stress distributions were examined via modelling a single molten metal droplet onto a comparatively large substrate. It was found that localised preheating by previously deposited droplets does not significantly affect final stress distributions after deposition of a second droplet on top of the first droplet. Their study on the residual stress on multi-layered part and successive deposition of a column of molten metal droplets on a large substrate further proved that the localised preheating by previously deposited material is not effective in reducing thermal stresses (Chin et al, 2001a). Existing stress states in previously deposited layers cannot significantly affect the final residual stress distributions in subsequent layers because the high temperatures from newly deposited material relax stresses in the existing deposited layers. Limited thermal interactions were also observed in the models with successive deposition of adjacent droplets in a row on a relatively large substrate (Chin et al., 2001b). However, the results from deposition of molten material droplets on a thin substrate showed that the preheating effect can reduce thermal gradients of the parts and substantially reduce the residual stress magnitudes. The same effect is expected when deposit a large amount of droplets on a thicker substrate. This self-generated stress reduction from the deposition process could be increased by choosing optimal deposition paths.

Mughal and colleagues (2006a) carried out a study on the distortions and residual stresses of a multi parallel layer metal AM part built by WAAM process using a 2D FE model. It was reported that continuous deposition without interpass cooling results in higher preheating of the substrate which consequently reduces the final deformation and residual stress. However, due to the nature of the 2D model, it cannot give predictions on the bending

distortion and longitudinal shrinkage. The mechanical effect of deposition patterns of the same multi parallel layer WAAM part was investigated using a 3D thermal-mechanical FE model (Mughal et al., 2006d). The result of this study is described in section 2.6 of this thesis.

The mechanical influence of the additional preheating on back of the substrate was examined by Labudovic et al. (2003) via a 3D FE model of an SLC process. It was found that preheating can reduce the stress level thus avoid cracking. The same conclusion was also summarised by Alimardani et al. (2007) in their paper.

2.6 Control of residual stresses and distortions

There are many techniques that have been developed for minimising the effects of residual stresses and distortions in welding process. These methods can be put into two categories depending on whether additional process is required or not. Techniques such as applying a proper clamping system (Masubuchi, 1980; Mahapatra et al., 2006; Schenk et al., 2009a; Schenk et al., 2009b), prebending (Masubuchi, 1980; Chen et al., 2005), preheating (Jung and Tsai, 2004; Labudovic et al.,2003), thermal tensioning (Deo and Michaleris, 2003; Li et al., 2004), global mechanical tensioning (Staron et. al. 2004; Price et. al., 2007; Altenkirch et. al. 2008), local mechanical tensioning (Altenkirch et al, 2009), and post-weld processing (Masubuchi, 1980; Chen et al., 2005; Berglund et al., 2003) are the main methods for mitigating residual stresses or distortions in welding process with extra manufacturing process and facilities.

In contrast, controlling the residual stresses and distortion level by using optimised welding parameter and welding sequence does not need additional manufacturing effort. This may not eliminate the mechanical issues to a desired amount for all the cases, however it can greatly reduce the extra work. The influence of welding parameters and welding sequence on the distortions and residual stresses can be investigated through numerical modelling.

Weld procedure has an important effect on distortion and residual stresses (Brust and Kim, 2005; Colegrove et al., 2009). Welding techniques with a low heat input result in narrower tensile residual stress zone and lower stress magnitude. Considering a certain welding process, the heat input can vary when set with different welding parameters. Brust and Kim (2005) analysed the residual stress in T-fillet weld with different travel speeds. The same level of maximum longitudinal stresses was observed in all the cases, however slower travel speeds bring larger area of the longitudinal residual stress from the weld. The transverse residual stresses are higher for the faster travel speeds but still insignificant compare to the residual stresses in the longitudinal direction. The relationship between welding parameters for aluminium alloy and thermo-mechanical responses was explored using statistical method (Song et al., 2007). Approximation models were developed to provide optimal welding parameters. The effects of process parameters on the residual stresses and part distortions in the fused deposition modelling process were studied by Zhang and Chou (2008) with a 3D FE model and design of experiment technique. It was found that the scan speed and layer thickness have significant effect on the residual stresses.

Weld sequencing has been widely utilised in controlling distortions and stress distributions in large fabrications. The best strategy was usually obtained from real world experimental trials and nowadays can be found using numerical modelling. Tsai et al. (1999) studied the distortion behaviours of welding thin-plate panel structures using a 3D FE model. The flatness of the panel was improved and the angular distortion was minimised using the optimum welding sequence which was found by case-by-case studies. Teng et al. (2003) analysed the effects of different welding sequences on single-pass butt-weld, multi-pass butt-weld and circular patch welds by evaluating the thermo-mechanical behaviours. It is suggested to leave more free space for expansion and shrinkage in the welding structure during the welding process to decrease the residual stresses. Sattari-Far and Javadi (2008) investigated the effect of welding sequences on welding deformations in pipe joining. The amount of

welding distortions was substantially reduced using the better welding sequences.

Song et al. (2005b) investigated the influence of different deposition paths of an wire and arc welding based deposition process on the final distortions, hardness and tensile stresses by conducting experimental trials. The effect of deposition patterns on the residual stress and deformation was studied on SMD process using FE models (Nickel et al., 2001). The FEM results of the deposition processes showed that the deposition pattern has a significant effect on the distortions, which was also proved by experimental results. For building long rectangular shaped components, raster pattern with lines perpendicular to the component's long axis produces the lowest deformation; and for building square shaped components, using the spiral pattern from outside to the inside produces the lowest distortion. Similar research was conducted by Mughal et al. (2006d) to find the best deposition sequence for building a square shape with seven parallel weld beads. According to the simulation results of the residual stresses and distortions the best building strategy is starting from the outer paths and ending to the centre path.

2.7 Research Gap

The FE method has been proved to be a reliable alternative to real world experiments in the research area of thermo-mechanical performance of welding and metal AM process. With the continuously improved FE tool the interaction between the thermal behaviour, residual stresses and final distortions can be accurately simulated. However, due to the huge computational effort that required by the conventional transient FE model the previous thermo-mechanical studies on AM process are constrained to a small scale. The thermo-mechanical performance of large scale WAAM process needs to be investigated.

There is a potential possibility of minimising the residual stresses and distortions though using optimised building parameters and building strategies. The optimisation of the process can be critical to the WAAM process, especially

for building large scale parts or when using extra processes and facilities for controlling distortion is difficult or completely impossible because of the implementation difficulty and huge cost. FE models could be a useful tool to help developing better building strategies. However, no previous FE model of AM process shows the capability of providing 3D thermo-mechanical predictions in a practical time.

It is especially impractical to use the conventional transient FE model for the simulation of the WAAM process as the scale of the WAAM parts can be several meters and their multi-layer structure multiply the total length of the deposition. Many computationally efficient FE approaches have been developed for analysing large scale welding process. However, they are not suitable to be applied to the WAAM components with complex multi-dimensional features.

There is a research gap and practical need of a new computationally efficient numerical approach for dealing with the WAAM process for large scale parts. The efficient FE models will enable the study of WAAM for different aspect which can provide information to control residual stresses and reduce distortion of the WAAM process.

2.8 Summary

The literature has examined the following areas related to this research:

- Additive layer manufacturing
- Thermo-mechanical issues during the metal deposition process
- Numerical modelling of welding process including methods to improve computational efficiency
- FE modelling of MALM process
- Methods of mitigating residual stresses and distortions

The findings of the literature review have helped to shape the focus of this research. The research aim and objectives of this thesis are formalised in Chapter 3 according to the research gap summarised in this chapter.

3 RESEARCH AIM AND OBJECTIVES

3.1 Introduction

In Chapter 2 the research gap has been summarised based on the extensive literature survey. This chapter clarifies the aim and objectives of this thesis to fulfil the research gap. The scope of this thesis is outlined according to the objectives. The methodology which this research follows to achieve the objectives is introduced and the main deliverables during the completion of the research are listed.

3.2 Research Aim

The overall aim of this research is to obtain better understanding of the thermo-mechanical performance of WAAM process through FE modelling. The focus of this research is on efficient FE approach for the large scale WAAM components.

3.3 Research Objectives

The specific objectives of this project are:

- Establish the state-of-the-art in research areas related to the thermo-mechanical modelling of WAAM processes.

- Investigate the thermo-mechanical phenomenon of WAAM process through FE models, and accurately predict the temperature distribution, residual stress and distortions of WAAM process. The accuracy of the model needs to be validated with experiments.

- Develop an efficient approach to provide the thermo-mechanical predictions for large WAAM components in a short time.

- Investigate the procedural influence of the WAAM process on the thermo-mechanical performance using FE approaches.

- Develop a robot programme generating prototype that is able to efficiently integrate the building strategies.

3.4 Research Scope

Based on the aforementioned objectives the research scope is as follows:

- Domain: this research focuses on the thermo-mechanical analysis of large scale WAAM process using FE approaches. Getting the thermo-mechanical performance of the WAAM efficiently is the main target of this research. The microstructure changes due to the thermal cycles are not in the research scope. The main material used in this research is mild steel S355.

- Literature survey: there is a concentration on AM techniques and the FE modelling techniques used to analysis the thermo-mechanical performance of AM process.

- FE model implementation: all the modelling work in this thesis is performed with the commercial FE software ABAQUS. However, the formulation and implementation of the finite element methods are out of the scope of the thesis.

- Efficient FE model for WAAM process: the efficient FE approaches that proposed in this thesis are developed to suit the WAAM process for large scale and comparatively simple geometries.

- Applications with the FE models: the FE models that developed in this thesis are used in the process study of the WAAM process which helps to obtain better building strategies.

3.5 Research Methodology

3.5.1 Problem Statement

The significant residual stresses and distortions which are induced during the thermal cycles of the WAAM process can be predicted and analysed with FE modelling approaches.

3.5.2 Literature Review

The literature survey undertaken as part of the research has covered the area of thermo-mechanical studies of the welding and WAAM process. The following steps were taken to complete this review:

- Keyword identification: the main keywords regarding additive layered manufacture and thermo-mechanical analysis of WAAM and welding processes were sought, for example, thermo-mechanical analysis, residual stresses, distortions, FEM, welding, additive manufacture, efficient numerical model.

- Database search: using the database provided by the library of Cranfield University, around 200 research papers, thesis, and books were sought.

- Paper filtering: papers were filtered based on their areas.

- Paper analysis: key papers from each area are identified at this stage and the current research stage has been analysed.

- Research gap: the research gap was identified from the analysis provided from the previous stage.

3.5.3 Research Focus Identification

The literature survey and the work description from the RUAM project narrowed the research focus of this thesis down to the aforementioned aim and objectives. The main research target is to understand the thermo-mechanical performance

of WAAM process via FE models and to develop an efficient FE approach which can provide fast predictions of residual stresses and distortions.

3.5.4 Transient FE Model Development and Verification

In the first phase, the widely used three-dimensional transient model was developed and verified to provide a good understanding of the WAAM process. The accurate transient model is also used as the 'base model' in this thesis to give reference data for the other models, thus the time and materials on the real experiments can be saved.

The complexities of the models generated in this PhD research follow Lindgren's modelling strategies for different modelling accuracy levels (L. Lindgren, 2007). A preliminary "basic simulation" model, where only the overall residual state is of interest, was chosen for the WAAM simulation. According to the recommendations by Lindgren, the volume change due to phase changes has been ignored. The temperature-dependent thermal and mechanical properties, as well as latent heat due to solidification were used.

Uncoupled thermo-mechanical models have been built to simulate the WAAM process on mild steel S355 and titanium alloy Ti6AL4V. To calibrate the parameters used of the models and to verify the models, real-world experiments have been performed. The details of the model generation and verification are introduced in Section 5.1.

3.5.5 Development of the Efficient FE Approaches for Large Scale WAAM Components

One of the main challenges for this research is how to build the model in a way that the computational prediction of large WAAM objects can be finished in a practical time with a reasonable accuracy. The following stages are involved in the development of the efficient FE approaches for the large scale WAAM components:

- Investigation of the current efficient FE models for welding processes – identify the suitable approach that can be implemented in the analysis of WAAM process.
- Development of the new thermal approach for large scale WAAM process based on the steady-state theory.
- Implementation of the mechanical model based on the transferred thermal history from the steady-state thermal results.
- Development of the simplified mechanical approach which can provide mechanical predictions efficiently.
- Model validation with the experimental results and transient FE results.

3.5.6 Application of the FE Models

The FE models developed in this thesis have been utilised in the process study of the WAAM process. A series of case studies have been performed to investigate the influence of the building parameters and building strategies on the thermo-mechanical performance of the WAAM components, including:

- Deposition parameter study
- Residual temperature study
- Crossing structure building study
- Deposition sequence study
- Balanced building strategy study

3.5.7 Robot Program Generation

An initial robot program generation prototype has been developed to efficiently integrate the building strategies extracted from the FE case studies into the real-world WAAM applications.

3.5.8 Contribution to Knowledge and Limitations

The research gap is fulfilled and contribution to knowledge is established during the completion of this research. The limitations of the proposed approaches are discussed and possible future improvements are outlined.

3.6 Research Deliverables

The following deliverables have been completed in this research:

- A literature survey covering the state-of-the-art in the areas of AM process, thermo-mechanical analysis of welding and AM process.
- Transient thermo-mechanical model of wall structured AM part and the experimental verification.
- Efficient FE approaches which can provide fast thermo-mechanical predictions for large scale WAAM components.
- A series of case studies performed with the FE models to investigate the influence of the building parameters and building strategies on the thermo-mechanical performance of the WAAM components.
- A robot path generation prototype that is capable of generating robot programmes directly from the CAD model and efficiently integrate the building strategies.

3.7 Summary

In this chapter the aim and objectives of this research have been identified. The research scope has been outlined to meet the research objectives. The methodology followed to achieve the objectives has been discussed. The following chapter contains the transient thermo-mechanical FE model and the verifications as a main deliverable of this research.

4 TRANSIENT THERMO-MECHANICAL ANALYSIS OF WAAM PROCESS AND VERIFICATION

4.1 Introduction

With the increasing performance of the modern computing systems, three-dimensional transient thermo-mechanical models have been widely utilised for studying welding processes and also additive manufacturing process. So far it is probably the most accurate model for predicting thermally induced residual stresses and distortions. Accurate FE models can be used as a complementary tool for real-world experiments to get thermo-mechanical information, and can provide data which are difficult or not possible to get from experiments.

In this chapter, a 3D transient thermo-mechanical FE model of multi-layered WAAM part is developed and verified with experimental results. Thermal histories are calculated first as the input thermal load of the subsequent mechanical model. A moving heat source is utilised to simulate the movement of the weld torch. This 3D transient thermo-mechanical model is used as the 'base model' to give reference data for the other models developed in the thesis.

The main material used in the models of this chapter and the following chapters is mild steel S355. The thermo-mechanical performance on Ti-6Al-4V is also introduced in this chapter as another main material used in the RUAM project due to its highly important role in aerospace industries. All the modelling work in this thesis is performed using the commercial finite element code ABAQUS. The FEM jobs were calculated by the grid computing system with 4 processors in IT department of Cranfield University.

4.2 Modelling Strategy

The target of the FE model is to provide overall predictions of thermo-mechanical performance of WAAM parts. The performance of the high temperature is not particularly interested, and the changes on the material's microstructure are not in the research scope. Different modelling strategies

have been discussed in Section 2.4 of the thesis based on literature. Some of the important findings are summarised here as the modelling strategy for this FE model of the WAAM process:

- The thermo-mechanical performance of the WAAM process can be solved sequentially as it can be treated as weakly coupled problems.

- It is suggested to use linear or quadratic brick elements for the thermal analysis and linear or quadratic reduced integration elements for the mechanical analysis. Dense meshes need to be adopted in the weld zone and its vicinity.

- Reliable temperature dependent thermal and mechanical material properties are required in the simulation, especially for the thermal conductivity and yield stress. A cut-off temperature which equals to $0.5T_m$ to $0.7T_m$ is needed to be decided, where T_m is the melting temperature of the material. Volume changes due to phase changes, rate dependent material properties and fluid flow effect can be ignored.

- Goldak's double ellipsoid model can be used as the heat source model. The net heat input needs to be defined accurately as it has significant influence on the temperature distribution. The geometric parameters of this model can to be decided from cross-section metallographic data of the weld and from weld pool surface ripple markings.

- The thermal boundary condition needs to include the radiation and convection. An equivalent convection coefficient needs to be defined if a cooling system is applied under the base plate. The mechanical boundary condition needs to include constraints from the clamps.

- Filler material can be modelled using the "element birth technique".

4.3 Thermo-mechanical Analysis of WAAM Component on S355

Mild steel S355 is one of the main materials used in the RUAM project. S355 is selected as the main material for developing the FE approaches in this thesis as the reliable temperature dependent material properties are available in literatures. The transient thermo-mechanical analysis of a 500 mm WAAM wall is described in this section.

4.3.1 Experimental Setup for WAAM on Mild Steel

Figure 4-1 shows the setup of the WAAM system which was used to build the S355 samples. A six-axis industrial robot was used to accurately reproduce the welding torch transverse speed and the layer upon layer build up sequence. The heat source is a Cold Metal Transfer (CMT) welding power source, a modified GMAW variant based on a controlled dip transfer mode mechanism, which can provide a high deposition rate capability at a relatively low heat input (Pickin and Young, 2006). The welding wire used in this study is 0.8 mm in diameter and the wire feed speed is 10 m min^{-1}. The travel speed of the welding torch is 8.33 mm s^{-1}. The welding process heat input is 270 J mm^{-1}, assuming an efficiency of 0.9 (Colegrove et al., 2010). A water cooled aluminium backing plate was utilised in order to cool the sample more rapidly. Six clamps were utilised to fix the base plate to the cooling bar. A waiting time of 400 seconds was used between subsequent layers enabling the sample to cool below 50°C before new layers were deposited.

The base plate dimension of the samples was 500 mm long, 60 mm wide and 12 mm thick. The multi-layer wall shaped samples were deposited along the centreline of the base plate with a width of 5 mm and an average height of 2 mm for each layer. The welding process parameters utilised in these experiments was obtained from a preliminary process model study in order to achieve a specified target wall.

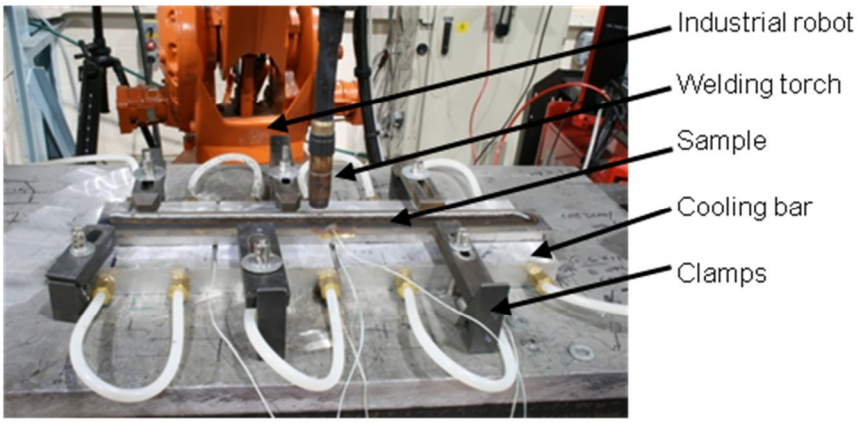

Figure 4-1: WAAM system setup.

The base plates used in the experiments were rolled structural steel plates (grade S355JR-AR). The chemical composition of the alloy (in wt. %) was 0.24% C, 1.60 % Mn, 0.55% Si, 0.045% P, 0.045% S, 0.009% N, 0.003-0.100% Nb and Fe balance. The selection of the consumable electrode was based on a strict chemical composition criterion in order to obtain optimum as welded mechanical properties. The chemical composition of the solid wire (in wt. %) was 0.08% C, 1.50% Mn, 0.92% Si, 0.16% Cu, ≤0.040% P, ≤0.035% S and Fe balance.

The dimensions of the samples are shown in Figure 4-2. To obtain the thermal cycles during the deposition process, four k-type thermocouples were located in the interior and on the surface of the base plate at the positions indicated in Figure 4-2. TP1, TP2 and TP3 were directly welded to the base plate surfaces, and TP4 was welded in a drilled hole which was four millimetres deep relative to the back surface.

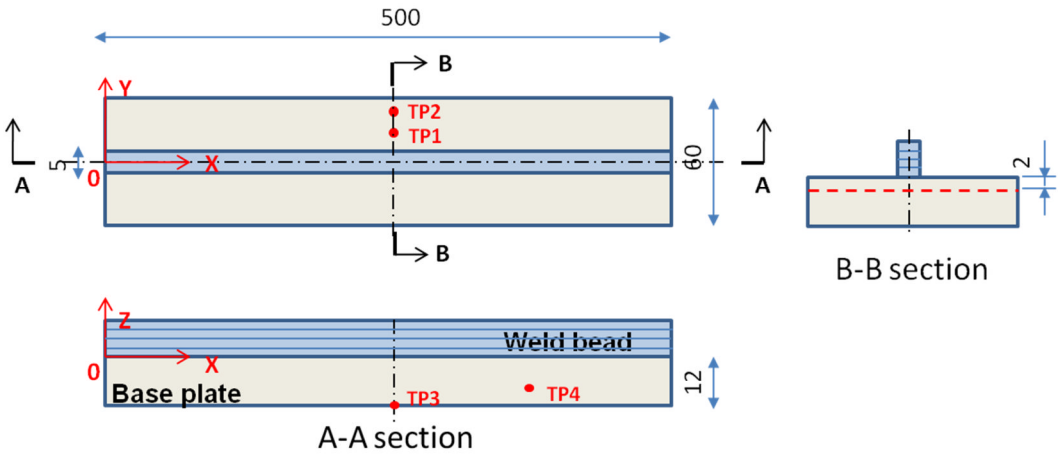

Thermocouple positions (unit: mm)			
	X	Y	Z
TP1	250	5	0
TP2	250	20	0
TP3	250	0	-12
TP4	375	0	-8

Figure 4-2: Geometry of the WAAM sample of S355.

To verify the mechanical model, distortion measurements were taken using a Romer Omega Arm with R-Scan 3D laser scanning system. Residual strain measurements were carried out at the ENGIN-X strain scanner at ISIS, Oxford, UK. Residual stresses data of three directions were taken in the base plate at the position 2mm below the top surface and located along the transverse direction of the mid-length section of WAAM samples, which is shown in B-B section of Figure 4-2. Residual stresses were also measured along the normal direction of the mid-length section of the deposited wall.

The time-of-flight principle of strain measurement was utilised to determine the lattice strain (Dann et al., 2004; Santisteban et al., 2006). The longitudinal strain direction was measured using a gauge volume of 2×2×2 mm^3, while the transverse and normal strain directions were measured using a gauge volume of 2×20×2 mm^3. The opening of the vertical dimension of the incoming beam during measurement of the transverse and normal strain directions would lead to faster measurement with a higher neutron flux without the loss of any spatial

resolution. The data analysis was performed for a time-of-flight spectrum of 20-40 milliseconds which contains the {110}, {200} and {211} families of crystallographic planes. The range and families of crystallographic planes analysed ensured an average macroscopic strain determination free from crystal anisotropy. The diffraction spectrum was analysed by Pawley refinement using GSAS software.

References for strain calculations were measured in the far field parent in a 3 mm thick slice removed from the edge of the specimens. As the penetration level of the deposited wire would not affect the composition of the measurement location in the base plate as the measurements were carried out at a depth lower than the weld metal penetration (as shown in Figure 4-3), a constant stress free value was used for the calculations of the stresses in the base plate in all the cases. This stress free value was measured from the 3 mm slice machined out from the end of the specimen of the 3 layers wall. Different reference slice was used for the measurements on the deposited material of the 20 layers wall sample.

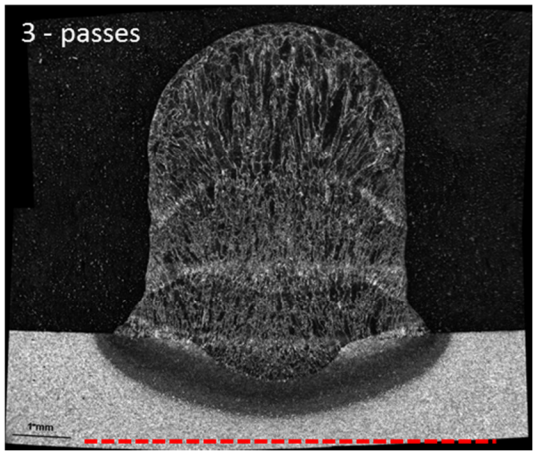

Figure 4-3: A macrograph of the three layer deposit and the measurement position (red dash line) in the base plate.

Strain measured in all the three directions were then combined to analyse the stress assuming the measured directions are the principal strain directions and following Hooke's law as shown in following equation:

$$\sigma_x = \frac{E}{(1+\upsilon)}\varepsilon_x + \frac{E\upsilon}{(1+\upsilon)(1-2\upsilon)}(\varepsilon_x + \varepsilon_y + \varepsilon_z) \quad (4\text{-}1)$$

Where $\varepsilon_x, \varepsilon_y$ and ε_z are the strains in the principal directions; E is the elasticity of the material; and υ is Poisson's ratio of the material.

4.3.2 Implementation of the Transient Thermo-mechanical Model

The thermo-mechanical analysis of the WAAM process in this chapter follows the procedure shown in Figure 4-4. The same FE meshes were employed in both thermal model and mechanical model with different element type. A 3D transient thermal analysis was conducted first, and the thermal results were loaded in a plastic-elastic model for calculating residual stresses and distortions.

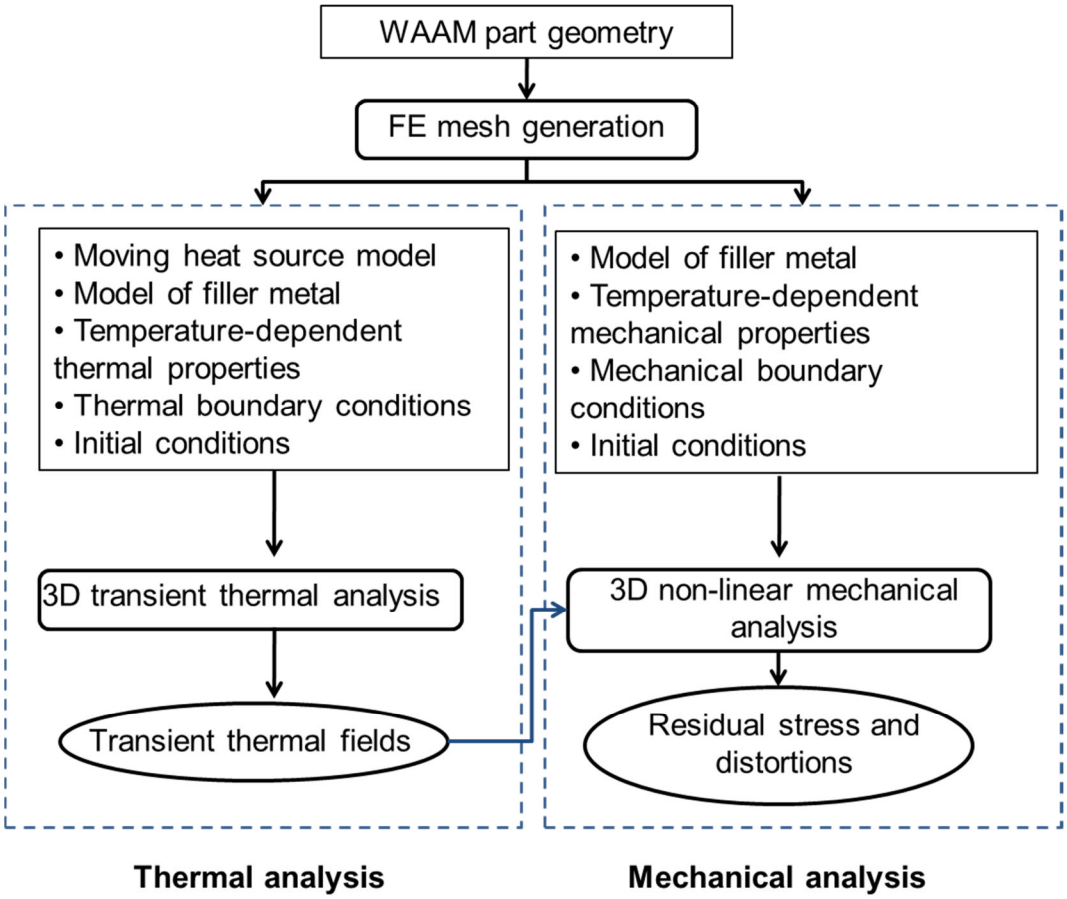

Figure 4-4: Procedure of transient thermo-mechanical modelling of the WAAM process.

4.3.2.1 Finite Element Meshes

The number and size of the FEM meshes can significantly influence the accuracy of the model and the computational time. With the same circumstances using smaller meshes in the model intend to give more accurate results. However, long calculating times and huge data storage space are required for completing the job. Thus, a balanced meshing strategy should be used to get the temperature and stress fields with acceptable accuracy while having the fewest number of elements in the model.

To obtain the proper meshing for the model, a mesh sensitivity study was conducted. The test was performed on three small scaled models with different meshing densities. The width and thickness of the base plate used in this study were the same to those used in the experiment, which were 60 mm and 12 mm respectively. To save computational time, the length of the base plate for the mesh sensitivity study was set to 50 mm. One layer of deposited material is modelled on top of the base plate which was 2 mm in height and 5 mm in width. After the deposition, 60 seconds waiting time was used in the last computing step to cool the components down.

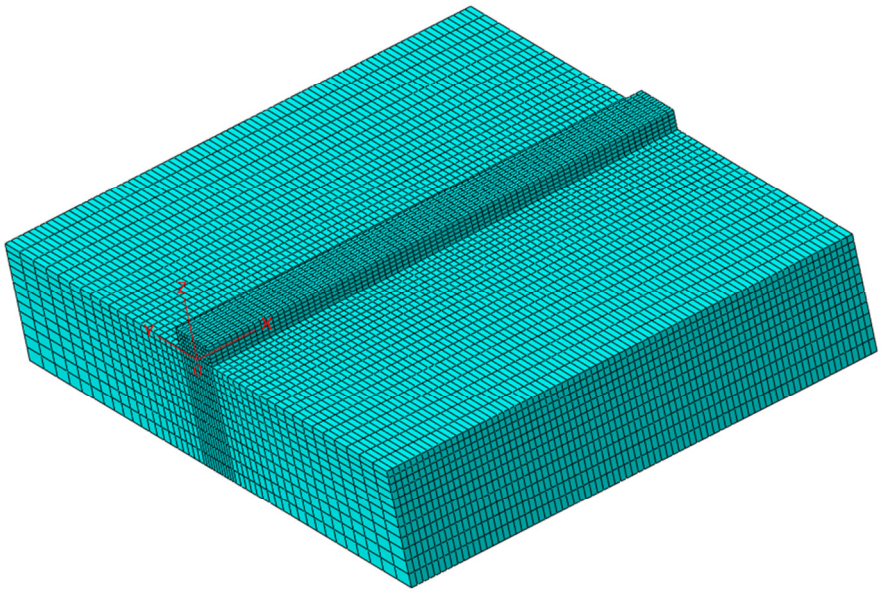

Figure 4-5: Mesh sensitivity study (Mesh 1).

Because the materials of the weld bead and in the Heat Affected Zone (HAZ) experience high temperature gradients, dense meshes were utilised in this area. Biased meshes were used for the base plate in the y and z directions as shown in Figure 4-5. The number of the elements in the three models was reduced gradually. The least element number of the model in the three directions was decided considering the accuracy of the model. It has been reported that there should be at least 6 linear elements spreading over bead width to achieve reasonably accurate temperature predictions (Cheng, 2005). Thus, six constant sized elements were set up for the deposited material area in the y direction. To accurately describe the heat source, at least three elements were used covering the length of the heat source. A total of 20 constant elements with the length of 2.5 mm were used in Mesh 3 in the x direction. Three constant sized elements were utilised in Mesh 3 over the bead height to capture the temperature variation in this direction. The detailed information about the three different meshes is listed in Table 4-1.

All the material properties, the heat source model, and the thermal boundary conditions were set up the same as the thermal model introduced in section 4.3.2.2. Linear brick elements with 8 nodes (DC3D8) and quadratic brick elements with 20 nodes (DC3D20) are the most commonly used elements for the thermal simulations. Compared to linear elements, quadratic elements are more accurate with the expense of significantly increased computational time. In this study the performance of both linear element and quadratic element is evaluated.

Table 4-1: Meshing descriptions for the mesh sensitivity study.

	Mesh 1	**Mesh 2**	**Mesh 3**
X direction	80 constant elements.	40 constant elements	20 constant elements
Y direction	12 constant sized elements for the	8 constant sized elements for the	6 constant sized elements for the

	deposited material area. 40 biased elements for the base plate away from the welding line.	deposited material area. 20 biased elements for the base plate away from the welding line.	deposited material area. 14 biased elements for the base plate away from the welding line.
Z direction	5 constant sized elements for the deposited material area. 12 biased elements for the base plate away from the welding line.	4 constant sized elements for the deposited material area. 8 biased elements for the base plate away from the welding line.	3 constant sized elements for the deposited material area. 4 biased elements for the base plate away from the welding line.
Total element number	39480	8432	2300
DOF for linear elements	44304	10080	3094
DOF for quadratic elements	172261	38597	11529

Temperature histories were extracted from the thermal models at five different positions in mid-section, which were P1 (25, 0, 0), P2 (25, 0, -2), P3 (25, 5, 0), P4 (25, 0, -8), P5 (25, 20, 0). As shown in Figure 4-6, all the models give similar temperature results for all the temperature plotting locations. The model with the

finest DC3D20 elements is expected to provide the most accurate thermal result as it has the highest number of nodes and the degrees of freedom (DOF), so the model with Mesh 1 DC3D20 elements was used as the reference model. A comparison of predicted peak temperatures from P1-P5 is given in Table 4-2, which also shows in percentage the difference of the predicted peak temperatures between the reference model and the other five models. In general, the model with the coarsest 8-noded elements shows the largest difference to the reference model. However, the differences are insignificant compared to the references in all the comparison positions except for P5 where this model gave a prediction about 8% higher than the data from the reference model. However as the peak temperature in this area is rather low and will not cause plastic flow, the thermal data in this area will not have a big influence on the stress prediction.

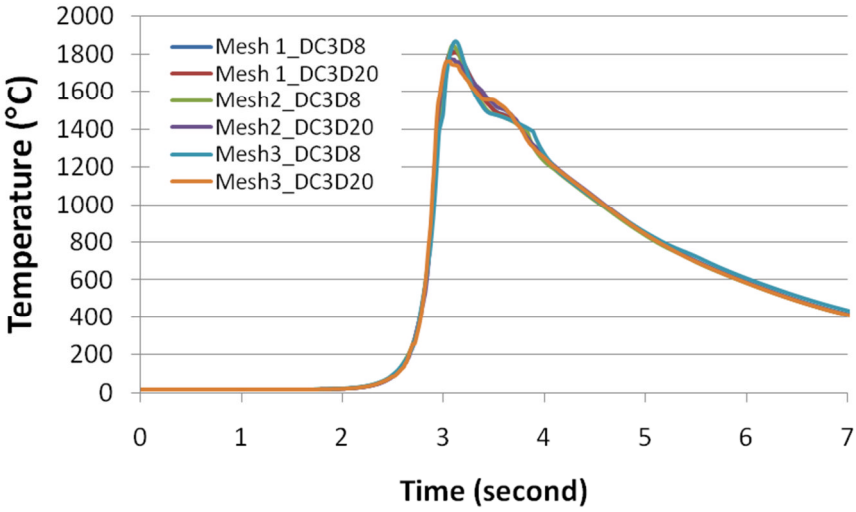

(a)

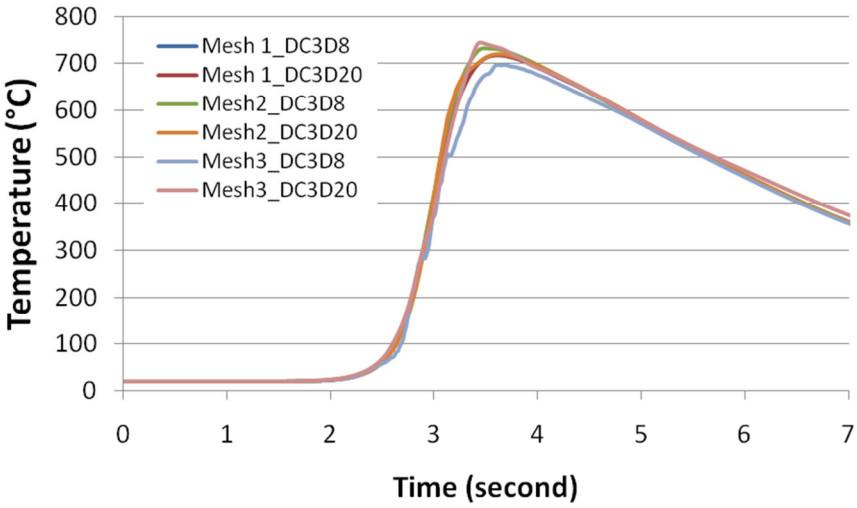
Temperature (°C)
800
700
600
500
400
300
200
100
0
0
1
2
3
4
5
6
7
Time (second)
Mesh 1_DC3D8
Mesh 1_DC3D20
Mesh2_DC3D8
Mesh2_DC3D20
Mesh3_DC3D8
Mesh3_DC3D20

(b)

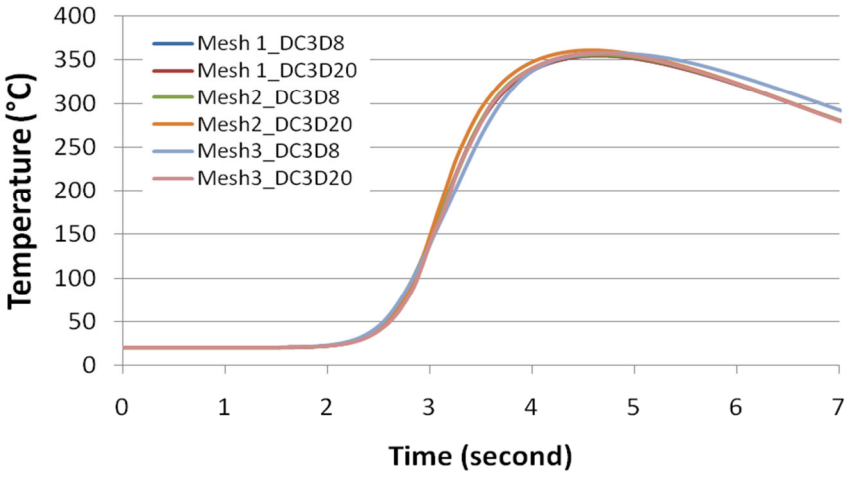
Temperature (°C)
400
350
300
250
200
150
100
50
0
0
1
2
3
4
5
6
7
Time (second)
Mesh 1_DC3D8
Mesh 1_DC3D20
Mesh2_DC3D8
Mesh2_DC3D20
Mesh3_DC3D8
Mesh3_DC3D20

(c)

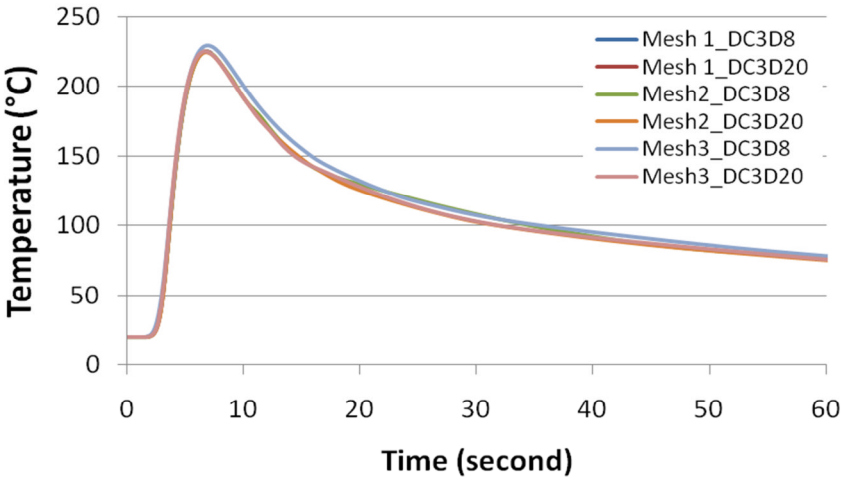
Temperature (°C)
250
200
150
100
50
0
0
10
20
30
40
50
60
Time (second)
Mesh 1_DC3D8
Mesh 1_DC3D20
Mesh2_DC3D8
Mesh2_DC3D20
Mesh3_DC3D8
Mesh3_DC3D20

(d)

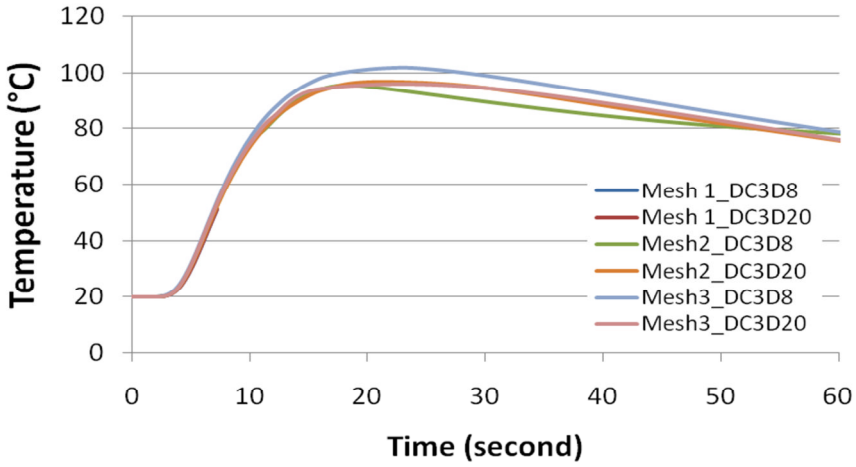

(e)

Figure 4-6: Temperature histories from: (a) P1, (b) P2, (c) P3, (d) P4, (e) P5.

Table 4-2: Comparison of the predicted peak temperatures (°C) from P1-P5.

Mesh type	Mesh 1 DC3D20	Mesh 1 DC3D8	Mesh 2 DC3D20	Mesh 2 DC3D8	Mesh 3 DC3D20	Mesh 3 DC3D8
P1	1812.3 (Ref.)	1814.7 (0.1%)	1779.2 (-1.8%)	1846.8 (1.9%)	1760.0 (-2.9%)	1866.6 (3.0%)
P2	718.1 (Ref.)	718.2 (0.0%)	719.3 (0.2%)	731.6 (1.9%)	743.9 (3.6%)	696.6 (-3.0%)
P3	225.5 (Ref.)	225.3 (-0.1%)	224.8 (-0.3%)	225.2 (-0.1%)	225.5 (0.0%)	229.5 (1.8%)
P4	355.1 (Ref.)	355.5 (0.1%)	361.4 (1.8%)	356.2 (0.3%)	358.0 (0.8%)	358.0 (0.8%)
P5	94.3 (Ref.)	94.2 (-0.1%)	96.8 (2.7%)	95.6 (1.4%)	94.3 (0.0%)	101.6 (7.7%)

Table 4-3 shows the comparison of total CPU time used for each models to complete the calculation. One can see that the slight accuracy advantage

results in huge computational effort. Compared to the model using coarsest linear brick elements DC3D8 in Mesh 3 category, the model with dense quadratic brick elements in Mesh 1 category had more than 50 times more DOF. As a result, the latter model required more than 300 times more computational time to complete the analysis than the first one. The linear DC3D8 elements with high density in Mesh 1 category and quadratic DC3D20 elements in Mesh 1 and Mesh 2 category all result in comparatively long computational time, which is not suitable to be used for the analysis of large scale WAAM process.

Table 4-3: Computational time comparison for the mesh sensitivity study of thermal analysis.

Mesh type	Mesh 3 DC3D8	Mesh 3 DC3D20	Mesh 2 DC3D8	Mesh 2 DC3D20	Mesh 1 DC3D8	Mesh 1 DC3D20
CPU time (second)	1671	5981	5229	37968	43757	609000
Time factor	---	3.6	3.1	22.7	26.2	364.5

As the thermal model with meshes in category Mesh 1 is not suitable for the large-scaled WAAM simulation, the mesh sensitive study for the mechanical model is performed only on Mesh 2 and Mesh 3. It has been reported (Elcoate et al., 2003) that fully integrated elements can be over constrained (element “locking”) in the area where high plastic strain generated. Reduced integration elements and the reduced integrated hybrid elements are suggested in the mechanical simulation of the welding process, however the reduced integrated hybrid elements will result in longer computational time (Elcoate et al., 2003). In this study reduced integrated linear elements (C3D8R) were utilised. The mechanical boundary was simplified that the base plate was perfectly fixed during the deposition time.

Figure 4-7 shows the stress distribution from the two models in three directions. It can be seen that in general the stress distributions of these two models are very similar. Using more elements did not gain much benefit on the simulation accuracy. However, comparing the computational time of the two models in Table 4-4 the model with Mesh 2 is 6 times slower than the one with Mesh 3. Thus, the similar element size of Mesh 3 is considered adequate to be used in the thermo-mechanical analysis of the 500 mm WAAM wall.

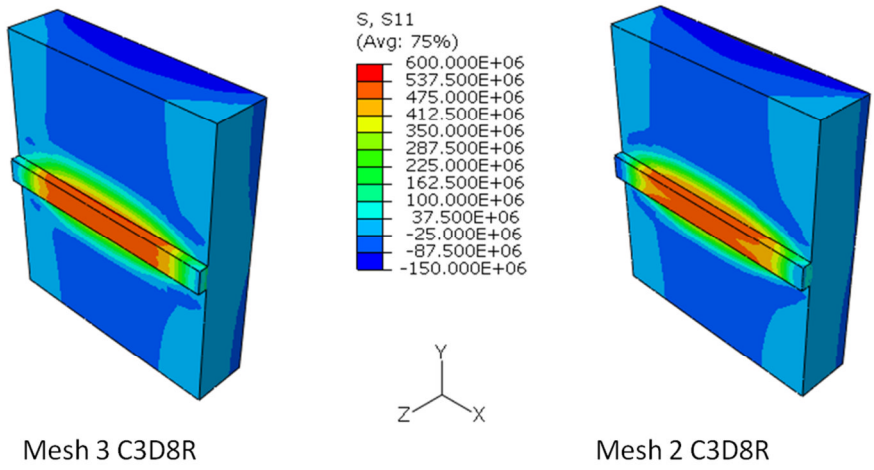

(a)

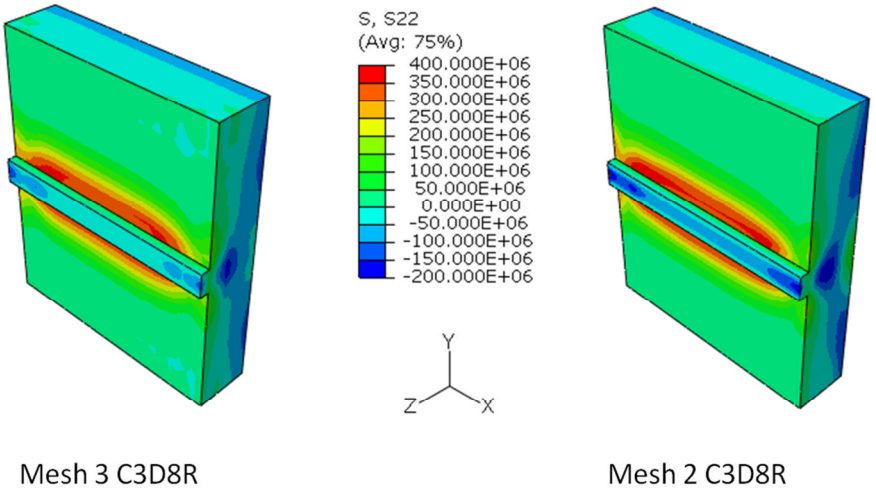

(b)

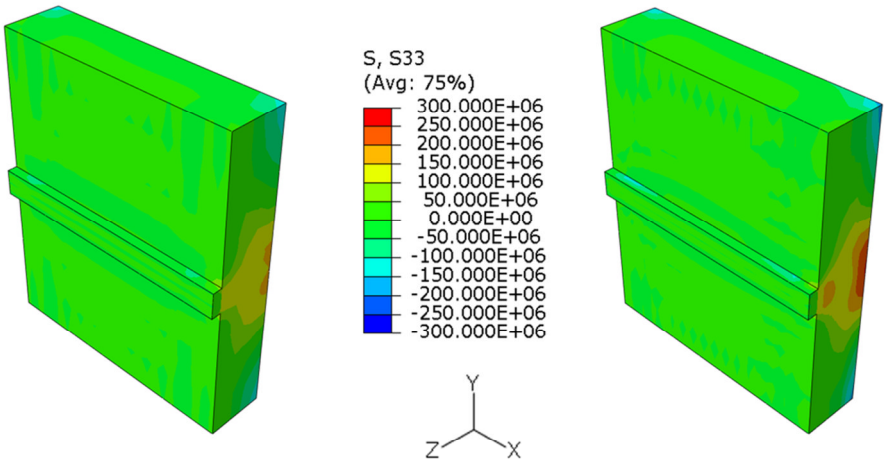

(c)

Figure 4-7: Mechanical results from models with different meshes: (a) longitudinal stress (Pa), (b) transverse stress (Pa), (c) normal stress (Pa)

Table 4-4: Computational time comparison for the mesh sensitivity study of mechanical analysis.

Mesh type	Mesh 3 C3D8R	Mesh 2 C3D8R
CPU time (second)	508	3237
Time factor	---	6.4

The multi-layer wall models were built using the measured dimensions from the samples built in the experiments. The dimension of the base plate is 500 mm x 60 mm x 12 mm. The deposited wall was modelled with a width of 5 mm and a height of 2 mm for each layer. Note that in reality the deposited beads are narrower and higher in the first few layers (as shown in Figure 4-8). This is because heat can be quickly conducted away through the backing plate or the backing cooling system for the first few layers. This influence becomes small after four or five layers of deposition and the geometry of the deposited wall becomes steady. The influence from the geometric change of the deposited bead on the thermal performance is not considered as a significant factor in

nearly all the thermal models of the AM process. Also in this study, constant width and height values are used for each layer of the deposition. The width was measured on the top part of the 20 layer wall where the geometry of the wall becomes steady. And the average layer height of the wall was taken as the layer height in the model.

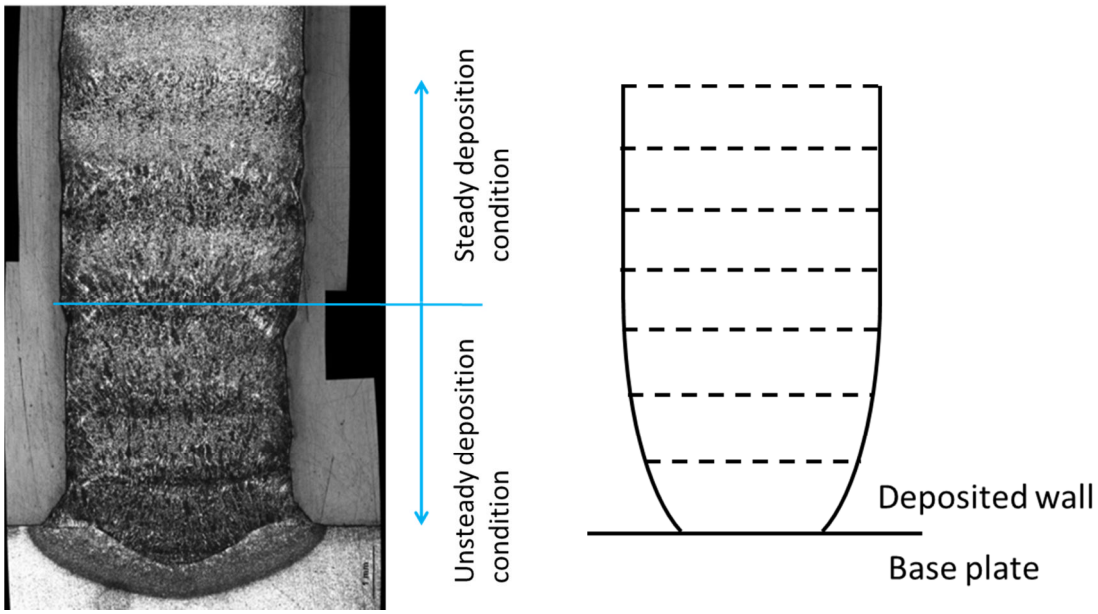

(a) (b)

Figure 4-8: Geometry of the deposited wall. (a) macrograph; (b) schematic sketch (Peyre et al., 2008).

The mesh for the 500 mm WAAM model was generated considering the findings from the mesh sensitivity study. Since the part was symmetric about the weld centreline, only half of the part was modelled with symmetry boundary conditions. The same sized small elements as in the Mesh 3 of the mesh sensitivity study, which were 2.5 mm × 0.833 mm × 0.667 mm, were used for the deposited wall and the area near the heating line to capture the high temperature gradients and significant stress changes during the deposition process. As the temperature and stress fields change slowly and distribute linearly, the mesh size was increased gradually in the y direction and –z direction away from the welding line (Figure 4-9). Transition elements were

used in these two directions to reduce the number of the elements rapidly for the area far away from the welding line where low sensitivity of different meshes to the temperature and stress results has been observed.

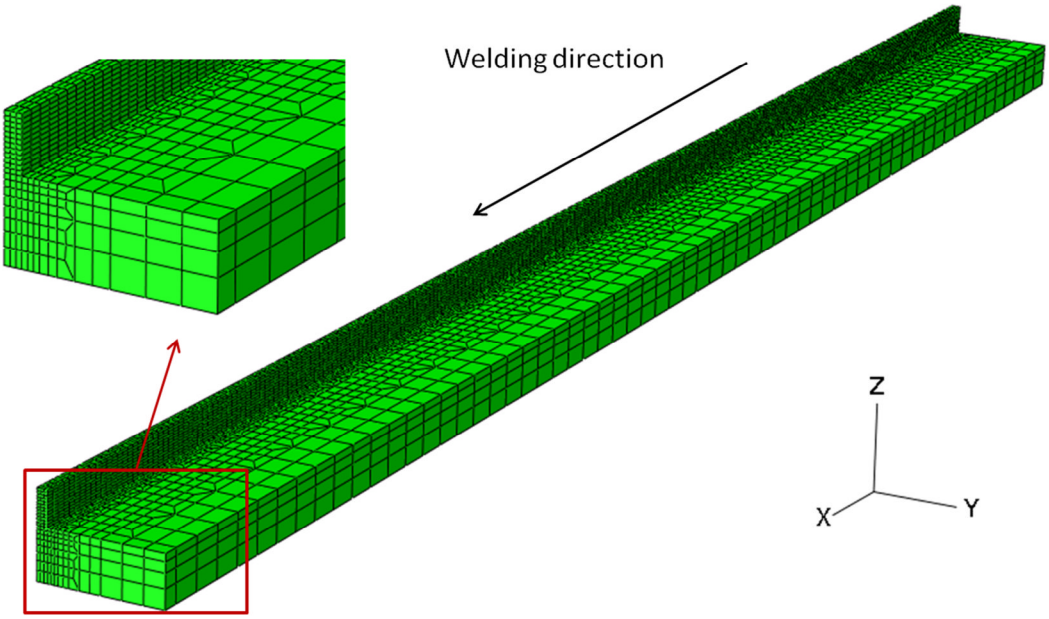

Figure 4-9: Mesh of transient thermal-mechanical model

4.3.2.2 Transient Thermal Modelling

Heat transfer during the WAAM process includes heat generation by the welding arc, heat conduction in the deposited components, and the heat loss through the free surfaces and through the cooling system under the base plate. The welding arc was simulated as a volumetric heat source with a power density moving along with the torch. This moving heat source was generated with the user subroutine DFLUX in the ABAQUS code. The Goldak double ellipsoidal heat source (Goldak et al., 1984) as shown in Figure 2-8 was used to apply the heat to the additive manufacture deposits. The power density of the region in front of the arc centre and the region behind the arc centre was defined separately using the equation 2-2 and equation 2-3 introduced in section 2.4.3. The parameter *b* was set using the value which equals to half of the width of the WAAM wall. The parameters c was set to the value which equals to the average layer height plus the penetration which was measured

from the cross-section of the metallographic profile (as shown in Figure 4-10 (a)). And the values for a_f and a_r were estimated from weld pool surface ripple markings (as shown in Figure 4-10 (b)). These detailed parameter settings for the heat source model used in this study are shown in Table 4-5.

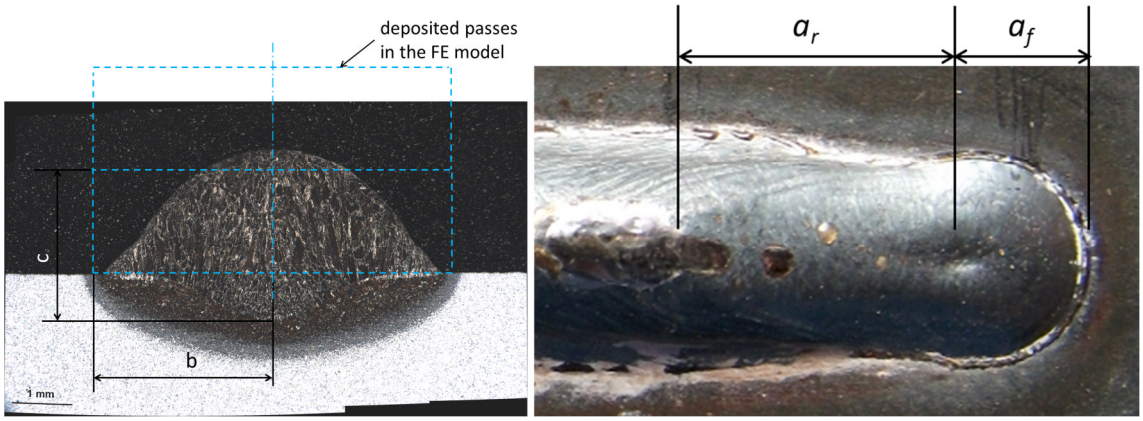

(a) (b)

Figure 4-10: The parameter settings for the Goldak double ellipsoidal heat source model. (a) Metallographic profile shows the settings for *b* and *c*; (b) weld pool surface ripple markings for a_f and a_r.

Table 4-5: Heat source parameters

a_f (mm)	a_r (mm)	b (mm)	c (mm)	Q (W)	f_f	f_r
2	6	2.5	3	2245.83	0.6	1.4

To simulate the material deposition process, the filler material was simulated using the "element birth technique" (Shan et al., 2007). With the *MODEL CHANGE option in ABAQUS, all the elements of the deposited wall were deactivated at the initial step of the analysis, and then sections of elements are activated in successive steps to simulate the metal deposition as the weld torch travels along the base plate. The smaller the size of the element section, the closer it is to the reality. However, this will cause high complexity when implementing the model and the computational time will be increased. Considering the length of the WAAM component, the length of the deposited

wall element sections added in each step was set up to 10 mm. The duration for the heating steps were set to 1.2 s which is the time for the welding torch travelling along the length of one weld bead element section. The duration for the element deactivated and activated steps are set to $1X10^{-10}$ s. The duration for the cooling step was set to 400 s which is the waiting time between subsequent layers in the real world experiment.

A pre-processing program was developed in Matlab to help efficiently generate the element sets and the input file for Abaqus. Automatic time incrementation was used in the simulation with the allowed maximum time increment of 0.1 s for the heating steps and the allowed maximum time increment of 15 s for the cooling steps. The steps in the thermal analysis were as follows:

Step 1 (1×10^{-10} s): All of the elements of the deposited wall are deactivated.

Step 2 (1×10^{-10} s): The first section of the deposited wall elements was activated.

Step 3 (0 – 1.2 s): Heat source moves, continuously applying heat flux.

Step 4 – 101 (1.2 s – 60 s): Steps 2 – 3 were repeated activating new element sections of the deposited wall and apply the heat flux.

Step 102 (60 s – 460 s): Torch removed and the component cools down to room temperature.

From Step 103 (from 460 s): Steps 2 – 102 were repeated to simulate the thermal performance of the material adding process from the second layer.

The same thermal properties were set for materials in the weld bead and base plate (as shown in Figure 4-11 and Table 4-6). Temperature dependent thermal conductivity and specific heat from Michaleris and Debiccari's paper (Michaleris and Debiccari, 1997) were taken as the reference. The specific heat was reduced when the temperature is above 723°C due to the phase transformation in this region (Totten et al., 2002; Cozzolino et al., 2011). An artificially high thermal conductivity is used for temperatures greater than 1500°C to capture

the convective heat transfer caused by the fluid flow in the weld pool. Constant material density at room temperature with a value of values to 7860 kg/m^3 was used in the simulation. The latent heat of fusion was accounted with the value of 270 kJ/kg between the solidus temperature 1450°C and the liquidus temperature 1500°C.

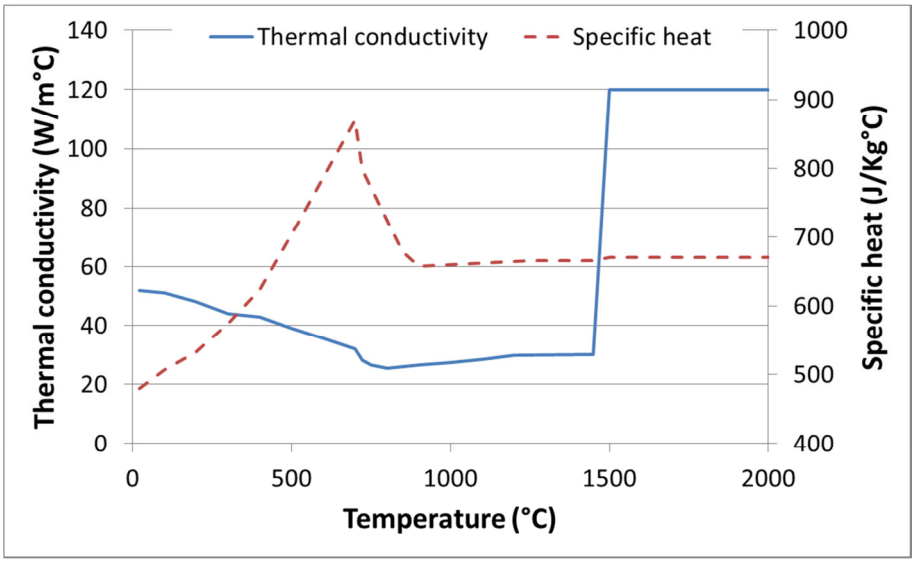

Figure 4-11: Thermal properties of S355 (Michaleris and Debiccari, 1997).

Table 4-6: Detailed thermal properties of S355 (Michaleris and Debiccari, 1997).

Temperature(°C)	Thermal conductivity (W/m°C)	Specific heat (J/Kg°C)
20	52	480
100	51	507
200	48	532
300	44	574
400	43	624
500	39	703
600	35.6	788
700	32	870
723	28	798
850	26	679
900	26.4	658
1250	30	666
1450	30	666
1500	120	670
2000	120	670

Figure 4-12 shows the thermal boundary conditions that were setup in this study. The heat loss due to radiation and convection is modelled in ABAQUS using the keywords *RADIATION and *FILMS respectively. The radiation coefficient and the convection coefficient were assumed independent of the temperature and were set to 0.2 and 5.7 W/(m^{2}K), respectively (Michaleris and Debiccari, 1997). The heat loss through the cooling system under the base plate was modelled with an equivalent convection coefficient. This coefficient was found by running a series of numerical trials, and tuning the value so that the predicted temperature profiles matched the experimental results. A value of 300 W/(m^{2}K) gave the best match with the experiments. The parameters for heat loss were not applied to the longitudinal mid-plane because of the symmetry thermal boundary. In the reality the clamps can also conduct some heat, however this was considered insignificant as the contact area of the clamps and the base plate was very small. Thus, the heat loss through the clamping devices was ignored in the model. The initial temperature was set at room temperature 20 °C. The Stefan-Boltzmann constant was set to 5.67x10^{-8} J/ (m^{2}K).

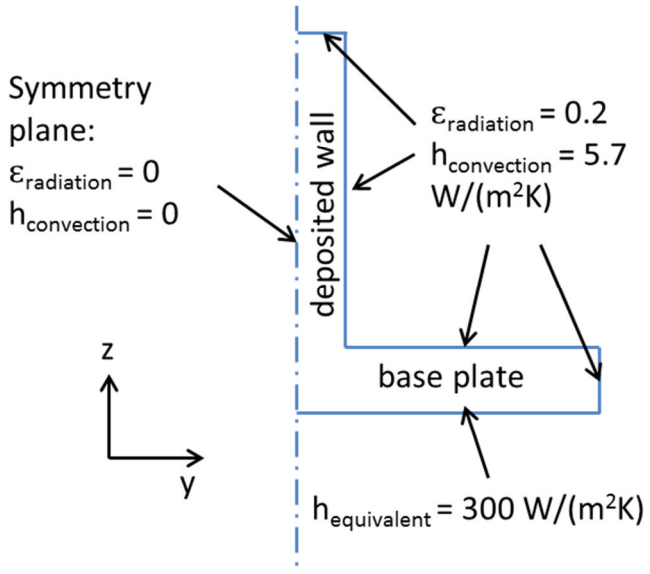

Figure 4-12: Thermal boundary conditions.

4.3.2.3 Transient Mechanical Modelling

It has been reported that the yield stress is the key mechanical property in welding simulation (Zhu et al., 2002). It has a significant effect on the residual stresses and distortions. Thus, accurate temperature dependent yield stresses must be used for the model. As the filler material is softer than the material of the base plate, different temperature-dependent yield stresses are used for the filler material and base plate. Temperature-dependent Young's modulus and thermal expansion coefficient values were also utilised in the mechanical model. The phase transformations are ignored in this study, as it has an insignificant effect on the welding residual stress for mild steel (Deng, 2009). To avoid difficulties in convergence, a 'cut-off temperature' of 1000°C was used in the material model. Young's modulus and the yield stress of the material remain at the same value for temperatures above the cut off temperature. The detailed temperature –dependant mechanical properties, which were taken from Michaleris and Debiccari's paper (1997), are shown in Figure 4-13 and Figure 4-14. The detailed temperature-dependent mechanical properties of S355 are listed in Table 4-7 and Table 4-8.

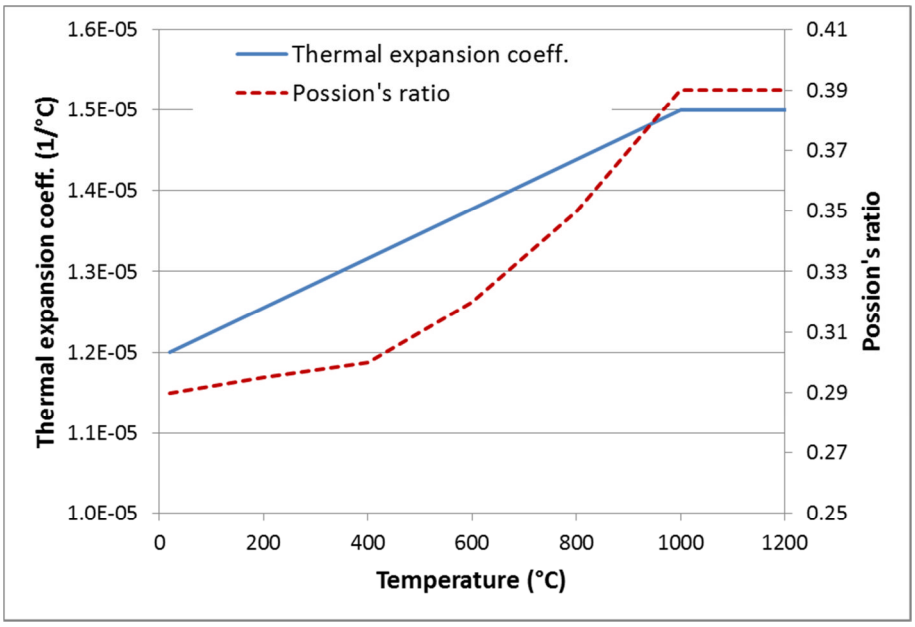

Figure 4-13: Temperature-dependent thermal expansion coefficient, and Poisson's ratio of S355 (Michaleris and Debiccari, 1997).

Table 4-7: Detailed temperature-dependent thermal expansion coefficient, and Poisson's ratio of S355 (Michaleris and Debiccari, 1997).

Temp. (°C)	Poisson's ratio	Temp. (°C)	Thermal expan. coeff. (1/°C)
20	0.29	20	1.20E-05
200	0.295	1000	1.50E-05
400	0.3	1500	1.50E-05
600	0.32		
800	0.35		
1000	0.39		
1500	0.39		

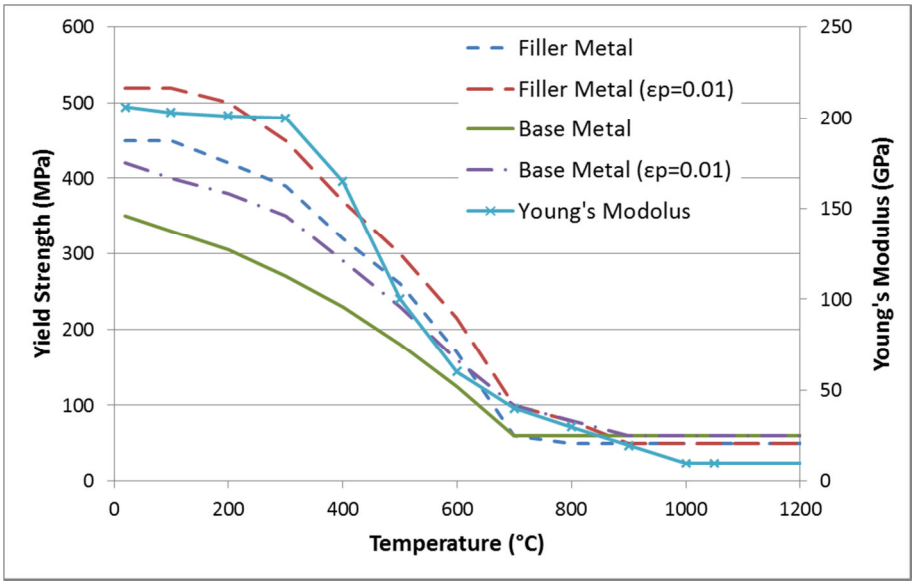

Figure 4-14: Temperature-dependent Young's Modulus, and yield strength for the filler material and base plate (Michaleris and Debiccari, 1997).

Table 4-8: Detailed temperature-dependent Young's Modulus, and yield strength for the filler material and base plate (Michaleris and Debiccari, 1997).

Temp. (°C)	Young's Modulus (GPa)	Yield Strength (MPa)			
		Filler metal	Filler metal (εp = 0.01)	Base metal	Base metal (εp = 0.01)
20	206	450	520	350	420
100	203	450	520	330	400
200	201	420	500	305	380
300	200	390	450	270	350
400	165	320	370	230	290
500	100	260	300	180	230

600	60	170	215	125	160
700	40	60	100	60	100
800	30	50	80	60	60
900	20	50	50	60	60
1000	10	50	50	60	60
1500	10	50	50	60	60

Continuous filler metal deposition changes the rigidity of the component as the solidification front advances with the weld pool. This gradually increased rigidity needs to be correctly developed in the model otherwise false weld distortion may be generated. Thus, the same “element birth technique” to the transient thermal model was also utilised in the mechanical model for simulating the deposition process of the filler material. The same number of computational steps and step durations of the thermal model were utilised in the mechanical simulation for the heating and cooling cycles. Another step was utilised at the end for simulating the mechanical performance after the clamps are released.

The critical procedure for this sequentially coupled thermo-mechanical analysis is applying the thermal results to the mechanical model. This is accomplished by assigning the nodal temperature histories which were recoded from the thermal analysis to the mechanical model using the *TEMPERATURE command in ABAQUS. The thermal load was deactivated in the releasing step.

The clamping system has a significant influence on the finial distortion (Mahapatra et al., 2006). To accurately simulate the clamping systems used in the WAAM process, a ‘backing plate’ was modelled with rigid material properties. A hard contact was set up between the bottom surface of the base plate and the top surface of the backing plate. It prevented the points on the base plate moving along the –z direction but not against the movement along the +z direction. In the model of the mild steel wall, the clamps were used on the four corners and the mid length of the base plate. These were modelled in this study by fixing the movements of the nodes which are demonstrated as the red dots in Figure 4-15. These constraints are removed in the step when the

base plate is unclamped. Apart from the clamps, symmetry boundary conditions were applied on the longitudinal symmetry plane.

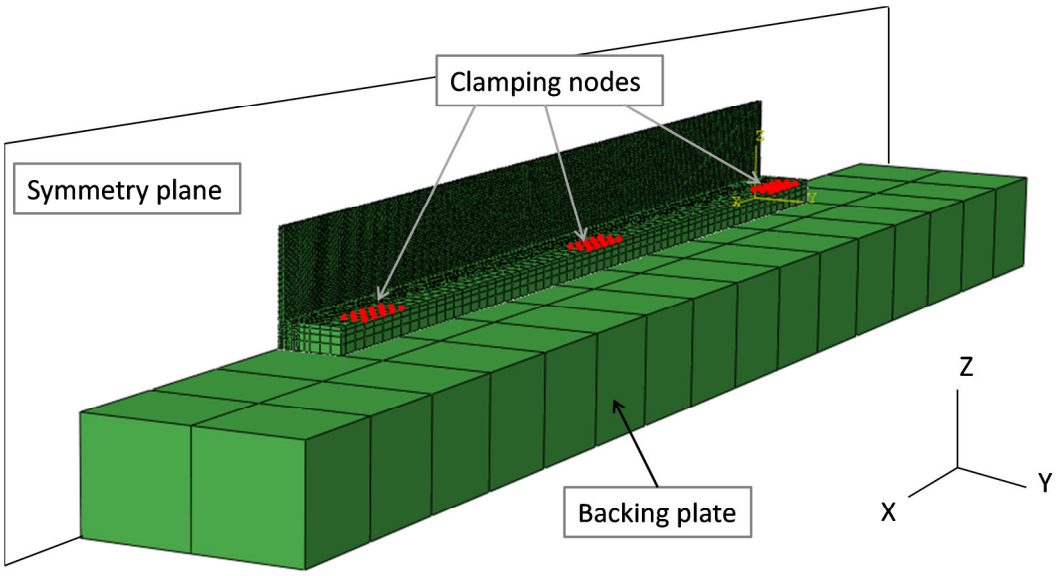

Figure 4-15: FE model for the mechanical analysis.

4.3.3 Results and verification

Figure 4-16 shows the comparison between the numerical thermal histories and the experimental thermal histories at the four measuring positions on the base plate which are demonstrated in Figure 4-2. The predicted temperatures were extracted from the nodal points in the model where the thermocouples were placed in the experiment. From the comparison, one can see that the transient thermal models give accurate predictions of the temperatures at the four thermocouple positions. Not only the peak temperatures are accurate, but the predicted heating and cooling rates are also well correlated to the measurements.

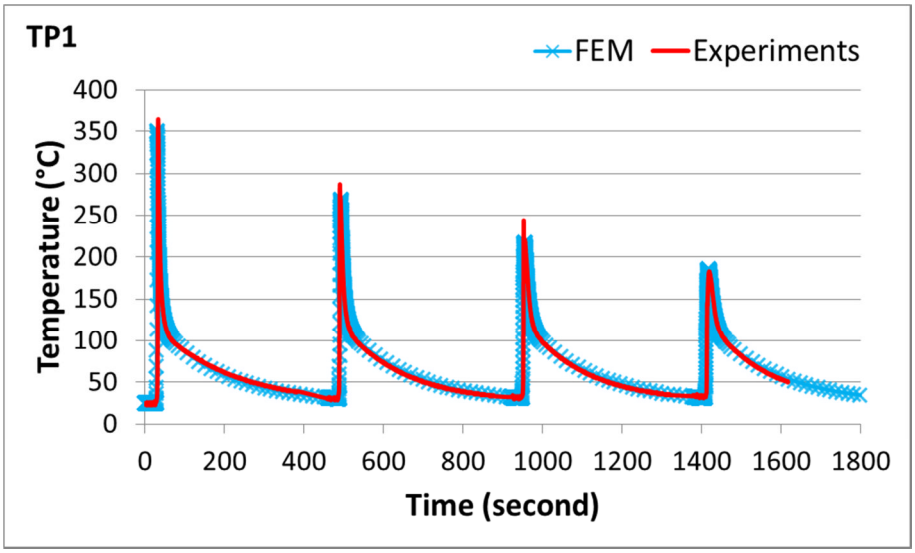
TP1
FEM
Experiments
Temperature (°C)
400
350
300
250
200
150
100
50
0
0
200
400
600
800
1000
1200
1400
1600
1800
Time (second)

(a)

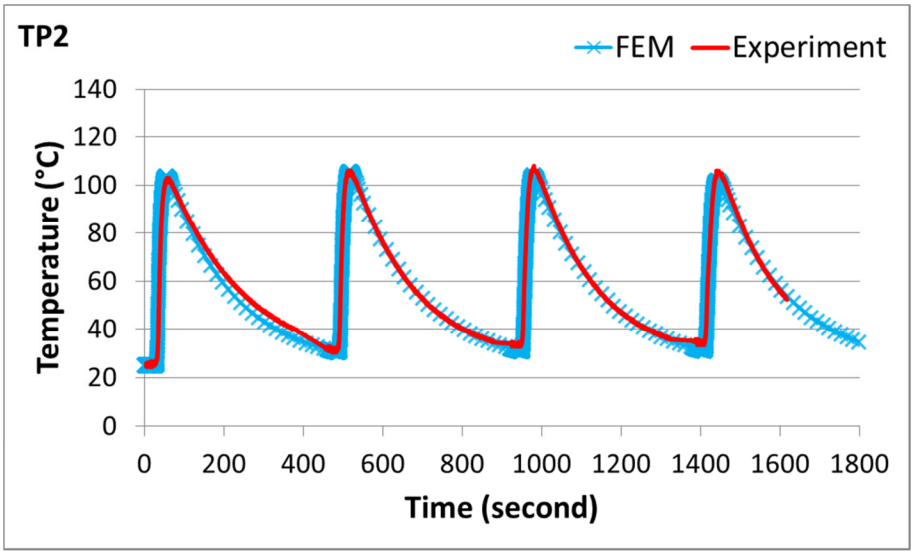
TP2
FEM
Experiment
Temperature (°C)
140
120
100
80
60
40
20
0
0
200
400
600
800
1000
1200
1400
1600
1800
Time (second)

(b)

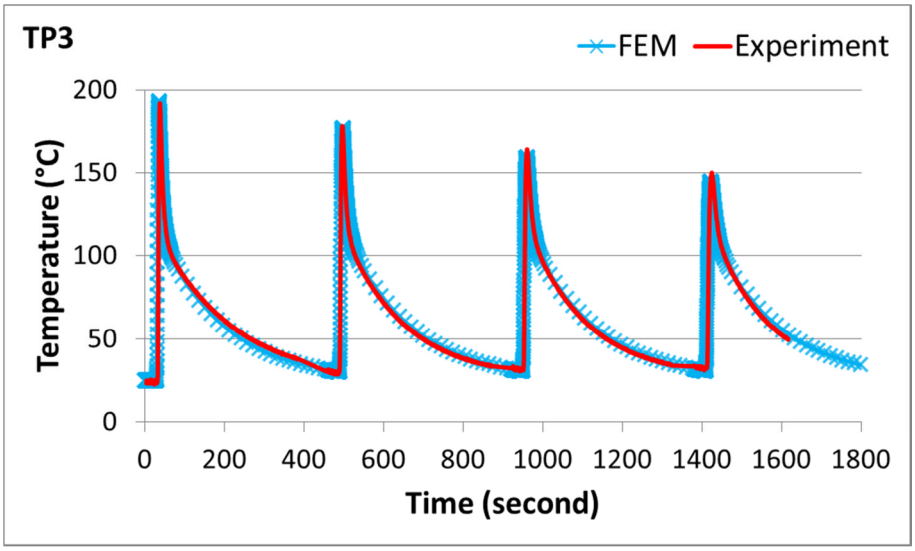

(c)

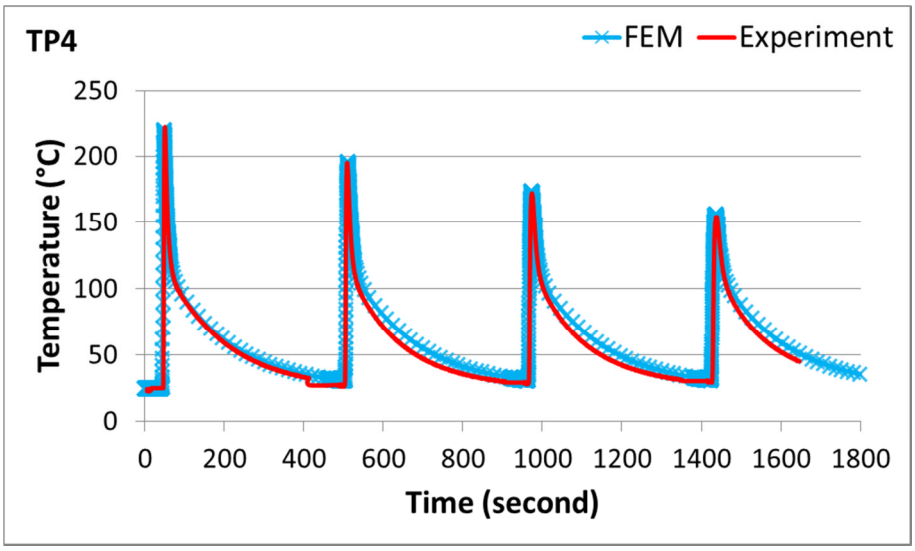

(d)

Figure 4-16: Temperature verification on the measuring positions of (a) TP1 (250, 5, 0), (b) TP2 (250, 20, 0), (c) TP3 (250, 0, -12), (d) TP4 (375, 0, -8).

Figure 4-17 (a) illustrates the predicted longitudinal residual stress of the four layer walls with clamping. From the mid-plane cross section shown in Figure 4-17 (b) one can see that tensile stresses are distributed nearly uniformly across all the layers of the deposited wall. The stresses in the base plate adjacent to the deposited wall are also tensile, and the longitudinal stresses go

into compression near the bottom of the base plate. The magnitude of the compressive stress is greatest where clamping has been applied due to the restraint in this region (shown in Figure 4-17 (a)). There is a significant distortion of the component and relaxation of the stresses after the clamping was removed which is illustrated in Figure 4-17 (c) and Figure 4-17 (d). The stress at the top of the deposited wall has a much lower value than at the interface due to the bending distortion of the sample. This distortion also causes the compressive stress at the bottom of the base plate to go into tension.

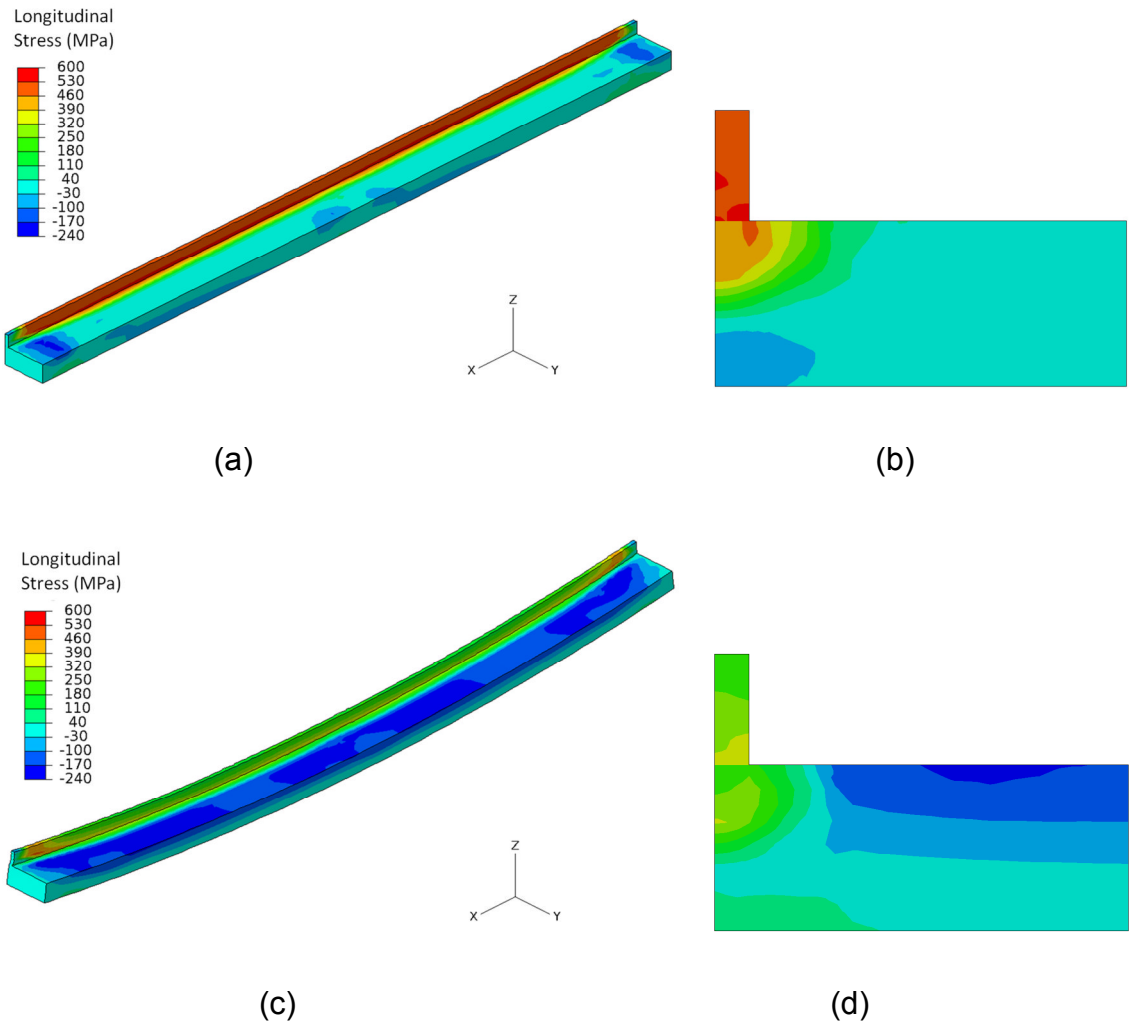

Figure 4-17: Longitudinal stress predictions of the 4 layer WAAM wall component: (a) with clamps; (b) cross section of (a); (c) after clamps are removed (deformation factor: 5); (d) cross section of (c).

To have an overall check of the mechanical results, the predicted distortion along the long edge of a four layer wall was compared with the measured distortion from the two long edges of the sample. Figure 4-18 shows that the predicted distorted shape agrees with the experimentally measured distortion. The distortion magnitude at the start of the component is slightly higher than it is at the stop end. This is because the rigidity of the component is continuously increasing during the deposition process. The rigidity of the component is higher when the whole layer of material added to the part which results in a lower distortion. This phenomenon can be correctly captured by the mechanical FE model using the “element birth” technique.

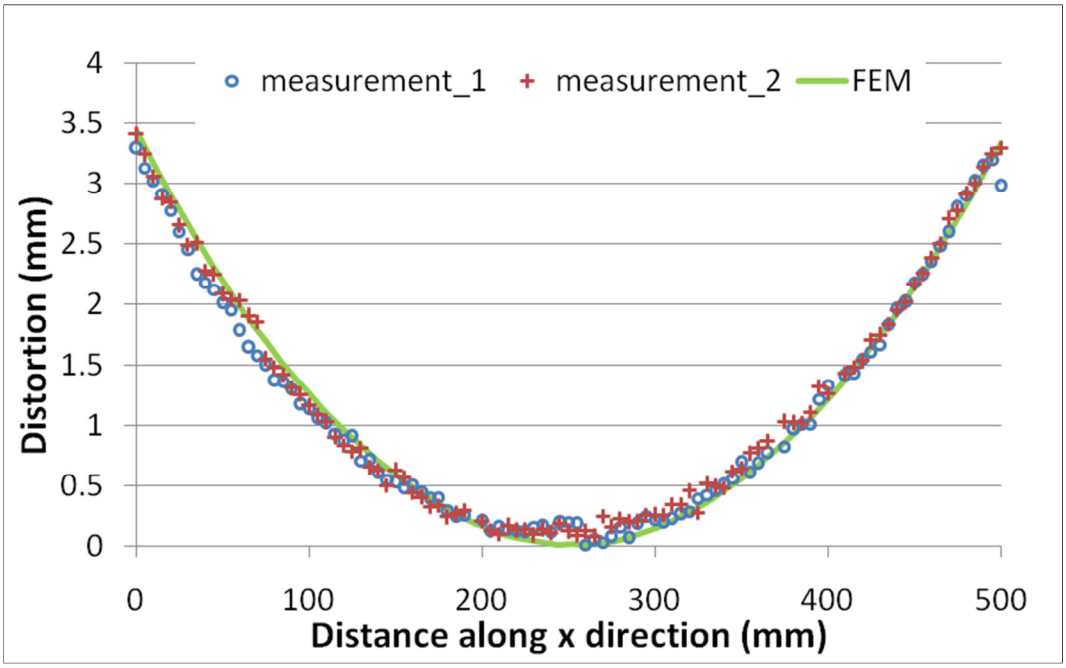

Figure 4-18: Distortion verification (S355) along the longitudinal direction.

Detailed validation of the residual stress data was provided by comparing the computational results for different numbers of deposited layers with those from neutron diffraction measurements. Figure 4-19 shows the comparison on the base plate. In both the modelling and experimental results the clamps have been removed, and three principal directions have been considered namely: longitudinal (σLD), transverse (σTD), and normal (σND). It can be clearly seen that the longitudinal stress dominates over the transverse and normal stresses.

The material around the heating line has large longitudinal tensile stresses. Along the transverse direction, the longitudinal stress becomes compressive in the area about 8 mm away from the heating line. However, the magnitude of the longitudinal tensile stress around the heating line is significantly higher than the surrounding longitudinal compressive stress. Transverse residual stresses are much smaller compare to the longitudinal stresses (shown in Figure 4-19). The transverse stress reaches its peak value close to the heating line and gradually reduces to zero towards the outer rim of the plate. The normal residual stresses are insignificant compare to the stresses of the other two directions.

The FE predictions match the experimental results well in all cases except the 1 layer wall where the model underpredicts the stresses. Moreover, there is a more significant reduction in the experimentally measured stresses between the 1 and 2 layer walls, than in the stresses predicted by the models. A possible explanation is that the model does not fully capture the microstructural changes which occur in the actual material.

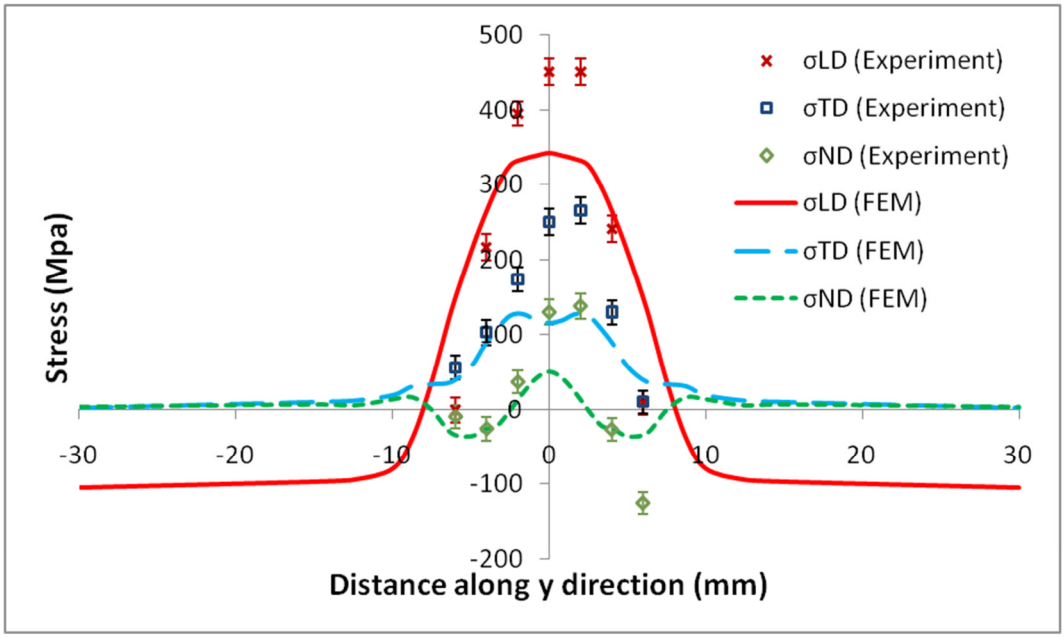

(a)

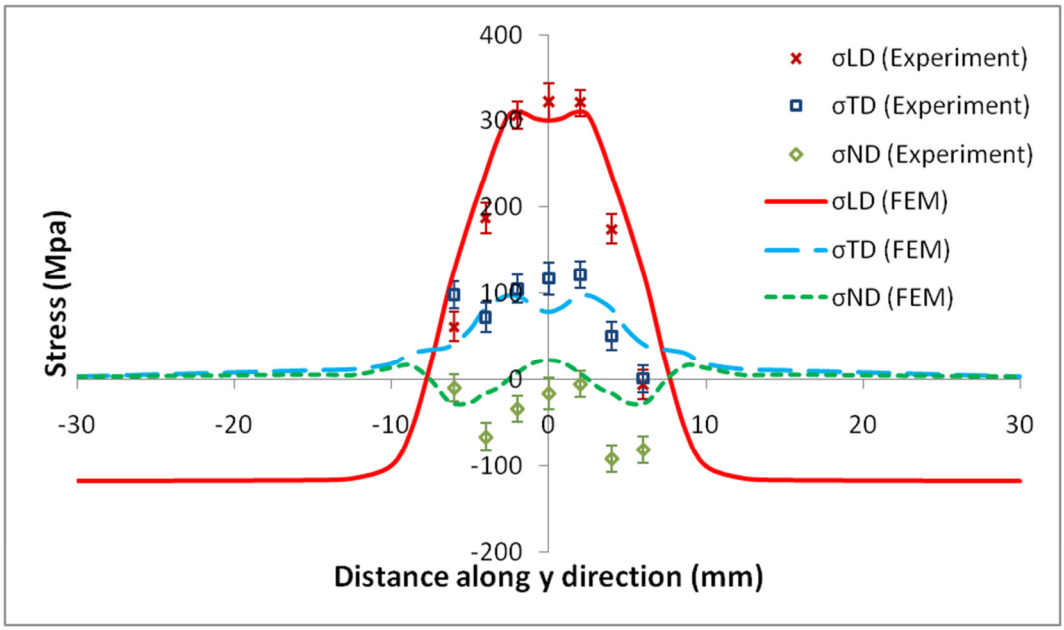

(b)

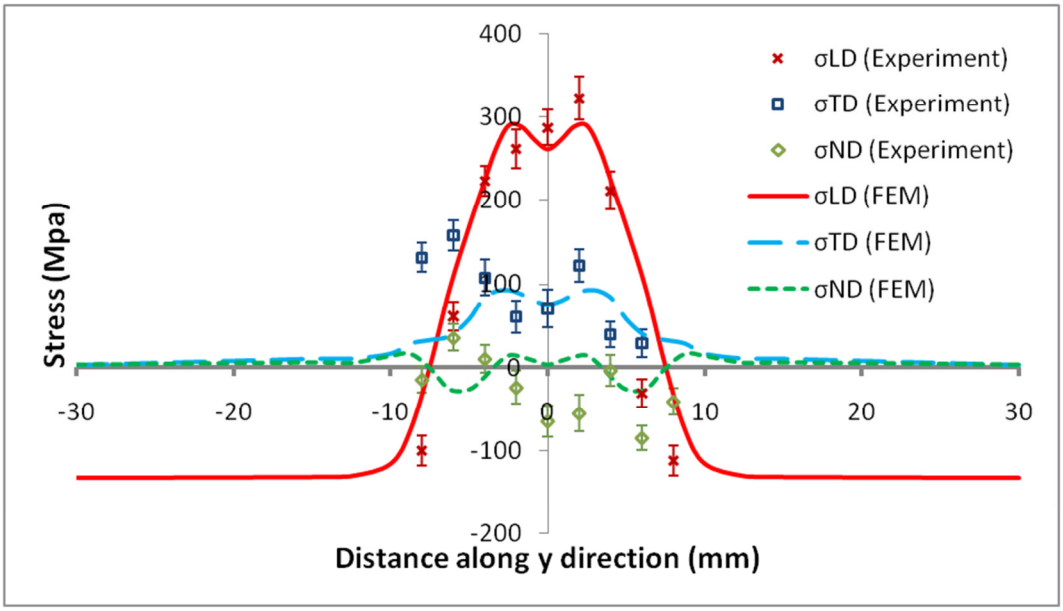

(c)

Figure 4-19: Principal stress distribution along the base plate in the S355 specimen with: (a) single bead, (b) two beads, (c) three beads.

A further analysis was carried out on the 20 layer WAAM wall. The thermal cycles at different heights of the deposited wall was acquired from the mid-length cross section of the model, and shown in Figure 4-20. One can see that

the thermal histories at these positions are similar except for the one at the middle point of the first layer. The peak temperatures of this point are lower due to the influence of the cooling system under the base plate.

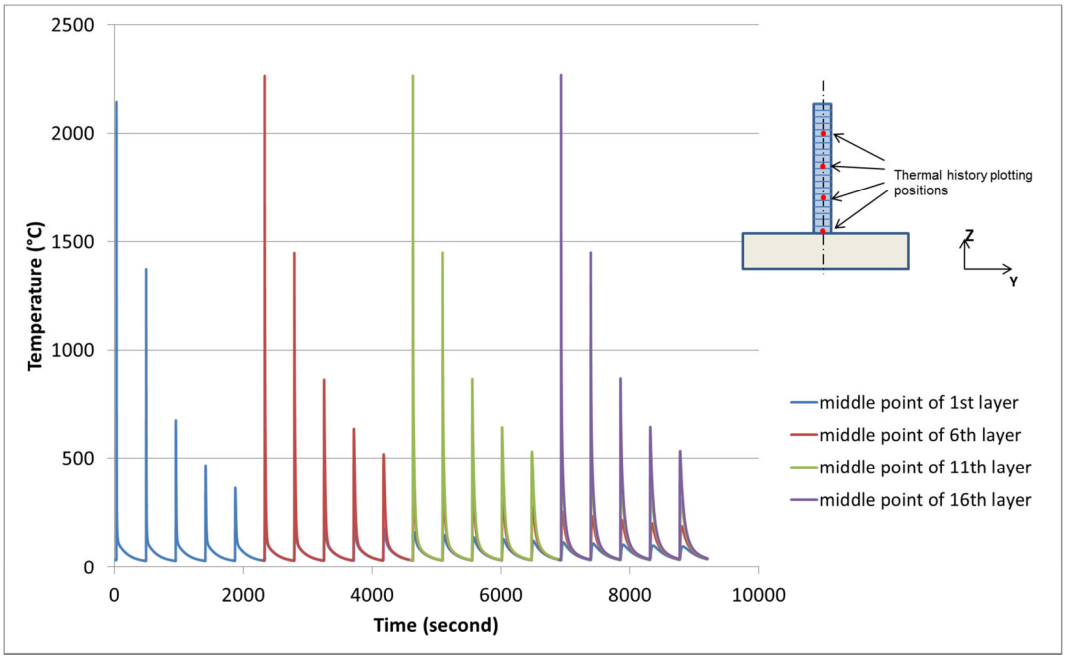

Figure 4-20: Thermal cycles at different heights of the deposited wall.

Figure 4-21 shows the distribution of the longitudinal stress on the 20 layer WAAM wall part. Similar to the stress distribution of the 4 layer WAAM wallshown in Figure 4-17, tensile stresses were generated on the deposited wall and in the base plate adjacent to the root of the wall. The magnitude of the longitudinal stresses on the two endings of the wall was zero because the material did not have constraint in the longitudinal direction. To balance the tensile stresses, compressive stresses were generated in the base plate further to the root of the deposited wall. The material in the area where the clamps were applied got the highest compressive stress due to the restraint.

After the clamping was removed the component was significantly bent along the longitudinal direction, and the stresses were redistributed (as shown in Figure 4-21 (c) and (d)). The stresses in the region of the root of the wall remained tensile, however the magnitude was significantly reduced. The magnitude of the tensile stress was gradually reduced on the wall further to the root, and it went

into compression at the top of the wall due to the bending of the component. Compressive stresses were also generated in the base plate further to the intersection of the wall to balance the tensile stress on the wall.

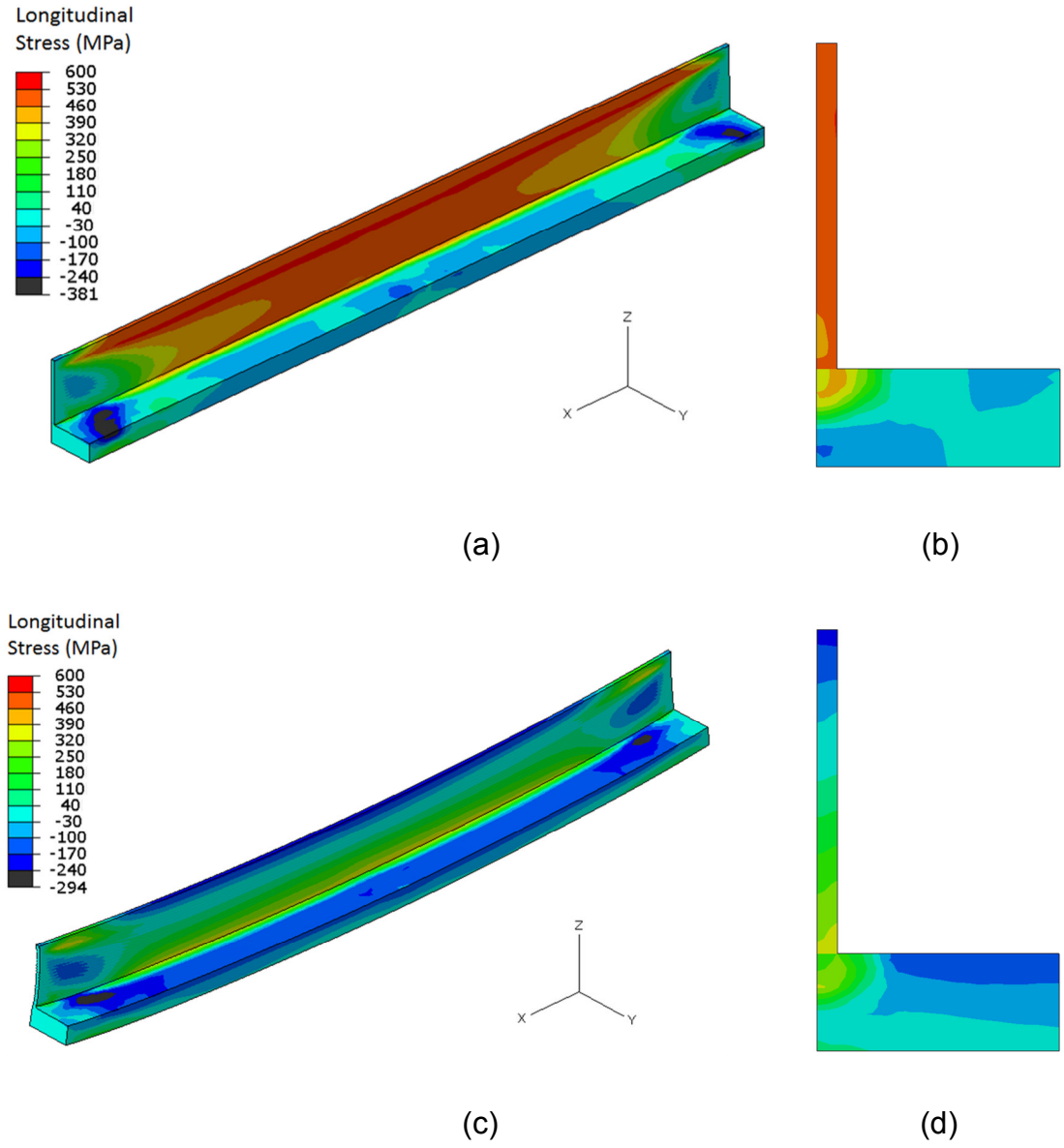

Figure 4-21: Longitudinal stress predictions of the 20 layer WAAM wall component: (a) with clamps; (b) cross section of (a); (c) after clamps are removed (deformation factor: 5); (d) cross section of (c).

The comparison of the experimental measurement and the numerical prediction of residual stress distribution on the deposited wall with 20 layers beads is shown in Figure 4-22. The comparison was made on the longitudinal stress

because it is dominant over the stresses from the other two directions. It shows that in general the predicted stress has the similar distribution as the measured result with a deviation near the base of the deposited wall. The possible reason of this error is that the complex dilution of the filler material and the base plate was ignored in the model. The maximum tensile stress was located in the base of the deposited wall. It decreased with the increased distance along z direction and turned to compressive stress after a certain height. The residual stress in the 20 layers wall after cutting the base plate was also analysed in this study. The simulation was performed by deactivating the base plate elements. The residual stress invoked by the cutting process was not considered in the model. The residual stress in the 20 layers wall changed to around zero after the base plate was cut, which can be observed from the experimental results as well as the simulation results.

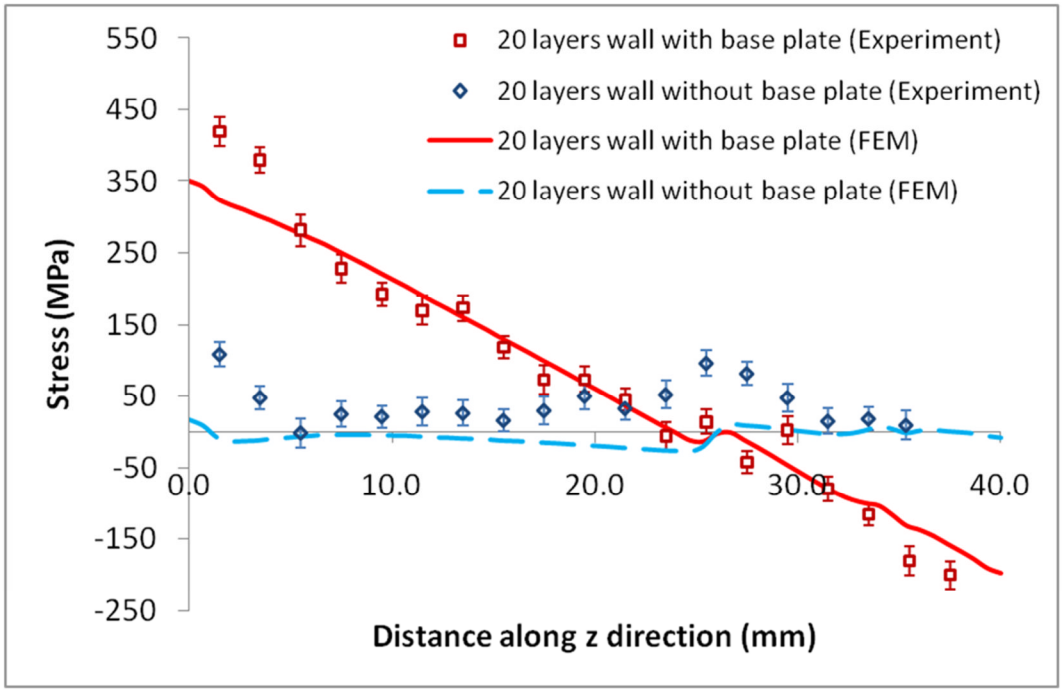

Figure 4-22: Longitudinal stress in the deposited wall.

4.3.4 Discussion

The transient temperature and stress performance of the WAAM process is analysed using the FE model. Figure 4-23 (a) shows the temperature profile

when the heat source travelled 350 mm along the fourth layer of the deposited wall. The area with grey colour represents the fusion zone where the temperature exceeds 1500 °C. As the welding torch travelled the melt metallic material added to the wall and heated up the adjacent area. The temperature dropped quickly in the area behind the fusion zone. The material from the previously deposited layers was reheated when the new material added.

Figure 4-23 (b) shows the corresponding longitudinal stress distribution. One can see that the stress in the area where the material was heated up by the welding torch is very low because of the significantly reduced yield stress level by the high temperatures. Compressive stress was generated in front of the fusion zone due to the thermal expansion of the heated material. Tensile stress was generated in the area behind the heat source due to the contraction of the cooling material which was constrained by the base plate to maintain the original length. This in turn results in longitudinal compressive residual stresses in the base plate, especially in the area where the clamps located. The tensile stress from the already deposited material was released as the material was reheated. However, similar level of tensile stress was generated back in this area after the heat source passed.

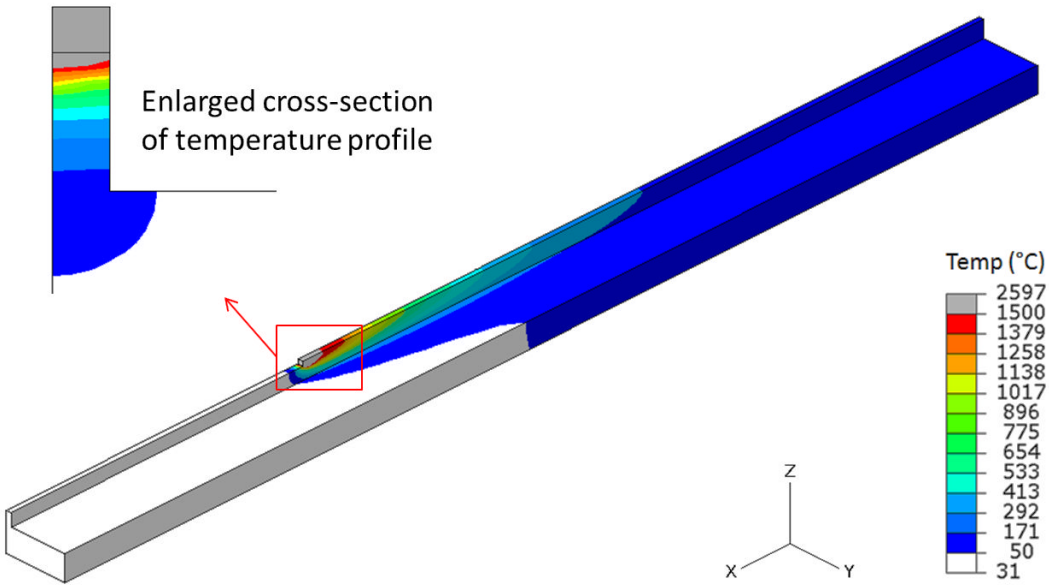

(a)

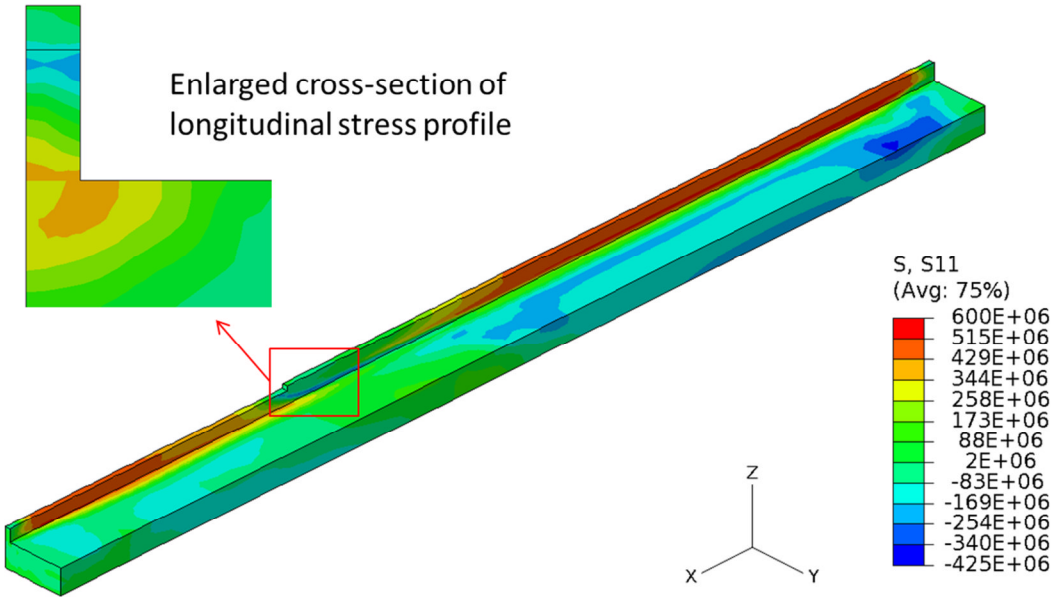

(b)

Figure 4-23: Transient thermo-mechanical performance: (a) temperature profile when the heat source travelled 350 mm along the fourth layer of the deposited wall; (b) corresponding longitudinal stress distribution.

The stress evolution during the thermal cycles of the WAAM process are analysed at different positions of the WAAM wall. In general, four main stress stages can be observed during the deposition. In stage A, the material is heated up as the heat source approaches. Compressive stress is generated in the heating area due to the expanding metal is restrained by the adjacent material. The resultant strain is accommodated elastically until the compressive stress exceeds the compressive yield stress. In stage B, plastic flow occurs when the compressive stress exceeds the yield limit. The magnitude of the compressive stress becomes smaller when temperature becomes higher due to the smaller yield strength of the high temperature. In stage C, the material starts cooling and a tensile stress develops due to the contracting material being restrained by the surrounding material. This tensile stress remains elastic until it exceeds the tensile yield stress. In stage D, plastic flow develops when the tensile stress exceeds the yield limit.

Figure 4-24 shows the transient history of temperature and longitudinal stress for a position on the mid-length section in the first layer of the deposited wall. It can be seen that as the material heated up compressive stress was generated in the filler material. For each layer, the magnitude of the compressive stress reached to the highest point before the temperature reached the peak. As indicated by P1 to P4, the magnitude of the highest compressive stress was increased as the material at the plotting position got more constraint when more layers of material added to the component. Tensile stress was generated when the material cooled down and the tensile stress remained the same level until the material was reheated when the heat source travelled to the subsequent layers.

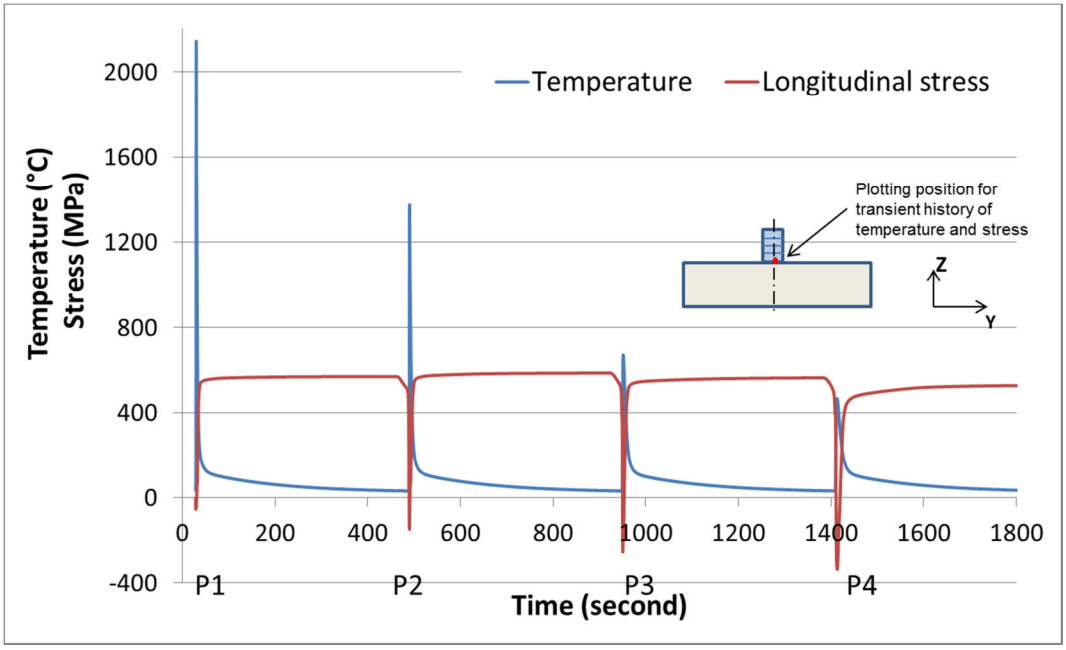

Figure 4-24: Transient history of temperature and longitudinal stress for the position in the first layer of the deposited wall.

Figure 4-25 further explains the stress evolvement of the filler material which results in the transient thermal-mechanical performance as shown in Figure 4-24. The four stress stages are indicated in the figures as A, B, C and D. The yield strength becomes lower for high temperatures. It should be noted that in reality no load can be carried within the fusion zone. However, in the FE model a ‘cut-off temperature’ was used in the material model to avoid difficulties in

convergence. Thus a small compressive stress can be generated in the FE model when the temperature exceeded the melting point.

Figure 4-25 (a) shows the stress development of the filler material in the first layer of the WAAM wall. The stress development of stage A, B and C are represented with dash line because in reality the filler material is added to the component as melt metallic droplet. When the filler material deposited to the component, it cooled down rapidly and generated plastic tensile stress. The maximum magnitude of the plastic tensile stress generated when the component cooled down to the room temperature.

As shown in Figure 4-25 (b), when the material was reheated by the second layer of deposited material the tensile stress that generated in the cooled material was released. As the temperature became higher, compressive stress was generated (indicated as stage A) elastically until the compressive stress exceeded the compressive yield stress. The magnitude of the compressive stress was reduced as the stress status of the material entered stage B when the plastic flow occurred. The compressive stress became very small when the material reached its peak temperature of about 1400 °C during the deposition of the second layer of the WAAM wall. Soon after the material started cooling down, plastic tensile stress generated (indicated as stage D) after a short elastic tensile stress stage (indicated as stage C). A similar level of maximum plastic tensile stress as Figure 4-25 (a) generated when the material cooled down to the room temperature.

The material experienced similar stress evolvements as demonstrated in Figure 4-25 (b) when the heat source travelled to the third and the fourth layer. As shown in Figure 4-25 (c) and Figure 4-25 (d), the tensile stress that generated in the previous process was released due to the reheat of the material. And the stress in the material experienced elastic compressive stage (stage A), plastic compressive stage (stage B), elastic tensile stage (stage C) and plastic tensile stage (stage D). However, after all these stress statues that evolved during the

thermal cycles, the stress returned to the point and gained the same level of tensile stress when the deposition started for each layer.

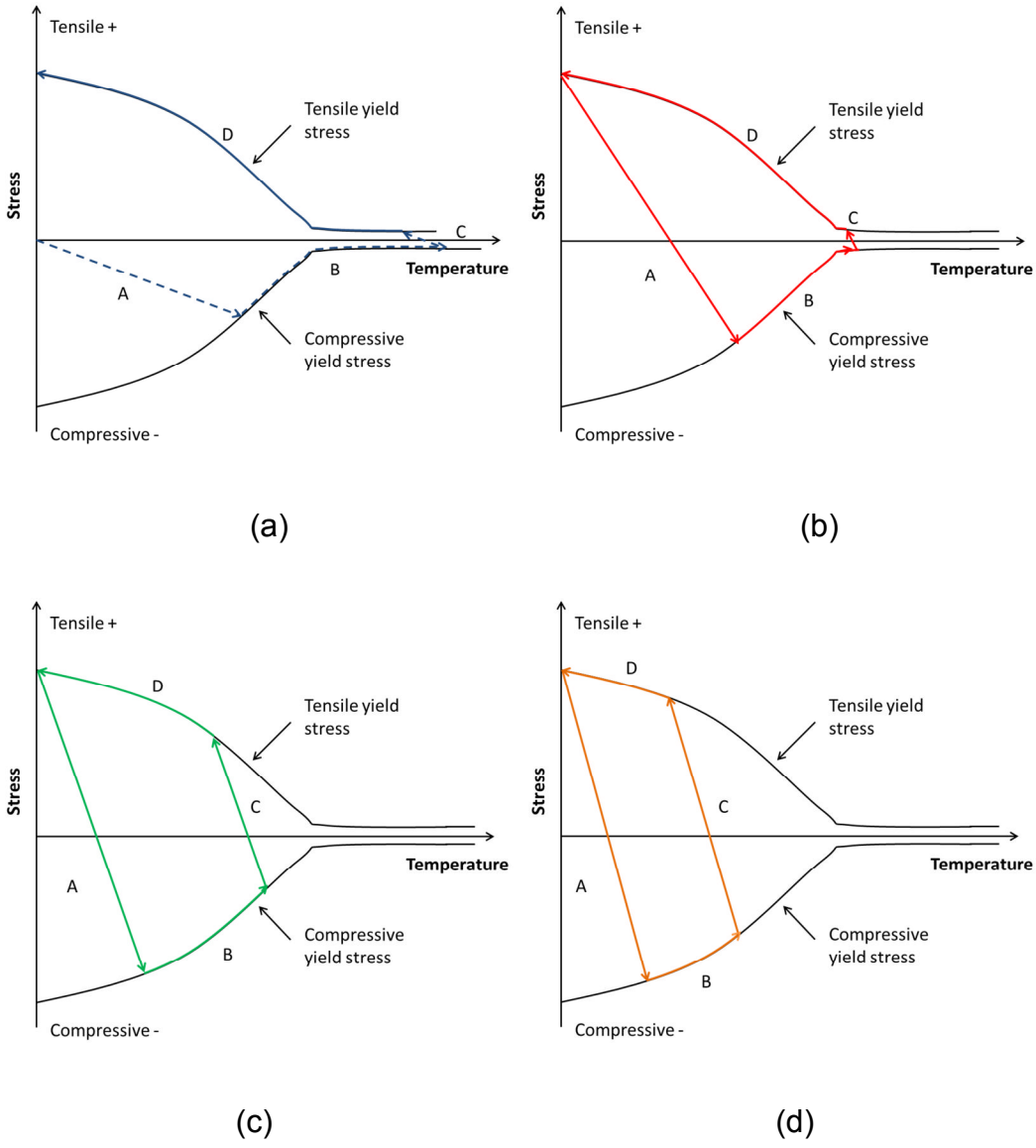

Figure 4-25: Stress evolution for the position in the first layer of the deposited wall when the heat source is on the: (a) first layer; (b) second layer; (c) third layer; (d) fourth layer.

Figure 4-26 shows the transient history of temperature and longitudinal stress for a position on the top surface of the base plate 5 mm to the heat line. Figure 4-27 illustrates the stress evolvement for the same position during the thermal cycles of the WAAM process. From Figure 4-27 (a) one can see that plastic

tensile stress generated after the material cooled down to the room temperature in the thermal cycle of depositing the first layer. It should be noted that the magnitude of the tensile stress in the base plate is lower than the one in the deposited wall because material in the base plate is softer than the weld metal. From the second layer of the WAAM process the peak temperature that the material experienced in the deposition process of each layer was not high enough to develop plastic flow. As shown in Figure 4-27 (b) and Figure 4-27 (c), the stress was evolved elastically which released the tensile stress generated from the first layer deposition, went to the compressive and returned back to the same tensile stress level. The stress status remained to tension from the fourth layer as the peak temperature was not high enough to fully release the tensile stress that generated from the previous process (shown in Figure 4-27 (d)).

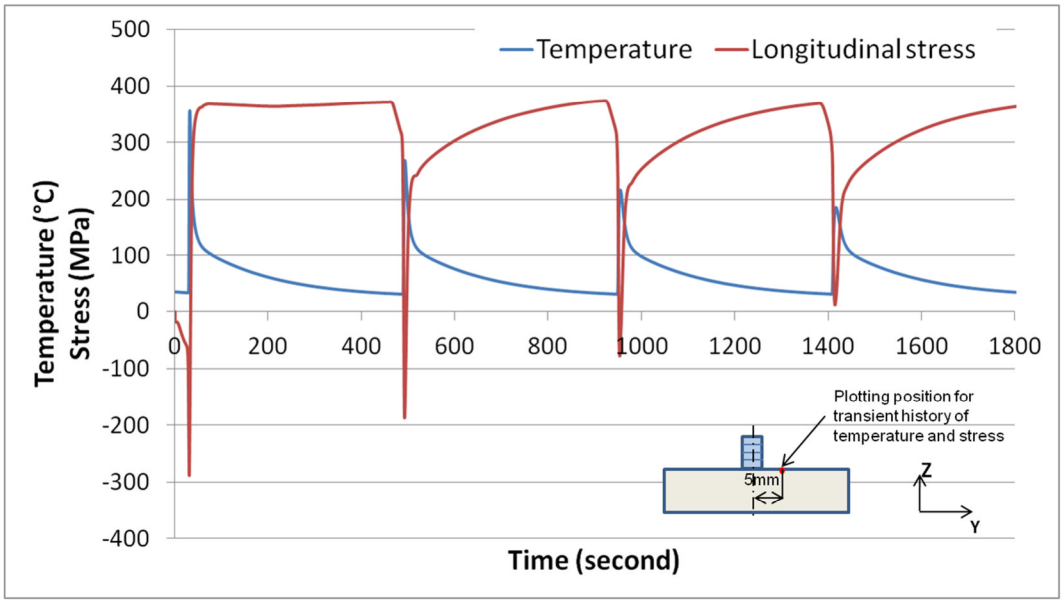

Figure 4-26: Transient history of temperature and longitudinal stress for the position on the top surface of the base plate 5 mm to the heat line.

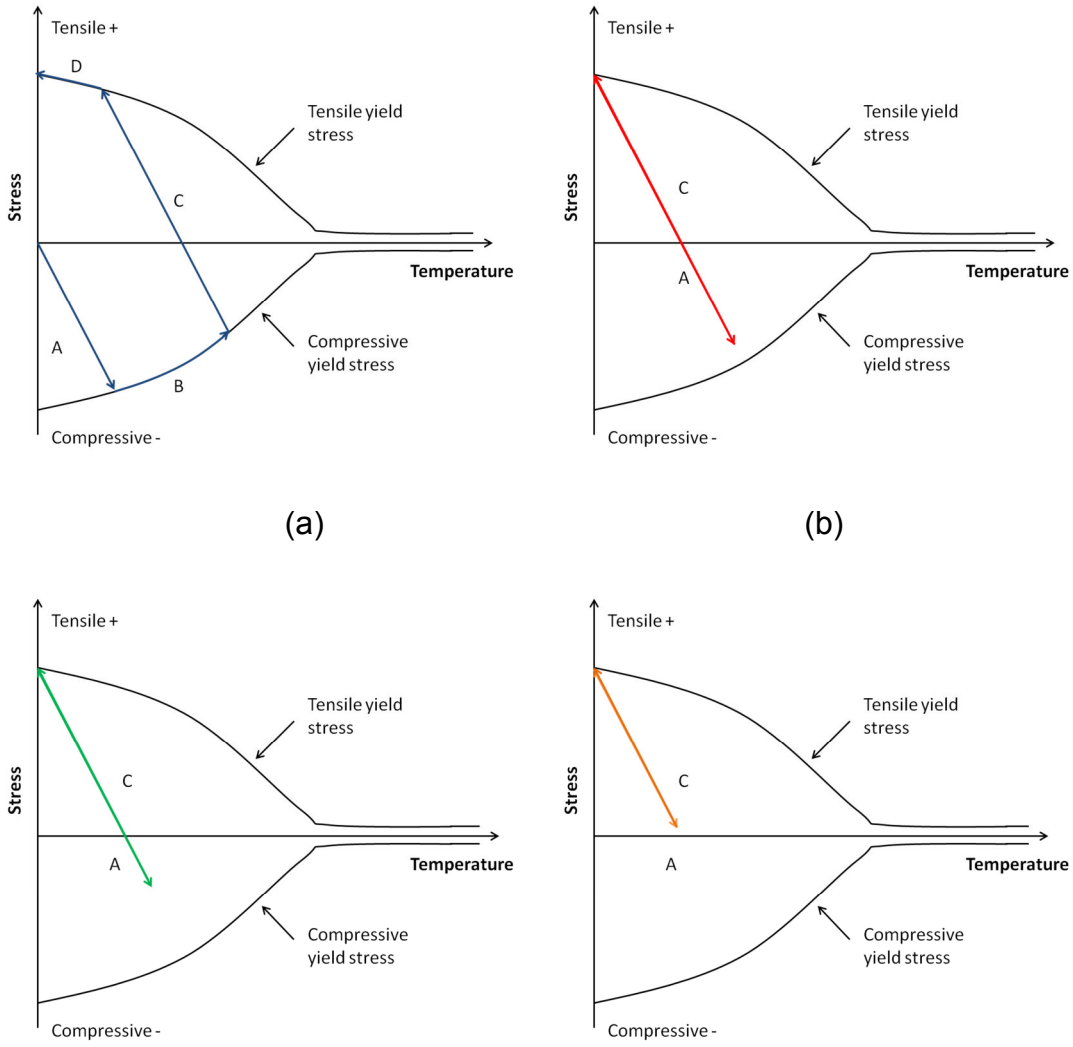

Figure 4-27: Stress evolution for the position on the top surface of the base plate 5 mm to the heat line when the heat source is on the: (a) first layer; (b) second layer; (c) third layer; (d) fourth layer.

Figure 4-28 shows the transient history of temperature and longitudinal stress for a position on the top surface of the base plate 20 mm to the heat line. Figure 4-29 illustrates the stress evolution for the same position. One can see that the peak temperatures that the material experienced during the thermal cycle are just around 100 °C. This only developed stresses elastically when the material was heated up, and no stress remained after the material cooled down to the room temperature.

It can be concluded that the whether or not the residual stresses can be developed in the material is decided by the magnitude of the peak temperatures that the material experienced during the deposition. If the peak temperature of the material is high enough to generate plastic flow, then tensile stress will be developed after the material cools down to the room temperature. Otherwise the stress evolution in the materials will be only elastically which cannot generate residual stresses.

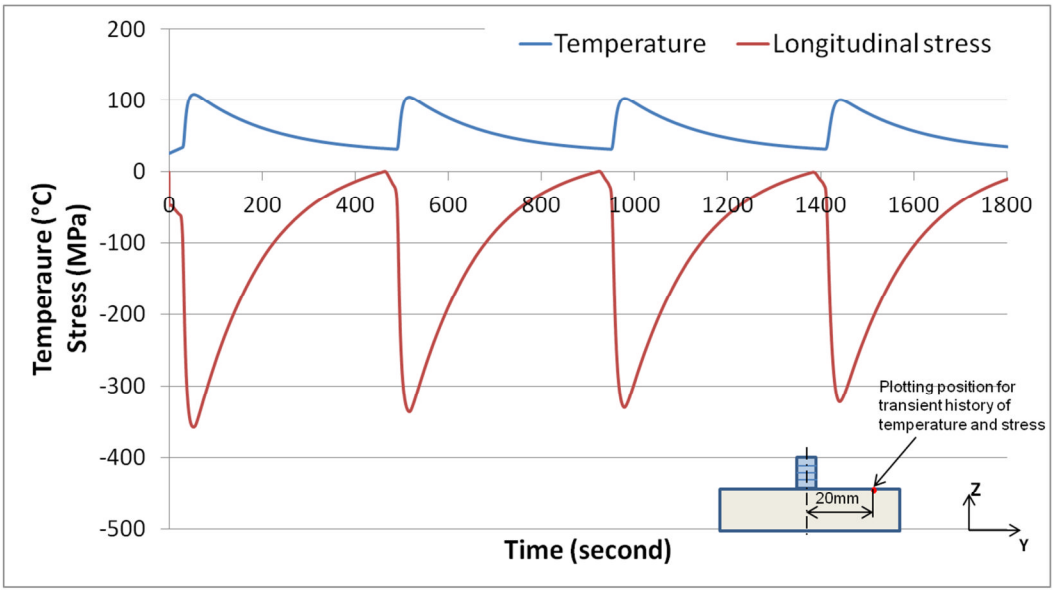

Figure 4-28: Transient history of temperature and longitudinal stress for the position on the top surface of the base plate 20 mm to the heat line.

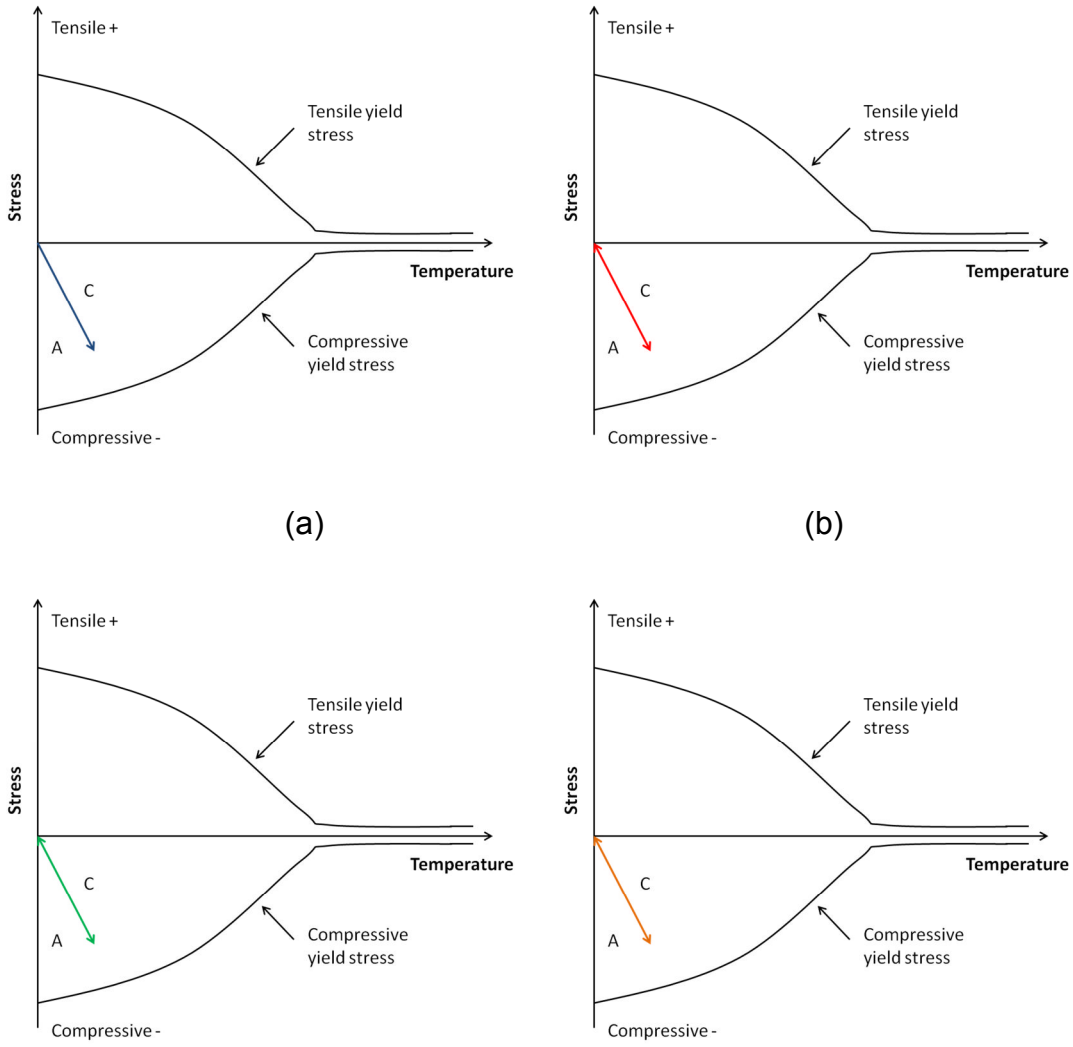

Figure 4-29: Stress evolution for the position on the top surface of the base plate 20 mm to the heat line when the heat source is on the: (a) first layer; (b) second layer; (c) third layer; (d) fourth layer.

4.4 THERMO-MECHANICAL ANALYSIS OF WAAM PART WITH TI6AL4V

Ti6Al4V is highly important for the Aerospace industry because of its light weight and excellent material performance. It is estimated that there is a requirement of about 20 million tonnes of billet titanium alloy over the next 20 years (Wood, 2009). With machining rates of ca. 90% and ever increasing

material costs in titanium conventional manufacturing strategies need reconsideration. The WAAM process is considered to be a promising solution as a new, sustainable, cost and time efficient manufacturing process. The thermo-mechanical performance of the WAAM process on Ti6Al4V is investigated in this section.

4.4.1 Experimental Setup for WAAM on Ti6AL4V

The experiment on Ti6Al4V utilised similar settings to the experiment on mild steel S355. A high frequency inter-pulse TIG welding torch was employed in this experiment to provide filler materials. The welding wire used in this study is 1.2 mm and the wire feed speed is 1.6 m/min. The travel speed of the welding torch is 4 mm/s. The welding process heat input is 234.1 J/mm, assuming an efficiency of 0.7. A local shielding system was used following the welding torch providing Argon gas with a flow rate of 20 l/min. The base plate was clamped on the two long edges to a water cooled aluminium backing bar. The parts were allowed to cool down below 50°C before depositing the new layer of materials.

As shown in Figure 4-30, the base plate of the Ti6Al4V wall model is 250mm long, 60mm wide, and 6mm thick. Multilayer wall shaped samples were produced using the WAAM process. Multilayer walls were deposited along the centreline of the base plate with the same welding directions for each layer. The average width measured from the deposited walls is 6.4 mm, and the average height of each layer is 1 mm.

Four k-type thermocouples were utilised in the interior and on the surface of the base plate to measure the transient thermal histories. As shown in Figure 4-30, TP1, TP2 and TP3 were directly welded to the front surface of the base plate, and TP4 was welded to the back surface of the base plate.

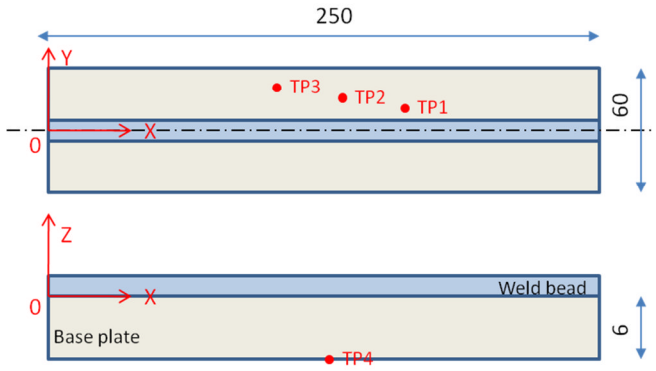

coordination of testing points (unit: mm)			
	X	Y	Z
TP1	135	5	0
TP2	125	10	0
TP3	115	20	0
TP4	125	0	-6

Figure 4-30: Geometry of the WAAM sample of Ti6Al4V.

4.4.2 Thermo-mechanical model of WAAM on Ti6Al4V

The key material parameters for the thermo-mechanical analysis, such as thermal conductivity, specific heat, Young's modulus, Possion's ratio, thermal expansion coefficient and yield strength, are set up with temperature-dependent date as shown in Figure 4-31 Figure 4-32 and Figure 4-33 (Boyer et al., 1994), with detailed data listed from Table 4-9 to Table 4-12. The model uses elastic perfectly plastic material properties and ignores the phase changes that occur in the real material. There is a lack of data in the literature for the temperature-dependent yield strength for the filler material. Average yield strength of the deposited wall, which values 784 MPa, has been measured under the room temperature. The yield strength curve for the filler material shown in Figure 4-33 is inferred by lowering the value of the yield strength for the base plate proportionally with the ratio which was calculated using the data under room temperature.

Constant value of 4420 kg/m^3 is used for the material density. The latent heat during the phase transformation is accounted for setting the value 286 J/g between the solidus temperature 1604°C and the liquids temperature 1660°C. The cut-off temperature is set to 800°C for the mechanical model.

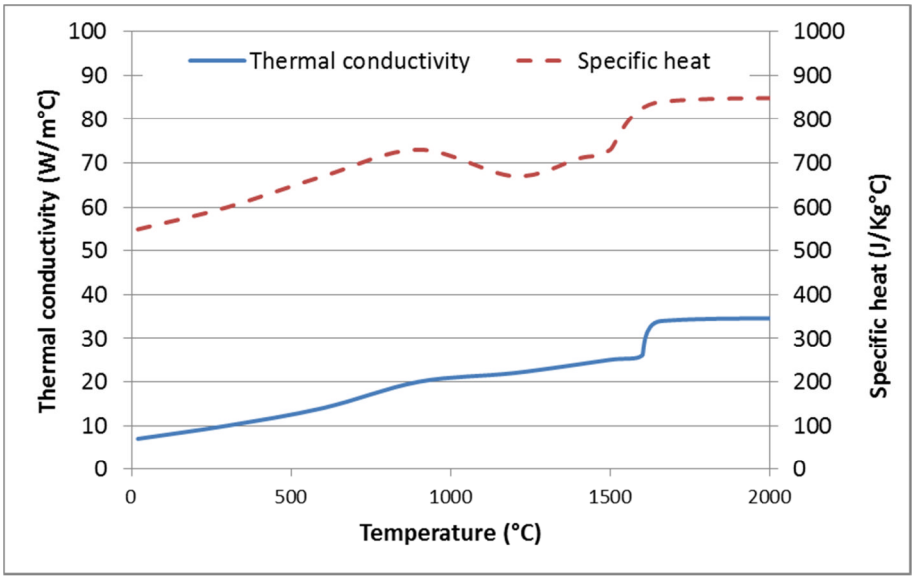

Figure 4-31: Thermal material properties of Ti-6Al-4V.

Table 4-9: Detailed thermal properties of Ti-6Al-4V.

Temperature (°C)	Thermal conductivity (W/m°C)	Specific heat (J/Kg°C)
20	7	550
300	10	600
600	14	670
900	20	730
1200	22	670
1500	25	710
1600	26	730
1660	34	840
3000	34	840

Table 4-10: Detailed temperature-dependent Young's modulus, Thermal expansion coefficient, and Poisson's ratio of Ti-6Al-4V.

Temperature (°C)	Young's Modulus (GPa)	Possion's ratio
20	118	0.33
200	102	0.33
400	87	0.33
500	75	0.33
600	53	0.33
700	40	0.33
800	35	0.33
1600	35	0.33

Table 4-11: Detailed thermal expansion coefficient of Ti-6Al-4V.

Temperature (°C)	Thermal expansion (1/°C)
20	9.00E-06
650	9.70E-06
1600	1.08E-05

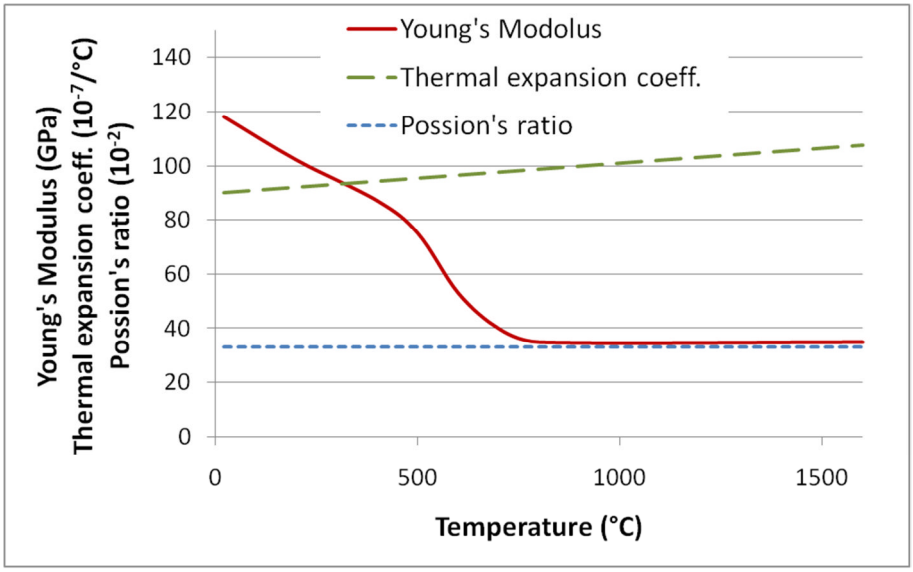

Figure 4-32: Young's modulus, Thermal expansion coefficient, and Poisson's ratio of Ti-6Al-4V.

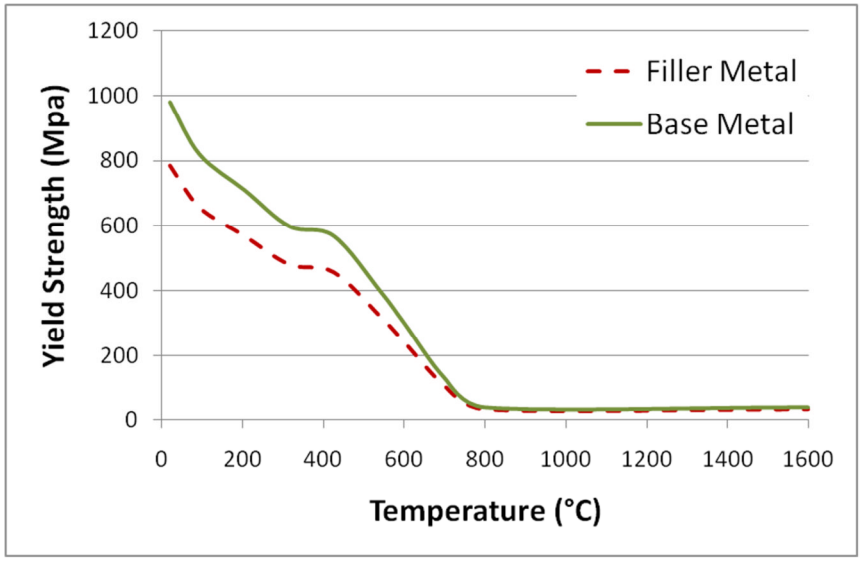

Figure 4-33: Temperature-dependent yield strength for the filler material and base plate.

Table 4-12: Detailed yield strength of Ti-6Al-4V.

Temperature (°C)	Yield strength (MPa)	
	Filler metal	Base metal
20	784	980
93	656	820
205	568	710
315	480	600
425	456	570
540	320	400
600	240	300
700	104	130
800	32	40
1600	32	40

Heat loss through radiation, convection, and the cooling bar was considered as the thermal boundary. The radiation coefficient and the convection coefficient are set to 0.3 and 5.7 $Wm^{-2}K^{-1}$, respectively. The equivalent convection coefficient for simulating the heat loss through the cooling system under the base plate was set up to 450 $Wm^{-2}K^{-1}$ which gave the best match with the experiments. Mechanical boundary conditions are modelled similar to the model for the mild steel wall which has been described in Section 4.3.3. The moving heat source is modelled utilising Goldak's double-ellipsoid model with detailed parameters shown in Table 4-13. The metal deposition process is modelled using the 'element birth technique'.

Table 4-13: Heat source parameters for the Ti-6Al-4V model

a_f(mm)	a_r(mm)	b(mm)	c (mm)	f_f	f_r	Q (W)
2	6	3.2	1	0.6	1.4	937

4.4.3 Results and verification

Figure 4-34 shows the comparison of the thermal histories from the four measuring positions between the predicted results and the experimental results.

One can see that the predicted thermal histories have a good match to the experimental results. The FE prediction shows a slightly higher cooling rate than the experimental measurement. The possible reason is that in practice the base plate distorted during the deposition process, which resulted in a gap between the base plate and the cooling system. This gap significantly decreased the heat transfer efficiency of the cooling system which was located under the base plate. However, an ideal attachment between the base plate and the cooling system was assumed in the thermal model, which overestimated the heat loss through the cooling bar.

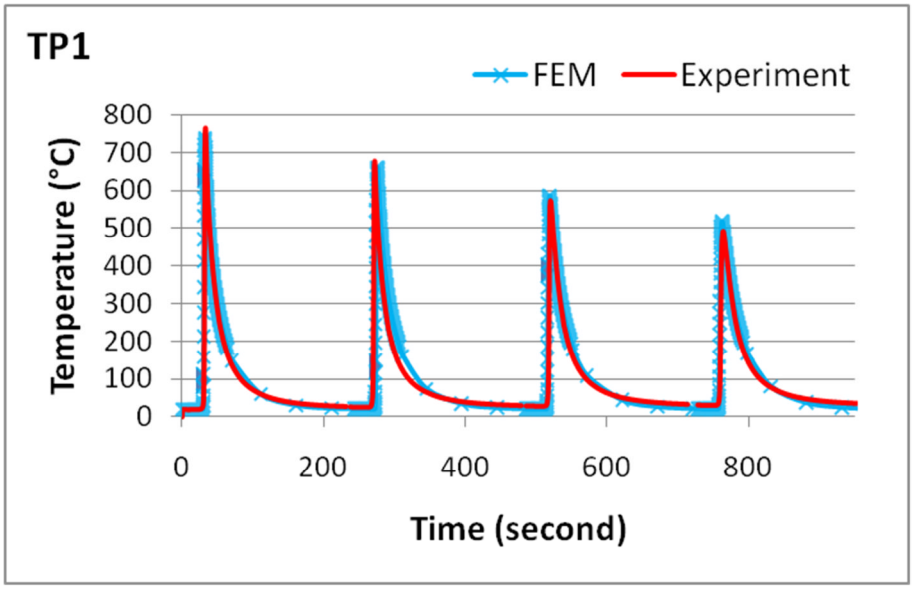

(a)

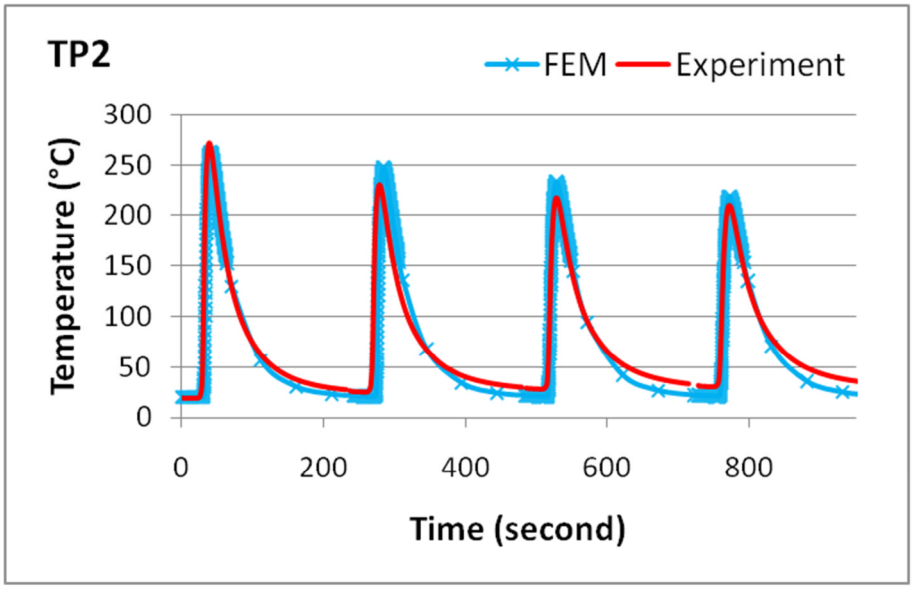
TP2
FEM
Experiment
Temperature (°C)
300
250
200
150
100
50
0
0
200
400
600
800
Time (second)

(b)

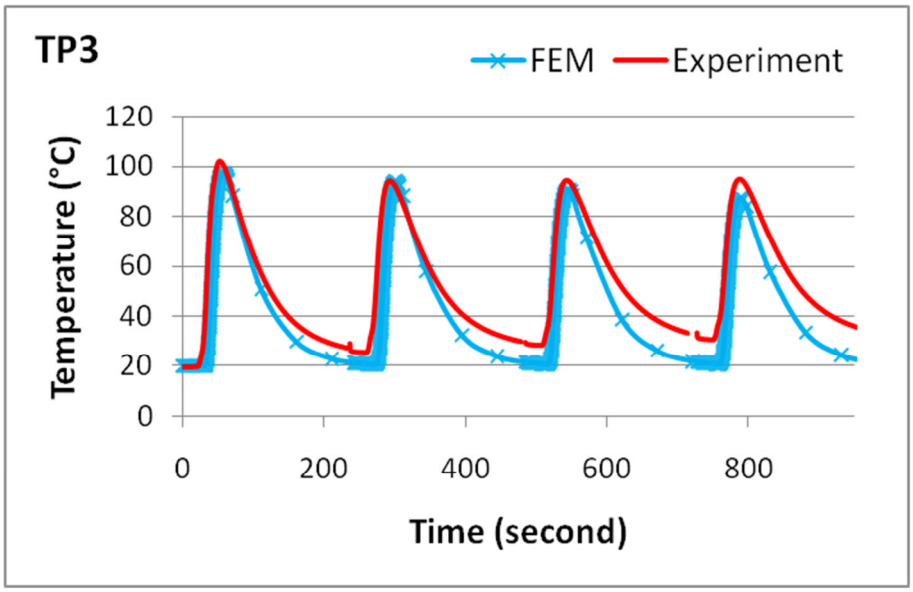
TP3
FEM
Experiment
Temperature (°C)
120
100
80
60
40
20
0
0
200
400
600
800
Time (second)

(c)

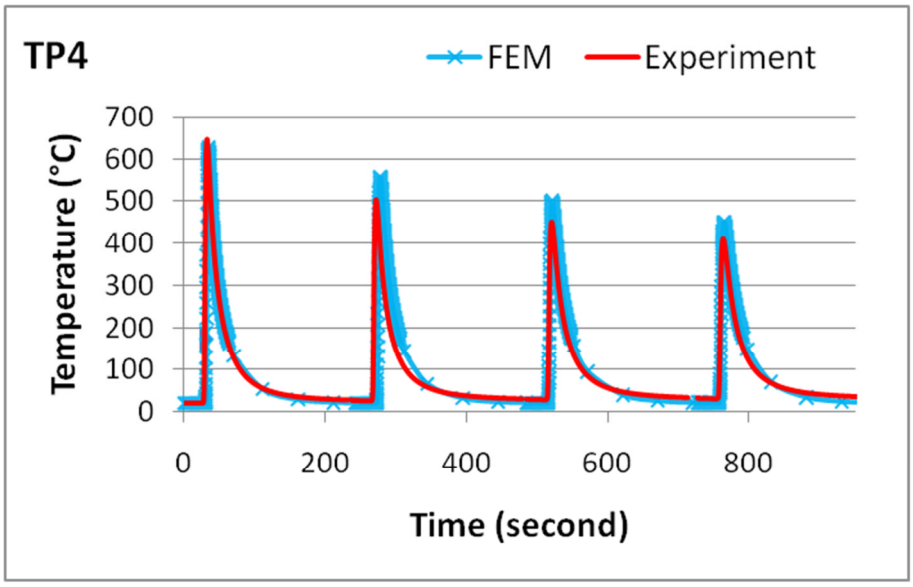

(d)

Figure 4-34: Transient thermal model verification on the measuring positions (Ti-6Al-4V) of (a) TP1 (135, 5, 0), (b) TP2 (125, 10, 0), (c) TP3 (115, 20, 0), (d) TP4 (125, 0, -6).

An initial mechanical verification was made by comparing the predicted distortions to the measured distortions on the specimens. The distortions were measured along the long edges of the specimens in the z direction with single layer bead, four layers beads, seven layers beads, and ten layers beads were measured using the laser scanning system Romer Arm. As shown in Figure 4-35, the current mechanical model is able to predict the generation of the distortion with a slight overestimation. Both the FE model and the experimental measurement show that the magnitude of the distortion increases when more layers of materials added to the component. However, the increment is getting smaller as less change on the stiffness can be made when more materials has deposited. The possible reason for the error is that the simplified mechanical material properties used in this model are not sufficient. A more accurate material model needs to be utilised in the future work, which should include accurate temperature-dependent yield strength data for the filler material and hardening material model.

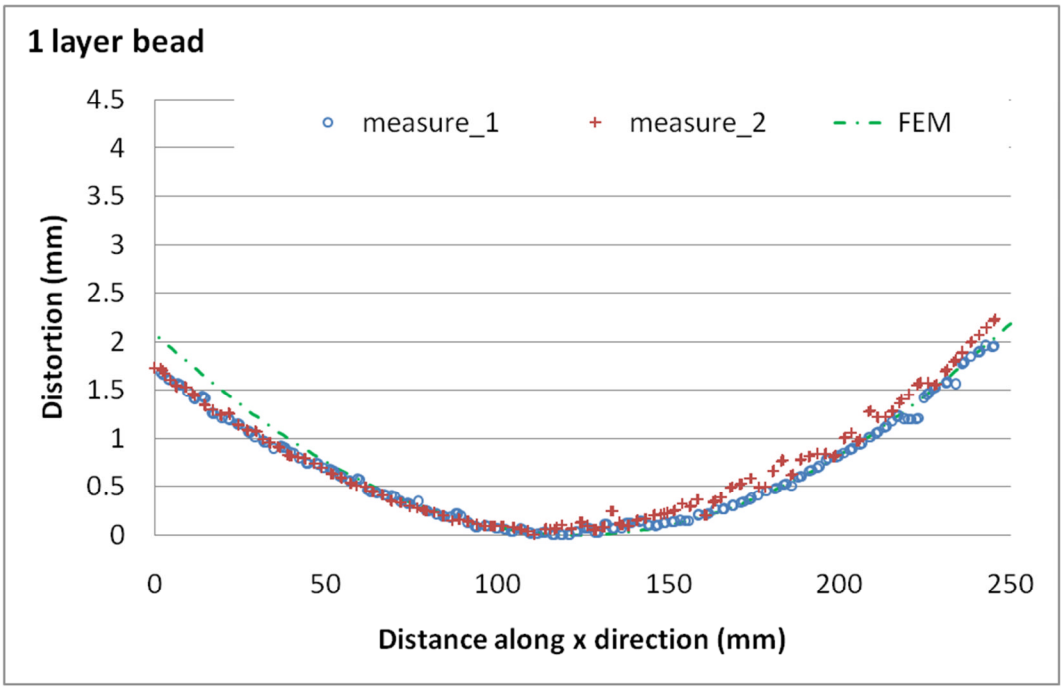
1 layer bead
measure_1
measure_2
FEM
Distortion (mm)
4.5
4
3.5
3
2.5
2
1.5
1
0.5
0
0
50
100
150
200
250
Distance along x direction (mm)

(a)

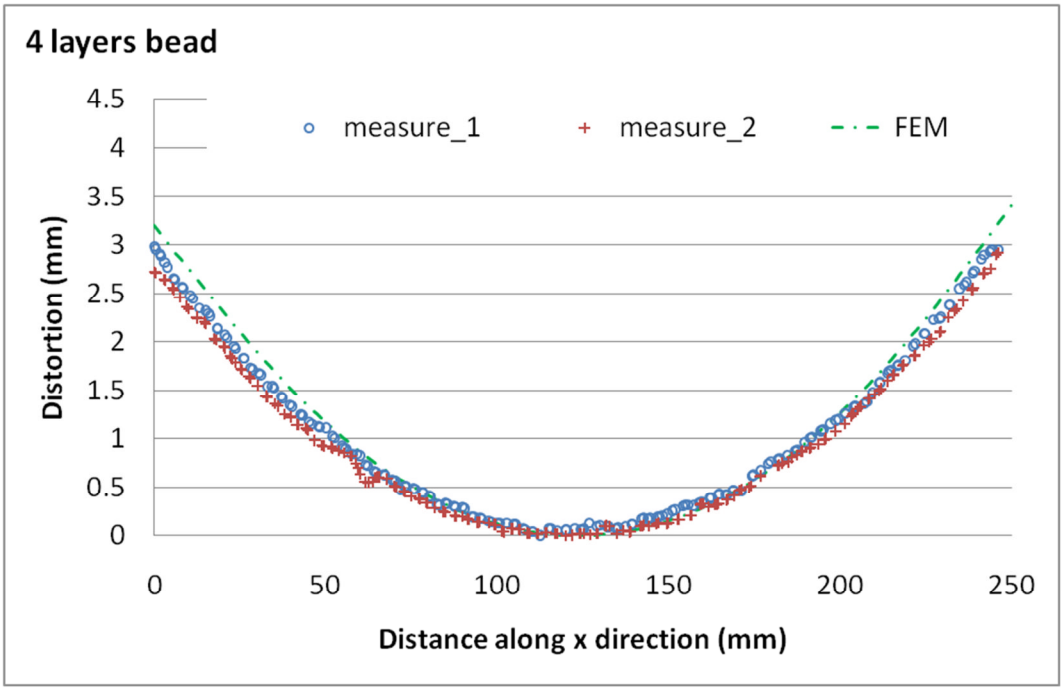
4 layers bead
measure_1
measure_2
FEM
Distortion (mm)
4.5
4
3.5
3
2.5
2
1.5
1
0.5
0
0
50
100
150
200
250
Distance along x direction (mm)

(b)

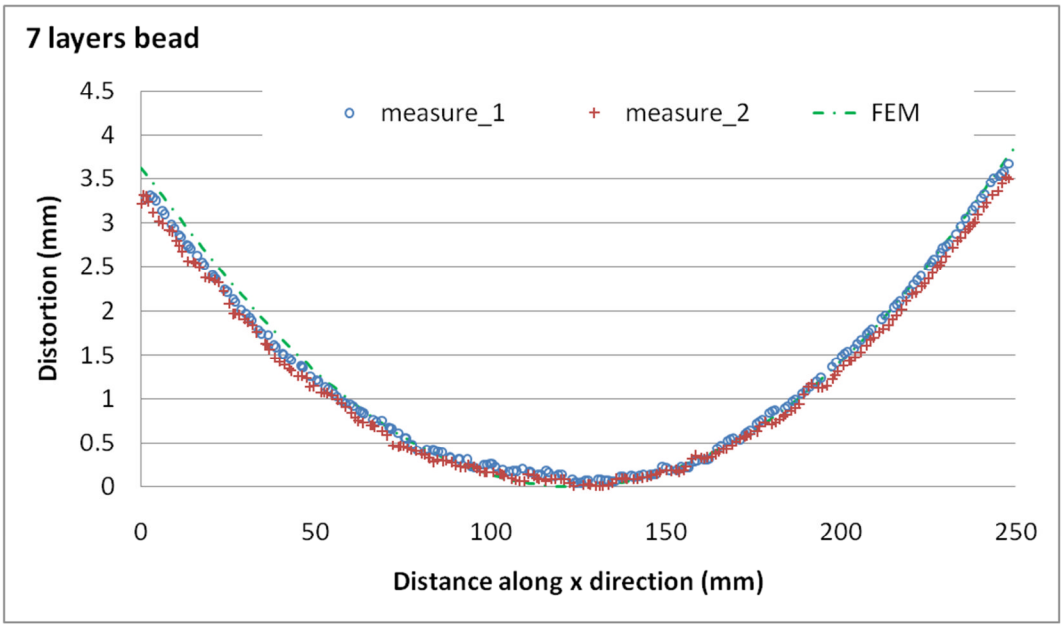

(c)

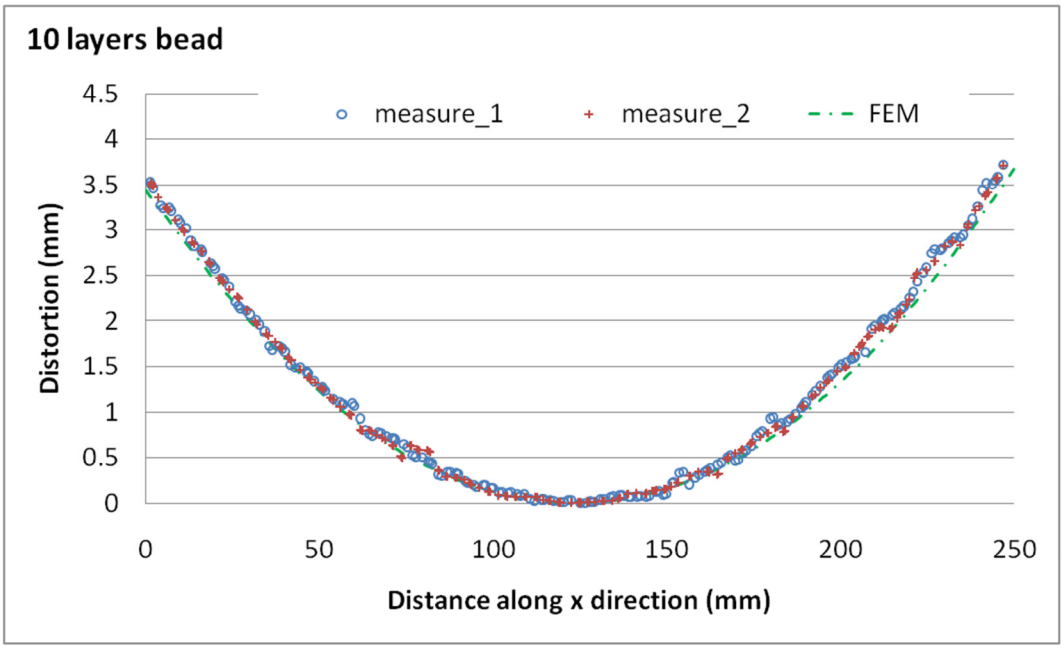

(d)

Figure 4-35: Distortion verification (Ti64) along the longitude of the specimen with: (a) single bead, (b) four beads, (c) seven beads, (d) ten beads.

Figure 4-36 shows the longitudinal stress distributions on the 10 layer Ti 64 WAAM wall model. Similar to the stress distribution on the mild steel model,

high tensile stress that has the similar value of the material's yield strength under room temperature was generated on the deposited wall and the intersection area to the base plate. The stress redistributed after the clamps were removed. High tensile stress was generated in the area of the base of the deposited wall. Balanced compressive stress was generated in the baseplate further away from the deposited wall. However, the stress results need to be verified with the experimental data in the future work.

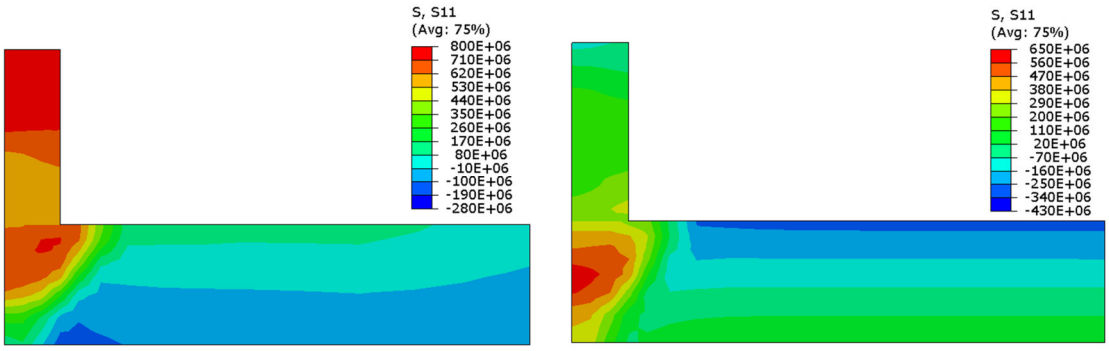

Figure 4-36: Longitudinal stress distribution on the 10 layer Ti64 WAAM model: (a) with clamps; (b) without clamps.

4.5 Summary

This chapter introduces a transient thermo-mechanical analysis of the WAAM process. This 3D FE model is developed to reflect the real-life WAAM process for giving predictions on residual stresses and distortions. With proper material models and moving heat source models, the model can provide accurate thermal and mechanical predictions which have been verified with experimental results.

As it is very difficult to analyse the stress evolvement of the WAAM process experimentally, the numerical simulation stands out as a good alternative. A better understanding of the thermo-mechanical performance of the WAAM process has been obtained with the help of the transient FE model. And this transient model will be used as the 'base model' in this thesis to give a reference to the other models described in the following chapters. However, huge computational time is required for this model. It is not applicable for the

analysis of large scale WAAM components. To use the FE predictions for improving the WAAM process more efficient approaches have been developed in this PhD research, and they are introduced in the next chapter.

5 EFFICIENT ENGINEERING FE APPROACH FOR THE WAAM PROCESS

5.1 Introduction

In the previous chapter it has been shown that the transient 3D thermo-mechanical simulation can provide detailed and accurate predictions on temperature distribution, stress distribution and the distortions. However, an apparent drawback of this method is that long computational time is required.

The huge amount of calculation increments in the transient thermo-mechanical model is the main reason of its expensive computational budget. In Section 2.4.4 a number of efficient FE approaches have been introduced to be used in the simulations of large scale welds. A common characteristic of their methods is that they all treat the transient process of welding as a static problem, which greatly saves the computational time.

The target components of the WAAM process are large scales which consist of long welding passes as the basic elements. Thus, the WAAM process has the similar characteristics of long welding process. Inspired from the efficient models for large scale welding simulation, new approaches are developed to solve the thermo-mechanical analysis of the large scale WAAM parts in a practical time. A steady-state thermal model for the WAAM process is introduced in the beginning of this chapter, which can save about 99% of the computational time required for the transient thermal calculation. This static temperature output can then be transferred as thermal histories and then be utilised in the same way in the mechanical model as the transient mechanical analysis.

A much more efficient mechanical model using the steady-state thermal data is also introduced in this chapter. This approach is based on the relation between the generation of the plastic stress and the nodal peak. Fast estimations of final residual stresses and distortions can be provided using this approach. Compared to the transient mechanical model, nearly 98% reduction on the

computational time can be achieved on the mechanical analysis by using the simplified mechanical model.

5.2 Steady-state Thermal Model

For a long weld with a constant welding speed, the thermal histories approach a steady state, particularly in the middle of the weld. This phenomenon has been utilised in FE models of welding processes which have used a steady state model (Shanghvi and Michaleris, 2002; Qin and Michaleris, 2009; Wang et al., 2009). Similar to a long weld, a quasi-steady state temperature field can be seen in the large scale WAAM process. Neglecting the different thermal performance on the end areas, steady-state thermal analysis can be performed to give a static temperature distribution, from where important thermal information can be obtained for the mechanical analysis.

5.2.1 Steady-state Thermal Model Implementation

Figure 5-1 shows the mesh used for the steady-state model. Unlike the transient model, the steady-state model does not require a uniform mesh with high density along the weld line. Small meshes are utilised around the heat source, and the element size increases dramatically along the x direction away from the heat source. The smallest elements are located in the heating area with a size of 1.667 mm × 0.833 mm × 0.667 mm, while the largest ones are at the outlet face with the size of 344.656 mm × 5.407 mm × 2.712 mm. Forced convection/ diffusion brick elements (DCC3D8) were utilised in this model. Instead of modelling the heat source moving along the weld line as in the transient model, the steady-state method attaches the reference frame to the welding torch and models the material “flow” through the meshes. A mass flow rate per area, which equals the welding speed multiplied by the material density, is used to represent the torch movement. The heat distribution for the steady state model is also represented with the same Goldak double ellipsoidal heat source as in the transient thermal model.

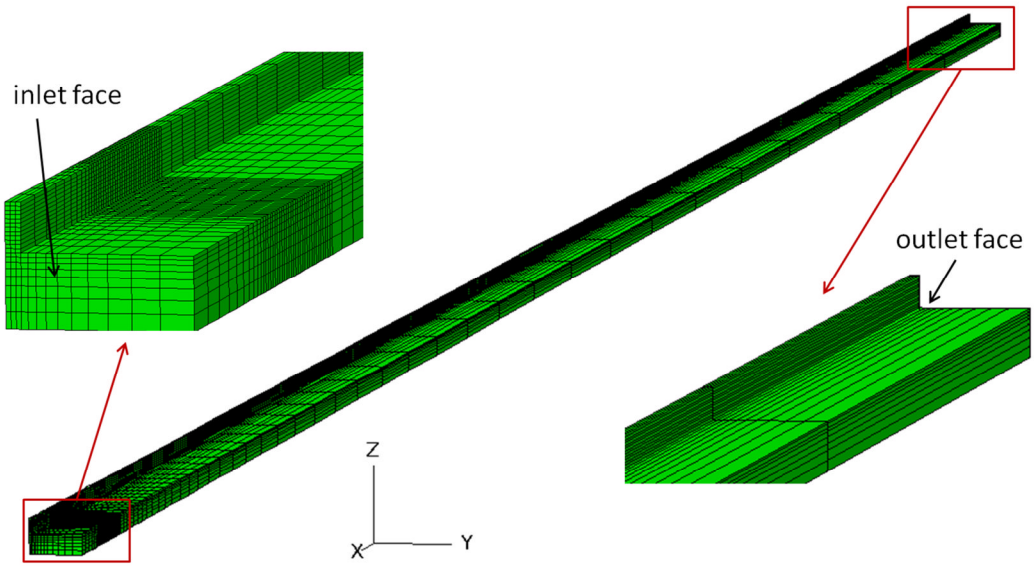

Figure 5-1: Mesh of the steady state thermal model.

The effect of the residual temperature needs to be taken into account if the component does not cool down to ambient temperature between deposits. This is modelled by taking the nodal temperatures from the outlet surface for the previous model and applying them to the inlet surface of the model for the next layer. To provide an accurate prediction of the outlet temperature the length of the model is set so that:

$$L = V_{torch} \times T_{waiting} + L_{actual} \quad (5\text{-}1)$$

Where L is the length of the steady-state thermal model;

V_{torch} is the travel speed of the welding torch; $T_{waiting}$ is the waiting time between subsequent layers; and L_{actual} is the actual length of the sample. Using this approach, the effective cooling time between subsequent layers is identical to the experimental condition.

The temperature-dependent thermal material properties as well as the thermal boundary conditions are set up with the same values to the transient thermal model which has been introduced in the previous chapter. The filler material is added in a layer by layer way which saves a huge number of steps that used to be in the transient thermal model. The duration for the heating step is set to 1

second. However, the duration does not have any effect on the computational results. The material constitutive behaviours are time (rate)-independent, and there is no transient effect caused by the temperature load as in the transient thermal model. Automatic time incrementation is used in the simulation with the allowed maximum time increment of 0.1 second.

5.2.2 Steady-state Thermal Result and Discussion

Figure 5-2 shows the steady-state temperature profile with four layers of filler materials. Similar temperature distributions can be seen comparing to the temperature profile predicted by the transient model (Figure 4-23). However, as shown in Figure 5-2 heat can be conducted via the elements in front of the heat source, which potentially causes an underestimation of the thermal performance in the steady-state model.

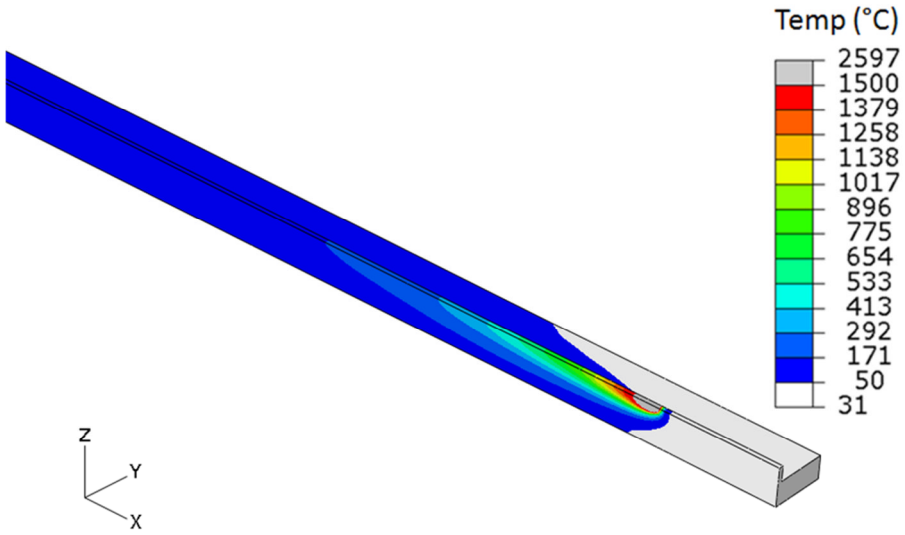

Figure 5-2: Temperature profile from the steady-state thermal analysis. The area with grey colour represents the fusion zone where the temperature exceeds 1500 °C.

Similar to the transient model, the steady-state thermal model is also verified by comparing the temperature histories from four different positions on the base plate to the measured results using thermocouples on the corresponding positions. These results are presented in Figure 5-3. The comparison of the

steady-state model and the transient model is also demonstrated in these plots. As the steady-state model does not have a time related history, the thermal cycle of the testing point is obtained by plotting the temperature along lines with fixed y, and z coordinates which correspond to the thermocouple positions shown in Figure 4-2. The time coordinate is generated by dividing the position in the x direction by the travel speed.

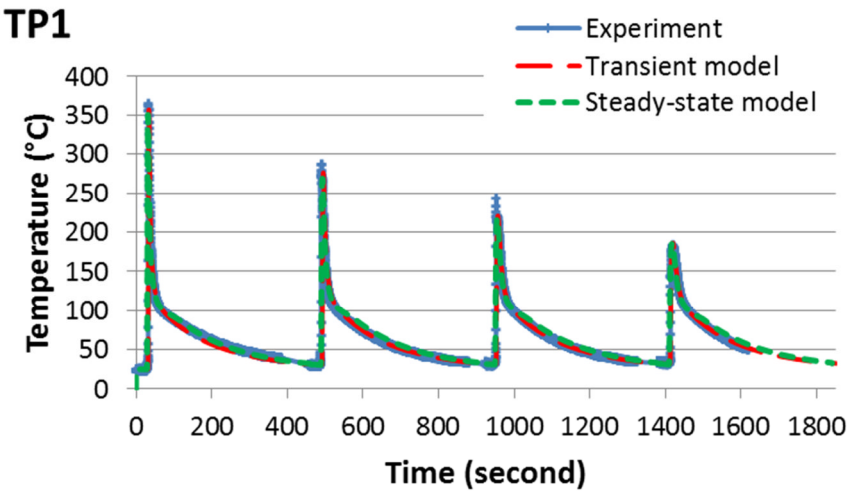

(a)

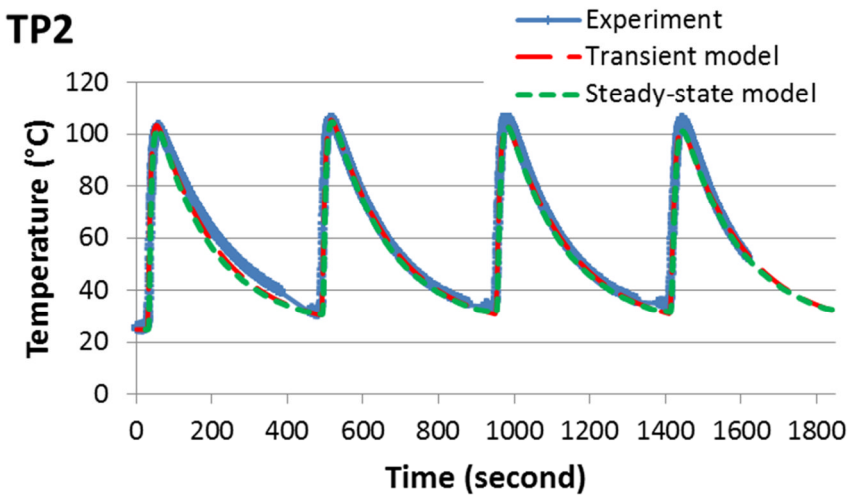

(b)

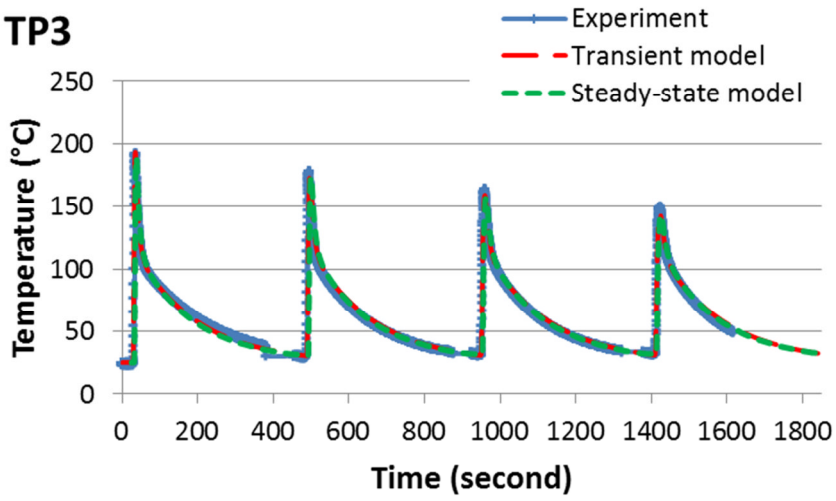

(c)

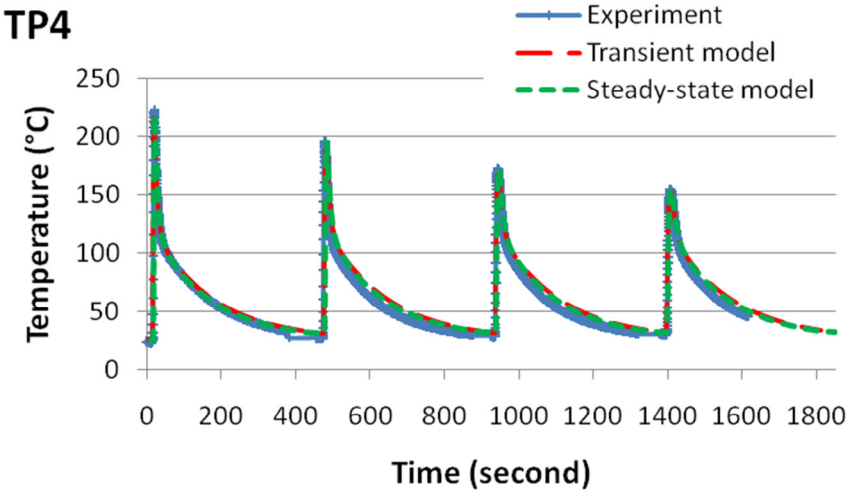

(d)

Figure 5-3: Temperature verification on the measuring positions of (a) TP1 (250, 5, 0), (b) TP2 (250, 20, 0), (c) TP3 (250, 0, -12), (d) TP4 (375, 0, -8).

The temperature histories from the two thermal models are nearly identical. As in the transient model, the steady-state thermal model also gives accurate predictions of the temperatures at the four thermocouple positions. The underestimation of the steady-state model due to the false deposited material behind the melt pool is marginal. The largest difference was made on the

predictions of TP3 where the steady-state model underestimated the peak temperature about 2% of the transient result. This can be explained compared to the high travel speed the heat conducted away from the “un-deposited” material is insignificant (Shan et al., 2007; Deng et al., 2006).

The significant time saving by using the steady-state model is presented in Table 5-1. The comparison of the computational time used for the two FE models is based on the same calculating conditions which employed a grid computing system with four processors. More than 99% computational time consumed by the transient thermal model can be reduced by using the steady-state model. Although the time saving can be varied when using different calculation situations, substantial reductions on the computational effort is expected from the steady-state model which is decided by its quasi-static fashion and the small amount of calculation increments.

Table 5-1: Computational time comparison between the transient thermal model and the steady-state thermal model on the four layered wall.

	Analysis time
Transient model	51hours, 24minutes
Steady state model	10minutes
Time saving	99.69%

5.3 Mechanical Model with Mapped Thermal History

The steady-state thermal model can provide fast predictions of temperature distribution for the long WAAM deposited walls. In this section, this static thermal result is transferred into nodal transient temperature histories to be used as the thermal load in the 3D mechanical model. In this way the residual stresses as well as the final distortions can be simulated.

5.3.1 Mechanical Model Implementation

A 3D elastic-plastic mechanical model is used to calculate the residual stress from the steady state thermal model data. The length of the mechanical model is 500 mm which is the actual length of the experimental sample. It was meshed with the same mesh spacing as the steady state thermal model in the y and z direction, however the spacing in the x direction was set to a constant value of 2.5 mm. 'Element birth technique' was used to simulate the filler material deposition. The temperature-dependent mechanical material properties, the mechanical boundary conditions, as well as the step setups were the same to the mechanical model which has been introduced in the previous chapter.

To use steady state thermal results as the input to the mechanical model, the static nodal temperature data was transferred to thermal histories by dividing the position in the x direction by the travel speed. Temperature histories were added sequentially using the results from the model with one layer bead to the model with four layer bead. The stress analysis was carried out by applying the transferred thermal history sequentially to the 3D mechanical model. The temperature field from the steady state model was effectively mapped to the mechanical model using a pre-processing programme generated in Matlab.

5.3.2 Mechanical Model Verification

To verify the distortion predictions from the mechanical model with transferred temperature history, the out-of-plane displacement along the long edge was compared with the transient thermo-mechanical model. As illustrated in Figure 5-4, the predicted distortions from both models are nearly identical. Both models show that the magnitude of the distortion is continuously increased as more layers of material were added to the component. Compared to the experimental measurements of the distortion of the four layer wall, both models gave good predictions.

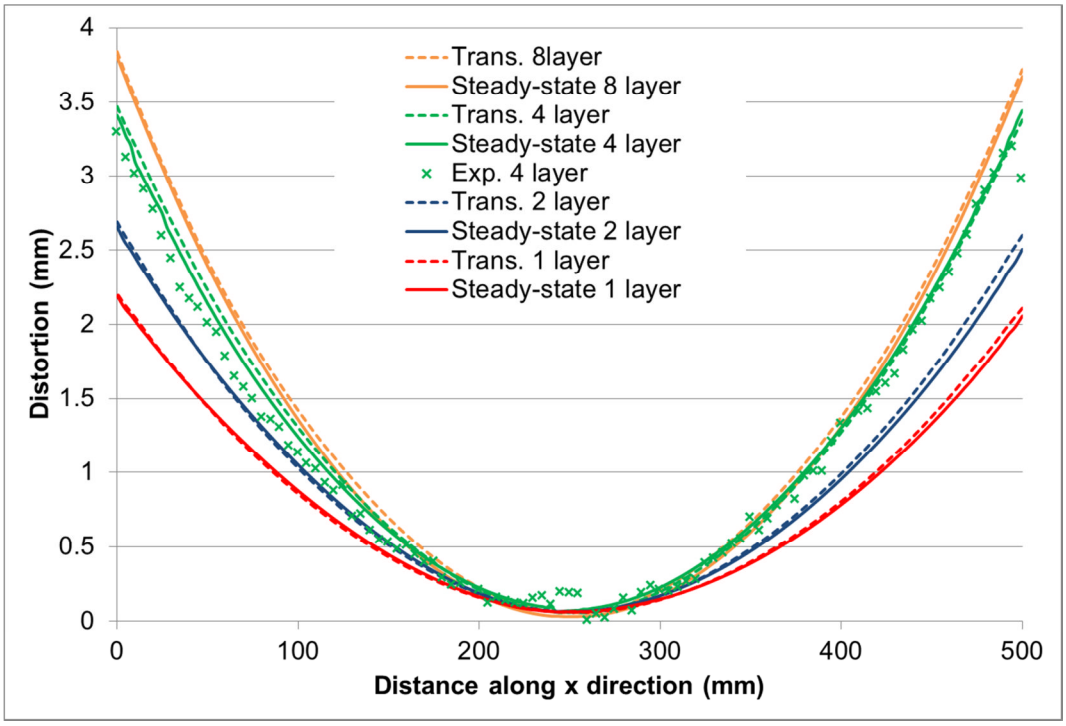

Figure 5-4: Distortion comparison between the mechanical approach based on the steady-state thermal results and the transient mechanical approach.

Figure 5-5 (a) to (c) illustrate the validation of the steady-state based mechanical model which is performed by comparing its residual stress predictions which were plotted from the mid-length section and 2 mm under the top surface of the base plate with those from the experimental measurements and the transient mechanical results. Like the transient mechanical model, the steady-state mapped mechanical model can provide accurate residual predictions.

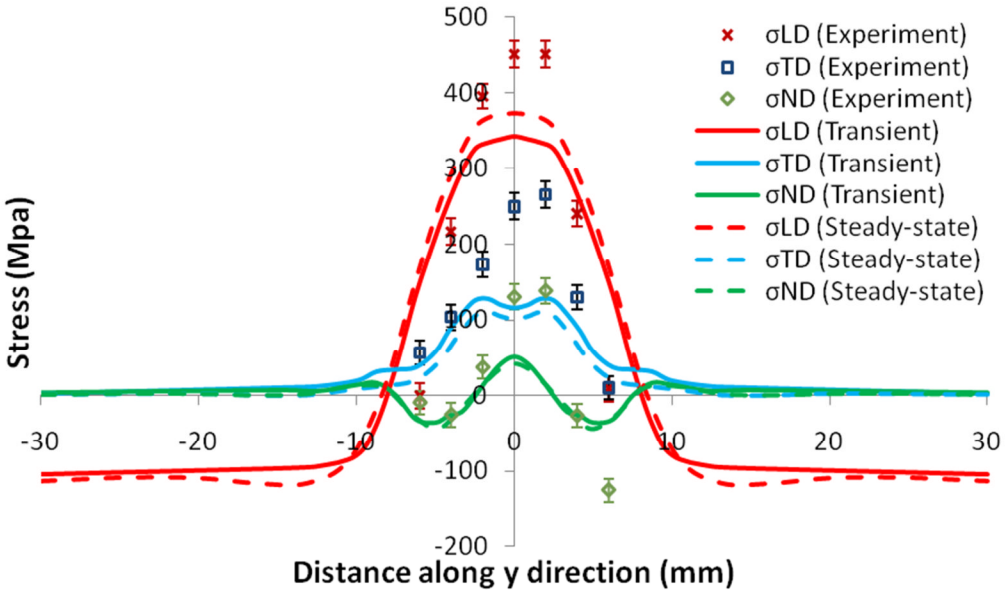
σLD (Experiment)
σTD (Experiment)
σND (Experiment)
σLD (Transient)
σTD (Transient)
σND (Transient)
σLD (Steady-state)
σTD (Steady-state)
σND (Steady-state)
Stress (Mpa)
Distance along y direction (mm)
500
400
300
200
100
0
-100
-200
-30
-20
-10
0
10
20
30

(a)

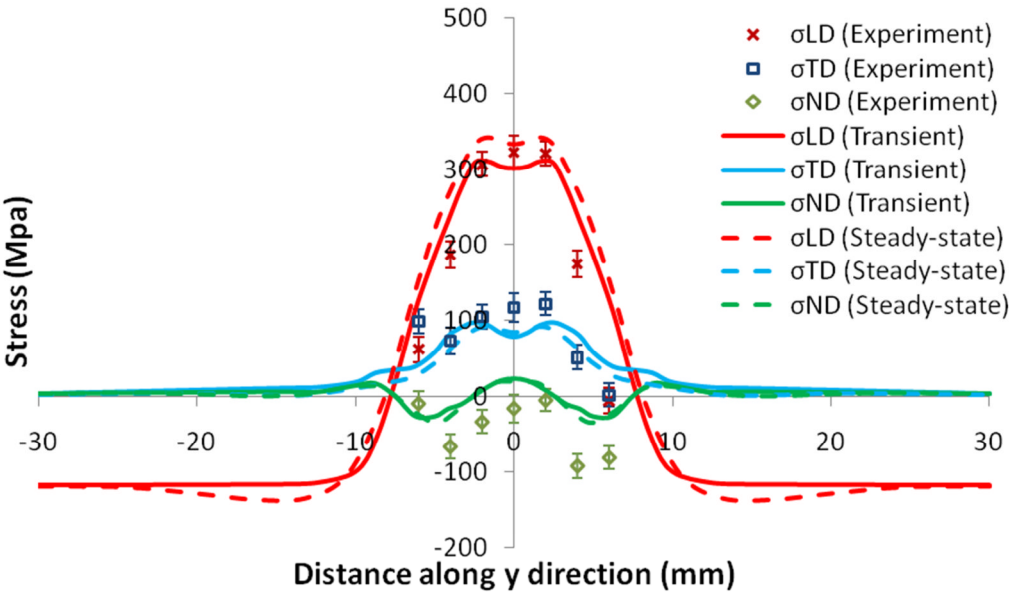
σLD (Experiment)
σTD (Experiment)
σND (Experiment)
σLD (Transient)
σTD (Transient)
σND (Transient)
σLD (Steady-state)
σTD (Steady-state)
σND (Steady-state)
Stress (Mpa)
Distance along y direction (mm)
500
400
300
200
100
0
-100
-200
-30
-20
-10
0
10
20
30

(b)

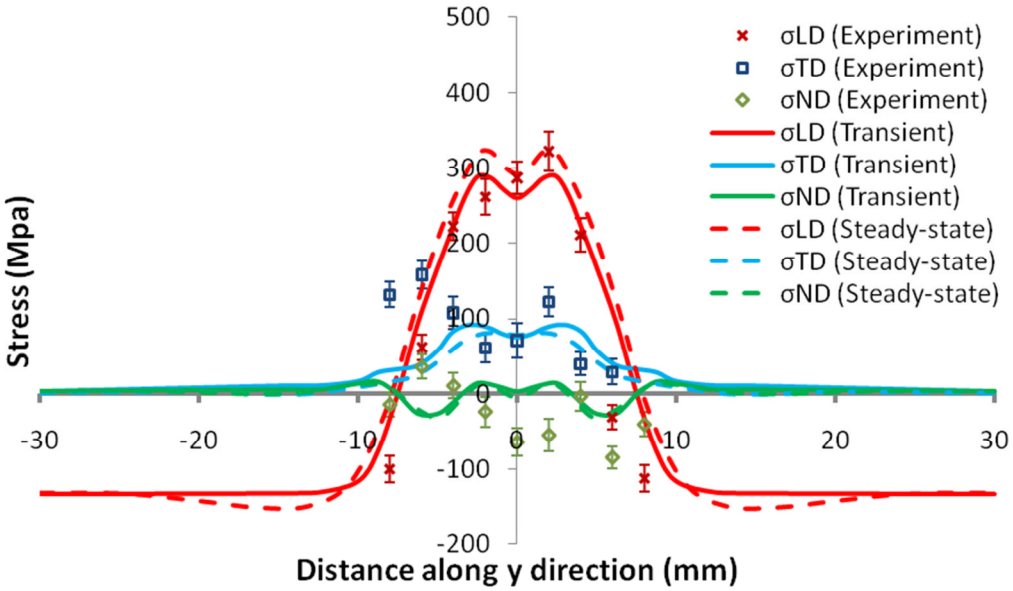

(c)

Figure 5-5: Stresses in the longitudinal (LD), transverse (TD) and normal (ND) directions along a transverse line in the base-plate indicated in Figure 4-2 for (a) single, (b) two, and (c) three layers.

Table 5-2 shows the comparison of the computational time between the transient mechanical model and the mechanical model using mapped steady-state thermal results. The time taken by the mechanical model based on the steady-state thermal result was reduced by around 40%. The transient thermal model provides much more data than the steady state model as it calculates the incremental temperature histories, which result in more time increments needed for completing the mechanical analysis. The number of time increment for completing one step with transient mechanical model is 32 increments on average, while the mechanical model using the mapped steady state thermal results needs only 20 increments to complete the same step. Counting the time spent on the thermal simulation, the combination of the steady-state thermal model and the mapped mechanical model can save around 80% in total comparing to the time required by the transient model.

Table 5-2: Computational time comparison between the transient mechanical model and the steady-state mapped mechanical model on the four layered wall.

	Analysis time
Transient model	24hours, 1minute
Steady state based mechanical model	14hours, 46minutes
Time saving	38.51%

5.4 Simplified Mechanical Model

Using the steady-state approach for the thermal predictions saves a lot of computational time for the thermal analysis. And the aforementioned mechanical model using the transferred thermal history can give accurate predictions of the distortions and stresses for the WAAM process. The mechanical model developed so far in this thesis is based on the transient thermal history which is either generated by the transient thermal model or transferred from the steady-state thermal model. The consequent mechanical model is also running in a transient way which requires a huge number of calculating steps. This is the key reason for the long computational time. If the mechanical performance can be predicted in a static way then the computational time will be saved greatly. Several approaches of solving the thermo-mechanical performance of welding processes through a static way have been introduced in the literature review (as seen in section 2.4.4). A common procedure for these approaches is applying an artificial temperature load on the mechanical model to generate the similar plastic strain patterns.

From the transient thermo-mechanical simulation of the WAAM process, it can be observed that during the deposition process the residual stresses appear mainly in the deposited material and in a narrow region in the base plate around

the deposition line; and the peak temperature that the material experienced during the thermal cycle of the deposition process decides what residual stresses are developed. Based on these observations, a simplified mechanical approach is developed to provide fast predictions of residual stresses and distortions for the large scale WAAM process.

5.4.1 Development of the Simplified Engineering Approach

Figure 5-6 shows the procedure of the mechanical analysis with the simplified mechanical model. The two key aspects of the simplified mechanical model are, the definition of the plastic effective zone; and the application of the equivalent temperature loads. The narrow area around the heating line where the thermal strain exceeds the yield strength during the thermal cycle is defined as the plastic effective zone. The material expansion and contraction in the area is the main source of the plastic strains which cause the residual stresses and the final distortions of the whole component. The region of the plastic effective zone was decided using the inequality: $T_{Mp} > \varepsilon_Y/\alpha + T_r$, where T_{Mp} is the maximum temperature experienced at a position p transverse to the deposition line, ε_Y is the yield strain, α is the expansion coefficient, and T_r is the room temperature. T_{Mp} was applied to the material in the mechanical model where this inequality is true (as shown in Figure 5-7). The maximum temperature was determined from the steady-state thermal model. It was calculated for all points in a plane transverse to the deposition direction.

To simulate the material contraction in the plastic zone during the deposition process, the maximum temperatures were applied to an elastic-plastic mechanical model that had the same geometry as the original part. All the elements of the deposited wall were deactivated at the first step of the analysis, and then the elements were activated sequentially in a layer by layer fashion. Initially, room temperature was applied to all the nodes in the model. In the first step, the first layer was activated, and the peak temperatures which were determined previously (T_{Mp}) were applied to all the nodes in the plastic zone, and the resulting plastic strain was determined. Note that the peak temperature was applied simultaneously to all the elements rather than sequentially as is

done with a conventional transient thermo-mechanical model. The minimum temperature that was achieved after the material had cooled down (T_{coolp}) was then applied and the stresses were recalculated. The whole process was then repeated for the next layer. When all the deposition layers were complete, room temperature was applied to the whole model and the clamps were released.

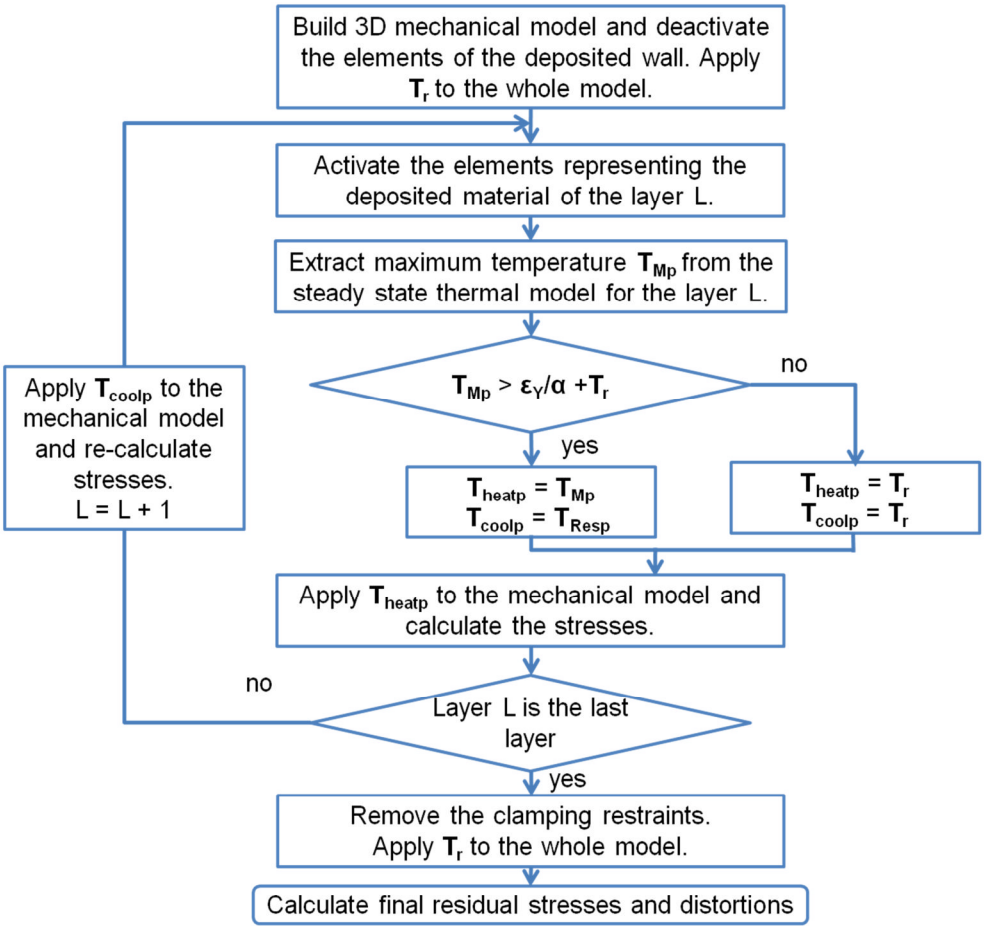

T_r: Room temperature.
T_{Mp}: Maximum temperature experienced at position p transverse to the deposition line.
ε_Y :Yield strain.
α: Expansion coefficient.
T_{heatp}: Equivalent temperature load at position p in the heating step.
T_{coolp}: Equivalent temperature load at position p in the cooling step.
T_{Resp}: Residual temperature at position p after the cooling step.

Figure 5-6: The process of the simplified mechanical approach.

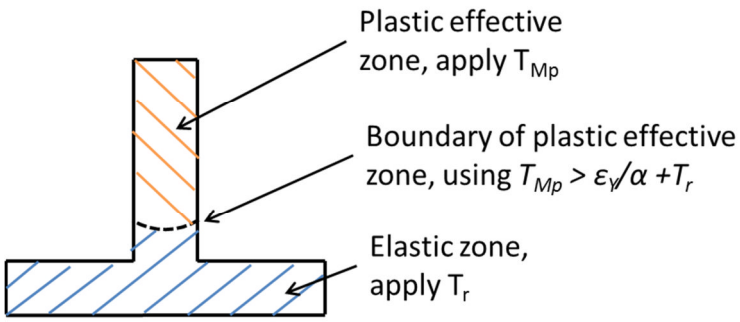

Figure 5-7: The definition of the plastic effective zone.

The materials outside this zone behave elastically during the deposition process. Although the materials of the connected area to the plastic effective zone may resist the contracting action of the heating zone elements, the contribution to the plastic strain and the total distortion of the component was considered very small. Thus, to simplify the model there is no temperature change outside the plastic zone during the deposition process. As only a small amount of elements and nodes of the FE model are involved in the plastic effective zone, very large computational effort can be saved.

Table 5-3: computational time comparison

	Analysis time
Transient model	24hours, 1minute
Simplified mechanical model	32 minutes
Time saving	97.8%

Table 5-3 shows the comparison on the computational time that is needed for the transient approach and the simplified mechanical model on a 4 layer 500 mm wall model. The computational time taken for the mechanical analysis can be significantly reduced by using the simplified mechanical approach. This is mainly due to the application of the equivalent loads which are simultaneously applied to the heating steps in the model. In addition, these artificial loads are

only applied to the plastic effective area where only a small part of the FE model experienced temperature changes during the calculation process. This also reduces computational effort.

5.4.2 Verification of the simplified mechanical model

The simplified mechanical model was verified on the distortions and the residual stress distributions. Figure 5-8 (a) and (b) illustrate the predicted longitudinal residual stress of the four layer wall after the clamps are removed from the two model types, which indicate nearly identical stress distributions. Tensile stresses are generated along the deposited wall due to material contraction during solidification, which consequently generates a balancing compressive residual stress in the base plate. Significant out-of-plane distortion of the component can be observed along the longitudinal direction after the clamps are removed.

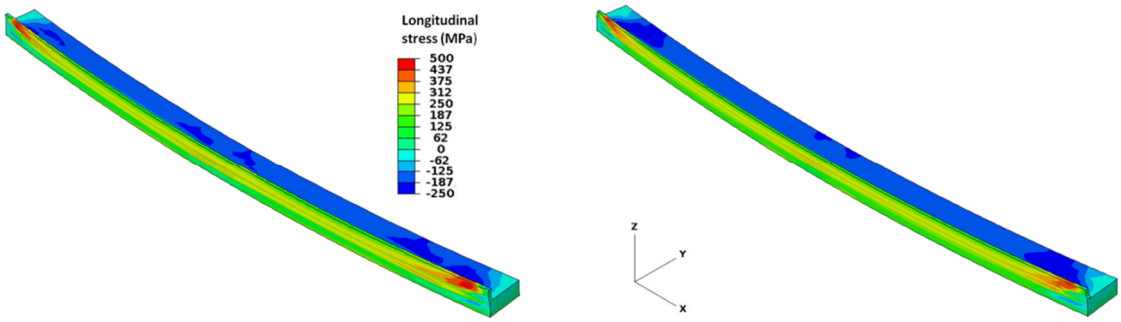

(a) (b)

Figure 5-8: Longitudinal residual stress predictions from: (a) transient mechanical model; (b) simplified mechanical model (a scaling factor of 5 is used for the distorted shape).

To have an overall check of the mechanical results, the predicted distortion along the long edge from the simplified mechanical model was compared with the result from the transient model. The distortions were plotted from FE mechanical models with different layer numbers after the clamps were removed and shown in Figure 5-9. Both models show that the magnitude of the distortion is continuously increased as more layers of material are added to the component. This change is getting smaller as the rigidity of the component is

higher when more material is deposited. As shown in Figure 5-10, the difference of the peak out-of-plane between the deposition of 5 layers' material and deposition of 8 layer's material is just around 0.2 mm.

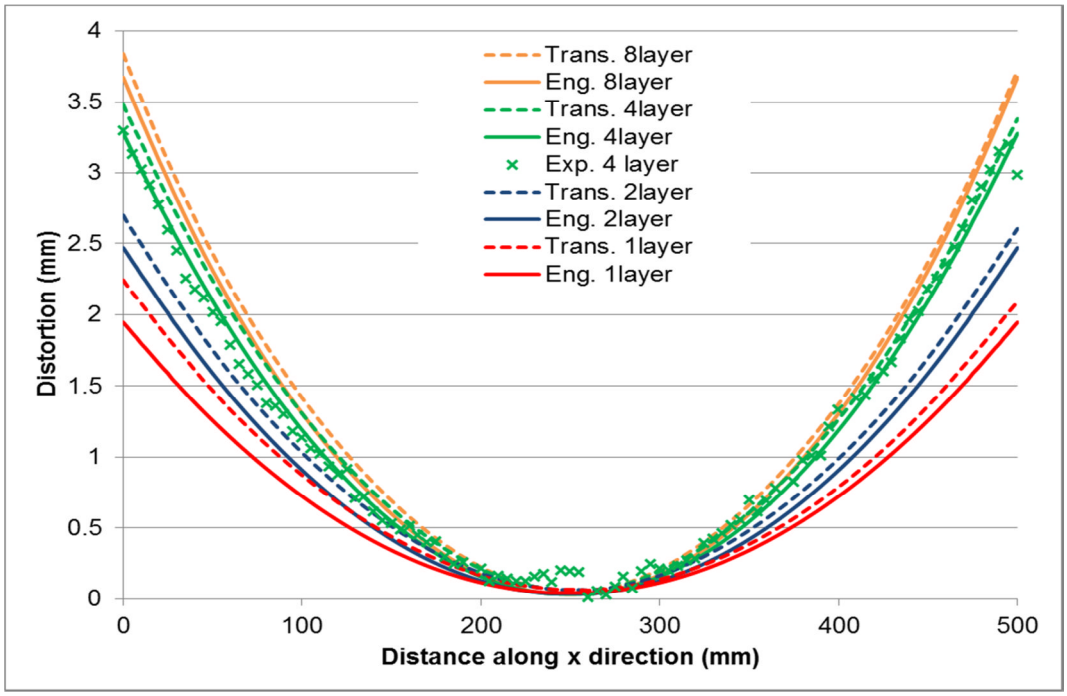

Figure 5-9: Distortion comparison between the engineering approach and the transient mechanical approach.

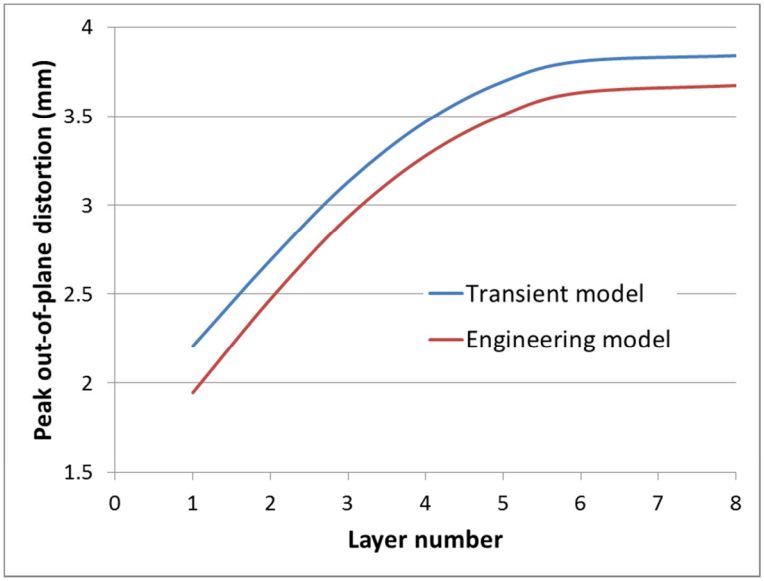

Figure 5-10: Comparison of peak out-of-plane distortion against layer number.

In general, the trend of the variation predicted by the simplified mechanical model matches the results from the transient model. And both FE models gave good predictions of the experimental values which are included for the four layer wall only. Compared to the transient model, the engineering model gave slightly lower distortion predictions. This underestimation is about 12% for the models of the first layer deposition and it reduced to 4% for the predictions of the 8 layer deposition. Moreover, the transient model showed a difference in the distortion predicted at the beginning and end of the deposit. A possible explanation is that the “element birth technique” utilised in the transient model gradually increased the stiffness of the component during the deposition process. In contrast, the whole layer of elements representing the newly added material was activated simultaneously in the simplified mechanical model, which resulted in a stiffer structure and consequently slightly lower distortion.

Figure 5-11 illustrates a detailed validation of the residual stress data which compares the FE predictions from the simplified mechanical model with those from the transient mechanical model as well as the measurements from the neutron diffraction experiments. The stress data were extracted along a transverse line in the middle cross section of the component 2 mm below the top surface of the base plate. In both the modelling and experimental results the clamps have been removed, and three principle directions have been considered namely: longitudinal (σLD), transverse (σTD), and normal (σND). The stress predictions given by the simplified mechanical model are similar to those from the transient model with slight over-estimations of the stress values in the longitudinal direction. And the simplified mechanical model gave good predictions of the experimental values in all the three directions.

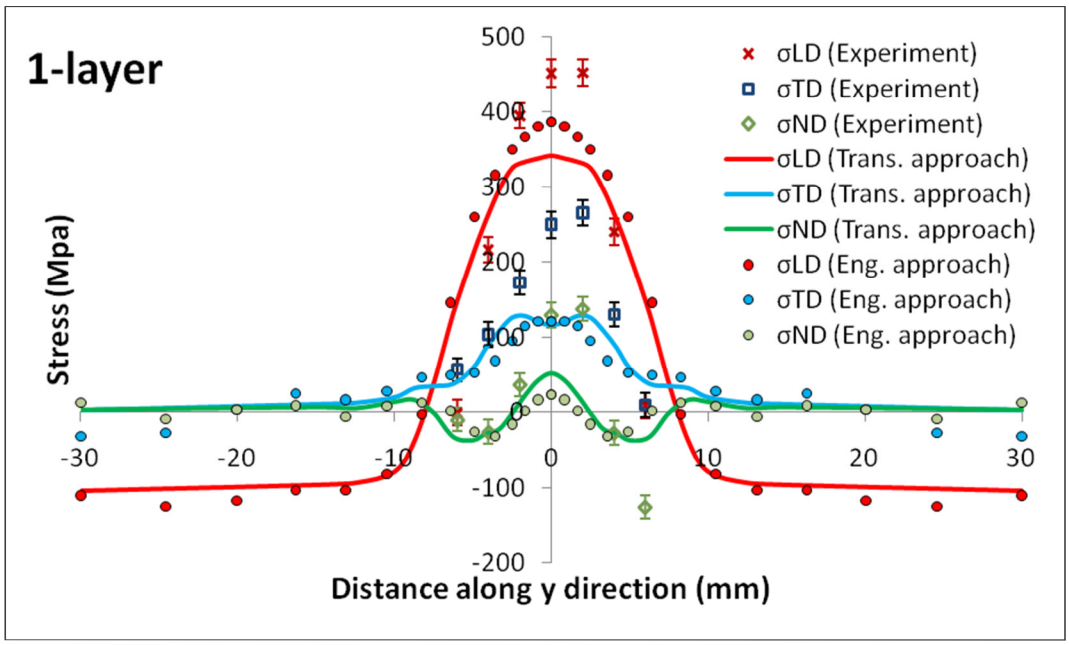
1-layer
Stress (Mpa)
Distance along y direction (mm)
σLD (Experiment)
σTD (Experiment)
σND (Experiment)
σLD (Trans. approach)
σTD (Trans. approach)
σND (Trans. approach)
σLD (Eng. approach)
σTD (Eng. approach)
σND (Eng. approach)
500
400
300
200
100
0
-100
-200
-30
-20
-10
0
10
20
30

(a)

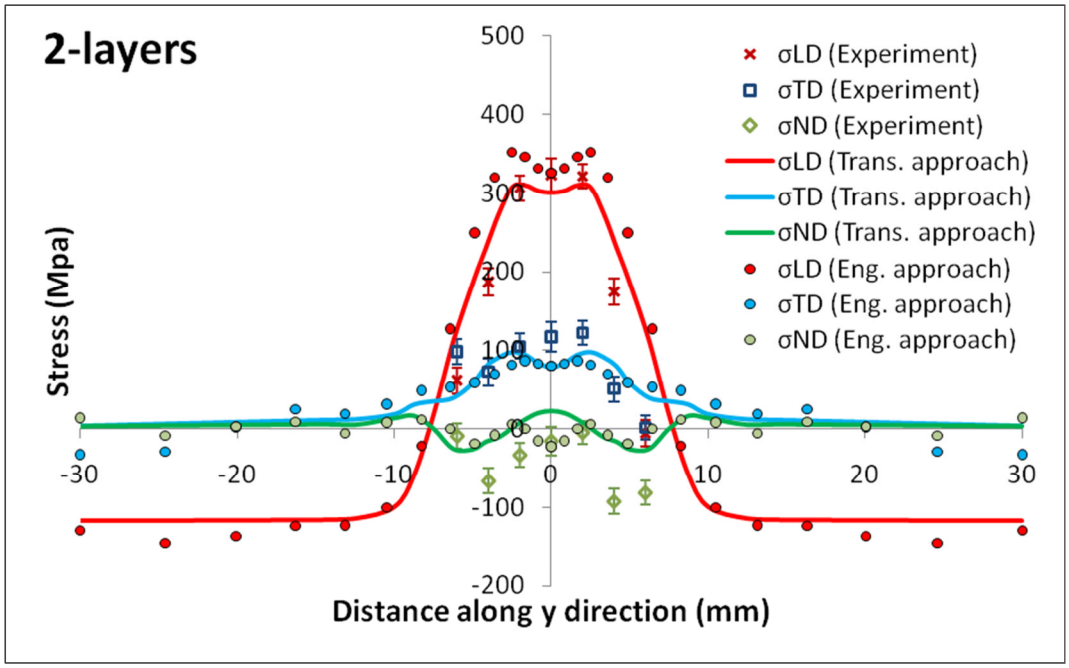
2-layers
Stress (Mpa)
Distance along y direction (mm)
σLD (Experiment)
σTD (Experiment)
σND (Experiment)
σLD (Trans. approach)
σTD (Trans. approach)
σND (Trans. approach)
σLD (Eng. approach)
σTD (Eng. approach)
σND (Eng. approach)
500
400
300
200
100
0
-100
-200
-30
-20
-10
0
10
20
30

(b)

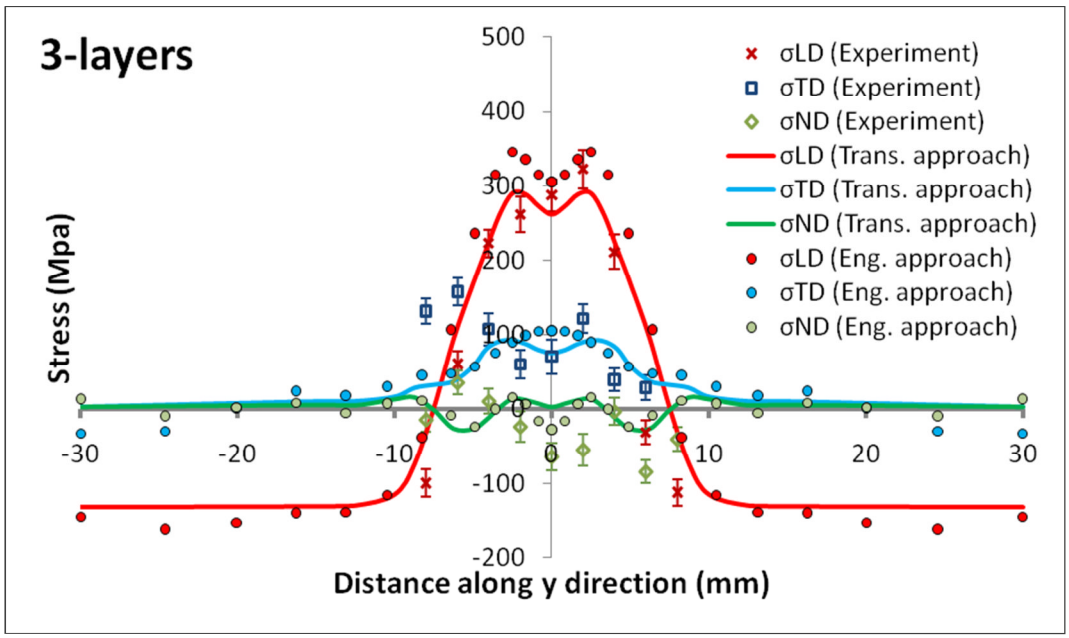

(c)

Figure 5-11: Stresses comparison in the longitudinal (LD), transverse (TD) and normal (ND) directions along a transverse line in the middle cross section of the component 2 mm below the top surface of the base plate for (a) single, (b) two, and (c) three layers.

5.5 Summary

This chapter introduced the efficient FE models that have been developed for predicting the thermo-mechanical performance of the large scale WAAM process. The thermal model is built on the steady-state phenomenon which occurs in the large deposition process. Compared to the conventional transient thermal model, this model can provide similar accurate thermal predictions but saves more than 99% of the computational time.

The static temperature results from the steady-state thermal model can be transferred to the temperature histories and be applied to the 3D mechanical model for the predictions of residual stresses and distortions. Another simplified mechanical model has been developed to further improve the efficiency of the thermo-mechanical predictions. This model was developed based on the

observation from the transient analysis that the peak temperature during the thermal cycles of the deposition process is the key element that decides the elastic-plastic response of the material. The residual stresses and distortions that predicted by this model have been validated with the transient model as well as the experimental results. Compared to the transient mechanical model this model showed a significant advantage, saving about 98% computational time.

The combination of the steady-state thermal model and the simplified mechanical model can give the most benefit of reducing the computational time. A steady-state thermal model can provide temperature data efficiently, while a simplified mechanical model can calculate the residual stresses and distortion in a short time. This combination can save totally around 99% of computational time that is required by the transient thermo-mechanical model. In this thesis this combination is named ‘engineering FE approach’ which enables the process study and optimisation of the WAAM process.

[Page left intentionally blank]

6 WAAM PROCESS STUDY USING NUMERICAL MODEL

6.1 Introduction

Residual stresses and distortions are inevitable issues for the WAAM process. Using optimal deposition parameters and welding sequence is a possible way to control and minimise the residual stresses and distortion level without additional manufacturing facilities. This is especially important to choose the optimal deposition parameters and building sequences in building large scale WAAM components when it is very difficult and extremely expensive to eliminate these thermally induced problems with extra processes. In this case, performing numerical predictions efficiently before the real deposition manufacturing turns out to be critical for the WAAM process. Best deposition parameters and building strategy can be decided based on the virtual results.

In the last two chapters different numerical approaches for simulating the thermo-mechanical performance of the WAAM process have been introduced. Conventional transient thermo-mechanical model can give an accurate prediction to the real world WAAM process, but the long computational time constrains its application to the large scale WAAM parts. The engineering FE approach which has been introduced in the last chapter can provide estimations of the final residual stresses and distortions in a short time, which greatly improves the ability of using the FE tool to study and optimise the WAAM process.

In this chapter, the FE models are applied to the process study of the WAAM process. The relationship between the residual stress distribution and the controllable process parameters is investigated using the efficient engineering FE models with the integration of the process models. The preheating effect on the stress distribution, which is induced from the residual temperatures after depositing each pass, is also analysed in this study using the FE approach. The significant benefit on minimising the final distortion by optimising the building

sequences is investigated using a case study on a large scale frame structured WAAM component.

6.2 Deposition Parameters Study

A deposition parameter study has been carried out to investigate the influence of the process parameters on the stress distribution of the deposited wall. As shown in Figure 6-1, the FE model was utilised to provide stress data. Statistical models were developed based on the real-world experiments which provide the FE model with geometric information of the deposited wall and the information for the heat source. The residual stress distributions from different deposition parameters were analysed and the result can be used to help decide the optimal parameters for the WAAM process in the future.

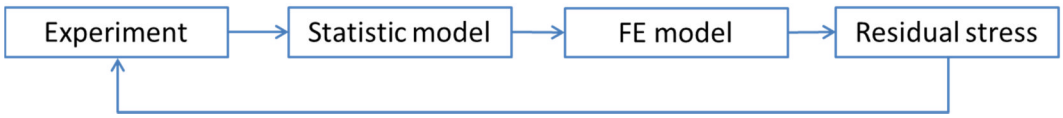

Figure 6-1: process of the deposition parameter study

In this study, the Wire Feed Speed (WFS) and the Travel Speed (TS) of the welding torch were selected as the most influential controllable factors for the WAAM process. The current process study is based on the experiments carried out with the 0.8 mm wire. The Contact Tip to Work Distance (CTWD) was kept to 13 mm throughout all the experiments. The experiments were carried out following the WAAM process study that has been done by Almeida (Almeida, 2012).

Table 6-1 shows the parameters used for the experimental trials for the process study. Six sets of trials were performed with different WFS values which were varied from 3.0 m/min to 15.0 m/min. The TS value was increased by 0.1 m/min from 0.1 m/min for each set until 0.9 m/min. However, the TS values shown in Table 6-1 are not complete because the investigation excludes the trials which result in unstable deposition conditions. In total, 43 trials with the parameter combinations shown in Table 6-1 were measured and examined in this process study.

Table 6-1 Parameter settings for the process study

Set	WFS (m/min)	TS (m/min)
1	3.0	0.1, 0.2, 0.3, 0.4, 0.5, 0.6
2	5.0	0.1, 0.2, 0.3, 0.4, 0.5, 0.6, 0.7
3	7.5	0.1, 0.2, 0.3, 0.4, 0.5, 0.6, 0.7, 0.8
4	10.0	0.2, 0.3, 0.4, 0.5, 0.6, 0.7, 0.8
5	12.5	0.2, 0.3, 0.4, 0.5, 0.6, 0.7, 0.8
6	15.0	0.2, 0.3, 0.4, 0.5, 0.6, 0.7, 0.8, 0.9

The outputs considered for geometric estimations were: effective wall width (EWW), surface waviness (Wav) and average layer height (ALH). As shown in Figure 6-2, the parameter of EWW has been introduced to present the width of the wall which is left after removing the building waviness on both sides of the deposited wall. Note that the measurement of EWW did not account for the first four layers of the deposited wall because the condition is not steady due to the cooling effect of the base plate. Heat input (HI), penetration (P) and the length of the heat source (LoHS) were also included as the outputs of the process study to provide information for the heat source.

Figure 6-2: Macrophotograph of WAAM sample

Walls 10 layers high were built on 6 mm thick mild steel plate using the parameters listed in Table 6-1. The deposited walls were 250 mm long in order

to guarantee steady state depositing conditions. EWW and P were measured from the etched cross-sectional macrophotographs. Wav was measured utilising a high resolution scanning type confocal optical microscope. ALH was taken the average value of the step increments after four layers of the wall. The values of LoHS were obtained by measuring the length of the isotherms noticeable from the weld pool surface ripple markings after the first layer of the deposition pass. To calculate the welding heat input, the electrical transient data was monitored and recorded utilising a Yokogawa DL750 ScopeCorder at 5 kHz acquisition rate pre-setting. The Average Instantaneous Power (AIP) method was employed to calculate the arc energy according to equation 6-1, and thereafter the heat input (shown as equation 6-2) was calculated.

$$Q[W] = \eta \cdot \sum_{i=1}^{n} \frac{I_i \cdot V_i}{n} \tag{6-1}$$

$$HI\,[J/mm] = \eta \cdot \frac{Q[W] \cdot 0.06}{TS\,[m/\min]} \tag{6-2}$$

The analysis was carried out by applying a least square and multiple linear regression technique, using Design Expert® 7.15 software. The following regression models were derived from the regression analysis undertaken.

$$\text{EWW (mm)} = 3.98 + 0.63 \times \text{WFS} - 9.50 \times \text{TS} - 0.51 \times \text{WFS} \times \text{TS} + 8.20 \times \text{TS}^2 \tag{6-3}$$

$$\text{Wav (mm)} = 0.61 + 0.181 \times \text{WFS} - 4.53 \times \text{TS} - 0.06 \times \text{WFS} \times \text{TS} - 0.020 \times \text{WFS}^2 + 7.83 \times \text{TS}^2 + 0.00084 \times \text{WFS}^3 - 3.79 \times \text{TS}^3 \tag{6-4}$$

$$\text{ALH (mm)} = 2.01 + 0.29 \times \text{WFS} - 6.82 \times \text{TS} - 0.08 \times \text{WFS} \times \text{TS} - 0.0089 \times \text{WFS}^2 + 5.67\,\text{TS}^2 \tag{6-5}$$

$$\text{HI (J/mm)} = 201.49 + 38.55 \times \text{WFS} - 578.23 \times \text{TS} - 24.26 \times \text{WFS} \times \text{TS} + 360.20 \times \text{TS}^2 \tag{6-6}$$

$$\text{P (mm)} = 0.04 + 0.17 \times \text{WFS} - 0.81 \times \text{TS} - 0.58 \times \text{WFS} \times \text{TS} + 0.018 \times \text{WFS}^2 + 3.74 \times \text{TS}^2 \tag{6-7}$$

$$\text{LoHS (mm)} = 0.32 + 0.64 \times \text{WFS} + 9.51 \times \text{TS} - 3.92 \times \text{WFS} \times \text{TS} + 0.17 \times \text{WFS}^2 + 17.21 \times \text{TS}^2 \tag{6-8}$$

Table 6-2 shows the statistical summary for the regression models with the values of the coefficients of determination (R^2), Adequate Precision and p-

values. The R^2 values indicate that the regression models can well represent the real data points. The Adequate Precision is a measure of the signal to noise ratio. The regression models have reasonable predictive ability as all the Adequate Precision values are above four. Finally the p-values are all less than 0.01% indicating that the models generated by the software are highly significant.

Table 6-2: Statistical summary for the regression models.

Statistic test	EWW	Wav	ALH	HI	P	LoHS
R^2	0.9786	0.8395	0.9434	0.9877	0.8895	0.9794
Adequate Precision	80.802	20.420	41.423	48.731	19.405	46.014
p-value	< 0.0001	< 0.0001	< 0.0001	< 0.0001	< 0.0001	< 0.0001

The influence of the process parameters on the geometry of the deposited wall is illustrated by the contour graphs in Figure 6-3. The red dots represent the design points used for the regression models. Figure 6-3 (a) indicates that higher WFS with lower TS result in wider deposited wall. This trend is understandable due to the higher volume of materials deposited per unit length. The relationship between the surface waviness and the deposition parameters shown in Figure 6-3 (b) suggests that WFS does not have a significant effect on the surface waviness while TS has a strong impact when it is below 0.4 m/min. There is an area with favourably low level of surface waviness when the TS value is higher than 0.4 m/min and WFS is smaller than 12 m/min. The surface waviness in this area stays below 0.3 mm which increases the efficiency of the deposited materials. Figure 6-3 (c) indicates that in general higher WFS with lower TS result in higher deposited layers. The average layer height is comparably stable in the area where TS is higher than 0.5 m/min, which varies from around 0.8 mm to around 1.5 mm.

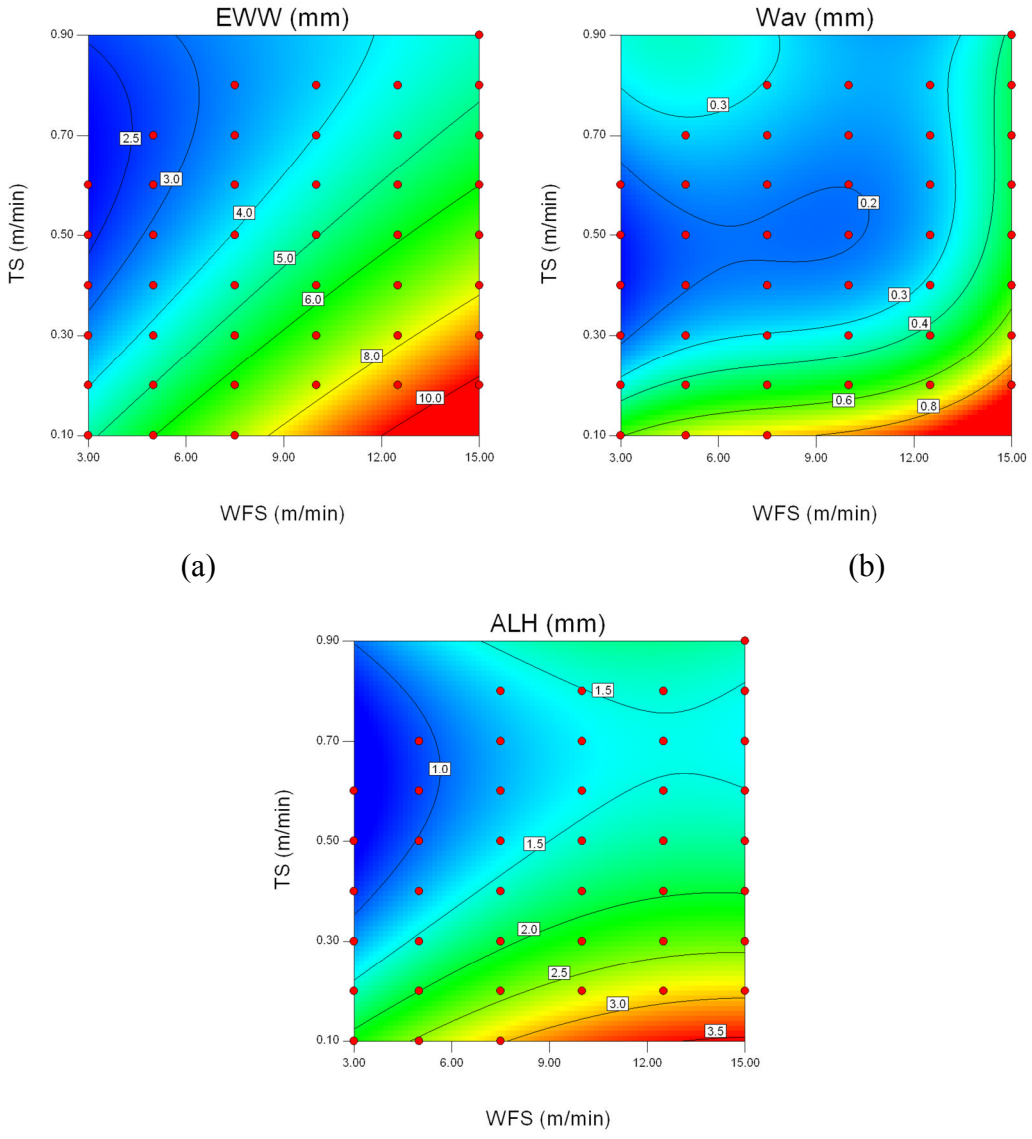

Figure 6-3: Plot of (a) EWW, (b) Waviness, and (c) ALH as functions of TS and WFS.

The relation between the deposition parameters and the stress distribution was investigated using the efficient engineering FE models. The thermo-mechanical approach utilised in this study has been demonstrated to provide accurate stress distributions. A total of 24 trials were analysed with the parameter combinations shown in Table 6-3. It should be noted herein that the WFS/TS ratio was selected as an independent factor instead of the travel speed to avoid erratic combinations of WFS and TS.

Table 6-3 Parameters used for the FE simulation trials.

Parameters	Values
Wire feed speed, WFS (m/min)	5.0, 6.0, 7.0, 8.0, 9.0, 10.0, 11.0, 12.0
Wire feed speed/travel speed, WFS/TS	10, 15, 20

The size of the base plate in each FE model was 250×60×6 mm, and the wall with 5 layers of material was modelled in the middle of the base plate. An efficient cooling time of 300 seconds between subsequent layers of material deposition was utilised in the models to cool the component down before the new layer of material was added. The cross section of the deposited wall was simplified in the FE model to be rectangular. The width of the wall was estimated with the value of EWW plus the value of Wav, and the height of the wall was decided by multiply the number of the layers to ALH. The material properties as well as the boundary conditions were set up as in model in section 4.2.2.

The Goldak double ellipsoidal heat source which was described in Equations 2-2 and 2-3 was used to apply the heat to the additive manufacture deposits. All the geometrical variables in this heat source model were linked with the regression functions that have been obtained from the experiments. The power density of the region in front of the arc centre and the region behind the arc centre was defined separately with a_f and a_r which are the length of the frontal ellipsoid and the rear ellipsoid, respectively. Although the value of these two parameters can be estimated from weld pool surface ripple markings (as shown in Figure 4-10 (b)), a simplification was made as these two parameters do not have significant influence on stress distribution. The value of a_f was set with the value of 0.25×LoHS, while the value of a_r was set equals to 0.75×LoHS; b is the width of the heat source which was set equal to the width of the wall; c is the depth of the heat source which was decided as the value of ALH+P; Q is the energy input rate which equals to HI×TS; f_f and f_r are the factors for distributing

the power to the front and rear of the heat source which are set to 0.5 and 1.5 respectively.

All the parameters for building the FE model have been linked to the WFS and TS with the process models. To simplify the implementation process, a script has been developed for Abaqus to develop the FE models and subroutines. Similar stress distribution patterns were generated from all the trials. Figure 6-4 shows the distribution of the longitudinal stress at the mid length section of the trial with WFS/TS ratio of 10 and WFS of 5 m/min. Nearly uniform tensile stress was generated along the deposited wall due to material expansion and then contraction during solidification, which caused compressive residual stress in the base plate far away from the heating line.

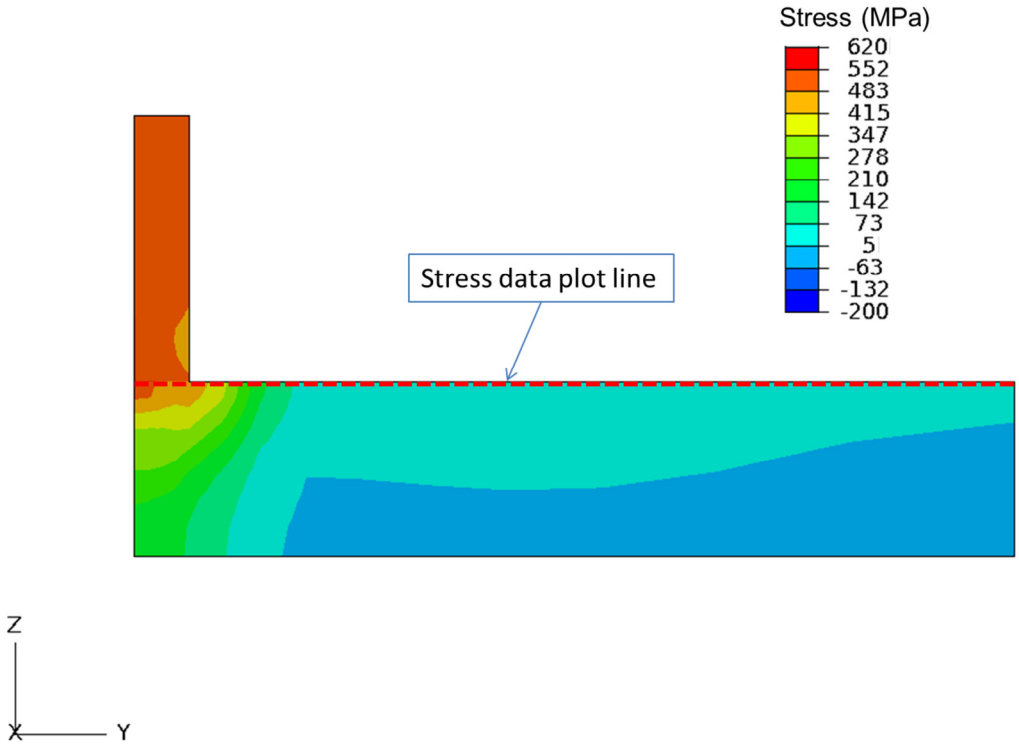

Figure 6-4: Longitudinal stress prediction from the trial with WFS/TS ratio of 10 and WFS of 5 m/min.

Detailed stress data were taken from the base plate in the mid-length section of each sample which is shown as the red dash line in Figure 6-4. As the longitudinal stress dominates over the transverse and normal stresses for the

long wall structure, the comparison of the stresses from different trials was performed only in the longitudinal direction. Figure 6-5 shows the stress comparison from the trials with the three different WFS/TS ratios and with WFS of 6 m/min, 9 m/min and 12 m/min. The same level of maximum longitudinal stresses with the magnitude of around 480 MPa can be observed at the interface area. The trials with WFS/TS ratio of 10 result in much narrower stress zone comparing to the trials with WFS/TS ratio of 20. Considering the same WFS/TS ratio, the stress zones generated by the trials with lower WFS values are slightly narrower than the ones with higher WFS values. However, the influence of this factor is not as significant as the WFS/TS ratio.

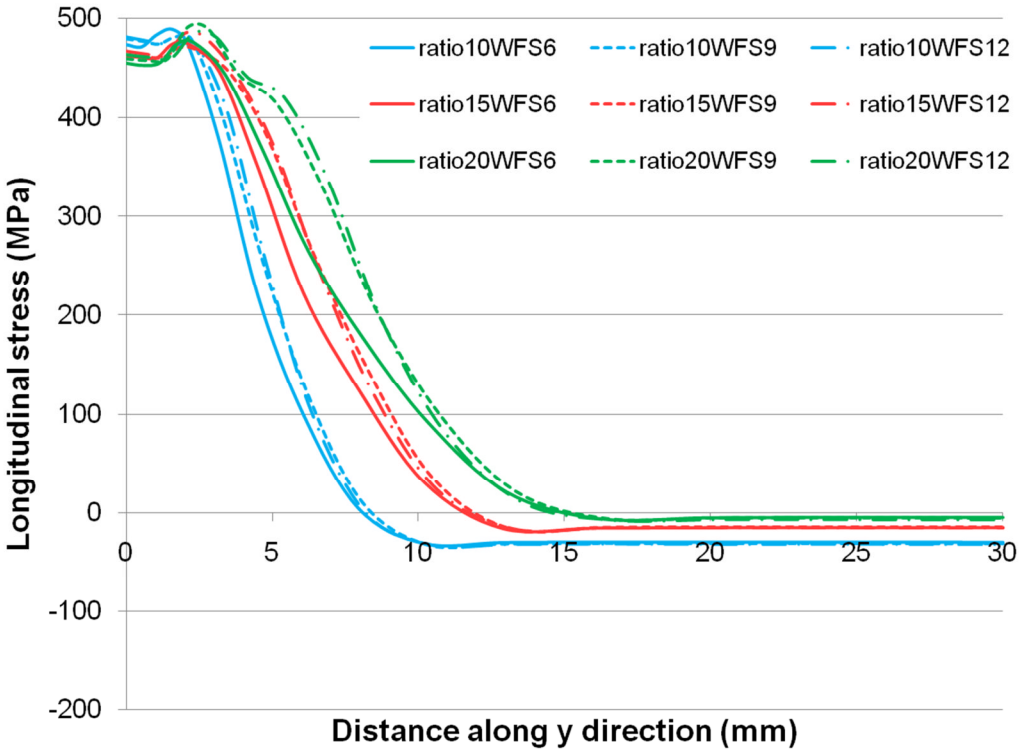

Figure 6-5: Longitudinal stresses with different process parameters.

In the CMT process, the heat input is correlated to the WFS/TS ratio (shown in Figure 6-6). The higher setting of WFS/TS ratio causes higher HI level. In consequence, it results in a wider area of high temperature where the thermal strain exceeds the yield strength during the thermal cycle, which causes a wider stress zone.

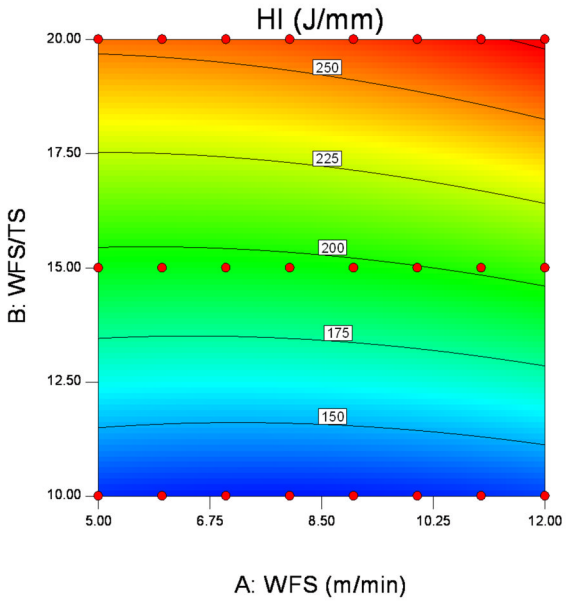

Figure 6-6: Heat input distribution plot.

Figure 6-7 shows the longitudinal stress distribution after the clamps were removed. A significant drop in the longitudinal stress can be seen after unclamping from all the cases. The trials with high WFS/TS ratio show much higher amount of the stress drop than the ones with low WFS/TS ratio. The possible reason for this is that the trials with higher WFS/TS ratio generate higher restrain stresses during the heating and cooling cycles on the clamping areas to balance the tensile stresses. Therefore, the impact of the clamps is higher for the trials with higher WFS/TS ratio which constantly causes a higher level of stress decrease after the clamps are removed.

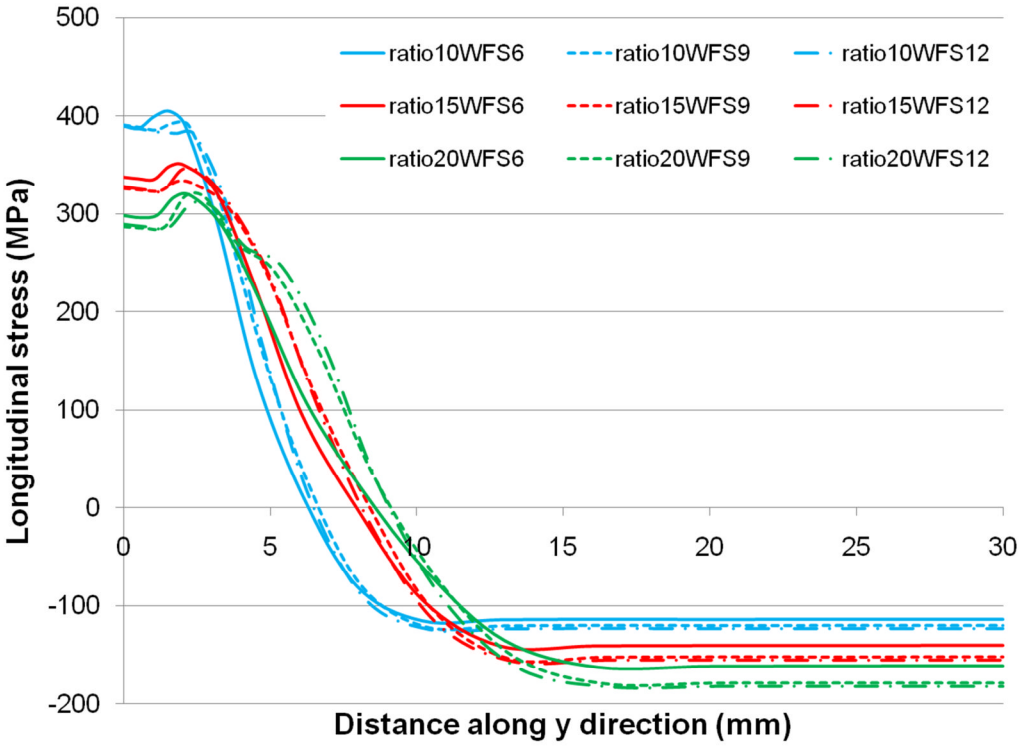

Figure 6-7: Longitudinal stresses with different process parameters after the clamps were removed.

6.3 Study of residual temperature

The preheating effect by the deposition process was studied using the engineering FE models. The size of the base plate is 500×60×12 mm. The average height of the deposited wall is 2 mm, and the width of the wall is 5 mm. Instead of cooling down the component, a 5 seconds interpass time was set in the model. The parameters for the materials (mild steel), boundary constraint conditions, as well as the heat source model were used the same to the model described in section 4.2.2.

Figure 6-8 shows the temperature distribution around the heat source when the welding torch travelled on the 1st, 2nd, 4th, 6th, and 8th layer. The melting pool is represented with grey colour where the temperature exceeds 1500 °C. The shape of the melting pool on the first four layers changed a lot due to the effect of the cooling bar under the base plate. However, this effect becomes small and the melting pool is nearly steady after the 4th layer.

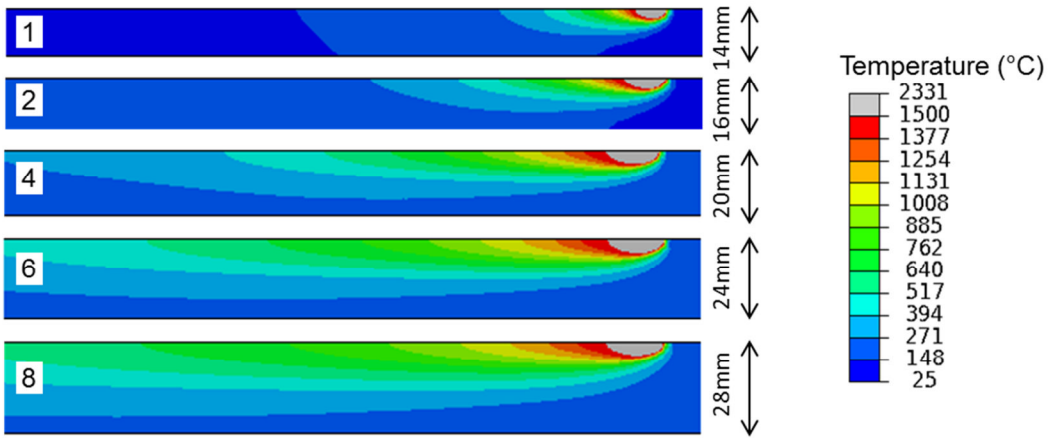

Figure 6-8: Temperature distribution of the trials with 1, 2, 4, 6, 8 layers of deposited materials.

The cooling time of 5 seconds is not enough for the component to cool down before the subsequent layer of material is being applied. Figure 6-9 shows the residual temperature from the midpoints after the deposition of each layer. One can see that the remaining temperatures from the preceding passes are nearly increased linearly after the 4th layer. The residual temperature increased more rapidly for the first four layers because of the impact of the cooling plate.

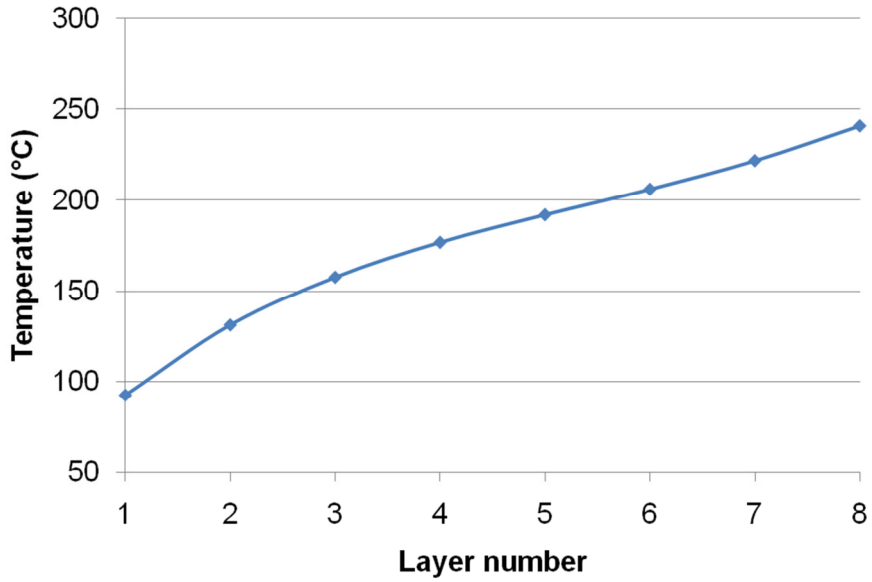

Figure 6-9: Residual temperature for the midpoints after the deposition of each layer.

The model of interpass time of 5 seconds has been compared with the model of interpass of 400 seconds to estimate the preheating effect of the residual temperature. Figure 6-10 shows the comparison of the stresses on the trials with 4 layer deposited walls. One can see that the stresses level on the trials with 5 seconds interpass time is lower than the one with 400 seconds interpass time on the base plate in longitudinal direction and transverse direction. The stress on the longitudinal direction is the dominant stress in both models. The comparison of the longitudinal stress on the z direction shown in Figure 6-10 (b) indicates that the preheating effect of the 5 seconds interpass time result in lower longitudinal stress in the base plate as well as the deposited wall. The significant difference of the stress magnitude in the interface area is because the material used in the base is softer than the weld metal.

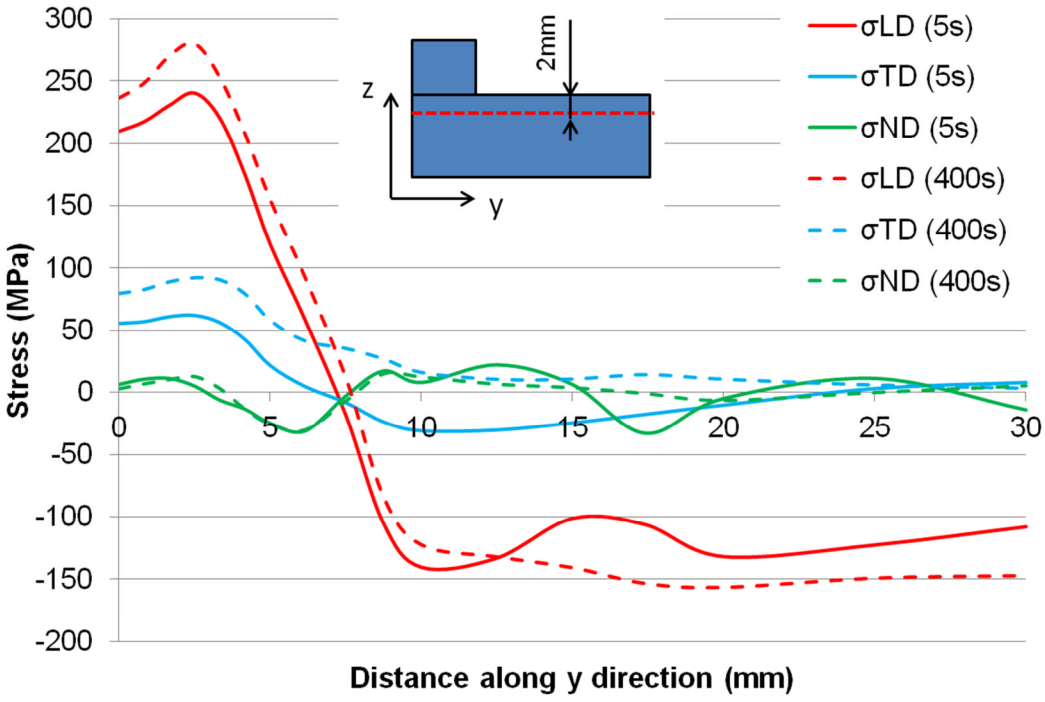

(a)

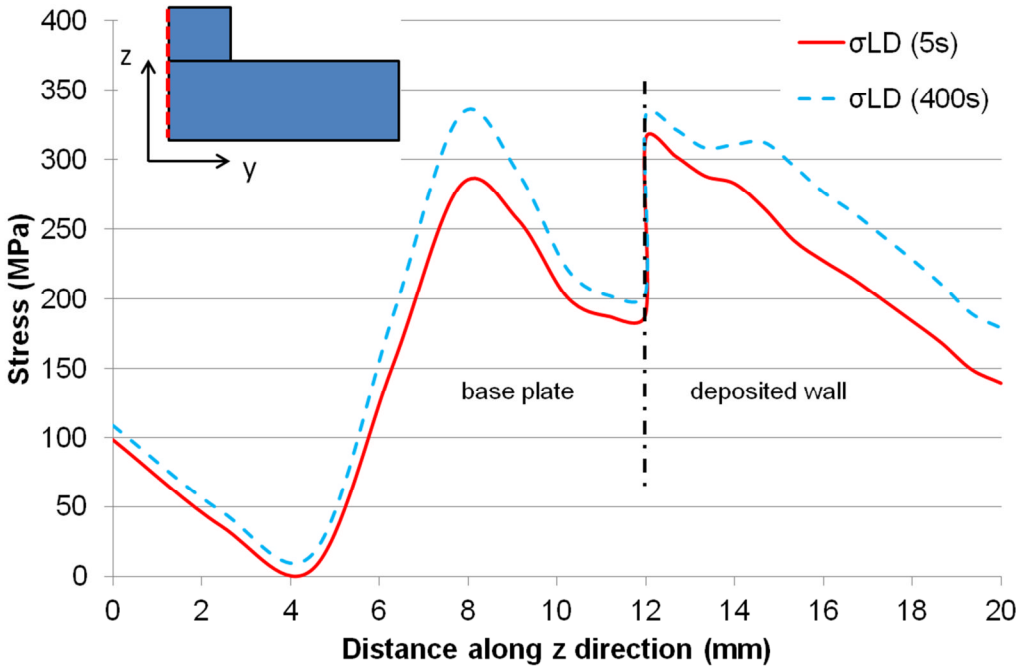

(b)

Figure 6-10: Stress comparison of the trials with 5 seconds of interpass time and 400 interpass time along: (a) y direction, and (b) z direction

Due to the preheat effect in the WAAM process, the deposition process with short interpass time results in less residual stresses. The results would seem to favour short interpass time because of lower residual stress level, distortion and higher production yield. However, in practice the residual temperature needs to be limited to a certain level, otherwise the residual temperature may cause problems like loss of dimension tolerances and poor surface finish.

6.4 Study of the crossing structure

One of the typical structures in the WAAM process is the crossing structure. A number of different build strategies have been investigated by Panos Kazanas (Kazanas, et al., 2012) in the RUAM project with different patterns (Figure 6-11). The difficulties of producing wall crossing using wire based ALM are associated with the build-up of peaks where the weld beads overlap at the crossing points.

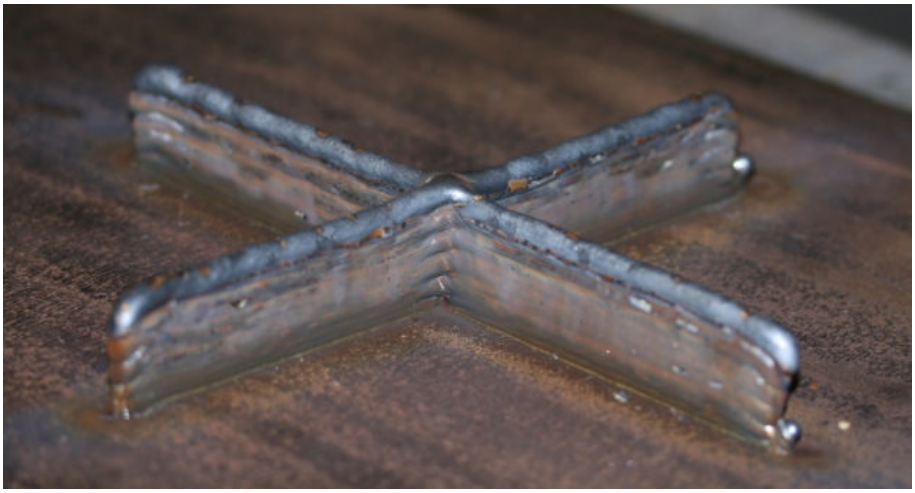

Figure 6-11: Example of crossing feature manufactured using pattern of opposite angles.

Two of the patterns have been proved to be able to achieve good quality. As shown in Figure 6-12 the first pattern adds materials in a direct crossing way, while the second one adds materials in an opposite angle way. The start and stop positions of each pass need to be swapped for both building patterns to achieve good ending quality.

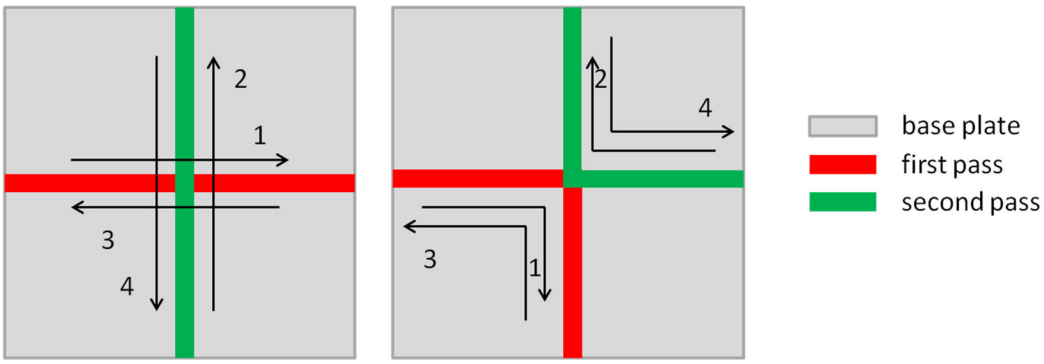

Figure 6-12: Deposition patterns of cross feature

FE models were built to investigate the stress distribution of the crossing structure during the deposition process. This study has been performed on the two patterns mentioned above. Transient thermal-mechanical approach was utilised to analyse the difference of the stress generation between the two patterns during the deposition process. The size of the base plate in the model is 100 X 100 X12 mm. The width of the crossing wall is 5 mm, and the layer

height is 2mm. Two layers for each pattern has been modelled with 5 second of interpass time between each pass in the model. The clamps were modelled on the four corners of the base plate.

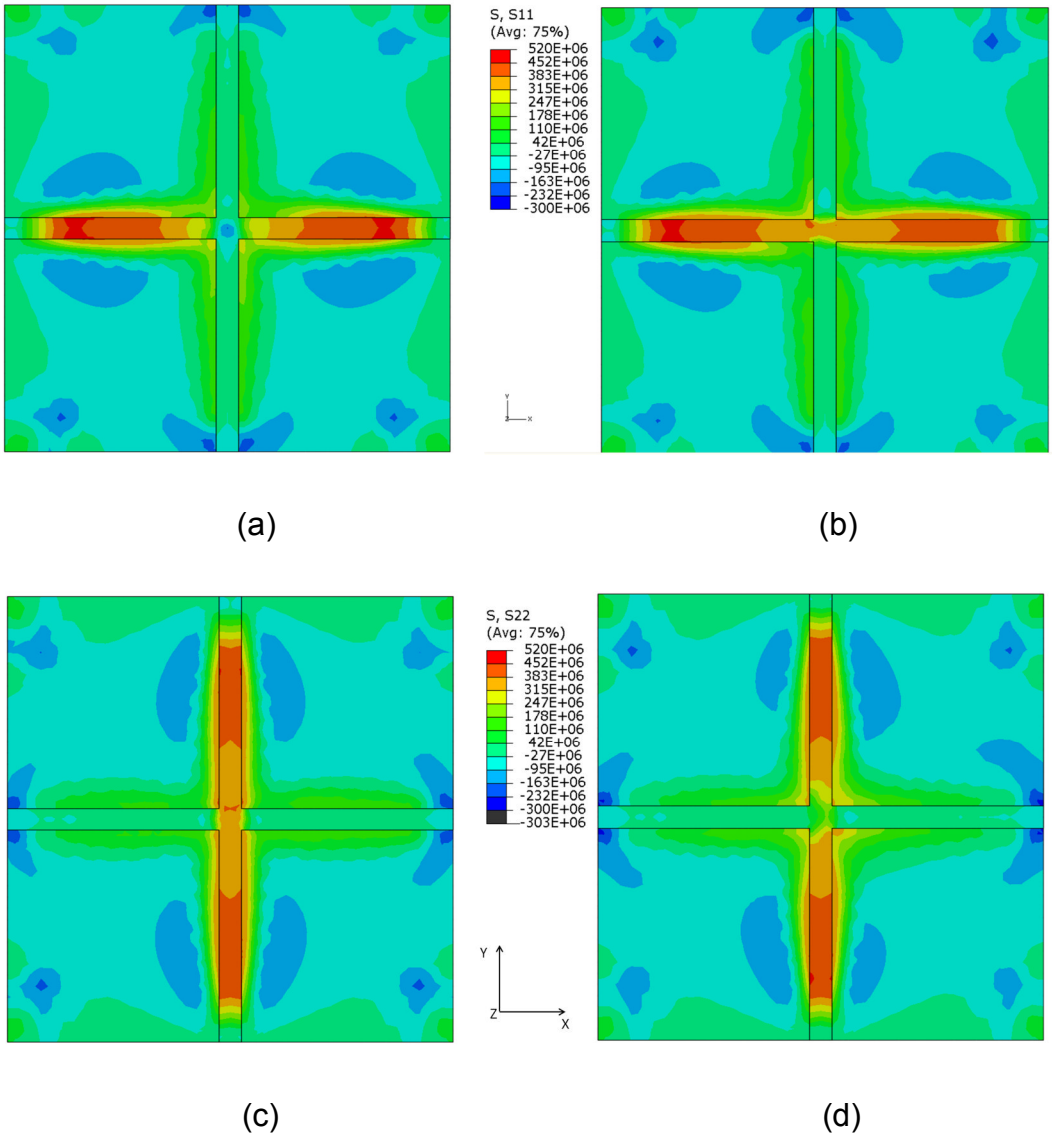

Figure 6-13: Stress distribution on cross structure: (a) stress along x direction of building pattern 1; (b) stress along x direction of building pattern 2; (c) stress along y direction of building pattern 1; (d) stress along y direction of building pattern 2.

As shown in Figure 6-13, the results from different building strategies gave very similar stress distributions. High level tensile stresses are generated along the walls on their deposition directions. Note that in both cases the stress level in

the middle area of the deposited cross is much lower than the rest of the deposited wall. The possible reason is that the crossing structure increased the stiffness of the component which reduced the stress level. Balanced compressive stresses are distributed in the surrounding areas of the deposited wall. Symmetric compressive stresses are developed in the component that built with building pattern 1, while dissymmetric compressive stresses are distributed in the component using building pattern 2. However, the difference of the residual stresses that generated by these two patterns is very small, which cannot be used to decide which pattern is better.

6.5 Deposition Sequences Study

One of the main target structures for the RUAM project is the large frame structure which can be used in the airplane manufacturing industries. The traditional way of making this kind of parts is by machining which wastes a huge amount of material. The design of the frame is also constrained by the capability of the machining process. The RUAM process plans to build this kind of structure with a totally different process. Instead of machining away materials, the RUAM process is using WAAM process for adding materials substrates. Only a small amount of material needs to be machined out to the final shape. It also gives the designer more flexibility for better structures.

The influence of the deposition sequence on the distortions distribution is not clear. To answer this question, a stiffened panel structure was studied with the efficient engineering FE model. As shown in Figure 6-14, the base plate with the dimensions of 500 mm x 300 mm x 4 mm was clamped at six positions which are indicated by the blue squares. The stiffened panel structure consisted of six straight walls. All of these walls used identical layer dimensions of 5 mm wide and 2 mm high. Ten different build sequences were considered in this study, which are described in Figure 6-14. The deposition process was performed on all these six walls before the next layer of deposition started. Each wall consisted of three layers, and a cooling time of 20 seconds was used after the deposition of each layer.

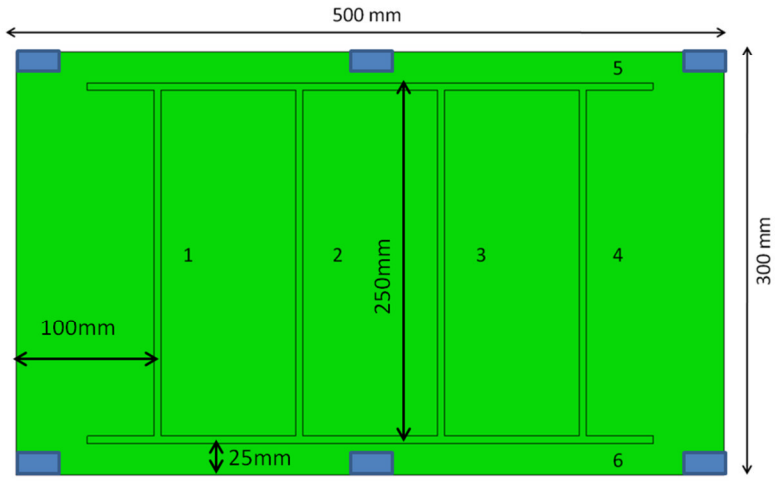

Name	Sequence
Case 1	1-2-3-4-5-6
Case 2	1-4-2-3-5-6
Case 3	2-3-1-4-5-6
Case 4	1-3-2-4-5-6
Case 5	2-3-5-6-1-4
Case 6	1-4-5-6-2-3
Case 7	5-6-1-2-3-4
Case 8	5-6-1-4-2-3
Case 9	5-6-1-3-2-4
Case 10	5-6-2-3-1-4

Figure 6-14: FE models for the building sequence study of the frame structure.

As this stiffened panel component was rather large and the deposited walls were located far apart, the heat from the deposition of one wall had little effect on the other walls. The whole component cooled rapidly to room temperature within the waiting time. Therefore, several simplifications were made in the thermal analysis. The thermal cycles of the six walls during the deposition of each layer were treated separately using a steady-state thermal model of a multi-layer wall structure with the same wall width and height. The residual temperature after the deposition of each pass was ignored. Equivalent temperature loads were extracted from this thermal model and used sequentially for each layer on the all the deposited walls for the plastic zones. The clamping system was modelled by constraining the movements of the nodes which represent the clamps during the deposition process. The backing plate below the base plate was not considered in the mechanical model to reduce the computational complexity involved with contact interactions.

The models from all the ten cases produced a similar distortion pattern. Figure 6-15 shows the out-of-plane distortion from the model of Case 1 as an example. There is nearly no distortion in the middle area. The largest distortions are generated at the four corners of the base plate. A comparison of the maximum distortions of all the ten models is illustrated in Figure 6-16. The average value

of the nodal distortion on the z direction is also calculated and presented in Figure 6-16 as the mean distortion for each model.

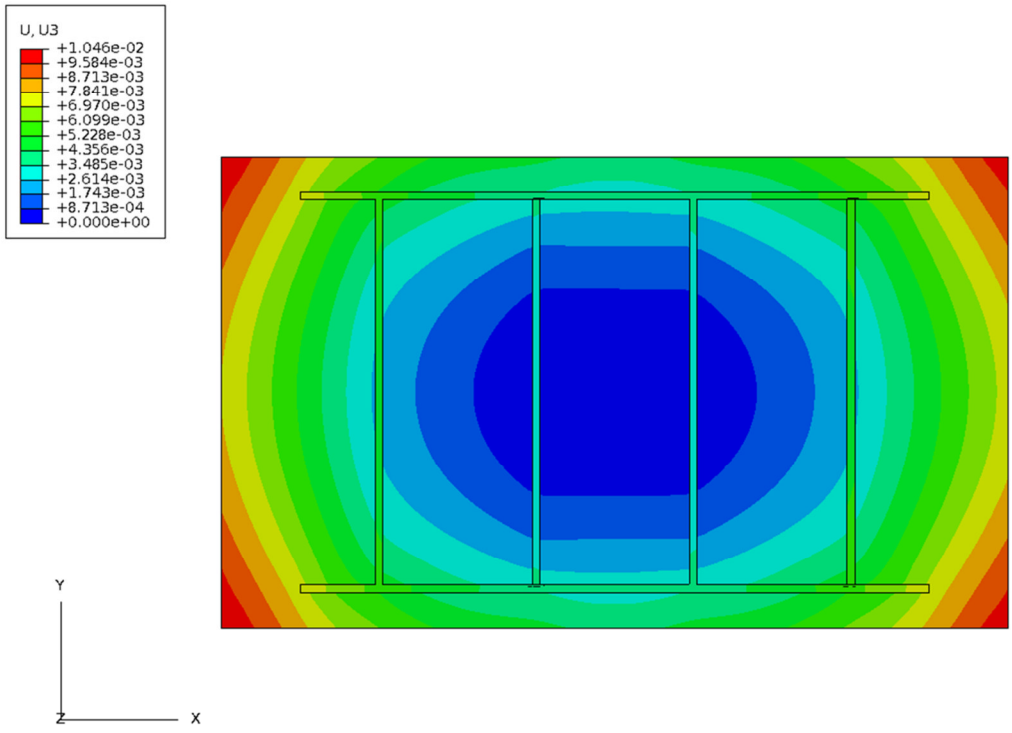

Figure 6-15: Predicted distortion distributions.

A significant difference on the distortion level can be observed between the different build sequences. In general, depositing the long walls first tends to give a lower level of distortion. The model of Case 8 gave the lowest distortion and was approximately 30% lower than Case 3, where the inner short walls were produced before the long walls. A possible reason is that the component built up with the sequence of Case 8 produced a part that had a higher stiffness during the deposition process.

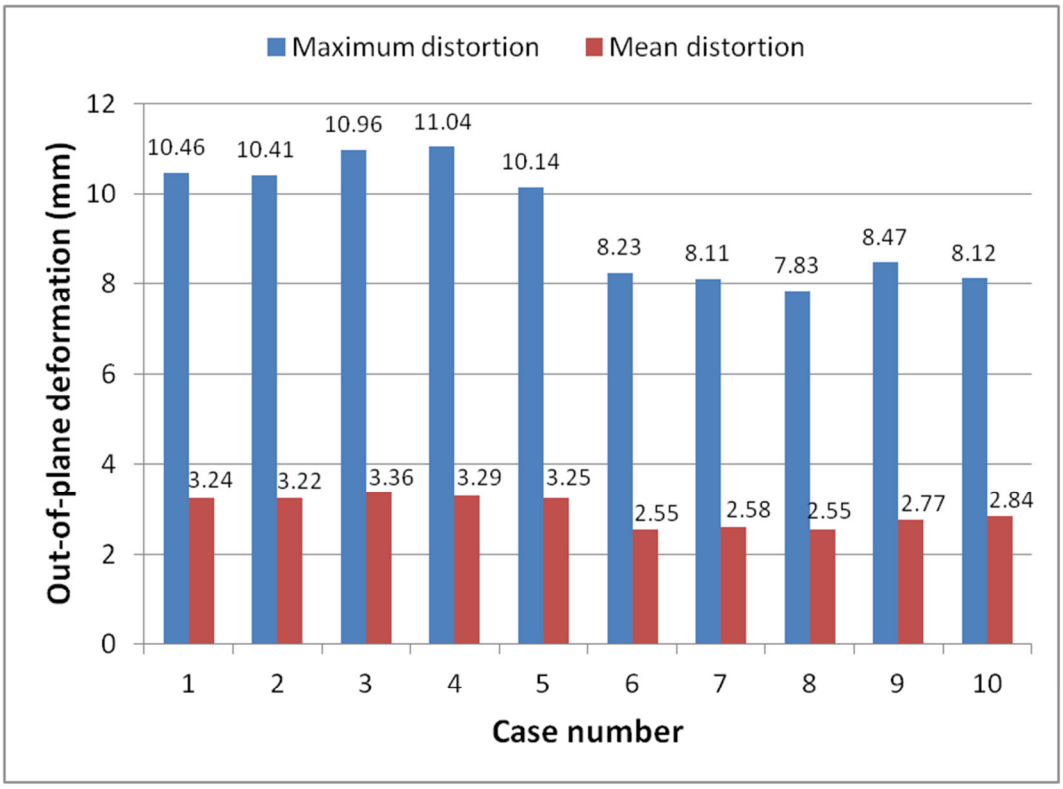

Figure 6-16: Maximum and mean out-of-plane distortion.

Experiments were conducted using the deposition sequences of Case 3 and Case 8. The experimental setup is shown in Figure 6-17. It is similar to the experimental set up for the verification experiment of the thermo-mechanical model of the 500 mm wall. Thus detailed information about the experiment can be seen in section 4.2.1 of this thesis.

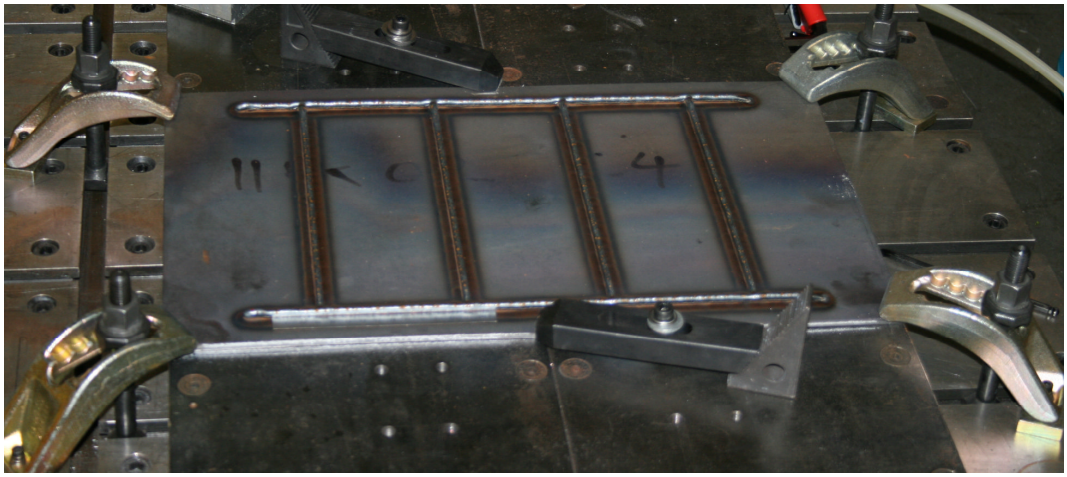

Figure 6-17: Experiment set up for the frame part.

To quantify the distortion of each sample, measurements were taken using Romer Omega-arm and an R-Scan laser scanning head. The samples were placed on a flat table and the upper surface of the trial samples were taken using this scanning device. The points representing the top surface of the base plate were extracted from the scanned point cloud for each sample which was fitted to a rectangular grid of 10 mm x 10mm elements. The out-of-plane displacements of these elements were averaged to provide the mean distortion.

The distortion predictions from the FE models were also fitted to the same grid. Figure 6-18 shows the comparison between the predicted out-of-plane distortions and the measured results. The overall predictions match the measurements. However, the distortions of the clamping areas were overestimated with the FE model. This can be explained by the simplified clamping system used in the model which did not use a backing bar. Table 6-4 provided further validation of the FE model. As stated previously, a significant drop in the distortion was achieved by using the build sequence of Case 8.

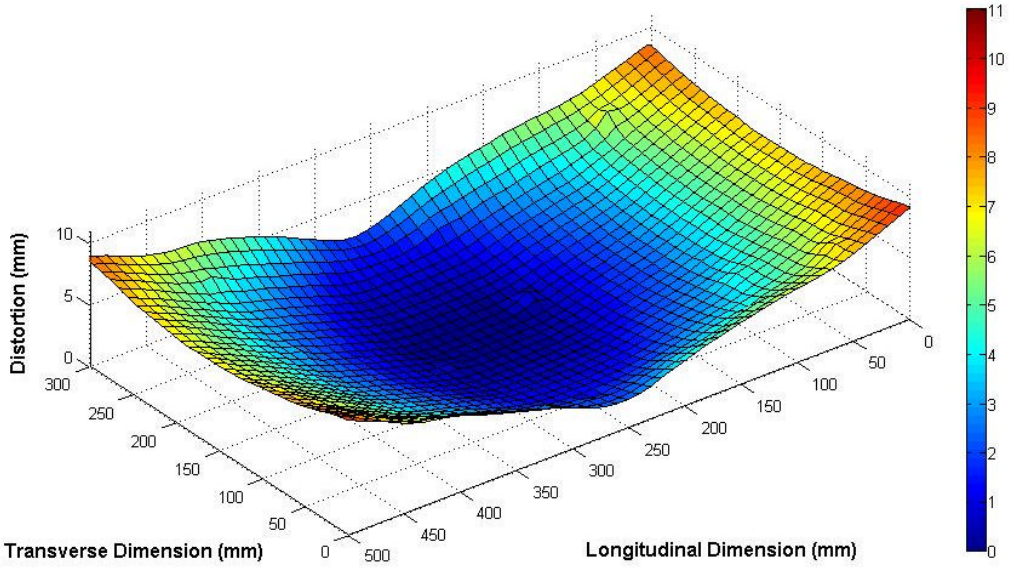

(a)

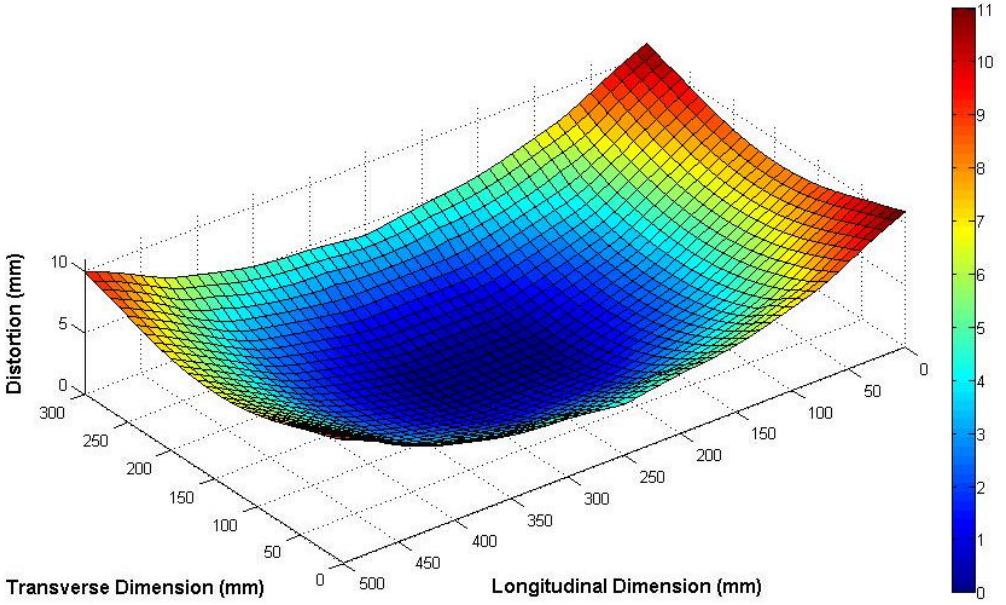
Distortion (mm)
10
5
0
300
250
200
150
100
50
0
Transverse Dimension (mm)
0
50
100
150
200
250
300
350
400
450
500
Longitudinal Dimension (mm)
11
10
9
8
7
6
5
4
3
2
1
0

(b)

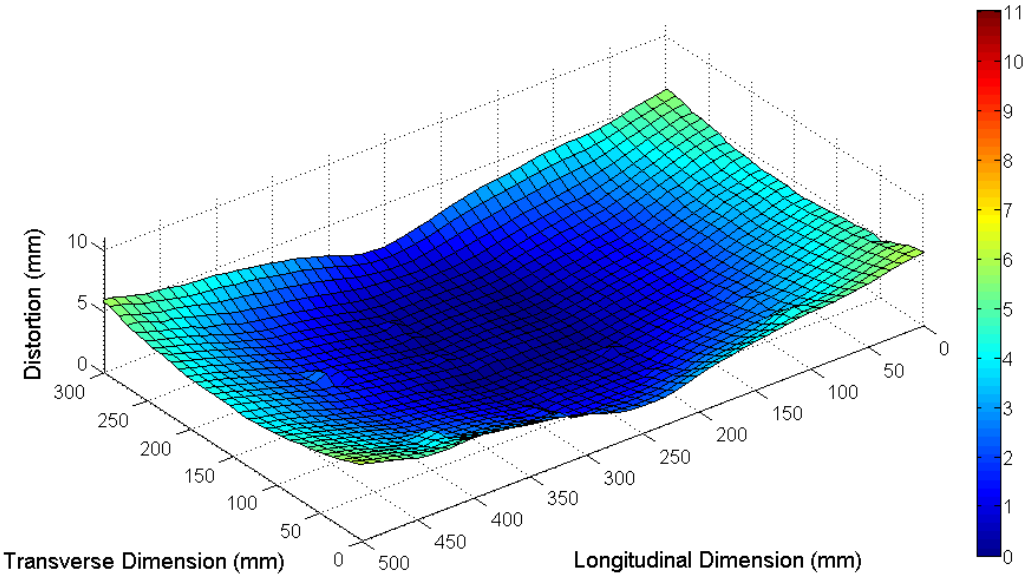
Distortion (mm)
10
5
0
300
250
200
150
100
50
0
Transverse Dimension (mm)
0
50
100
150
200
250
300
350
400
450
500
Longitudinal Dimension (mm)
11
10
9
8
7
6
5
4
3
2
1
0

(c)

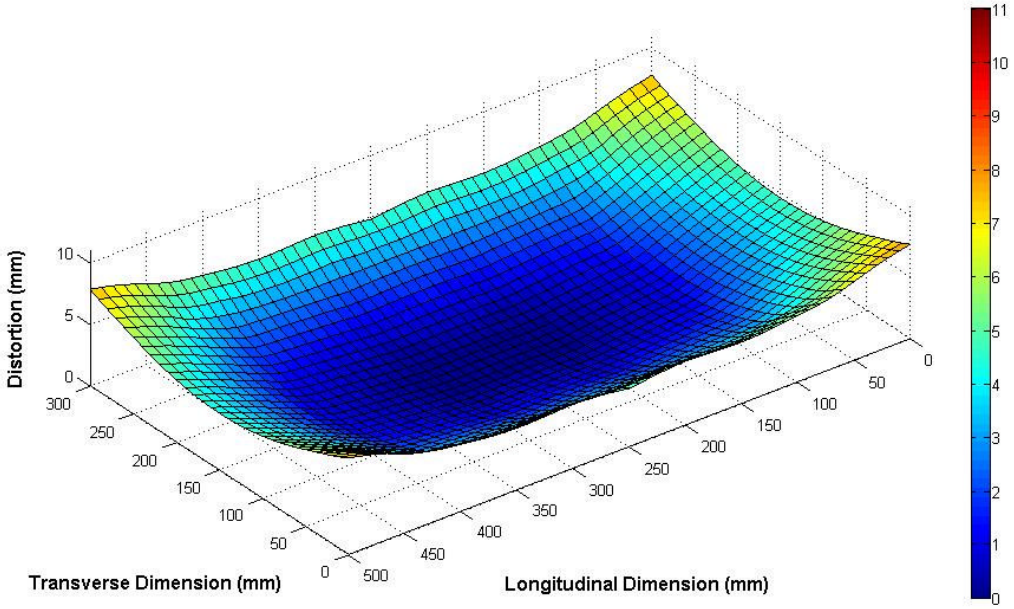

(d)

Figure 6-18: Plot of out-of-plane distortion from: (a) the experimental measurement of Case 3; (b) the FE prediction of Case 3; (c) the experimental measurement of Case 8; (d) the FE prediction of Case 8.

Table 6-4: Comparison between the mean out-of-plane distortion for the model and the experiments.

	Measured mean distortion (mm)		**Predicted mean distortion (mm)**
	Measurements	**Average**	
Case 3	3.47, 3.51, 3.38	3.45	3.36
Case 8	2.24, 2.95, 2.60	2.59	2.55

6.6 Balanced building

In the RUAM project, a balanced building strategy has been developed which adds material on both sides of the base plate. It has been proved with

experiments that the out-of-plane deformation can be greatly reduced using this method. Figure 6-19 shows a Ti6Al4V frame structure manufactured with the balanced building strategy. The walls with frame features were built on one side of the base plate first and then the base plate was turned over for depositing the same structures on the other side. As can be seen from Figure 6-19, nearly no out-of-plane distortion can be observed on the final component.

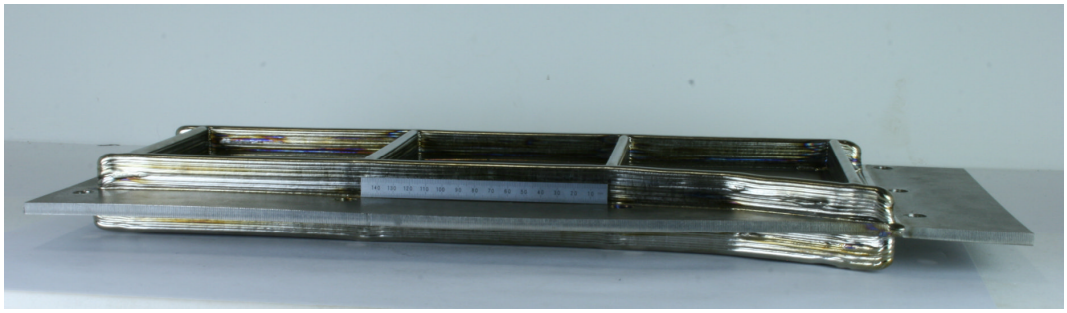

Figure 6-19: Frame structure manufactured with the balanced building strategy.

The thermo-mechanical performance of a double sided wall structure has been studied to help understand the mechanism behind the balanced building strategy. The engineering FE models were utilised for this study. Two 5 layered walls are modelled on the both side of a base plate with the dimension of 250 mm x 60 mm x 6 mm. The weld beads are 5 mm in width and 2 mm in height. The clamping system is set on the long edge of the base plate which constrains the movement of the component during the deposition process. Two different deposition plans are used in this study. In the first plan five layers of material are deposited on one side of the base plate and then another five layers of materials are added on the other side of the base plate. In the second plan, the deposition passes are added to the different sides of the base plate in turn. The deposition parameters were set the same to the study introduced in section 4.2.2. The interpass time was set to 500 seconds.

Figure 6-20 shows the stress distribution after the completion of the deposition. An extra model with five layer materials built on the single side of the base plate is also provided to have a comparison with the models with the balanced building strategy. It can be observed from Figure 6-20 (b) and (c) that tensile

stresses are generated along the deposited walls on both sides of the base plate. The maximum magnitude of the longitudinal stress is at the similar level to the stress generated on the deposited wall of the single sided wall structure. The tensile stress on the deposited wall of plan 1 is slightly lower than the one generated by plan 2. The potential reason is that the residual temperature before depositing a new layer of material is higher for plan 1 than for plan 2, which causes a more significant 'pre-heat' effect.

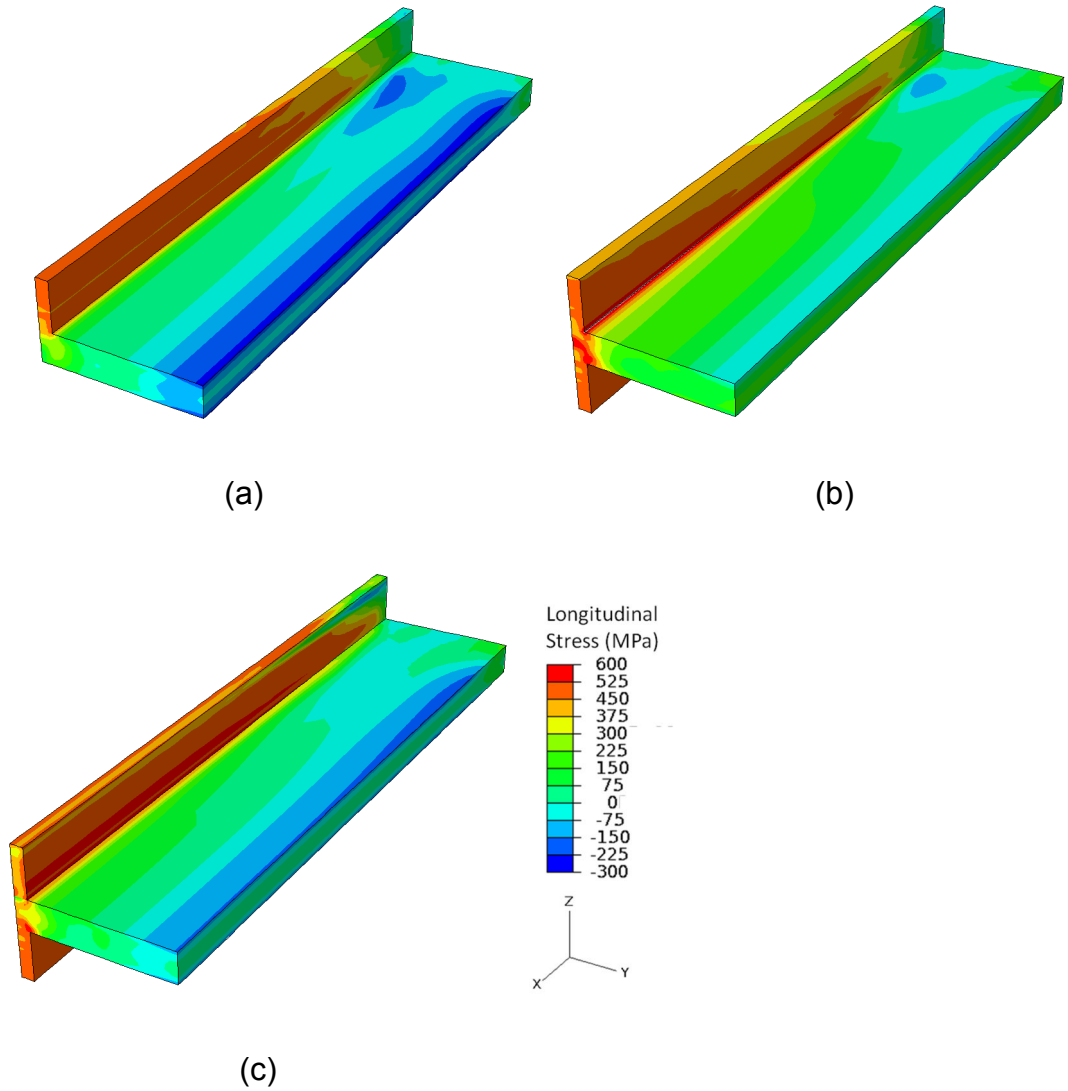

Figure 6-20: Stress distribution of: (a) single sided wall structure, (b) double sided wall structure built with deposition plan 1, and (c) double sided wall structure built with deposition plan 2 (view cut has been applied on the mid-length of the models).

Figure 6-21 shows the distortions after the clamps are removed. One can see that the single-sided wall structure generated significant out-of-plane distortions. In contrast, the distortions generated by both of the double-sided wall structures are negligible. Balanced stresses can be generated by building from both sides of the base plate, thus very little distortion generated.

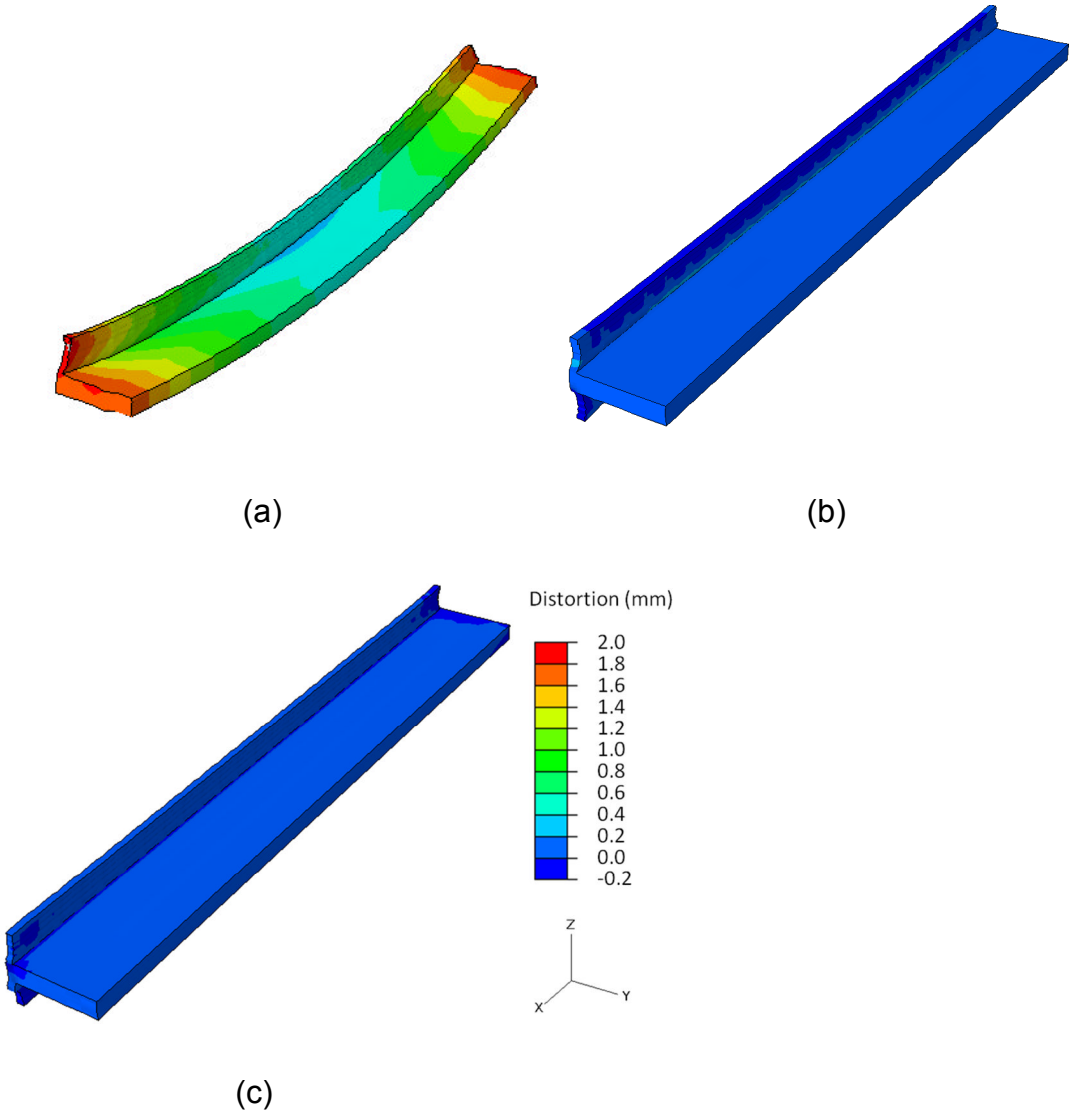

(a) (b)

(c)

Figure 6-21: Distortion after clamps are removed: (a) single sided wall structure, (b) double sided wall structure built with deposition plan 1, and (c) double sided wall structure built with deposition plan 2 (deformation scale factor: 10).

6.7 Summary

In this chapter, process studies have been performed on several aspects of the WAAM process. The following findings can be summarised:

- The efficient engineering FE model can be applied as a useful tool for the process studies which efficient thermo-mechanical predictions.

- The process parameter settings do not have significant effect on maximum longitudinal stresses. However, the models with higher WFS/TS values tend to generate a wider area of longitudinal residual stress in the clamped base plates than the trials with lower WFS/TS ratio. The trials with high WFS/TS ratio result in a more significant stress decrease than the ones with low WFS/TS ratio after the clamps were removed.

- Shorter interpass cooling time results in higher remaining temperature, which has a preheat effect on the materials of the subsequence passes. A lower level of residual stresses can be achieved consequently.

- The two different deposition patterns that were studied for the crossing structure gave similar stress distributions. One of the interesting finding is that the stress level in the conjunction area of the crossing wall is much lower than it on the rest of the deposited wall.

- The building sequence can have a significant effect on the distortion level of WAAM components. The case study on the stiffened panel WAAM structure shows the potential benefit of optimising the build sequence using FE models for minimising final distortion.

- A balanced building strategy can significantly reduce the component distortion. However, the residual stress remained the same as for the single sided building structures.

[Page left intentionally blank]

7 ROBOT PROGRAM GENERATION

7.1 Introduction

Chapter 6 discussed the procedural influence of the WAAM process. It has been proved that the FE models especially the efficient engineering FE model can be used to provide useful thermo-mechanical information for the WAAM process study, therefore make building recommendations to control the residual stresses and distortions. In the real-world WAAM process these recommendations can be achieved through robot programs. However, it is very tedious and time-consuming to use the robot teach pedant or the off-line programming software to generate the robot path for complicated WAAM parts. Thus, an automatic robot path generation tool is needed to efficiently convert the designed CAD model and the integrated building rules into a robot programme.

Different CAD guided tool path planning and generation systems have been developed for the AM process. Tool path generation can be accomplished by “mirroring” milling paths generated from CAM module in commercial CAD/CAM software (Ericsson et al. 2005). Many researchers have built their own tools which are more flexible for their AM processes (Hatrmann, et al., 1994; Hensinger, et al., 2000; Kim, et al., 2004; Riberiro, 1995). Slicing and path planning are the two major steps for these tools.

This chapter sets out the initial robot program generation tool the author developed for the RUAM project. It generates the ready-to-use robot programme directly from CAD models of the designed parts. This robot interface first generates sliced contours from the CAD model of the designed component, and then generates the robot programme with the points on these sliced iso-lines. The possibility for integrating the optimised building strategy has been considered in this tool. The robot programme can be tested in the Fanuc robot off-line programming software Roboguide© to make sure the path is correctly generated and there is no collision during the movement.

This robot path generation tool greatly increased the efficiency of robot programming work. Figure 7-1 shows the WAAM components that were fabricated with the help of this programme.

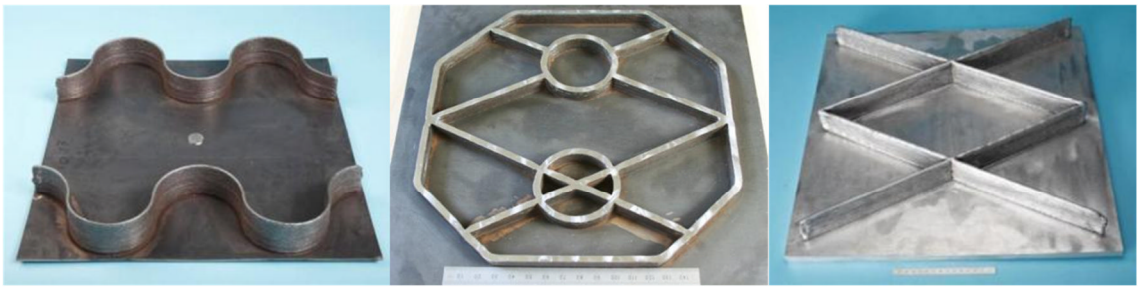

(a)

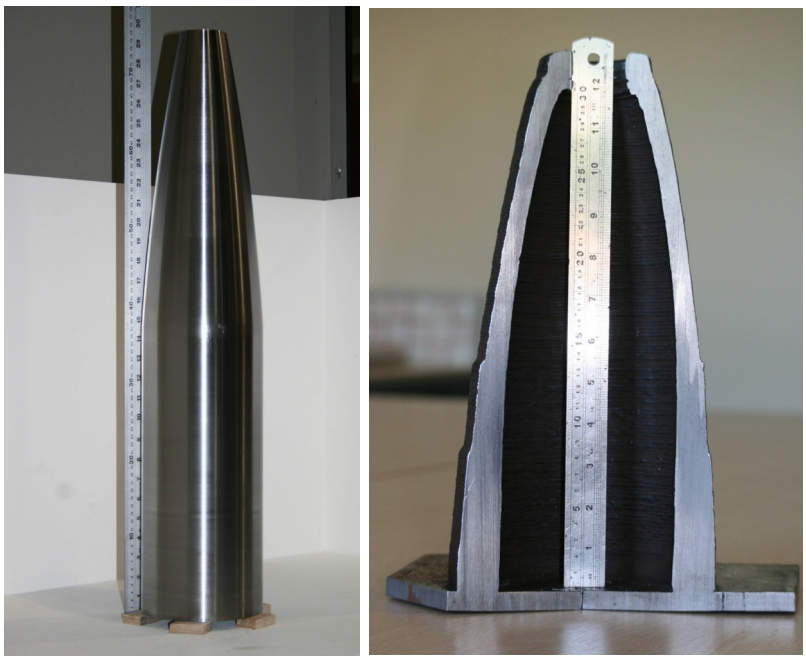

(b)

Figure 7-1: WAAM components: (a) wall shaped components; (b) 3D component with changed thickness.

7.2 WAAM process from CAD model to real component

For the RUAM project, a robot path generation prototype for the FANUC robot – RUAMROB- has been developed in Matlab. Figure 7-2 shows the general process of building a WAAM component from a CAD model. In the first step, the

CAD model in STL format needs to be input to RUAMROB program. RUAMROB first slices the CAD model into isoline paths, and then generates the robot programme in ASCII format. Some key parameters for the welding process can be easily set by the users from the graphic interface of RUAMROB, including welding process parameters such as travel speed of the welding torch, waiting time between layers, building sequence for the part with several sub-parts, etc. The output robot program can be simulated and checked using the Fanuc robot off-line software ROBOGUIDE©. The ASCII code can also be translated into binary format in ROBOGUIDE© which can be executed by the robot. After uploading the binary code into the robot control, the robot can fabricate the WAAM component automatically without supervision.

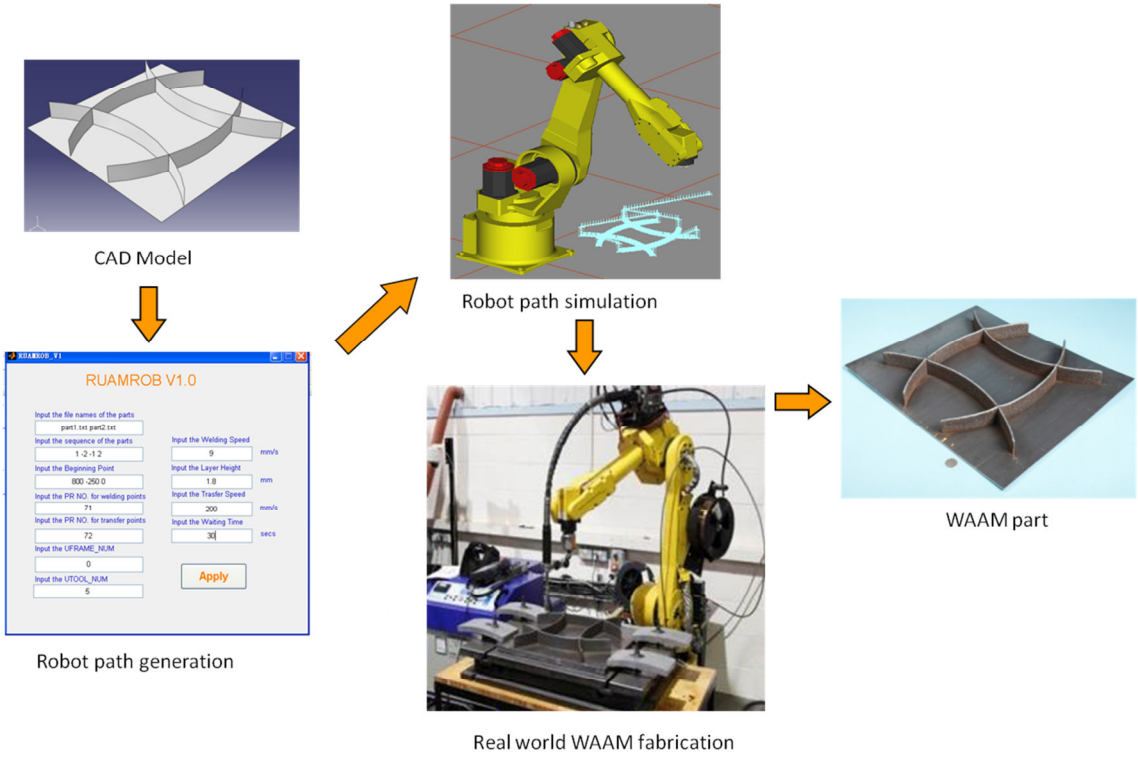

Figure 7-2: WAAM process chart

7.2.1 RUAMROB programme

The RUAMROB programme consists of two main modules – a slicing module and a robot program generation module. The function of the slicing module is to generate isolines from the CAD. Depending on the shape of WAAM parts, two

different robot path generating strategies have been developed. The first one is built to deal with the extruded wall shaped components which follow the same paths for different layers (as shown in Figure 7-2 (a)). In practice, the wall shaped part is one of the main classes that the WAAM process aims to fabricate. For building this kind of part, one sub-program has been developed based on an offsetting strategy which picks up the nodes on the bottom boundary of the CAD file then copies these nodes with a defined offset distance. As no slicing process is involved, the robot path programme can be generated efficiently.

The second strategy is based on a slicing process which can deal with 3D parts (as shown in Figure 7-2 (b)). Figure 7-3 shows two examples of sliced 3D WAAM components. Figure 7-3 (a) is a geometry which is combined from a cylinder and a pyramid. The slicing process for this geometry is comparatively easy as the triangular meshes of the STL file are nicely distributed. Figure 7-3 (b) is a geometry using a transition free surface between the circle on the top and ellipse on the bottom. More process time is needed as the quality of some of the triangular meshes in this geometry is poor. However, the RUAMROB programme successfully generate the slices. As this strategy generates isolines for each deposition layer it needs more processing time than the strategy for the wall shaped component, and the generated robot programme is also much longer.

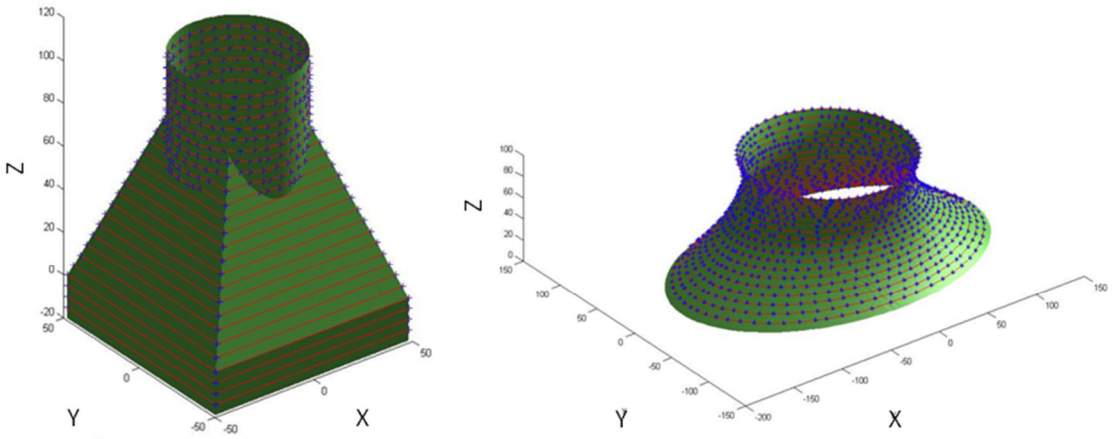

(a) (b)

Figure 7-3: Sliced 3D WAAM parts: (a) geometry with simple shape combination; (b) geometry with free surface.

The robot program generation module sequentially picks the points from the sliced isolines and generates a Fanuc robot program in ASCII format. In the first step all the points of intersection from the sliced isolines are picked out in a sequence which is defined by identifying these points from the adjacent triangular in the STL files. Then an algorithm is utilised that can remove duplicate points which usually appear when CAD models with poor triangulation quality are sliced. In addition, the resolution of the points on the path can be changed by setting up the tolerance value. In this way a compromise can be made for different applications between the accuracy and the length of the robot code which is important for building large complex parts.

The welding parameters, such as travel speed of the welding torch, deposition layer height, and interpass waiting time need to be integrated into the robot code. To simplify the parameter setting, a user-friendly graphic interface has been developed for the RUAMROB programme as shown in Figure 7-4. This preliminary interface also takes the building sequences into consideration. Complex geometries need to be split into smaller sub-parts and uploaded through the interface of RUAMROB as separate part files. However, the

identification of sub-parts is performed manually at the current stage. The building sequence can be set by putting the sub-part numbers in a designed order. The symbol of '-' in front of the part number is used to identify the process of reverse building.

Figure 7-4: RUAMROB user interface

7.2.2 Binary code generation and robot path simulation

The output robot code in ASCII format from RUAMROB programme cannot be recognised directly by the robot controller. The FANUC robot off-line programming package Roboguide was applied to translate the ASCII code into the robot pedant code which can be executed by the robot controller. In addition, the generated robot path can be simulated and checked in Roboguide. Potential collisions and programme errors can be detected in this virtual environment which can save a lot of time on the programme checking in the practical work.

7.3 Robot path limitations

Not all shapes can be created with WAAM due to the limitations of the process. There are several aspects that need to be considered when designing the robot path:

- In the practice of the WAAM process, the deposited surface is not smooth in the areas where the arc starts and stops. To ensure the best surface quality of the component a path design should be made before the fabrication to minimise the arc start and stop time.

- Although using this robot programme generation tool components with rather complex geometries can be fabricated, the complexity is suggested to be reduced in the design stage to reduce the work on the sub-parts identifications. Features with short welds need to be avoided to get good surface quality.

- A proper interpass cooling time need to be considered to make sure the component is not over heated. Problems like loss of dimension tolerances and poor surface finish can occur if the component gets too hot. A multiple component building strategy can be used to avoid this kind of problem while keep high production speed. As shown in Figure 7-5, a set of WAAM components are produced at the same time. The robot path was designed to complete the deposition process for all these four components before it moved to a new layer. In this way the materials of the first component already cool down before the new material is added.

Figure 7-5: Example of building multiple components.

7.4 Summary

In this chapter a robot program generating programme prototype RUAMROB is introduced. By using this tool it just needs a couple minutes to generate the robot path from the CAD model, which greatly improved the efficiency and flexibility of the robot programme generation process. The deposition parameters as well as the building sequence can be easily set up through the graphic interface of RUAMROB, which shows the possibility of the applying the optimal building strategies from the FE process studies in the real work WAAM process.

8 CONCLUSIONS

This thesis has shown that the computational modelling can be used as a useful and effective tool for investigate the thermo-mechanical performance of the WAAM process. With the efficient FE models the thermally induced residual stresses and distortions of large scale WAAM process can be predicted in a short time. Furthermore, the influence of the process parameters and the building strategies can be examined systematically using the FE approaches, whereas in real world test it is difficult to obtain idealised conditions. This chapter summarises the main findings and observations of the research presented in this thesis.

8.1 Conclusions of the research

Development of the transient thermo-mechanical model and validation

- The thermal model with moving heat source can provide accurate predictions on transient temperature distributions which have been proved by comparing the simulated temperature history with experimental data from thermal couples. The mechanical model which uses the thermal histories as the input load can provide accurate predictions on distortions and residual stresses. The distortion results have been verified with the measurements using the laser scanning facility, and the simulated residual stress of the S355 wall match well with the measurements from the neutron diffraction strain scanner ENGIN-X.

- The material is only locally heated when the heat source passes. The heat from the welding process causes a tensile residual stress along the weld bead due to material contraction during solidification, which causes a balancing compressive residual stress in the base plate. The stress evolution analysed using the numerical model shows that stress across the deposit is very uniform with very little influence of the preceding layers on the following layers. A significant stress redistribution is observed after unclamping. The stress at the top of the deposited wall

has a much lower value than at the interface due to the bending distortion of the sample.

- During the deposition process, stresses are mainly generated in a narrow area in the deposited material and in the base plate around the heating line. The peak temperature that the material experienced in the thermal cycle of the WAAM process decides whether or not the residual stress can be generated.

Efficient FE approaches for large scale WAAM process

- A steady-state thermal model has been generated which can provide similar accurate temperature predictions as the transient thermal model. About 99% computational time that is needed by the transient model can be saved by using the steady-state thermal model.

- This static temperature result from the steady-state thermal model can be transferred as thermal histories and then be utilised in the same way to a mechanical model as the transient mechanical analysis. Accurate predictions on residual stresses and distortions can be achieved using this approach.

- A more efficient mechanical had been generated based on the relation between the plastic stress generation and the peak temperatures. Equivalent temperature loads are applied to the material of this zone, while the materials outside the plastic effective zone keep the room temperature. In this way nearly 98% reduction on the computational time can be achieved compare to the transient mechanical model. The accuracy of this simplified mechanical model has been verified by comparing the residual stresses and distortions results with the simulated results from the transient model as well as the experimental data.

Process study of the WAAM process

- It has been found that the different parameter settings on wire feed speed and travel speed result in similar level of maximum longitudinal stresses. However, the models with higher WFS/TS values generated wider area of longitudinal residual stress in the clamped base plates than the trails with lower WFS/TS ratio. The trials with high WFS/TS ratio result in higher amount of the stress decrease than the ones with low WFS/TS ratio after the clamps were removed.

- The process with shorter interpass cooling time can result in a reduction on residual stresses.

- For the crossing structure, deposition patterns do not have a significant effect on the stress distributions. The stress level in the intersection area is much lower than it on the rest of the deposited wall.

- The distortion level can be minimised by using optimised building sequence. The optimal building sequence can be found with the help of the efficient engineering FE models.

- Using balanced building strategy, stresses with similar level will generate on both sides of the base plate which can significantly reduce the distortion of the WAAM component.

Robot programme generation of WAAM

- An initial robot code generating prototype RUAMROB has been developed to improve the efficiency of the robot programme generation process. The building recommendations from the process studies can be integrated in to the robot code through RUAMROB easily.

8.2 Future work

The research that introduced in this thesis can be further extended into many research directions as follows:

- **Microstructure prediction and phase transformation model integration:** For the materials which the microstructure has a significant effect on the mechanical performance, it is important to predict the microstructure of the materials during the deposition process and integrate the phase transformation model into the FE mechanical model in order to get accurate residual stress and distortion. This can be done in the FE models through developing a subroutine in the FE software which describes the interactions among temperature, microstructure and its corresponding mechanical properties. The integration of the phase transformation model into the FE models will provide the accurate thermo-mechanical predictions to a wider range of materials.

- **Hybrid FE model for wider range of WAAM structures:** The efficient FE approaches overcome the application bottleneck of the huge computational time required for the transient model. However, the application of steady-state based approach is currently only utilised to large scale and straight wall based structures. The constrains and limitations of this approach need to be investigated in the future. On the contrast, the transient model has the advantage of analysing small scale and complicated structures. Therefore, a hybrid FE model can be considered in the future that can combine the advantages of steady-state based approaches and the transient model to enable the thermo-mechanical prediction for a wider range of WAAM structures.

- **Residual stress and distortion mitigation process:** The current research in this thesis did not consider the mitigation methods of residual stress and distortion using additional facilities. However, there are a number of mitigation processes that can be used in the WAAM process, such as rolling, prebending, thermal tensioning, mechanical

tensioning, etc. FE models can be developed on the efficient FE approaches that proposed in this thesis to help generating better methods for minimising the residual stresses and distortions of the WAAM process.

- **Development of an automatic WAAM building planner:** In the current research stage complicated WAAM structures need to be divided manually into many simple walls and the building sequence is decided based on the experience and results from experimental or FE trials. An automated CAD-guided building planner need to be developed in the future research which can automatically divide the complicated geometries into multiple and easy-to-handle sub-structures. Advanced optimisation techniques and algorithms need to be developed for this planner which uses the optimal building strategies based on the knowledge gained from the research of the RUAM team. The efficient FE models that introduced in this thesis can be integrated in the building planner to provide thermo-mechanical information for deciding the best building strategy.

[Page left intentionally blank]

REFERENCES

Abaqus User's Manual. (2010), HKS Co. USA.

Alberg, H. and Berglund, D. (2003), Comparison of plastic, viscoplastic, and creep models when modelling welding and stress relief heat treatment, *Computer Methods in Applied Mechanics and Engineering,* vol. 192, no. 49-50, pp. 5189-5208.

Alimardani, M., Toyserkani, E. and Huissoon, J. P. (2007), A 3D dynamic numerical approach for temperature and thermal stress distributions in multilayer laser solid freeform fabrication process, *Optics and Lasers in Engineering,* vol. 45, no. 12, pp. 1115-1130.

Almeida, P (2012), Process control and development in wire and arc additive manufacturing. PhD Thesis, Cranfield University. U. K.

Altenkirch, J., Steuwer, A., Peel, M. J., Richards, D. G. & Withers, P. J. (2008), The effect of tensioning and sectioning on residual stresses in aluminium AA7449 friction stir welds. *Materials Science and Engineering A*, vol. 488, pp. 16-24.

Altenkirch, J., Steuwer, A., Withers, P. J., Williams, S. W., Poad, M. & Wen, S. W. (2009), Residual stress engineering in friction stir welds by roller tensioning. *Science and Technology of Welding and Joining*, vol. 14, pp.185-192.

Baker, R. (1925), Method of Making Decorative Articles, US Patent 1,533,300, filed Nov. 12 1920, patented 14th April 1925.

Baufeld, B., Biest, O., Gault, R. (2010), Additive manufacturing of Ti-6Al-4V components by shaped metal deposition: Microstructure and mechanical properties.

Baufeld, B., Brandl, E., Biest, O. (2011), Wire based additive layer manufacturing: Comparison of microstructure and mechanical properties of Ti–6Al–4V components fabricated by laser-beam deposition and shaped metal

deposition. *Journal of Materials Processing Technology,* vol. 211, no. 6 pp. 1146-1158.

Benzley, S., Perry, E., Merkley, K., Clark, B. and and Sjaardema, G. (1995), A Comparison of All-Hexahedral and All-Tetrahedral Finite Element Meshes for Elastic and Elasto-Plastic Analysis, October 1995, pp. 179.

Berglund, D., Alberg, H. and Runnemalm, H. (2003), Simulation of welding and stress relief heat treatment of an aero engine component, *Finite Elements in Analysis and Design,* vol. 39, no. 9, pp. 865-881.

Bouchard, P. J. (2009), The NeT bead-on-plate benchmark for weld residual stress simulation, *International Journal of Pressure Vessels and Piping,* vol. 86, no. 1, pp. 31-42.

Boyer, R., Welsch, G. and Collings, E. W. (1994), *Materials properties handbook : titanium alloys,* .

Brice, C.A., Rosenberger, B. T., Sankaran, S. N., Taminger, K. M. (2009), Chemistry control in electron beam deposited titanium alloys, *Materials Science Forum*, Gold Coast, QLD. pp. 155-158.

Brust, F. W., and Kim, D. S. (2005), Mitigating welding residual stress and distortion, in: Z. Feng (Eds.), *Processes and mechanisms of welding residual stress and distortion*, Woodhead.

Camilleri, D., Comlekci, T., Grey, T. G. F. (2004), Computatinoal prediction of out-of-plane welding distortion and experimental investigation, *The Journal of Strain Analysis for Engineering Design*, vol. 40, no. 2, pp. 161-176.

Camilleri, D. and Gray, T. G. F. (2005), Computationally efficient welding distortion simulation techniques, *Modelling and Simulation in Materials Science and Engineering,* vol. 13, no. 8.

Camilleri, D., Mollicone, P., Gray, T. G. F. (2007), Computational methods and experimental validation of welding distortion models, *Proceedings of the*

Institution of Mechanical Engineers, Part L: Journal of Materials: Design and Applications, vol. 221, pp. 235-249.

Cao, W. and Miyamoto, Y. (2006), Freeform fabrication of aluminium parts by direct deposition of molten aluminium, *Journal of Materials Processing Technology,* vol. 173, no. 2, pp. 209-212.

Casalino, G. and Ludovico, A. D. (2008), Finite element simulation of high speed pulse welding of high specific strength metal alloys, *Journal of Materials Processing Technology,* vol. 197, no. 1-3, pp. 301-305.

Charles, C. (2008), Modelling microstructure evolution of weld deposited Ti-6Al-4V, PhD Thesis, Luleå University of Technology.

Cheng, W. (2005), In-plane shrinkage strains and their effects on welding distortion in thin-wall structures, PhD Thesis, Ohio State University, U. S.

Chen, X. L., Yang, Z., Kim, D. S. (2005), Modeling distortion and residual stress during welding: practical applications, in: Z. Feng (Eds.), *Processes and mechanisms of welding residual stress and distortion*, Woodhead.

Chin, R. K., Beuth, J. L. and Amon, C. H. (2001), Successive Deposition of Metals in Solid Freeform Fabrication Processes, Part 1: Thermomechanical Models of Layers and Droplet Columns, *Journal of Manufacturing Science and Engineering,* vol. 123, no. 4, pp. 623-631.

Chin, R. K., Beuth, J. L. and Amon, C. H. (2001), Successive Deposition of Metals in Solid Freeform Fabrication Processes, Part 2: Thermomechanical Models of Adjacent Droplets, *Journal of Manufacturing Science and Engineering,* vol. 123, no. 4, pp. 632-638.

Chin, R. K., Beuth, J. L. and Amon, C. H. (1996), Thermomechanical modeling of molten metal droplet solidification applied to layered manufacturing, *Mechanics of Materials,* vol. 24, no. 4, pp. 257-271.

Chiumenti, M., Cervera, M., Salmi, A., Saracibar, C., Dialami, N., Matsui, K. (2010), Finite element modeling of multi-pass welding and shaped metal deposition processes, *Computer Methods in Applied Mechanics and Engineering,* vol. 199, no. 37-40, pp. 2343-2359.

Choi, J. and Chang, Y. (2005), Characteristics of laser aided direct metal/material deposition process for tool steel, *International Journal of Machine Tools and Manufacture,* vol. 45, no. 4-5, pp. 597-607.

Colegrove, P., Ikeagu, C., Thistlethwaite, A., Williams, S., Nagy, T., Suder, W., Steuwer, A., Pirling, T. (2009), Welding Process Impact on Residual Stress and Distortion, *Science and Technology of Welding and Joining*, vol.14, pp. 717-725.

Costa, L., Vilar, R., Reti, T., Deus, A. M. (2005), Rapid tooling by laser powder deposition: Process simulation using finite element analysis, *Acta Materialia,* vol. 53, pp. 3987-3999.

Cozzolino, L., Coules, H., Colegrove, P., Wen, S. (2011), Modelling distortion reduction on pre-and post-weld rolled gas metal arc welded plates, *Proceeding of International Workshop on Thermal Forming and Welding Distortion,* Bremen, Germany, pp. 169-179.

Das, S. (2003), Physical Aspects of Process Control in Selective Laser Sintering of Metals, *Advanced Engineering Materials*, vol. 5, no. 10, pp. 701-711.

Dann, J. A., Daymond, M. R., Edwards, L., James, J. A., Santisteban, J. (2004), A comparison between Engin and Engin-X, a new diffractometer optimized for stress measurement, *Physica B,* vol. 350, pp. 511-514.

Deng, D. and Murakawa, H. (2008), Prediction of welding distortion and residual stress in a thin plate butt-welded joint, *Computational Materials Science,* vol. 43, no. 2, pp. 353-365.

Deng, D. (2009), FEM prediction of welding residual stress and distortion in carbon steel considering phase transformation effects, *Materials and Design*, vol. 30, pp. 359-366.

Deng, D. and Murakawa, H. (2006), Numerical simulation of temperature field and residual stress in multi-pass welds in stainless steel pipe and comparison with experimental measurements, *Computational Materials Science,* vol. 37, no. 3, pp. 269-277.

Deng, D., Murakawa, H. and Liang, W. (2008), Prediction of welding distortion in a curved plate structure by means of elastic finite element method, *Journal of Materials Processing Technology,* vol. 203, no. 1-3, pp. 252-266.

Deng, D., Murakawa, H. and Liang, W. (2007), Numerical simulation of welding distortion in large structures, *Computer Methods in Applied Mechanics and Engineering,* vol. 196, no. 45-48, pp. 4613-4627.

Deo, M. V., Michaleris, P., Sun, J. (2003), Prediction of buckling distortion of welded structures, *Science and Technology of Welding and Joining,* vol. 8, no. 1, pp. 55-61.

Domack, M.S., Taminger, K.M.B., Begley, M. (2006), Metallurgical mechanisms controlling mechanical properties of aluminum alloy 2219 produced by electron beam freeform fabrication, *Materials Science Forum*, Vancouver, pp. 1291-1296.

Dong, P. (2005), Residual stresses and distortions in welded structures: a perspective for engineering applications, *Science and Technology of Welding and Joining,* vol. 10, no. 4, pp. 389-398.

Elcoate, C., Bouchard, P., Smith, M. (2003), 3-Dimensional Repair Weld Simulation – Based on Plate Comparison, *ABAQUS World User's Conference*, Munich.

Ficquet, X., Smith, D. J., Truman, C. E., Kingston, E. J. and Dennis, R. J. (2009), Measurement and prediction of residual stress in a bead-on-plate weld benchmark specimen, *International Journal of Pressure Vessels and Piping,* vol. 86, no. 1, pp. 20-30.

Gilles, P., El-Ahmar, W. and Jullien, J. (2009), Robustness analyses of numerical simulation of fusion welding NeT-TG1 application: Single weld-bead-on-plate, *International Journal of Pressure Vessels and Piping,* vol. 86, no. 1, pp. 3-12.

Goldak, J., Chakravarti, A., Bibby, M. (1984), New Finite Element Model for Welding Heat Sources*, Metallurgical and Material Transactions B-process Metallurgy and Materials Processing Science,* vol. 15B , pp. 299-305.

Goldak, J. and Akhlaghi, M. (2005), Computational Welding Mechanics, New York, Springer.

Grey, D., Long, H., Maropoulos, P. (2005), Effects of welding speed, energy input and heat source distribution on temperature variations in butt joint welding, *Journal of Material Processing Technology,* vol. 167, no. 2-3, pp. 393-401.

Gu, M. and Goldak, J. A. (1994), Steady-state formulation for stress and distortion of welds, *Journal of Engineering for Industry*, vol. 116, pp. 467-474.

Gu, S., Murakawa, H., Okumoto, Y., Ishiyama, M. (1997), Simulation of out-of-plane deformation in butt welding of large size steel plate, *Mathematical Modelling of Weld Phenomena 3*, pp. 689-712.

Guyot, F. (1947), A note on the shrinkage and distortion of welded joints, *The Welding Journal – Welding Research Supplement,* vol. 16, no. 7, pp. 29-39.

Hamide, M., Massoni, E. and Mughal, M. P. (2008), Adaptive mesh technique for thermal-metallurgical numerical simulation of arc welding processes, *International Journal for Numerical Methods in Engineering,* vol. 73, no. 5, pp. 624-641.

Hartmann, K., Krishnan, R., Merz, R., Neplotnik, G., Prinz, F.B., Schultz, L., Terk, M. and Weiss, L.E., (1994), Robot-assisted shape deposition manufacturing, *Proceedings of IEEE International Conference on Robotics and Automation*, San Diego, USA.

Hensinger, D.M., Ames, A.L. and Kuhlmann, J.L., (2000), Motion planning for a direct metal deposition rapid prototyping system, *Proceedings of IEEE International Conference on Robotics and Automation,* San Francisco, USA.

Heralic, A., Christiansson, A., Ottosson, M. and Lennartson, B. (2010), Increased stability in laser metal wire deposition through feedback from optical measurements, *Optics and Lasers in Engineering,* vol. 48, no. 4, pp. 478-485.

Hu, D., Mei, H., Kovacevic, R. (2002), Improving solid freeform fabrication by laser-based additive manufacturing. *Proceedings of the Institution of Mechanical Engineers, Part B: Journal of Engineering Manufacturing,* vol. 216, no. 9, pp. 1253-1264.

Hu, D. and Kovacevic, R. (2003), Modelling and measuring the thermal behaviour of the molten pool in closed-loop controlled laser-based additive manufacturing, *Proceedings of the Institution of Mechanical Engineers, Part B: Journal of Engineering,* , no. 4, pp. 441-452.

Hyun, S. and Lindgren, L. (2001), Smoothing and adaptive remeshing schemes for graded element, *Communications in Numerical Methods in Engineering,* vol. 17, pp. 1-17.

Jandric, Z. and kovacevic, R. (2004), Heat management in solid free-form fabrication based on deposition by welding, *Proceedings of the Institution of Mechanical Engineers, Part B: Journal of Engineering Manufacturing,* vol. 218, pp.1525-1540.

Jiang, W., yahiaoui, K., Hall, R., Laoui, T. (2005), Finite element simulation of multipass welding: full three-simensional versus generalized plane strain or

axisymmetric mothods, T*he Journal of Strain Analysis for Engineering Design*, vol. 40, no. 6, pp. 587-597.

Jung, G. H. and Tsai, C. L. (2004), Fundamental studies on the effect of distortion control plans on angular distortion in fillet welded T-joints. Welding Journal. 83, no. 7, pp. 213-223.

Karunakaran, K. P., Suryakumar, S., Pushpa, V., Akula, S. (2010), Low cost integration of additive and subtractive processes for hybrid layered manufacturing. *Robotics and Computer-Integrated Manufacturing*, vol. 25, no. 5, pp. 490-499.

Kadivar, M. H., Jafarpur, K., Baradaran, G. H. (2000), Optimizing welding sequence with genetic algorithm. *Computational Mechanics*, vol. 26, pp. 514-519.

Kazanas P, Deherkar P, Almeida P, Lockett H & Williams S. (2012) Fabrication of geometrical features using wire and arc additive manufacture, *Proceedings of the Institution of Mechanical Engineers Part B-Journal of Engineering Manufacture*, vol. 226, no. 6, pp. 1042-1051.

Kim, H. J., Kim, Y. D. and Lee, D. H. (2004), Scheduling for an arc-welding robot considering heat-caused distortion, *Journal of the Operational Research Society,* vol. 56, no. 1, pp. 39-50.

Kruth, J. P., Van Der Schueren, B., Bonse, J. E. and Morren, B. (1996), Basic powder metallurgical aspects in selective metal powder sintering, *CIRP Annals – Manufacturing Technology,* vol. 45, no. 1, pp. 183-186.

Kruth, J. P., Froyen, L., Rombouts, M., Van Vaerenbergh, J. and Mercelis, P. (2003a), New ferro powder for selective laser sintering of dense parts, *CIRP Annals -Manufacturing Technology,* vol. 52, no. 1, pp. 139-142.

Kruth, J. P., Wang, X., Laoui, T. Froyen, L. (2003b), Lasers and material in selective laser sintering. *Assembly Automation,* vol. 23, no. 4, pp. 357-371.

Kruth J P, Levy G, Klocke F, Childs T (2007) Consolidation phenomena in laser and powder-bed based layered manufacturing. *Annals of the CIRP*, vol. 56, no. 2, pp. 730-759.

Kumar, V. and Dutta, D. (1997), An assessment of data formats for layered manufacturing, *Advances in Engineering Software,* vol. 28, no. 3, pp. 151-164.

Labudovic, M., Hu, D., Kovacevic, R. (2003), A three dimensional model for direct laser metal powder deposition and rapid prototyping, *Journal of Materials Science*, vol. 38, pp. 35-49.

Lee, C-H., Chang, K., Lee, C-Y. (2008), Comparative study of welding residual stresses in carbon and stainless steel butt welds, *Proceedings of the Institution of Mechanical Engineers, Part B: Journal of Engineering Manufacturing*, vol. 222, no. 12, pp. 1685-1694.

Leggatt, R., Smith, D., Smith, S., Faure, F. (1996), Development and experimental validation of the deep hole method for residual stress measurement, Journal of Strain Analysis for Engineering Design, vol. 31, no. 3, pp. 177-186.

Levy, G. N., Schindel, R. and Kruth, J. P. (2003), Rapid manufacturing and prapid tooling with layer manufacturing (LM) technologies, state of the art and future perspectives, *CIRP Annals - Manufacturing Technology,* vol. 52, no. 2, pp. 589-609.

Li, J., Guan, Q., Shi, Y. W., Guo, D. L. (2004), Stress and distortion mitigation technique for welding titanium alloy thin sheet, *Science and Technology of Welding and Joining,* vol. 9, no. 5, pp.451-458.

Lindgren, L. (2002), Modelling for residual stresses and deformations due to welding-‘knowing what isn’t necessary to know’, *Mathematical Modelling of Weld Phenomena 6*, pp. 491-518.

Lindgren, L. (2001a), Finite element modelling and simulation of welding: 1. Increased complexity, *Journal of Thermal Stresses,* vol. 24, no. 2, pp. 141–192.

Lindgren, L. (2001b), Finite element modelling and simulation of welding: 2. Improved Material Modeling, *Journal of Thermal Stresses,* vol. 24, no. 3, pp. 195–231.

Lindgren, L. (2001c), Finite element modelling and simulation of welding: 3. Efficiency and Integration*, Journal of Thermal Stresses,* vol. 24, no. 4, pp. 305–224.

Lindgren, L. (2006), Numerical modelling of welding, *Computer Methods in Applied Mechanics and Engineering,* vol. 195, no. 48-49, pp. 6710-6736.

Lindgren, L., Häggblad, H., McDill, J. M. J. and Oddy, A. S. (1997), Automatic remeshing for three-dimensional finite element simulation of welding, *Computer Methods in Applied* Mechanics *and Engineering,* vol. 147, no. 3-4, pp. 401-409.

Lindgren, L. (2007), Computational welding mechanics, Cambridge, Woodhead.

Liu, C. and Zhang, J. X. (2009), Numerical simulation of transient welding angular distortion with external restraints, *Science and Technology of Welding and Joining*, vol. 14, no. 1, pp. 26-31.

Mahapatra, M. M., Datta, G. L., Pradhan, B., Mandal, N. R. (2006), Modelling the effects of constrains and single axis welding process parameters on angular distortions in one-sided fillet welds, *Proceedings of the Institution of Mechanical Engineers, Part B: Journal of Engineering Manufacturing,* vol. 221, no. 3, pp. 397-407.

Mahin, K., Winters, W., Holden, T., Hosbons, R. (1991), Prediction and measurements of residual elastic strain distributions in gas tungsten arc welds, *Welding Journal,* vol. 70, no. 9, pp. 245–260.

Martina, F. (2010), Study of the bebefits of plasma deposition of Ti-6Al-4V structures made by additive layer manufacturing, MSc Thesis, Cranfield.

Masubuchi ,K. (1980), Analysis of welded structures, Oxford, Pergammon

Mazumder, J., Dutta, D., Kikuchi, N., Ghosh, A. (2001), Closed loop direct metal deposition: Art to Part. *Optics and Lasers in Engineering*, vol. 34, no. 4-6, pp. 397-414.

Mcdill, J. M., Goldak, J. A., Oddy, A. S. (1989), An adaptive mesh-management algorithm for three-dimensional automatic finite element analysis, *Proceedings of the Twelfth Canadian Congress of Applied Mechanics,* vol. 1-2, pp. 766-767

Medrano, A., Folkes, J., Segal, J., Pashby, I. (2008), Fibre laser metal deposition with wire: parameters study and temperature monitoring system, in *Proceedings of SPIE - The International Society for Optical Engineering*. 2008. Lisboan.

Mehnen, J. and Trautmann, H. (2008) Robust multi-objective optimisation of weld bead geometry for additive manufacturing. *ICME 2008 Intelligent Computation in Manufacturing Engineering.*

Michaleris, P. and DeBiccari, A. (1997), Prediction of welding distortion, *Welding Journal,* vol. 76, no. 4, pp. 172-181.

Michaleris, P., Zhang, L., Bhide, S. R. and Marugabandhu, P. (2006), Evaluation of 2D,3D and applied plastic strain methods for predicting buckling welding distortion and resitual stress, *Science and Technology of Welding and Joining,* vol. 11, no. 6, pp. 707-716.

Miranda, R.M., Lopes, G., Quintino, L., Rodrigues, J. P., Williams, S. (2008), Rapid prototyping with high power fiber lasers, *Materials and Design,* vol. 29, no. 10, pp. 2072-2075.

Mollicone, P., Camilleri, D., Gray, T. G. F. and Comlekci, T. (2006), Simple thermo-elastic–plastic models for welding distortion simulation, *Journal of Materials Processing Technology,* vol. 176, no. 1-3, pp. 77-86.

Mollicone, P., Camilleri, D., Gray, T. G. F. (2008), Procedural influences on non-linear distortions in welded thin-plate fabrication, *Thin-walled Structures*, vol. 46, pp. 1021-1034.

Mok, S., Bi, G., Folkes, J., Pashby, I. (2008a), Deposition of Ti-6Al-4V using a high power diode laser and wire, Part I: Investigation on the process characteristics, Surface and Coating Technology, vol. 202, no. 16, pp. 3933-3939.

Mok, S., Bi, G., Folkes, J., Pashby, I., Segal, J. (2008b), Deposition of Ti-6Al-4V using a high power diode laser and wire, Part II: Investigation on the mechanical properties, Surface and Coating Technology, vol. 202, no. 19, pp. 4613-4619.

Morrow, W.R., Qi, H., Kim, I., Mazumder, J., Skerlos, S. J. (2006), Environmental aspects of laser-based and conventional tool and die manufacturing. *Journal of Cleaner Production*, vol. 15, no. 10, pp. 932-943.

Moshaiov, A. and Song, H. (1991), Modeling of Welding Distortion in Stiffened Rings. *Journal of Ship Research*, vol. 35, no. 2, pp. 162-171.

Mughal, M. P., Fawad , H. and Mufti, R. (2006a), Finite element prediction of thermal stresses and deformations in layered manufacturing , *Acta Mechanica,* vol. 183, no. 1, pp. 61-79.

Mughal, M. P., Fawad, H. and Mufti, R. (2006b), Parametric thermal analysis of a single molten metal droplet as applied to layered manufacturing, *Heat and Mass Transfer,* vol. 42, no. 3, pp. 226-237.

Mughal, M. P., Fawad, H. and Mufti, R. (2006c), Three-Dimensional Finite-Element Modelling of Deformation in Weld-Based Rapid Prototyping, *Proceedings of the Institution of Mechanical Engineers, Part C: Journal of Mechanical Engineering Science,* vol. 220, no. 6, pp. 875-885.

Mughal, M. P., Mufti, R. and Fawad, H. (2006d), The mechanical effects of deposition patterns in welding-based layered manufacturing, *Proceedings of the Institution of Mechanical Engineers, Part B: Journal of Engineering Manufacture,* vol. 221, no. 10, pp. 1499-1509.

Murugan, S., Rai, S. K., Kumar, P. V., Jayakumar, T., Raj, B. and Bose, M. S. C. (2001), Temperature distribution and residual stresses due to multipass

welding in type 304 stainless steel and low carbon steel weld pads, *International Journal of Pressure Vessels and Piping,* vol. 78, no. 4, pp. 307-317.

Muscato, G., Spampinato, G. and Cantelli, L., (2008), A closed loop welding controller for a rapid manufacturing process, *Proceedings of IEEE International Conference on Emerging Technologies and Factory Automation*, Hamburg, pp. 1080-1083.

Nickel, A. H., Barnett, D. M. and Prinz, F. B. (2001), Thermal stresses and deposition patterns in layered manufacturing, *Materials Science and Engineering: A – Structural Materials: Properties, Microstructure and Processing,* vol. 317, no. 1-2, pp. 59-64.

Nishikawa, H., Serizawa, H., Murakawa, H. (2007), Actual application of FEM to analysis of large scale mechanical problems in welding*, Science and Technology of Welding and Joining,* vol. 12, no. 2, pp. 147-152.

Pavelic, V., Tanbakuchi, R., Uyehara, O. A., Myers, P. O. (1969), Experimental and Computed Temperature Histories in Gas Tungsten-Arc Welding of Thin Plates, *Welding Journal*, vol. 48, no. 7, pp. 295-305.

Peyre, P., Aubry, P., Fabbro, R., Neveu, R., Longuet, A. (2008), Analytical and numerical modelling of the direct metal deposition laser process, *Journal of Physics D: Applied Physics,* vol. 41, no. 2, pp. 1-10.

Pickin, C.G. and Young, K. (2006), Evaluation of cold metal transfer (CMT) process for welding aluminium alloy, *Science and Technology of Welding and Joining,* vol. 11, no. 5, pp. 583-585.

Ploshikhin, V., Prihodovsky, A., Ilin, A., Heimerdinger, C. (2010), Advanced numerical method for fast prediction of welding distortions of large aircraft structures, *International Journal of Microstructure and Materials Properties*, Vol. 5, no. 4-5, pp. 423-435.

Preston, R. V. (2001), Modelling of residual stresses in welded aerospace alloys, PhD thesis, University of Cambridge.

Prevey, P. (1977), A method of determining the elastic properties of alloys in selected crystallographic directions for X-ray diffraction residual stress measurement, *Advances in X-ray Analysis,* vol. 20, pp. 345-354.

Price, D. A., Williams, S. W., Wescott, A., Harrison, C. J. C., Rezai, A., Steuwer, A., Peel, M., Staron, P., Kocak, M. (2007) Distortion control in welding by mechanical tensioning. *Science and Technology of Welding and Joining,* vol. 12, no. 7, pp. 620-633.

Price, D., Paradowska, A., Joshi, S., Finlayson, T. (2006), Residual stresses measurement by neutron diffraction and theoretical estimation in a single weld bead. *International Journal of Pressure Vessels and Piping,* vol. 83, no. 5, pp. 381-387.

Prime, M. (2000) The contour method; simple 2D mapping of residual stress*. In: 6th International conference on residual stress. Oxford: Institute of Materisl.*

Qi, H., Azer, M., and Singh P. (2009), Adaptive toolpath deposition method for laser net shape manufacturing and repair of turbine compressor airfoils, *International Journal of Advanced Manufacturing Technology*, vol.48, no. 4, pp. 121-131.

Qian, Y.P., Huang, J.H., Zhang, H.O. (2010), Study on the factors influencing the layer precision in hybrid plasma-laser deposition manufacturing, *Advanced Materials Research*, vol. 97-101, pp. 3828-3831.

Qin, X. and Michaleris, P. (2009), Themo-elasto-viscoplastic modelling of friction stir welding, *Science and Technology of Welding and Joining*, vol. 14, no. 7, pp. 640-649.

Radaj D (1992), Heat effects in Welding, Berlin, Springer-Verlag

Ribeiro, A. F. M. and Norrish, J. (1996), A 'Square to Round' shape made using metal based rapid prototyping, *5th UK Mechatronics Forum International Conference and 3rd International Conference on Mechatronics and Machine Vision In Practice,* Escola de Engenharia da Universidade do Minho.

Ribeiro, A. F. M., Norrish, J., Mcmaster, R. (1994), practical case of Rapid Prototyping using Gas Metal Arc Welding, University of Minho, Portugal.

Ribeiro, A. F. M. and Norrish, J. (1996), Rapid prototyping using robot welding: slicing system developments, University of Minho, Portugal

Ribeiro, A. F. M. (1998), 3D printing with metals, *Computing and Control Engineering Journal,* vol. 9, no. 1, pp. 31-38.

Ribeiro, A. F. M. and Norrish, J., (1997), Making components with controlled metal deposition. *Proceedings of the IEEE International Symposium on Industrial Electronics,* Guimaraes , Portugal, vol. 3, pp. 831-835.

Rombouts, M., Kruth, J. P., Froyen, L. and Mercelis, P. (2006), Fundamentals of selective laser melting of alloyed steel powders, *CIRP Annals - ManufacturingTechnology,* vol. 55, no. 1, pp. 187-192.

Rosenthal, D. (1946), The theory of moving sources of heat and its application to metal treatments, *Transaction of ASME,* vol. 68, pp. 849-866.

Runnemalm, H. and Hyun, S. (2000), Three-dimensional welding analysis using an adaptive mesh scheme, *Computer Methods in Applied Mechanics and Engineering,* vol. 189, no. 2, pp. 515-523.

Santisteban, J. R., Daymond, M. R., James, J. A., Edwards, L. (2006), ENGIN-X: A third-generation neutron strain scanner, *Journal of Applied Crystallography*, vol. 39, pp. 812-825.

Santos, E. C., Shiomi, M., Osakada, K. and Laoui, T. (2006), Rapid manufacturing of metal components by laser forming, *International Journal of Machine Tools and Manufacture,* vol. 46, no. 12-13, pp. 1459-1468.

Sattari-Far, I. and Javadi, Y. (2008), Influence of welding sequence on welding distortions in pipes, *International Journal of Pressure Vessels and Piping,* vol. 85, no. 4, pp. 265-274.

Sequeira Almeida, P. M. and Williams, S. (2010), Innovative process model of Ti-6Al-4V additive layer manufacturing using cold metal transfer (CMT) , *Proceedings of the Twenty-First Annual International Solid Freeform Fabrication Symposium,* University of Texas at Austin, Austin, TX, USA, August 9-11, 2010.

Schenk, T., Richardson, L. M., Kraska, M., Ohnimus, S. A study on the influence of clamping on welding distortion, *Computational Materials Science*, vol. 45, pp. 999-1005.

Schenk, T., Richardson, I. M., Kraska, M., Ohnimus, S. (2009), Influence of clamping on distortion of welded S355 T-joints, *Science and Technology of Welding and Joining,* vol. 14, no. 4, pp. 369-375.

Schmidt, J., Dorner, H., Tenckhoff, E. (1990), Manufacture of complex parts by shape welding. *Journal of Muclear Materials,* vol. 171, no. 1, pp. 120-127.

Shan, X., Davies, C. M., Wangsdan, T., O'Dowd, N. P. and Nikbin, K. M. (2009), Thermo-mechanical modelling of a single-bead-on-plate weld using the finite element method, *International Journal of Pressure Vessels and Piping,* vol. 86, no. 1, pp. 110-121.

Shan, X. Y., Tan, M. J. and O'Dowd, N. P. (2007), Developing a realistic FE analysis method for the welding of a NET single-bead-on-plate test specimen, *Journal of Materials Processing Technology,* vol. 192-193, pp. 497-503.

Shanghvi, J. Y. and Michaleris, P. (2001), Thermo-elasto-plastic finite element analysis of quasi-state processes in Eulerian reference frames, *International Journal for Numerical Methods in Engineering*, vol. 53, no. 7, pp. 1533-1556.

Sheng, W., Xi, N., Chen, H., Chen, Y. and Song, M. (2003a), Part geometric understanding for tool path planning in additive manufacturing, *Computational Intelligence in Robotics and Automation, 2003.Proceedings.2003 IEEE International Symposium on,* vol. 3.

Sheng, W., Xi, N., Chen, H., Chen, Y. and Song, M. (2003b), Surface partitioning in automated CAD-guided tool planning for additive manufacturing,

Intelligent Robots and Systems, 2003.(IROS 2003).Proceedings.2003 IEEE/RSJ International Conference on, vol. 2.

Smith, M. C. and Smith, A. C. (2009b), NeT bead-on-plate round robin: Comparison of residual stress predictions and measurements, *International Journal of Pressure Vessels and Piping,* vol. 86, no. 1, pp. 79-95.

Smith, M. C. and Smith, A. C. (2009a), NeT bead-on-plate round robin: Comparison of transient thermal predictions and measurements, *International Journal of Pressure Vessels and Piping,* vol. 86, no. 1, pp. 96-109.

Song, Y., Park, S., Choi, D., Jee, H. (2005a), 3D welding and milling: Part I–a direct approach for freeform fabrication of metallic prototypes, *International Journal of Machine Tools and Manufacturing,* vol. 45, no. 9, pp. 1057-1062.

Song, Y., Park, S., Chae, S. (2005b), 3D welding and milling: part II—optimization of the 3D welding process using an experimental design approach, *International Journal of Machine Tools and Manufacturing,* vol. 45, no. 9, pp. 1063-1069.

Song, Y. and Park, S. (2006), Experimental investigations into rapid prototyping of composites by novel hybrid deposition process, *Journal of Materials Processing Technology,* vol. 171, no. 1, pp. 35-40.

Song, C. Y., Park, Y. W., Kim, H. R., Lee, K. Y., Lee, J. (2007). The use of Taguchi and approximation methods to optimize the laser hybrid welding of a 5052-H32 aluminium alloy plate, *Proceedings of the Institution of Mechanical Engineers, Part B: Journal of Engineering Manufacturing,* vol. 222, no. 2, pp. 507-518.

Souloumiac, B., Boitout, F. and Bergheau, J. (2001), A new local-global approach for the modelling of welded steel component distortions, *Mathematical Modelling of Welde Phenomena 6,* pp.573-590.

Spencer, J. D., Dickens, P. M. and Wykes, C. M. (1998), Rapid prototyping of metal parts by three-dimensional welding, *Proceedings of the Institution of*

Mechanical Engineers, Part B: Journal of Engineering Manufacture, vol. 212, no. 3, pp. 175-182.

Spraragen, W., and Claussen, G. E. (1950), Shrinkage distortion in welding –A review of the literature to Jan 1937, Welding Journal, pp. 292-294.

Sreenivasan, R., Goel, A., Bourell, D. L. (2010), Sustainability issues in laser-based additive manufacturing, *Physics Procedia,* vol. 5, no. 1, pp. 81-90.

Staron P, Kocak M, Williams S W and Wescott A (2004), Residual stress in friction stir-welded Al sheets, *Physica B: Condensed Matter,* vol.350, no. 1-3, pp. 491–493.

Syed, W.U.H. and Li, L. (2005a), Effects of wire feeding direction and location in multiple layer diode laser direct metal deposition. *Applied Surface Science*, vol. 248, no. 1-4, pp. 518-524.

Syed, W., Pinkerton, A. J., Li, L. (2005b), A comparative study of wire feeding and powder feeding in direct diode laser deposition for rapid prototyping, *Appplied Surface Science,* vol. 247, no. 1-4, pp. 268-276.

Taminger, K. M., and Hafley, R. A. (2006), Electron Beam Freeform Fabrication (EBF3) for Cost Effective Near-Net Shape Manufacturing, *NASA/TM-2006-214284*, Langley Research Center, Hampton, Virginia.

Tebedge, N., Alpsten, G., and Tall, L. (1973), Residual-stress measurement by the sectioning method. *Experiment Mechanics*, vol. 13, no. 2, pp 88-96.

Tekriwal, P. and Mazumder, J. (1991), Transient and residual thermal strain-stress analysis of arc welding processes. *Proc. of the 5th Int. Conf. Modeling of Casting, Welding and Advanced Solidification process, The Minerals, Metals & Materials Society*, pp. 211

Teng, T., Chang, P. and Tseng, W. (2003), Effect of welding sequences on residual stresses, *Computers & Structures,* vol. 81, no. 5, pp. 273-286.

Totten, G., Howes, M., Inoue, T. (2002), Handbook of Residual Stress and Deformation of Steel. Materials Park, Ohio.

Tsai, C. L., Park, S. C., Cheng, W. T. (1999), Welding distortion of a thin-plate panel structure, *Welding Journal,* vol. 78, pp. 156-165.

Ueda, Y. and Yuan, M. G. (1993), Prediction of residual stresses in butt welded plates using inherent strains, *Journal of Engineering Materials and Technology*, vol. 115, pp. 417-423.

Vasinonta, A., Beuth, J. L. and Griffith, M. L. (2001), A Process Map for Consistent Build Conditions in the Solid Freeform Fabrication of Thin-Walled Structures, *Journal of Manufacturing Science and Engineering,* vol. 123, no. 4, pp. 615-622.

Wang, F., Williams, S., and Rush, M. (2011), Morphology investigation on direct current pulsed gas tungsten arc welded additive layer manufactured Ti6Al4V alloy. *The International Journal of Advanced Manufacturing Technology*, vol. 57, no. 5-8, pp. 597-603.

Wang, S., Goldak, J., Zhou, J., Tchernov, S., Downey, D. (2009), Simulation on the thermal cycle of a welding process by space-time convection-diffusion finite element analysis, *International Journal of Thermal Science*, vol. 48, no. 5, pp. 936-947.

Wang, R., Zhang, J., Serizawa, H. and Murakawa, H. (2009), Study of welding inherent deformations in thin plates based on finite element analysis using interactive substructure method, *Materials & Design,* vol. 30, no. 9, pp. 3474-3481.

Webster, P., Djapic Oosterkamp, L., Browne, P., Hughes, D., Kang, W., Withers, P., Vaughan, G. (2001), Synchrotron X-ray residual strain scanning of a friction stir weld, *The Journal of Strain Analysis for Engineering Design*, vol. 36, no. 1, pp. 61-70.

Withers, P., Bhadeshia, H. (2001), Residual stress Part 1 – Measurement techniques. *Materials Science and Technology*, vol. 17, pp. 355-365.

Withers, P., Turski, M., Edwards, L., Bouchard, P., and Buttle, D. (2007), Recent advances in residual stress measurement, *International Journal of Pressure Vessels and Piping*, vol. 85, pp. 118-127.

Wood, D. (2009), Additive Layer manufacturing at Airbus – Reality check or view into the future?, TCT, vol. 17, no. 3, pp. 23-27.

Yang, J. and Wang, F. (2006), 3D finite element temperature field modelling for direct laser fabrication, *The International Journal of Advanced Manufacturing Technology*, vol. 43, no. 11-12, pp. 1060-1068.

Ye, R., Smugeresky, J. E., Zheng, B., Zhou, Y. and Lavernia, E. J. (2006), Numerical modeling of the thermal behavior during the LENS® process, *Materials Science and Engineering: A,* vol. 428, no. 1-2, pp. 47-53.

Zain-ul-Abdein, M., Nelias, D., Jullien, J., Deloison, D. (2009), Prediction of laser beam welding-induced distortions and residual stresses by numerical simulation for aeronautic application, *Journal of Material Processing Technology*, vol. 209, no. 6, pp. 2907-2917.

Zhang, L. J., Zhang, X. J., Serizawa, H., Murakawa, H. (2007), Parametric study of welding distortion in fillet welded structure based on FEA using iterative substructure method, *Science and Technology of Welding and Joining*, vol. 12, no. 8, pp. 703-707.

Zhang, L. and Michaleris, P. (2004), "Investigation of Lagrangian and Eulerian finite element methods for modeling the laser forming process", *Finite Elements in Analysis and Design*, vol. 40, no. 4, pp. 383-405.

Zhang, Y. M., Li, P., Chen, Y. and Male, A. T. (2002), Automated system for welding-based rapid prototyping, *Mechatronics,* vol. 12, no. 1, pp. 37-53.

Zhang, Y., Chen, Y., Li, P. and Male, A. T. (2003), Weld deposition-based rapid prototyping: a preliminary study, *Journal of Materials Processing Technology,* vol. 135, no. 2-3, pp. 347-357.

Zhang, Y. and Chou, K. (2008). A parametric study of part distortion in fused deposition modelling using three-dimensional finite element analysis. Parametric thermal analysis of a single molten metal droplet as applied to layered manufacturing*,* vol. 222, no. 8, pp. 959-967.

Zhu, X. K. and Chao, Y. J. (2002), Effects of temperature-dependent material properties on welding simulation, *Computers & Structures,* vol. 80, no. 11, pp. 967-976.